UNIVERSITÄT PADERBORN

High energy resolution X-ray absorption and emission based studies on the mono-nuclear spin crossover complex $[Fe(L\text{-}N_4Bn_2)(NCS)_2]$

Dissertation

Vorgelegt von
Dipl.-Chem. Rahel Schepper

Fakultät für Naturwissenschaften
Universität Paderborn

Zur Erlangung des akademischen Grades
„Doktor der Naturwissenschaften“
im Department Chemie

Paderborn 2018

Promotionskommission

Prof. Dr.-Ing. Hans-Joachim Warnecke	Kommissionsvorsitz
Prof. Dr. Matthias Bauer	Erstgutachter
Jun.-Prof. Dr. Stephan Hohloch	Zweitgutachter
Prof. Dr. Thomas Kühne	Drittprüfer

Der Mensch muß bei dem Glauben verharren,
daß das Unbegreifliche begreiflich sei:
er würde sonst nicht forschen.

Johann Wolfgang von Goethe
28.08.1749 – 22.03.1832

Eidesstattliche Erklärung

Hiermit versichere ich, dass ich die vorliegende Arbeit selbstständig und nur unter Verwendung der angegebenen Quellen und Hilfsmittel angefertigt habe. Alle wörtlich oder inhaltlich übernommenen Stellen habe ich als solche gekennzeichnet.

Ich erkläre außerdem, dass die vorliegende Arbeit weder in gleicher noch in ähnlicher Form bereits in einem anderen Prüfungsverfahren vorgelegen hat.

Paderborn, 10.09.2018

Rahel Schepper

Abstract

The steadily increasing demand for digital storage due to the increasing amount of data is a topic that has concerned scientists during the last years. In the future, spin crossover compounds (SCO) could play an important role as new compact storage media or molecular switches.
SCO complexes are an example of potential molecular bistability. This effect describes the ability of a system to undergo a transition from a low spin (LS) state to a high spin (HS) state by an external perturbation such as temperature, pressure or irradiation with light. The exact mechanisms underlying a spin transition are not completely understood yet, since complex processes take place both at the structural and the electronic level. With the most relevant standard methods, these changes cannot be investigated simultaneously in one experiment (Structure change: XRD, XAS, spin state: Mößbauer, SQUID). Therefore, the subject of this thesis is the implementation of modern synchrotron-based hard X-ray spectroscopic methods, namely high-resolution X-ray absorption and X-ray emission spectroscopy, for the investigation of SCO processes. With the help of these methods, it is possible to determine the structural (bond lengths) and electronic changes (spin) in one experiment quasi-simultaneously, without changing the experimental conditions.
Temperature-dependent EXAFS, HERFD-XANES, core-to-core XES, and valence-to-core XES experiments were performed on a mononuclear Fe (II) model complex showing a gradual SCO behaviour. All obtained spectra showed more or less pronounced characteristic changes caused by the transition from the LS to the HS state. To quantify these spectral changes, various already known analysis methods were tested and modified, or new methods were established to obtain the best possible correlation with the present spin state. By comparison with SQUID magnetization data it could be shown that in principle all applied methods are well suited for the investigation of SCO processes.
Using EXAFS spectroscopy, the structural changes could be traced, and it was even possible to resolve the changes in the Fe-N bond lengths of the axial and equatorial N backscatterers. For the analysis of the temperature-dependent HERFD-XANES spectra, a procedure for background correction was developed and it could be shown that the extracted prepeak exhibits a signal whose intensity is directly correlated with the HS fraction in the sample. In the case of core-to-core emission spectroscopy, a large number of different analysis methods was tested, based either on experimentally determined parameters or on fit parameters. The best match with the magnetization data was achieved by the so-called ΔE_{CP} method and the correlation of the energetic position of the maximum of the $K\beta_{1,3}$ line with the spin state. The most surprising result was obtained by the analysis of the valence-to-core spectra. Due to small spectral changes occurring with the spin transition, these spectra were described as being of little benefit for the investigation of

SCO effects in the literature. Despite this, careful analysis of the background corrected spectra allowed a direct correlation of small intensity changes with the HS fraction.

Kurzzusammenfassung

Der ständig wachsende Bedarf an digitalem Speicherplatz aufgrund der immer größer werdenden Datenmengen ist ein Thema, das die Wissenschaft seit vielen Jahren beschäftigt. Spin Crossover-Verbindungen (SCO) könnten als neue kompakte Speichermedien oder molekulare Schalter in Zukunft eine wichtige Rolle spielen.
SCO-Komplexe stellen ein Beispiel für potentielle molekulare Bistabilität dar, d. h. die Systeme sind durch physikalische Einflüsse, wie z. B. Temperatur, Druck oder Licht, von einem Low-Spin-Zustand (LS) in einen High-Spin-Zustand (HS) konvertierbar. Die genauen Mechanismen die einem Spin-Übergang zu Grunde liegen, sind noch nicht vollständig verstanden, da sowohl auf struktureller als auch auf elektronischer Ebene komplexe Prozesse stattfinden, die mit den bisherigen Standardmethoden nicht gleichzeitig in einem Experiment untersucht werden können (Strukturänderung: XRD, XAS; Spin-Zustand: Mößbauer, SQUID).
Thema dieser Arbeit ist deshalb die Etablierung moderner Synchrotron-basierter röntgenspektroskopischer Methoden, der hochauflösenden Röntgenabsorptions- und Röntgenemissions-Spektroskopie, zur Untersuchung von SCO-Prozessen. Mit Hilfe dieser Methoden ist es möglich die strukturellen (Bindungslängen) und elektronischen Änderungen (Spin) in einem Experiment quasi-simultan, unter gleichen experimentellen Bedingungen zu bestimmen.
An einem mononuklearen Fe(II) Modell-Komplex, der ein graduelles SCO-Verhalten zeigt, wurden temperaturabhängige EXAFS-, HERFD-XANES-, Core-to-Core-XES- und Valence-to-Core-XES-Experimente durchgeführt. Alle erhaltenen Spektren zeigten mehr oder weniger ausgeprägte, charakteristische Änderungen beim Übergang vom LS- zum HS-Zustand. Zur Quantifizierung der spektralen Änderungen wurden verschiedene bereits bekannte Analysemethoden getestet und modifiziert, beziehungsweise neue Methoden etabliert um eine bestmögliche Korrelation mit dem vorliegenden Spin-Zustand zu erhalten. Durch Vergleiche mit SQUID-Magnetisierungs-Daten konnte gezeigt werden, dass grundsätzlich alle angewendeten Methoden gut geeignet sind um SCO-Prozesse zu untersuchen.
Die strukturellen Änderungen konnten mittels EXAFS-Spektroskopie nachverfolgt werden, wobei es sogar möglich war, die Änderung der Fe-N-Bindungslängen der axialen und der äquatorialen N-Rückstreuer aufzulösen. Zur Analyse der temperaturabhängigen HERFD-XANES-Spektren wurde eine Untergrundkorrektur entwickelt und es konnte gezeigt werden, dass der extrahierte Prepeak ein Signal aufweist, dessen Intensität direkt mit dem HS-Anteil in der Probe korreliert. Im Fall der Core-to-Core-Emissionsspektroskopie wurde eine große Anzahl verschiedener Analysemethoden getestet, die entweder auf experimentell bestimmten Parametern oder auf Fitparametern basierten. Die beste Übereinstimmung mit den Magnetisierungs-Daten lieferten die sogenannte ΔE_{CP}-Methode sowie die Korrelation der energetischen Lage des Maximums der $K\beta_{1,3}$-Linie mit

dem Spin-Zustand. Das überraschendste Ergebnis lieferte die Analyse der Valence-to-Core-XES-Spektren, die aufgrund geringer spektraler Änderungen in der Literatur als wenig geeignet für die Untersuchung von SCO-Effekten beschrieben wurden. Durch eine sorgfältige Analyse der untergrundkorrigierten Spektren konnten geringe Intensitätsänderungen jedoch direkt mit dem HS-Anteil korreliert werden.

Danksagung

An dieser Stelle möchte ich einigen Personen danken, die zum Erfolg dieser Arbeit beigetragen haben.
An erster Stelle möchte ich Matthias Bauer dafür danken, dass er mich in seinen Arbeitskreis aufgenommen und mir die Möglichkeit zur Promotion auf dem interessanten Gebiet der Röntgenspektroskopie geboten hat. Für sein Vertrauen, die Unterstützung sowie alle (nicht-)fachlichen Ratschläge möchte ich mich ebenso bedanken, wie für die ermöglichte Teilnahme an zahlreichen Messzeiten, Konferenzen und die Mitarbeit in diversen Kooperationsprojekten.
Des Weiteren möchte ich Juniorprofessor Dr. Stephan Hohloch für seine unkomplizierte Art und die Übernahme des Zweitgutachtens danken.
Dem Arbeitskreis Krüger aus Kaiserslautern, insbesondere Markus Schmitz und Manuel Reh danke ich für die Synthese und Bereitstellung diverser SCO-Komplexe sowie Referenzen. Meinem Vertiefungspraktikanten Dominic Bernhard möchte ich für die Bearbeitung einiger CtC-Daten danken, die ihren Weg in diese Arbeit gefunden haben.
Allen Kooperationspartnern danke ich für die erfolgreiche Zusammenarbeit, die einige Früchte in Form von Publikationen getragen hat.
Bei allen aktuellen und ehemaligen Mitarbeitern des Arbeitskreises Bauer bedanke ich mich für eine lange gemeinsame Zeit, die immer unterhaltsam war. Insbesondere gilt mein Dank dem gesamten „Röntgen-Team“, das auf vielen Messzeiten mitgelitten, gefuttert und durchaus auch viel Spaß gehabt hat. Britta Fremerey danke ich für die netten Gespräche sowie für die Versorgung mit wichtigen Infos, Telefonnummern, Briefumschlägen und vielem mehr.
Weiterhin möchte ich Roland Schoch für die nette Aufnahme in das damalige „Arbeitsdreieck“ Bauer und für die Hilfe bei den ersten Schritten auf dem Gebiet der Röntgenspektroskopie, speziell der EXAFS-Auswertung danken. Außerdem für viele, viele lustige aber auch anstrengende Messzeiten mit Schokoladenstudien, die ersten gemeinsamen Schritte in Paderborn, diverse Laufrunden, Kochabende (hier sei natürlich auch Anke Schoch gedankt) und vieles mehr.
Ganz besonders bedanke ich mich bei meinem langjährigen Büropartner Patrick Müller für die vielen Gespräche über alle möglichen, auch fachlichen Themen, Teerunden und Sporteinheiten. Für seine aufgebrachte Geduld mir sämtliche (auch durchaus blöde) Fragen zum Thema Quantenchemie und Theorie zu beantworten sowie für seine unerschütterliche Ruhe, die vor allem auf vielen gemeinsamen Messzeiten nützlich war, danke ich ihm herzlich.
Meinen Katzen Lilly und Milka, die den Abschluss dieser Arbeit leider nicht mehr miterleben konnten, möchte ich dafür danken, dass sie mir immer viel Freude bereitet haben und mich an schlechten Tagen immer wieder aufmuntern konnten. Besonders Lilly gilt

mein Dank, die beim Schreiben dieser Arbeit viele Stunden auf meinem Schoß verbracht und mich somit an den Schreibtisch gefesselt hat.
Zu guter Letzt möchte ich meiner Familie, ganz besonders meiner Mama, danken. Durch ihr Vertrauen und ihre Unterstützung wurde es mir überhaupt erst ermöglicht dieses Ziel zu erreichen. Peter danke ich von ganzem Herzen dafür, dass er auch in schwierigen Phasen einfach da war, für die Unterstützung und den Antrieb, was letztendlich doch noch zur Fertigstellung dieser Arbeit geführt hat.

List of Beamtimes

Ångstrømquelle Karlsruhe (ANKA)

XAS	◦ 23.-29.05.2013	◦ 02.-06.12.2014
	◦ 27.-31.10.2013	◦ 19.-23.05.2015
	◦ 03.-06.06.2014	◦ 12.-14.11.2015

Berliner Elektronenspeicherring-Gesellschaft für Synchrotron-strahlung (BESSY II)

U41-PGM	◦ 27.07.-04.08.2013	◦ 25.-31.08.2014

Deutsches Elektronensynchrotron (DESY)

P65	◦ 02.-06.06.2016	◦ 20.-25.04.2017
	◦ 27.07.-02.08.2016	◦ 03.-09.04.2018
P64	◦ 05.-12.09.2017	

Diamond Light Source

B18	◦ 07.-11.08.2017

European Synchrotron Radiation Facility (ESRF)

BM01B	◦ 04.-10.02.2014	
BM23	◦ 12.-17.06.2014	
BM25A	◦ 09.-14.07.2014	
ID26	◦ 21.-26-02.2013	◦ 14.-21.04.2015
	◦ 25.03.-01.04.2013	◦ 16.-22.11.2016
	◦ 13.-19.11.2013	

List of Publications

Publications in Journals

1. Irene Bräunlich, Antoni Sánchez-Ferrer, Matthias Bauer, Rahel Schepper, Philippe Knüsel, Julia Dshemuchadse, Raffaele Mezzenga and Walter Caseri: "Polynuclear Iron(II)−Aminotriazole Spincrossover Complexes (Polymers) In Solution", *Inorg. Chem.* **2014**, *53*, 3546-3557.

2. Antoni Sánchez-Ferrer, Irene Bräunlich, Janne Ruokolainen, Matthias Bauer, Rahel Schepper, Paul Smith, Walter Caseri and Raffaele Mezzenga: "Gels, xerogels and films of polynuclear iron(II)–aminotriazole spin-crossover polymeric complexes", *RSC Adv.* **2014**, *4*, 60842-60852.

3. Claudia Wilfer, Patricia Liebhäuser, Alexander Hoffmann, Hannes Erdmann, Oleg Grossmann, Leander Runtsch, Eva Paffenholz, Rahel Schepper, Regina Dick, Matthias Bauer, Maximilian Dürr, Ivana Ivanović-Burmazović and Sonja Herres-Pawlis: "Efficient Biomimetic Hydroxylation Catalysis with a Bis(pyrazolyl)-imidazolylmethane Copper Peroxide Complex", *Chem. Eur. J.* **2015**, *21*, 17639-17649.

4. Peter Zimmer, Patrick Müller, Lukas Burkhardt, Rahel Schepper, Adam Neuba, Jakob Steube, Fabian Dietrich, Ulrich Flörke, Stefan Mangold, Markus Gerhards and Matthias Bauer: "N-Heterocyclic Carbene Complexes of Iron as Photosensitizers for Light-Induced Water Reduction", *Eur. J. Inorg. Chem.* **2018**, *11*, 1504-1509.

5. Peter Zimmer, Lukas Burkhardt, Aleksej Friedrich, Jakob Steube, Adam Neuba, Rahel Schepper, Patrick Müller, Ulrich Flörke, Marina Huber, Stefan Lochbrunner and Matthias Bauer: "The Connection between NHC Ligand Count and Photophysical Properties in Fe(II) Photosensitizers: An Experimental Study", *Inorg. Chem*. **2018**, *57*, 360-373.

6. Antara Garai, Sebastian Sobottka, Rahel Schepper, Woormileela Sinha, Matthias Bauer, Biprajit Sarkar and Sanjib Kar: "Chromium Complexes with Oxido and Corrolato Ligands: Metal-Based Redox Processes versus Ligand Non-Innocence", *Chem. Eur. J*. **2018**, *24*, 12613-12622.

7. Peter Zimmer, Lukas Burkhardt, Rahel Schepper, David Gosztola, Kaibo Zheng, Adam Neuba, Ulrich Flörke, Christoph Wölper, Roland Schoch, Wojciech Gawelda, Sophie E. Canton and Matthias Bauer: "Towards noble-metal free dyads: Ground and excited state tuning by a cobalt dimethylglyoxime catalyst connected to an iron N-heterocyclic carbene photosensitizer", DOI: 10.1002/ejic.201800946.

8. Rahel Schepper, Markus Schmitz, Hans-Jörg Krüger and Matthias Bauer: "Insights into the spin crossover behaviour of $[Fe(L\text{-}N_4Bn_2)(NCS)_2]$ with high energy resolution hard X-ray absorption and emission spectroscopy", manuscript in preparation.

9. Reni Grauke, Rahel Schepper, Jabor Rabeah, Matthias Bauer and Angelika Brückner: "Influence of the activator on the chromium catalysed ethylene tetramerization: A combined EPR and XAS study", manuscript in preparation.

10. Rahel Schepper, Oliver Groß and Matthias Bauer: "Influence of Oxidation State and Ligand Environment on the Cr K-edge XANES Spectra", manuscript in preparation.

Talks

Rahel Schepper, Matthias Bauer: "High energy resolution X-ray absorption and emission spectroscopy for the investigation of spin crossover processes", XAFS16, Karlsruhe, August 27, 2015.

Poster Presentations

1. Rahel Schepper, Markus Schmitz, Hans-Jörg Krüger, Matthias Bauer: "X-ray spectroscopy as powerful tool in spin crossover research on iron complexes", 2^{nd} International Conference on Bimetallic Complexes, Karlsruhe, September 23-25, 2013.

2. Rahel Schepper, Matthias Bauer: "High energy resolution X-ray absorption and emission: New techniques to push the limits in hard X-ray catalysis research", Bunsentagung, Hamburg, May 29-31, 2014.

3. Rahel Schepper, Markus Schmitz, Hans-Jörg Krüger, Matthias Bauer: “High energy resolution X-ray absorption and emission spectroscopy for the investigation of spin crossover processes”, Koordinationschemie-Tagung, Paderborn, March 22-24, 2015.

4. Rahel Schepper, Markus Schmitz, Hans-Jörg Krüger, Matthias Bauer: “High energy resolution X-ray absorption and emission spectroscopy for the investigation of spin crossover processes”, Bunsentagung, Bochum, May 14-16, 2015.

5. Rahel Schepper, Markus Schmitz, Hans-Jörg Krüger, Matthias Bauer: “High energy resolution X-ray absorption and emission spectroscopy for the investigation of spin crossover processes”, Bunsentagung, Rostock, May 05-07, 2016.

6. Rahel Schepper, Markus Schmitz, Hans-Jörg Krüger, Matthias Bauer: “High energy resolution X-ray absorption and emission spectroscopy for the investigation of spin crossover processes”, International Workshop on Photoionization & Resonant Inelastic X-ray Scattering, Aussois (France), March 26-31, 2017.

Table of Contents

List of Abbreviations

A	Area
$\mathbf{A}$	Electro-magnetic vector field
$A_j(k)$	Amplitude of scattering event at j^{th} shell
afac	Amplitude reducing factor, $S_i(k)$
ax	Axial
bian	Bis(phenyl)iminoacenaphtene
c	Speed of light: 2.99792 10^8 m/s
COM	Centre of mass
C_p	Molar heat-capacity under constant pressure
CT	Charge transfer
CtC	Core-to-core
d	Lattice constant
d_0	Density of the solvent
d_s	Density of solution
DFT	Density functional theory
ΔE_{CP}	Energy splitting between maximum of $K\beta_{1,3}$ peak and centre of mass of the spectrum
ΔE^0_{HL}	Zero-point energy difference between HS and LS
ΔE_M	Magnetic dipole splitting
ΔE_Q	Electric quadrupole splitting
Δ_O	Ligand field splitting
E	Energy
E_0	Threshold or zero-point energy
$E_{binding}$	Binding energy of an electron
E_f	Fermi energy
E_f	Energy of final state
E_g	Energy of initial state
E_{kin}	Kinetic energy
E_n	Energy of intermediate state
EPR	Electron paramagnetic resonance
eq	Equatorial
EXAFS	Extended X-ray absorption fine structure
f	Spectrometer frequency
f	Final state

FC	Fit curve
$F_j(k)$	Backscattering amplitude
F_{KH}	Kramers-Heisenberg cross-section
FEL	Free electron laser
FT	Fourier transformation
FWHM	Full width at half maximum
G	Molar Gibbs energy
h	Planck constant: 6.6260755 10^{-34} J s
H	Molar enthalpy
H	Magnetic field vector
HAXIESST	Hard X-ray induced excited spin state trapping
HERFD	High energy resolution fluorescence detected
HOMO	Highest occupied molecular orbital
HS	High spin
i	Initial state
I	Intensity
I_0	Incident intensity
I_f	Fluorescence intensity
Inten.	Intensity
IR	Infrared
k	Force constant
k	Wave vector
L-N_4Bn_2	N,N′-Dibenzyl-2,11-diaza[3.3](2.6)pyridinophane
L-N_4Me_2	N,N′-Dimethyl-2,11-diaza[3.3](2.6)pyridinophane
LIESST	Light-induced excited spin state trapping
LS	Low spin
LUMO	Lowest unoccupied molecular orbital
m	Mass of electron: 9.10938356 10^{-31} kg
M	Magnetization
MLCT	Metal-to-ligand charge transfer
n	Intermediate state
n	Diffraction order
N_j	Number of atoms
NFS	Nuclear forward scattering
NIS	Nuclear inelastic scattering
NIESST	Nuclear decay induced excited spin state trapping
NMR	Nuclear magnetic resonance
$\hat{O}'^{\dagger}$, $\hat{O}$	Transition operator
p	Momentum of electron

p	Pressure
P	Spin pairing energy
PdAdH	2,6-pyridindialdihydrazone
PFY	Partial fluorescence yield
phen	1,10-Phenanthroline
QXAFS	Quick X-ray absorption fine structure
r	Metal-donor atom bond length
r_j	Distance absorbing atom – scattering atoms in j^{th} shell
R	Radius
R	Gas constant: 8,314472 J mol^{-1} K^{-1}
R_{HS}, R_{LS}, R_T	Metal-donor atom bond length for HS, LS and at temperature T
RIXS	Resonant inelastic X-ray scattering
S	Molar entropy
S	Spin
$S_i(k)$	see afac
SCO	Spin crossover
SOXIESST	Soft X-ray induced excited spin state trapping
SQUID	Superconducting quantum interference device
T	Temperature
$T_{1/2}$	Spin transition temperature (conversion of 50 % of SCO-active complex molecules)
v	Velocity
VtC	Valence-to-core
x	Path length
XAFS	X-ray absorption fine structure
XANES	X-ray absorption near edge structure
XAS	X-ray absorption spectroscopy
XES	X-ray emission spectroscopy
XRF	X-ray fluorescence spectrometry

γ_{HS}	High spin fraction
γ_{LS}	Low spin fraction
Γ_{CEE}	Energy / lifetime broadening of constant emission energy scan
Γ_f, Γ_n	Energy / lifetime broadening of final and intermediate state
δ	Isomer shift

λ	Wavelength
ε	Polarisation
θ	Bragg angle
μ	Reduced mass: $\mu = \frac{m_1 m_2}{m_1 + m_2}$
$\mu_0(E)$	Atomic background
$\mu(E)$	Linear absorption coefficient
ν	Frequency
σ	Photoelectric absorption cross section
σ_j	Debye-Waller-like factor
τ	Scattering cross section (elastic and inelastic)
$\phi_{ij}(k)$	Total phase shift
χ_M, χ_{HS}, χ_{LS}	Molar magnetic susceptibility, HS respective LS contribution
$\chi(E)$	Energy-dependent, isolated and normalized fine structure
ω	Incident energy
ω_{in}, ω_{out}	Angular velocity of incoming and outgoing photon
Ω	Emitted energy

1 Introduction

1.1 Outline

The spin crossover (SCO) phenomenon is still a challenging research field for physicists and chemists today. In a time of steadily increasing requirements of smaller electronic devices and growing need of data storage capacities, researchers are focused on the exploration of appropriate new materials for these purposes. Due to the possible application of SCO compounds as electronic devices, like for example molecular switches or displays, a detailed understanding of the working principles is mandatory.[1–7] The concept of molecular bistability, which describes the ability of a system to be observed in two different electronic states depending on the degree of an external perturbation, is necessary for the realization of such applications.[8] Enormous insights into the properties of SCO compounds have been gained since its discovery about 80 years ago.[9] Extensive and comprehensive reviews covering all aspects of current SCO research have been published during the last years.[10–14] Nevertheless, it still remains difficult to describe or to predict the processes occurring during the spin transition exactly. Therefore, this work is focused on the development and improvement of different synchrotron radiation based spectroscopic methods, namely X-ray absorption and emission spectroscopy, for the investigation of SCO compounds and the SCO transition process. These methods show great potential for SCO research since they can provide structural as well as electronic information simultaneously and element specific and are applicable to samples in every state of aggregation. The main focus of this work lies on the development of new analysis tools and procedures that allow to correlate spin changes at the metal centre of SCO compounds with localized structural changes.

Chapter 1.2 describes the essential basics of SCO, like the different types of SCO and how it can be induced, and gives an overview on the standard methods applied for SCO research. Chapter 1.3 aims to give an insight into the background of the X-ray spectroscopic methods and the possibilities these techniques offer for the examination of SCO processes.

1.2 The Spin Crossover Phenomenon

SCO is a very fascinating process in coordination chemistry of mainly 3d transition metals with an electronic configuration of d^4-d^7. For ions of the second and third transition series (4d and 5d) SCO is very rare due to the stronger ligand fields induced by these metals.[15] The electronic ground state of an octahedral complex could be either low spin (LS) or high spin (HS) depending on how the electrons are distributed to the non-bonding t_{2g} and σ-antibonding e_g^* levels. The energy difference between the two sets of orbitals is called ligand field splitting Δ_O following the simplified ligand field theory ($\Delta_O = 10Dq$ for octahedral complexes), which depends on the central metal ion as well as on the type of coordinating ligands. If Δ_O is much higher than the energy needed for spin pairing (P) the electrons occupy the t_{2g} orbitals of lowest energy first (strong ligand field). In systems with more than six electrons the e_g^* orbitals are occupied afterwards. The resulting ground state in this case is a $^1A_{1g}$ LS state. A ligand field splitting Δ_O much smaller than the spin pairing energy P leads to a distribution of the electrons according to Hund's rule (weak ligand field). The ground state is then a $^5T_{2g}$ HS state.[16]
In addition to the both mentioned extreme cases $\Delta_O << P$ and $\Delta_O >> P$, it is possible that the ligand field splitting and the spin pairing energy are of similar magnitude. Triggered by an external perturbation, like a change of temperature T, pressure p or irradiation with light $h\nu$, the system is able to undergo a transition from a LS state to a HS state with a higher spin multiplicity.[1,2,8,17–21] Scheme 1.1 illustrates the case for an iron(II) system with an electronic configuration of d^6.

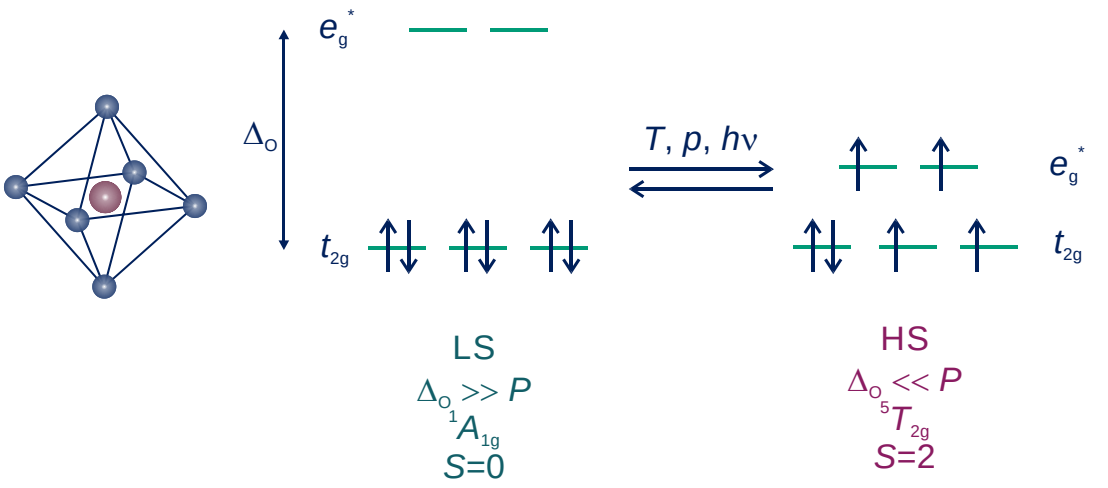

Scheme 1.1: Schematic depiction of SCO for an octahedral system with an electronic configuration of d^6. The SCO can be induced by T, p or hν.

In the 1930s, *Cambi and co-workers* observed an unusual magnetic behaviour of iron(III) complexes with various dithiocarbamate ligands, that lead to the discovery of temperature dependent spin state switching between two different spin states.[9] About 30 years later, in the early 1960s, *Busch et al.* performed several studies to define the SCO regions for iron(II) and cobalt(II). With $[Co(PdAdH)_2]I_2$ the first cobalt SCO complex was reported (PdAdH = 2,6-pyridindialdihydrazone).[22–24] Almost at the same time *König* and *Madeja* conducted a study to identify the SCO region of different $[Fe(phen)_2X_2]$ complexes (phen = 1,10-phenanthroline). For this, they varied the anionic X-ligand systematically (X^- = Br^-, Cl^-, SCN^-, N_3^-, OCN^-, $HCOO^-$, CN^-...) and found out that depending on the induced ligand field a LS or HS state was adopted.[25] In frame of these studies the first synthetically produced iron(II) SCO complex $[Fe(phen)_2(NCS)_2]$ was found.[26–28] In 1964, *Ewald et al.* extended the previous studies on the different iron(III) dithiocarbamate systems of *Cambi and co-workers* and proved the pressure dependency of the magnetic behaviour. As it was expected, the LS state corresponding to a lower molecular volume due to shorter bond lengths was favoured with rising pressure (refer Le Chatelier's principle).[29] In the following years the number of monomeric SCO compounds increased steadily and with Mößbauer spectroscopy a further method suitable for the investigation of spin transition effects was established.[30–32] Especially for iron(II) a wide variety of SCO complexes with primary N-donor ligands, like different substituted phenanthroline and bipyridine ligands, was synthesized and their magnetic and spectroscopic properties were examined with a number of different experimental techniques (e.g. X-ray diffraction, Mößbauer, UV/Vis or infrared spectroscopy, heat capacity measurements etc., for more details see chapter 1.2.2.2). The results of the early years of SCO research are summarized in several reviews by *König* (1968)[33], *Goodwin* (1976)[34] and *Gütlich* (1981)[35]. Especially the work of *Gütlich* gives an extensive review on the applied experimental methods and the classes of ligands used for the design of mononuclear iron(II) SCO complexes. Although until now, most of the known SCO compounds are Fe(II) (d^6)[8,19,20,36–38] and to a far lesser extend Fe(III) (d^5)[37,39] and Co(II) (d^7)[40–42] compounds, several examples for further 3d transition metals like Co(III) (d^6), Mn(III) (d^4), Mn(II) (d^5) and Cr(II) (d^4) were identified.[15] About ten years ago *Gütlich* and *Goodwin* published a detailed series of three books covering all aspects of current SCO research.[12–14] In recent times, SCO research started to diverge in many different directions. In "Spin-Crossover Materials" edited by *Halcrow* several up-to-date topics like novel mononuclear, polynuclear or polymeric SCO compounds, SCO in oxides as well as recent improvements in the theoretical description of spin transitions or new characterization methods are summarized.[10]

After this brief historical review, the different ways to induce a spin transition will be discussed shortly in the following section.

1.2.1 Physical Perturbations Influencing Spin Crossover Systems

As mentioned before the spin transition can be initiated by various external perturbations. Besides the change of temperature, that will be used to describe further aspects of SCO in a separate section later, the change of pressure can induce or modify a spin transition as well. By application of pressure to a SCO system in most cases the LS state is stabilized due to a reduction of the molecular volume. This is caused by a shortening of the metal-donor atom distances in the LS compared to the HS state,[17] since the e_g^* molecular orbitals are usually of antibonding nature.

Irradiation with light plays an important role for possible future applications of SCO compounds as molecular switches, too. In solution the spin equilibrium between LS and HS can be disturbed by irradiation with pulsed laser light into the charge transfer (CT) band of the LS state. The respective absorption band is bleached due to a subsequent decay into the HS state, which then rapidly decays back to the LS ground state. The return to the equilibrium conditions can be monitored by the increasing intensity of the CT absorption band.[43] A very similar effect in the solid state was found by *Decurtins et al.* and was named light-induced excited spin state trapping (LIESST).[44,45] At cryogenic temperatures ($T < 50$ K) a SCO system can be partially or completely converted from the LS to a meta-stable HS state by irradiation with light. This HS state exhibits a very long lifetime

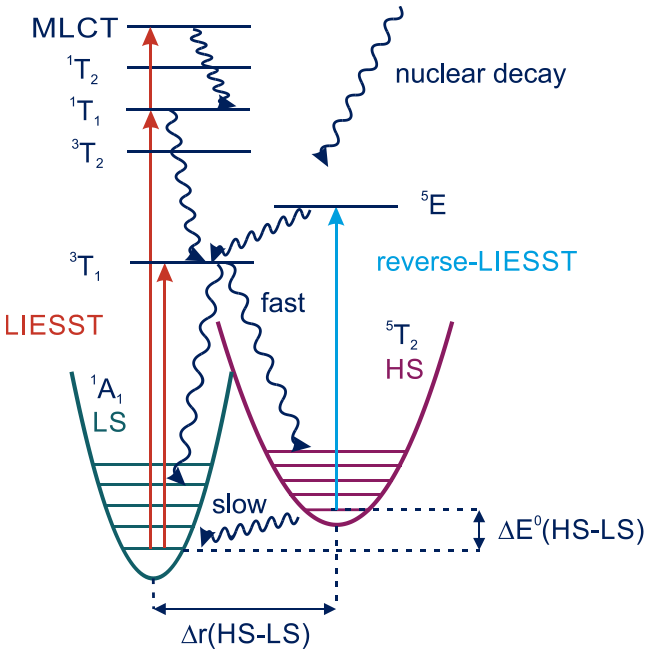

Scheme 1.2: Schematic illustration of the electronic structure of an iron(II) d^6 complex in the SCO region. The mechanisms of LIESST, reverse-LIESST and nuclear decay are depicted. Straight arrows indicate spin allowed d-d transitions while non-radiative relaxation processes are denoted by wavy lines.[48]

if the temperature is sufficiently low. So the system is "trapped" in the HS state at low temperatures since the possibility to overcome the energy barrier between the HS and LS spin potential thermally is reduced significantly. With the discovery of the "reverse-LIESST" effect *Hauser et al.* could show that irradiation of this meta-stable HS state with light of longer wavelengths could switch the system back to the thermodynamically stable LS state.[46–48] Scheme 1.2 illustrates the electronic structure of an iron(II) d^6 system with the respective mechanisms of the LIESST and reverse-LIESST effect. Considering the complete reversibility of the LS↔HS transition, the potential use of SCO compounds as molecular switches or memory devices is strongly emphasized.
Irradiation with soft (SOXIESST)[49] or hard X-rays (HAXIESST)[50] leads to essentially the same phenomenon, with the only difference that the spin transition is induced by much higher energies. Apart from this, the nuclear decay-induced excited spin state trapping (NIESST) based on the Mößbauer effect (see chapter 1.2.2.2 for further details) is a further possibility to induce a spin transition.[51]

1.2.2 Detection of Spin Crossover

Considering the information gained in the previous sections, SCO obviously influences a number of physicochemical properties. Certainly the two most important consequences are the changes in the magnetic properties and in the metal-donor atom distances. The latter originate from the change in occupancies of the non-bonding t_{2g} and anti-bonding e_g^* levels while the magnetic changes result from an increase of the paramagnetism of the system in course of the LS→HS transition and the thereby increased spin. Furthermore, the thermodynamic as well as light absorbing properties, resulting in a change of the colour of the system, are influenced (for further details see chapter 1.2.2.2).

1.2.2.1 Types of Spin Crossover

Based on all these effects, a number of different experimental techniques for detection and monitoring of SCO are available today and will be discussed subsequently. But first of all, the main characteristics of a SCO process will be elucidated and illustrated. The main objective of the characterization by the analytical methods is to describe the course of the spin transition and to determine the spin transition temperature $T_{1/2}$, which is defined as the temperature at which 50% of the SCO active complexes are converted to the other spin state. In general, a spin transition curve can be obtained by plotting the HS fraction γ_{HS} vs. temperature. As shown in Figure 1.1, the spin transition can take place in a number of different forms and the most important source for these differences is the degree of cooperativity. Cooperativity describes to which extent the changes induced by the spin transition, like for example the change of the volume of the molecule, are propagated throughout the crystal lattice. It can be influenced by two different factors: On the

one hand by the nature of the intermolecular interactions, like Van-der-Waals- or π-π interactions or hydrogen bridge bonds, and on the other hand by the dimension of the network.[52]

Probably the most common SCO type is a gradual spin transition (Figure 1.1a)) where cooperativity is only weak. This is mainly the case for solutions, where a Boltzmann distribution of the molecular states is involved, but a high number of solid systems show a gradual transition, too.[8]

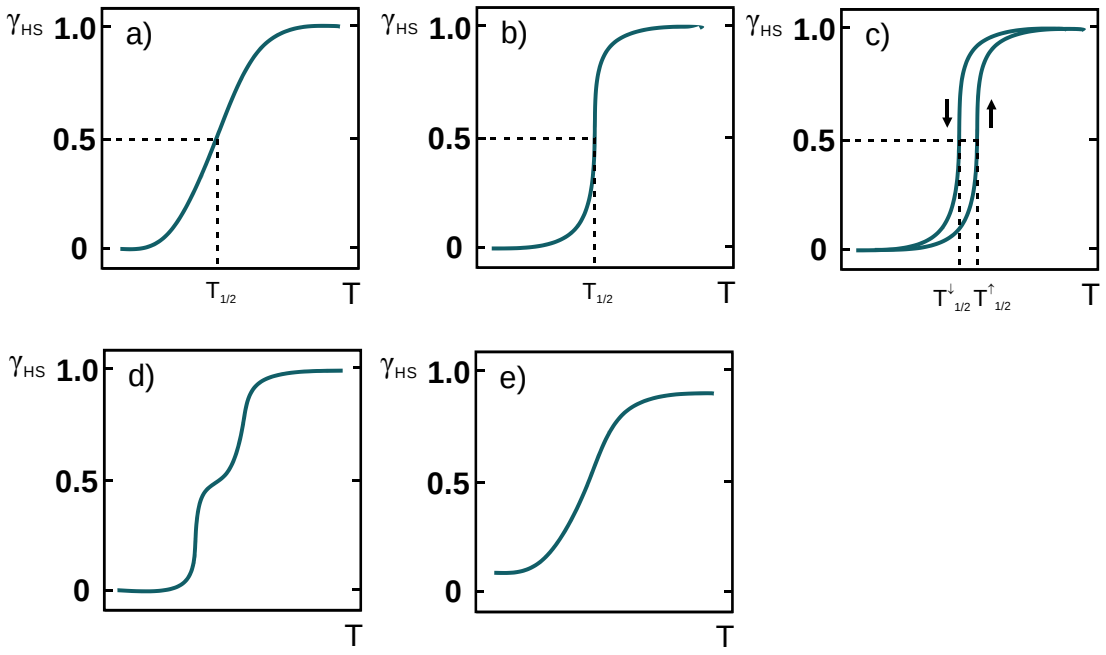

Figure 1.1: Representation of the different types of spin transition curves in terms of HS fraction vs. temperature: a) gradual; b) abrupt; c) with hysteresis; d) two-step; e) incomplete.[8]

If a strong cooperativity is present, the spin transition occurs in an abrupt way like shown in Figure 1.1b). Hysteresis (Figure 1.1c)) may occur in cases with particularly strong cooperativity. Then the spin transition is often accompanied by a crystallographic phase change that confers bistability on the system. Bistability, and therefore a memory effect, serves as a prerequisite for the potential use of SCO compounds as molecular switches or storage devices. Mainly two different origins for the occurrence of hysteresis are known. As mentioned before, the spin transition can be associated with a phase change in the lattice, which leads to the hysteresis. As a second possibility, the intramolecular changes of the structure are communicated to the neighbouring molecules by a highly effective cooperative interaction. Possible origins of these interactions, as described above, can be covalent bonds in polymeric systems, hydrogen bonds or π-π interactions which can be more or less pronounced depending on the spin state and external perturbation.[8]

In SCO complexes with two different lattice sites or in binuclear systems a two-step transition (Figure 1.1d)) can occur, but this type of transition is rather rare. In this kind of transition, the spin transition occurs stepwise and can even show a plateau. The last type to mention, is a so-called incomplete spin transition (Figure 1.1e)). In this case, either a HS fraction remains at low temperatures or scarcer a LS fraction at high temperatures. Various sources can lead to this case, for example a certain amount of the SCO molecules may be present in a different lattice site with a lower ligand field strength, so the HS state is preferred. Another explanation is based on a kinetic effect: at low temperatures the conversion rate from HS to LS becomes very low, so a part of the molecules remains in the HS state, like described for the LIESST effect before.[8]

1.2.2.2 Experimental Techniques for the Detection of Spin Crossover

The following subsection deals with the different techniques for detection of SCO processes. The possibilities and limitations of each method as well as the obtainable information are discussed shortly.

Magnetic Susceptibility Measurements

The most common technique to characterize SCO compounds is the measurement of the magnetic susceptibility as a function of temperature, $\chi(T)$, which follows the transition from a paramagnetic HS at high temperatures to a less paramagnetic or even diamagnetic LS state at low temperatures.[8,16,38,53] Usually, the HS ↔ LS transition is reflected in a drastic change of the magnetic susceptibility χ, which describes the extent of magnetization **M** of a sample in an external magnetic field **H** following $\mathbf{M} = \chi\mathbf{H}$.

Diamagnetic compounds (with $S = 0$) are characterized by a negative magnetic susceptibility, since in accordance to Lenz's law an external magnetic field induces a magnetic field in the compound that counteracts the external field. In contrast, paramagnetic substances (with $S \neq 0$) exhibit a positive magnetic susceptibility, because the external magnetic field results in an alignment of electron spins, which in turn results in an increased magnetic flux density in the compound.

Today, measurements of solid samples are mainly performed by SQUID (superconducting quantum interference device) magnetometry, which has more or less replaced the former used balance methods by Faraday or Gouy, due to a much higher sensitivity (up to four magnitudes) and accuracy. The method is based on the sensitivity of a superconductive ring-shaped sensor with a small isolating barrier, a so-called Josephson contact, to changes of the magnetic flux as a function of the magnetic susceptibility of the sample.[53] For liquid solutions the nuclear magnetic resonance (NMR) method by Evans is applied, which is described later.[54]

According to $\chi(T) = \gamma_{HS}(T)\chi_{HS} + (1 - \gamma_{HS})\chi_{LS}$, the temperature-dependent magnetic susceptibility of a SCO species can be determined. If the temperature-dependent contributions of the pure HS and pure LS (χ_{HS}, χ_{LS}) are known, the mole fraction of each spin state (γ_{HS}, γ_{LS}) can be derived at any temperature from which the spin transition curve can be produced by plotting γ versus temperature (compare Figure 1.1).

Mößbauer Spectroscopy

Another standard method for the characterization of solid SCO compounds is Mößbauer spectroscopy.[32] The Mößbauer effect that is based on the recoilless nuclear absorption of γ-radiation, has been found for around 40 elements.[55,56] But due to several limitations like the lifetime and energy of the nuclear excited state involved in the Mößbauer transition, only for approximately 15 of them a practical application is suitable. Taking the example of ^{57}Fe, which is the most suited element and by far the most studied one, the principals of Mößbauer spectroscopy will be explained.[8,56]

A source of ^{57}Co isotopes (source) produces excited ^{57}Fe nuclei through a nuclear decay via electron capturing. These excited ^{57}Fe nuclei decay to the ground state and emit γ-quants of 14.4 keV. In case of a resonance effect, the γ-quants are absorbed by ground state ^{57}Fe nuclei (absorber or sample), which change to the excited state. The nuclei exited by resonant absorption relax to the ground state by emitting their energy to all room directions, so the detector in line of source and absorber detects a dip in the count rate. If the source is moved with a constant velocity v relative to the absorber, the emission line is shifted relative to the absorption line.[56] Figure 1.2a) depicts the setup of a Mößbauer spectrometer schematically.

Different parameters can be extracted from a Mößbauer spectrum (Figure 1.2b)). The so-called isomer shift δ describes an electric monopole interaction between the nucleus and the s-electrons. It is further indirectly influenced by the d-electron population in the valence shell. Therefore, it gives information about the oxidation state and the spin state as well as insights into the bonding properties. If an inhomogeneous electric field at the Mößbauer nucleus is present, the electric quadrupole splitting ΔE_Q is observed, that describes the interaction between the electric quadrupole of the nucleus with this electric field. The information content is similar to that of the isomer shift, since it gives insights into the symmetry of the molecule and the oxidation as well as spin state. The third parameter obtained by Mößbauer spectroscopy is the magnetic dipole splitting ΔE_M, which accounts for the magnetic dipole interaction between the nucleus and a magnetic field around it.

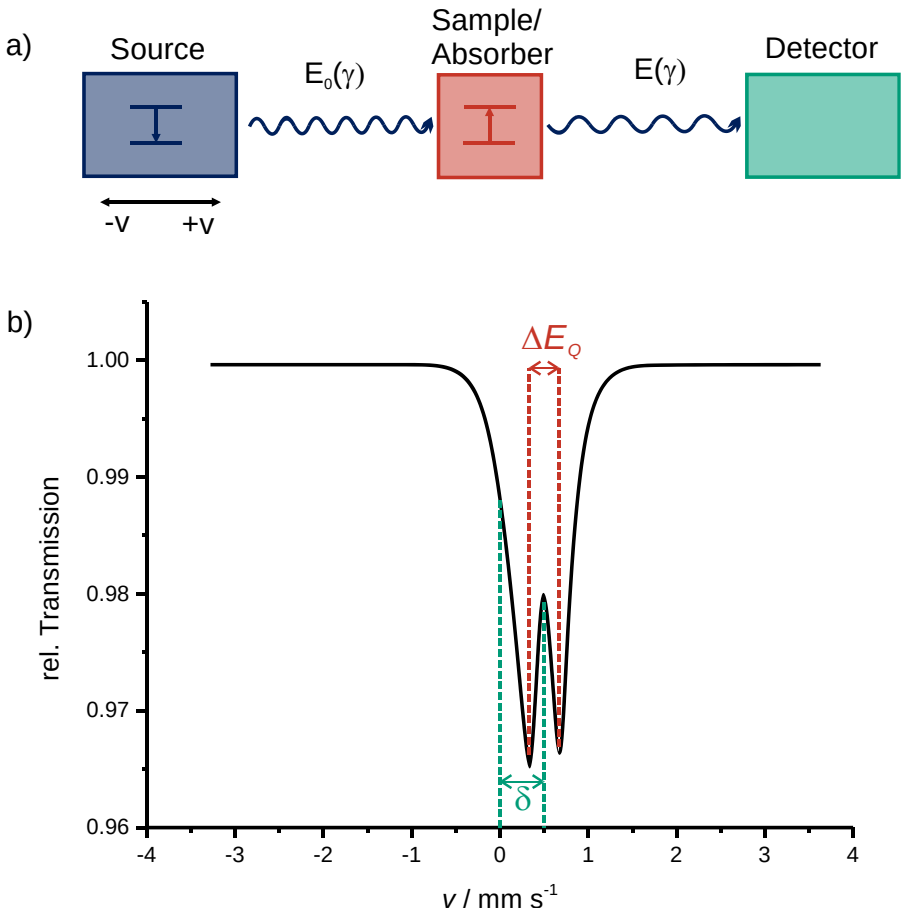

Figure 1.2: a) Schematic setup of a Mößbauer spectrometer. b) Sketched Mößbauer spectrum with marked isomer shift δ and quadrupole splitting ΔE_Q.

For the investigation of SCO compounds only the isomer shift and the electric quadrupole splitting are of interest, since they differ significantly for the HS and LS states. As a result, the two spin states show characteristic subspectra and from the area fractions of the two states the HS and LS fraction can be derived.[8,11,57]

Measurement of Electronic Spectra

Besides the two important methods to monitor a spin transition described in the previous two sections, several other methods can be used to characterize SCO compounds. Optical spectroscopy is one of them and can yield more information about the electronic changes occurring during a SCO process. A thermal spin transition is always accompanied by a change of colour, so-called thermochromism. This effect makes it easy to observe the spin transition because of the various colours at different temperatures. If the visible colour is caused by d-d bands only, a pronounced effect from colourless (HS) to violet (LS) is observable in Fe(II) compounds, like in $[Fe(alkyltetrazole)_6]^{2+}$ systems.[47] In the HS

case, the transition is shifted to higher wavelengths, often located in the (near) infrared region, therefore the complexes appear colourless or weakly coloured. Since d-d-transitions are Laporte-forbidden, they are very weak and often masked by more intense MLCT transitions (spin- and parity-allowed) occurring in the visible region. The MLCT bands are shifted to slightly lower frequencies due to the transition from HS to LS since the higher lying ^{5}MLCT band is replaced by the lower lying ^{1}MLCT band. Furthermore, the intensity is increased visibly due to the smaller metal-ligand bond length, resulting in a better overlap between metal-centred and ligand-centred orbitals.[58]
In addition to these visible effects, temperature dependent UV/Vis spectroscopy can be used to obtain an electronic spectrum of a SCO compound at the different spin states, providing energetic positions and intensities of optical transitions. These are needed for the performance of LIESST experiments.[8]

Vibrational Spectroscopy

Vibrational spectroscopy, namely infrared (IR) or Raman spectroscopy, is a further technique which can be applied to follow the spin transition and to derive a spin transition curve.[8,11] In course of the transition from HS to LS the occupancy of the d-orbitals is changing in terms of redistribution of electrons from the antibonding e_g^* orbitals to the slightly bonding t_{2g} orbitals. The electrons of the antibonding e_g^* orbitals are completely

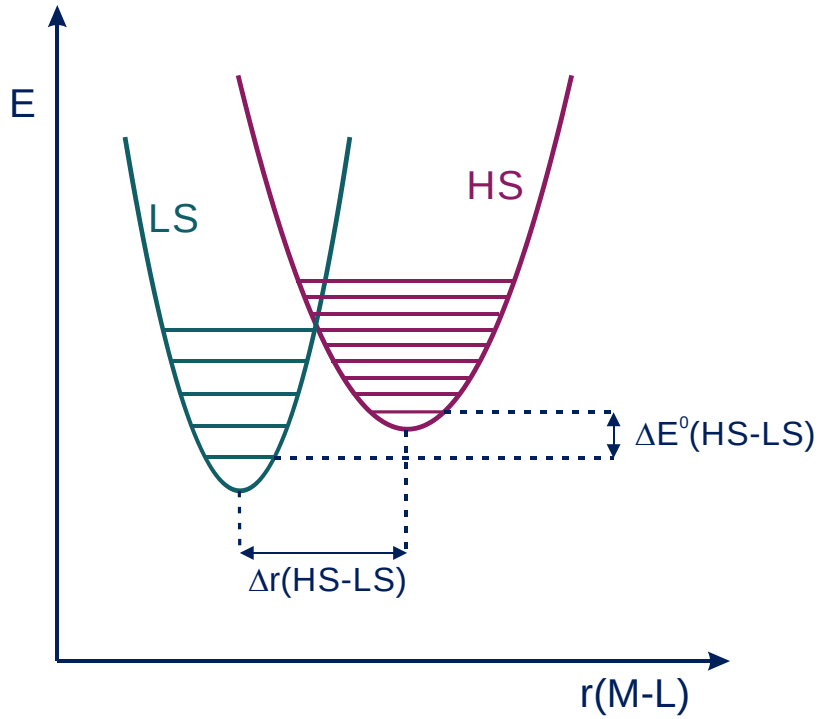

Figure 1.3: Schematic representation of the potential curves for HS and LS state on the reaction coordinate.

removed in case of d^4, d^5 and d^6 compounds and as a result, the metal-donor atom bonds are strengthened. As a consequence, the metal-donor atom bond lengths *r*(M-L) are shortened (see Figure 1.3) and the vibrational frequencies are shifted to higher values in the LS case compared to the HS according to $\nu = \frac{1}{2\pi}\sqrt{k/\mu}$ (with k = force constant and μ = reduced mass). The changes can be monitored in the vibrational spectrum in the lower fingerprint region from around 250 cm^{-1} to 500 cm^{-1} where the metal-donor atom stretching vibrations are located.[59–61] Since there are different specific signals for LS and HS, it is possible to perform temperature dependent studies to follow the increase and decrease of the intensity of the respective signals. By a careful quantification of the normalized area fractions the derivation of a spin transition curve is possible, too.[62–64]

Furthermore, several ligand vibrations are influenced by a change of spin state, as well. For example, the often employed NCS^- or $NCSe^-$ ligands show a strong doublet for the C-N stretching vibration. In case of the HS state the signal appears at 2060-2070 cm^{-1}, while this signal decreases and a second doublet at 2100 -2110 cm^{-1} arises during the transition to the LS state.[8,59,65,66]

Heat Capacity Measurements

Calorimetric measurements are a valuable method to gain more information about the thermodynamic aspects of SCO compounds.[67] By these experiments, the change in enthalpy (d*H*) and entropy (d*S*) of a spin transition, as well as the transition temperature can be determined.

At the beginning of SCO research, it was presumed that the driving force of the transition is the change of the spin multiplicity. But heat capacity (C_p) measurements by *Sorai et al.* on $[Fe(phen)_2(NCS)_2]$ revealed a phase transition at 176.29 K with an entropy change of ΔS=48.8±0.7 J/molK. This entropy value was much too high to be caused by a change of the multiplicity only, e.g. for $[Fe(phen)_2(NCS)_2]$ the contribution of the multiplicity change can be determined as $\Delta S = R \ln \frac{(2S+1)_{HS}}{(2S+1)_{LS}} = R \ln 5 = 13.4$ J/molK.[67] Since the metal-ligand bond lengths change significantly during the SCO process (see previous section), the density of the vibrational states is changing, too. Therefore, in case of the HS situation the degree of freedom is greater than in the LS case. Consequently, the spin transition is also an entropy driven process.[8,67,68] Only about 25% of the entropy gain can be assigned to the change of the spin multiplicity, while the major contribution originates from intramolecular vibrations.[8,65,67]

Magnetic Resonance Studies

Magnetic resonance techniques, like NMR or EPR (electron paramagnetic resonance) are well suited for the investigation of SCO processes in solution. As already mentioned, with the so-called Evans method, the magnetic susceptibility of liquid SCO systems can be quantified via proton NMR spectroscopy.[54,69,70] The paramagnetic susceptibility of a system can be determined from the extend of the shift of a signal induced by a paramagnetic centre compared to a solution with a standard substance according to equation (1):

$$\chi_g = \frac{3\Delta f}{2\pi f m} + \chi_0 + \frac{\chi_o(d_0 - d_s)}{m} \qquad (1)$$

With χ_g = mass susceptibility of the solute / $cm^3\ g^{-1}$
Δf = observed frequency shift of reference resonance / Hz
f = spectrometer frequency / Hz
χ_0 = mass susceptibility of solvent / $cm^3\ g^{-1}$
m = mass of substance per cm^3 of solution
d_0 = density of the solvent / g cm^{-3}
d_s = density of solution / g cm^{-3}

Compared to NMR spectroscopy, EPR spectroscopy is used more frequently for the investigation of SCO complexes.[71–74] For the application of EPR spectroscopy at least one unpaired electron needs to be present, what limits the number of possible systems to investigate. Fe(III) and Co(II) yield well resolved characteristic signals for HS and LS, which allow extraction of several structural and electronic information. In case of Fe(III) HS, the relaxation times are long, since there is no spin-orbit coupling. In the LS state spin-orbit coupling does occur, but measurements at low temperatures slow down the vibrations and therefore the relaxation times are quiet long, too. For Co(II), good EPR spectra can only be obtained at temperatures close to the spin transition temperature, since otherwise the spin-orbit coupling shortens the relaxation times significantly.[8]

X-ray Structural Studies

X-ray structural analysis is a further option to characterize SCO compounds in terms of its structural changes. SCO from LS to HS results in a change of the coordination environment of the central metal atom and an elongation of the metal-ligand bond length, which is caused by the changes of the electron distribution between the e_g^* and t_{2g} orbitals (see above).

Depending on the change of total spin ΔS and the resulting occupancy of the d-orbitals, the variation of the metal-ligand bond lengths differs significantly for different metal ions and oxidation states. In the case of Fe(II), the change of total spin is ΔS=2 and the change

in metal-donor atom bond lengths is rather large (Δr≈14-24 pm).[68,75] This can be explained by the fact, that the spin transition from HS to LS changes the orientation of two electrons, resulting in t_{2g} orbitals occupied with solely paired electrons, whereas no electrons remain in the antibonding e_g^* orbitals. The change in bond lengths of about 10% causes a change in the volume of the elementary cell of 3-4%.[8,11,68,75,76]

For Fe(III) the change in total spin is ΔS=2, too, but the t_{2g} orbitals are not fully filled after the HS→LS transition, since there are only five d-electrons. Therefore, the change in bond lengths is with Δr≈10-13 pm smaller than in the Fe(II) case.[68,76] The observed Δr in Co(II) (d^7) compounds is even lower ($\Delta r \leq 10$ pm). Since only one electron can be transferred from the e_g^* to the t_{2g} orbitals, one electron remains in the antibonding e_g^* orbitals.[8,68]

In addition to the observation of bond lengths changes, distortions of the metal environment, like modifications of angles or changes in the crystal lattice can be monitored. Even the nature of a spin transition can be obtained by temperature variable measurements.

Synchrotron Radiation Studies

Within the last few years, the use of synchrotron radiation lead to the development of further methods suitable for the investigation of SCO processes.

Nuclear Forward Scattering (NFS) is an elastic and coherent scattering process that is related to conventional Mößbauer spectroscopy. The technique can probe hyperfine interactions in condensed matter, even on samples with extremely low concentrations of the resonating nuclei. Simultaneous to NFS the Nuclear Inelastic Scattering (NIS) can be measured, which provides information on the vibrational properties of the system.[77]

Even though, X-ray absorption spectroscopy (XAS) is ideally suited for the investigation of SCO compounds, only a small number of studies have been performed until now.[78–86] Extended X-ray absorption fine structure (EXAFS) measurements provide structural information like the number and type of coordinating ligands, as well as the distance to the central metal ion, while X-ray absorption near edge structure (XANES) gives details on the coordination geometry and the oxidation state. Furthermore, X-ray emission spectroscopic (XES) studies emerged in the last few years, that provide electronic information like the spin state.[87–89]

Benefits and Limitations of Experimental Methods

Although the above mentioned standard methods provide good insights into the electronic and geometric changes occurring during SCO processes and several compounds have been extensively characterized by combinations of them (e.g. $Fe(phen)_2(NCS)_2$[36,44,49,79,90–93]), many of these methods bear several limits. Most of these techniques need defined working conditions or are limited to a specific aggregation state or element (e.g. Mößbauer spectroscopy). Furthermore, most of these methods cannot provide structural and electronic information simultaneously; therefore, a combination of results from different methods is necessary to obtain a complete view on the SCO process. According to this, experimental methods that could provide both structural and electronic information in one experiment are of great interest for SCO research. Methods that meet with this criterion are the above mentioned X-ray absorption (XAS) and emission (XES) spectroscopic techniques. These methods offer the possibility to investigate samples under various conditions, e.g. at cryogenic or elevated temperatures, under high pressure or under irradiation with light. Moreover, X-ray measurements are suitable for all states of aggregation and can be applied to several elements, including the whole group of 3d transition metals.[94]

Since this work is based on the implementation of these methods for the investigation of SCO compounds, the basics of X-ray absorption and emission spectroscopy will be described in more detail in chapter 1.3.

1.3 X-ray Absorption and Emission Spectroscopy

After the description of the fundamental basics of SCO and the short overview on the mainly applied techniques for the investigation of SCO compounds in the previous chapter, this chapter is focused on the basics of XAS and XES. The generation of X-rays, as well as the different techniques and instrumentations will be elucidated and the potential of these techniques for SCO research will be highlighted.

1.3.1 Generation of X-rays

X-rays are high-energy electromagnetic radiations with relatively short wavelengths of λ = 0.01-100 Å, therefore this radiation is located between γ-rays and ultraviolet light in the electromagnetic spectrum. Depending on their wavelengths, X-rays can be divided into hard X-rays (short wavelengths) and soft X-rays (long wavelengths).[95]

X-ray Tube

In general, X-rays are produced by conversion of kinetic energy of charged particles (e.g. electrons) into radiation or by excitation of atoms in a target material by impinging with fast electrons. In an X-ray tube, used traditionally for the generation of X-rays in laboratories, two metal electrodes are located in a vacuum chamber, see Figure 1.4.

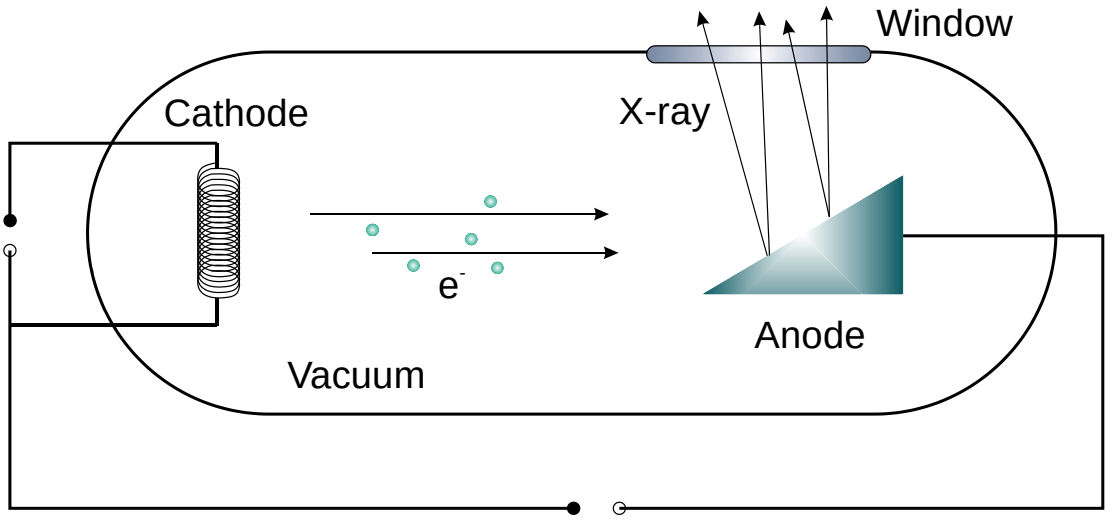

Figure 1.4: Schematic depiction of an X-ray tube.

As cathode a tungsten filament is used. By applying a high negative potential, the filament is heated up and it thermally emits electrons, which are accelerated towards the anode by an applied positive potential. Bombardment of the anode by these fast electrons leads to two different processes generating X-ray radiation:

1) The accelerated electrons collide with several atoms of the anode material and with each collision a part of their kinetic energy is transferred and emitted as X-ray radiation. Since the electrons lose their kinetic energy in a unique way each, a continuous X-ray spectrum is emitted. This continuous spectrum is also called white radiation or bremsstrahlung.[95]
2) If the accelerating voltage reaches a certain threshold value, which is dependent on the target/anode material, it is possible that the fast electrons resonantly excite electrons of the inner atomic shells (K-shell) of the anode atoms. The inner shell vacancy produced by this procedure is then refilled by relaxation of an electron from a higher shell under emission of a characteristic fluorescence line. These characteristic lines are superimposed on the continuous bremsstrahlung and have well defined energies. Depending on the atomic levels involved, the transitions are designated as for example $K\alpha_1$, $K\alpha_2$ for transitions from L→K shell or $K\beta_1$, $K\beta_2$ for transitions from M→K shell.[95]

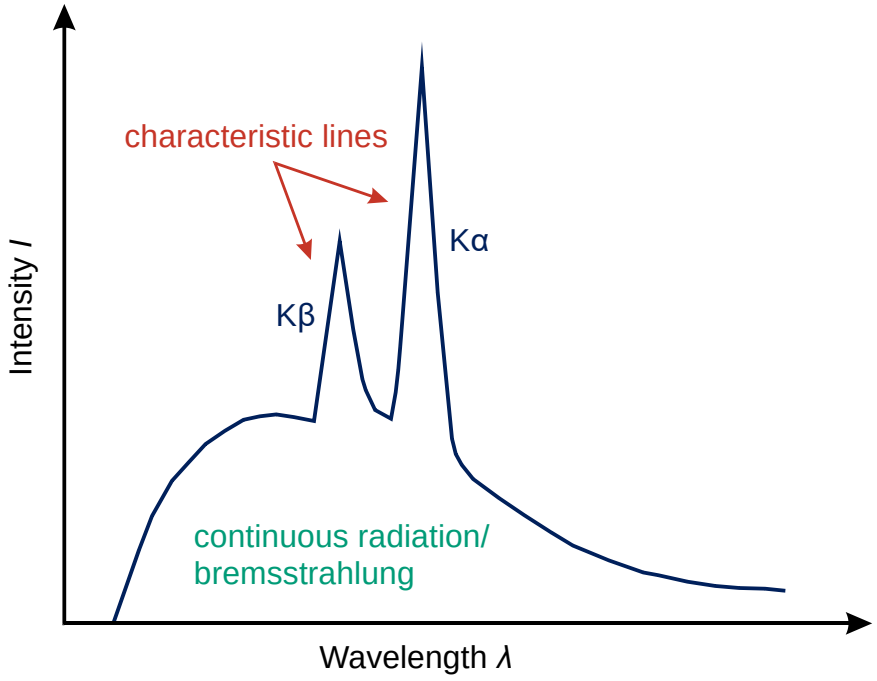

Figure 1.5: Schematic X-ray spectrum with continuous radiation and characteristic fluorescence lines Kα and Kβ.

To illustrate the different "types" of X-ray radiation, Figure 1.5 shows a schematic X-ray spectrum with characteristic Kα and Kβ lines. Due to their higher intensity, the characteristic lines are mainly used for X-ray diffraction studies, while the continuous white radiation can be used for X-ray absorption fine structure (XAFS) experiments, since for this type of experiments radiation with tuneable energy is required. As the intensity of the X-rays generated by an X-ray tube is rather low, experiments on diluted systems are scarcely feasible. Therefore, the use of synchrotron radiation is preferred for these experiments.

Synchrotron Radiation

Synchrotron radiation provides several advantages for XAFS experiments compared to X-rays produced by an X-ray tube. The intensity of synchrotron radiation is about 10^3 times higher than the characteristic fluorescence lines and about 10^6 times higher than the continuous radiation emitted by an X-ray tube. In addition, the energy is tuneable over a wide energy range with a continuous spectrum and shows high collimation. Furthermore, the radiation exhibits a plane polarization and a well-defined pulsed time structure.[95]

For the classification of the performance of an X-ray source several important parameters have to be considered. The term *flux* is defined as the total number of photons per second in a beam, while *intensity* represents the number of photons per second and area, so to speak flux per area. A third useful quantity for the description of X-ray sources is the so-called *brilliance*. The brilliance of a source is defined as photons per second, source area and source angular divergence. Due to the fact that brilliance is an invariant quantity, that means that a reduction of the spatial size (source area) is only possible at the costs of increasing angular divergence, it is a characteristic value of a source. A brilliant source emits a high number of photons per second, with a small source area as well as a small angular divergence.[96]

In a synchrotron charged particles are accelerated until they reach a velocity v that is close to the speed of light c. According to the Maxwell equations,[97] each accelerated charged particle generates electromagnetic radiation. The charged particles, in most cases electrons, are accelerated in an evacuated pipe with a nearly circular geometry and are guided to their trajectory by vertically arranged magnetic fields. Every time the electrons are deflected by the magnets from a straight path, they are accelerated and therefore emit radiation in a tangential direction. Since synchrotrons are designed in circular geometry, the electrons are continuously accelerated and thus emit radiation continuously.[96]

Originally, synchrotrons were developed to perform high-energy physics experiments and the emission of synchrotron radiation was only an annoying by-product for physicist, as their accelerated particles lost a significant part of their kinetic energy through the emission of this radiation.[96] After recognition of the beneficial properties of synchrotron radiation for X-ray experiments and the early success in this research field, a second generation of synchrotrons was developed in the early 1970s. These facilities were built solely for the production and storage of synchrotron radiation. Instead of protons, which were preferred in high-energy physics experiments, electrons are used as charged particles, due to their higher efficiency for emission of radiation. In second generation synchrotrons deflection of the electrons is realized by bending magnets (Figure 1.6, left).[96]

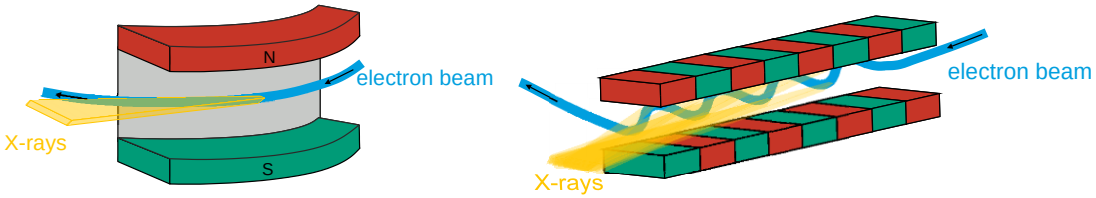

Figure 1.6: Schematic depiction of a bending magnet (left) and an insertion device (right). The number of alternating magnet pairs is responsible for the main difference between wigglers and undulators. Wigglers emit a continuous spectrum while undulators emit radiation with a narrow bandwidth.

Development of so-called insertion devices, for example undulators and wigglers (Figure 1.6, right), lead to the construction of third generation synchrotrons. These devices are inserted between the bending magnets into straight parts of a storage ring and force the electron beam on a slalom trajectory. Due to the repeated deflection, the electrons emit radiation on the straight parts of the storage ring, too. Through the use of undulators the brilliance of third generation sources increased by several orders of magnitude compared to second generation facilities.[96,98,99] The latest improvements in accelerator physics, the use of free electron laser (FEL) technology, lead to the fourth generation sources with further increased brilliance. Compared to synchrotrons, which provide radiation with a rather broad bandwidth, FELs offer radiation with a narrow bandwidth. Since the emitted X-ray pulses are highly coherent and of extremely short pulse duration, combined with high intensities and relatively low repetition rates, they are perfectly suited to perform so-called one-shot experiments and time-dependent measurements.[98] The intensity of the beam is high enough to generate a diffraction pattern in a single shot, but as a small drawback, the sample will be destroyed instantly. In general, these new fourth generation sources are not compatible for standard XAFS experiments, since a beam with a broad bandwidth or tuneable energy is mandatory.[96]

1.3.2 Interaction of X-rays with Matter

In principal, there are four different ways of interaction between X-ray radiation and matter, namely X-ray absorption, elastic scattering, inelastic scattering and the production of electron-positron pairs. The latter can only be observed at very high energies (E>1.022 MeV) and is caused by collision of particles. Therefore, in the energy range of XAFS experiments, pair production is negligible. [96]

Elastic scattering, also referred to as unmodified, coherent or Rayleigh scattering, occurs, when a photon of a specific energy impinges on a sample and is scattered on the tightly bound atomic electrons in a way, that no ionisation or excitation takes place. Then a photon of the same frequency – thus the designation "unmodified" – but with a different direction is emitted.

A classic description for this kind of interaction is as follows: an incident electromagnetic wave causes oscillations of bound electrons of an atom. By these oscillations an own secondary wave field is produced, which exhibits the same frequency as the incident wave.[96] Elastic scattering is generally less important than absorption, except for low energies and light atoms.[95]

Inelastic scattering, also called modified, incoherent or Compton Scattering, arises if the frequency of the scattered photon is not the same, more precisely lower than that of the incident photons. The collision of the photon with loosely bound electrons leads to an energy transfer to the sample, resulting in electronic transitions comparable to that in an absorption process.[96]

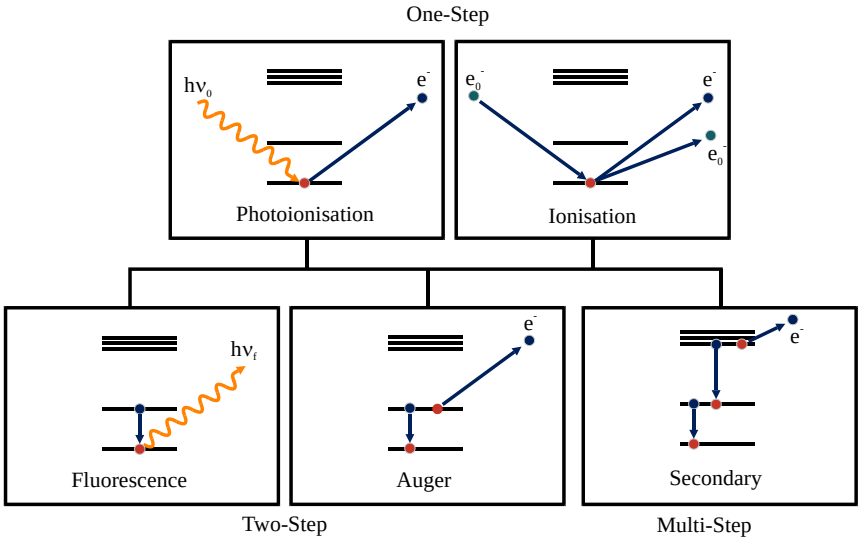

Figure 1.7: Possible interactions of photons ($h\nu$) or electrons (e_0^-) with core electrons.

If an incident photon interacts with electrons of the sample by transferring its whole energy, one speaks of an absorption process. The incident photon is fully consumed and the energy of the photon causes transitions from electrons of lower atomic levels to higher ones or into the continuum. This process is called photoionisation and essentially the same process can be induced by incoming electrons instead of photons, which is then named ionisation. The excitation results in vacancies in the lower lying levels, which are subsequently refilled by relaxation of electrons from higher levels (see Figure 1.7). Relaxation of the excited atom can then take place through several mechanisms, namely emission of X-ray fluorescence, ejection of Auger electrons or secondary electrons.

The energy difference between the two involved electronic levels characterises the emission of the above mentioned characteristic fluorescence lines (compare chapter 1.3.1, Figure 1.5). If the vacancy exists in the K shell (1s orbital) and is filled by electrons from the L shell (L→K), Kα lines can be detected, while relaxation from the M shell (M→K) results in Kβ lines. According to the notation of Siegbahn, this series of transitions is called K series, while the series resulting from transitions into an L hole is called L series. Figure 1.8 gives an overview on selected absorption and emission lines. Notation of the shells is that of Sommerfeld,[100] while transitions are designated according to Siegbahn, as mentioned above.

The ratio of emitted X-ray photons to the number of primary created core holes is defined as fluorescence yield or radiative probability. It increases monotonically as a function of atomic number *Z* and in general, the fluorescence yield is larger for K lines than for the subsequent L or M lines.[95]

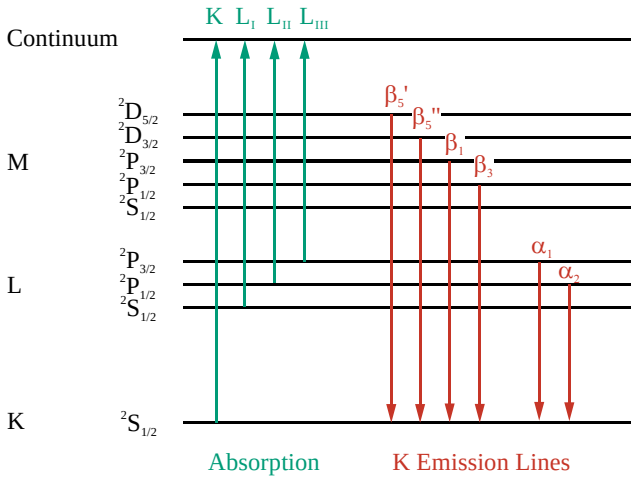

Figure 1.8: Selection of absorption edges and emission lines.

Besides the just described radiative decay, non-radiative decay via emission of Auger electrons can occur.[95,96] In this case, the core hole is refilled by an electron from a higher shell and simultaneously an electron from the same (or higher) shell is ejected. Since the energy released by the decay of the first electron is transferred to the second one, this process is non-radiative. Consequently, the kinetic energy of the ejected electron corresponds to the energy difference of the initial and the final state and therefore, the detection of Auger electrons provides information about the involved energy levels. Especially for light atoms and low energies the probability of generation of Auger electrons is quite high, but with increasing energy the probability of radiative decay is predominating[95,96] Another possibility of non-radiative decay is the production of secondary electrons. By leaving the atom, emitted fluorescence photons or Auger electrons can induce ejections of electrons from higher shells. These secondary electrons show less defined kinetic energies and will not be further discussed in this context.[95]
The three described interactions with matter – absorption, elastic and inelastic scattering – are closely related processes and occur at the same time. Since this work is focused on X-ray absorption and emission spectroscopy, only the first one will be elucidated in more detail.

1.3.3 X-ray Absorption Spectroscopy

As mentioned in chapter 1.2.2.2 before, X-ray absorption fine structure spectroscopy is a unique spectroscopic tool for the investigation of electronic and structural properties of matter under various conditions. It provides information about the local structure of probed absorbing atoms, like the central metal ion in SCO complexes, as well as information about the oxidation state or spin state. Previous to the more detailed description of this method, a short review on the historical development will be given in the next section.

1.3.3.1 History of XAFS

In 1913, *Maurice de Broglie* measured the first absorption edges.[101] In his own laboratory, he mounted a single crystal on a rotating plate and exposed it to X-rays generated by an X-ray tube. Since the crystal rotated, it worked as a kind of monochromator and therefore all angles between the incident beam and the diffraction planes were recorded on a photographic plate. He obtained an X-ray line spectrum from the X-ray tube with two additional absorption bands, that could be assigned to the absorption edges of Ag and Br, the material of the photographic plate.[102] About seven years later, in 1920, *Hugo Fricke* observed the first complicated fine structures of K-edges of Cr, V and Ti compounds.[103] The energy-dependent variation of the absorption was displayed by more or less intense lines on the photographic plate. At the same time, *Gustav Hertz* found the

first L-edge fine structures for the elements Cs to Nd.[104] In the following years, *Lindh* performed several X-ray absorption experiments on a number of different elements (e.g. Cl, Si, Ti, V, Cr and many more).[105–107] The experimental technique was continuously improved[108–111] and first attempts for the theoretical description of the findings were made.[112–114] During the next approximately 40 years, confusion about the different proposed theories existed, as reviewed by *Azároff*.[115] In 1971, *Sayers, Stern and Lytle* published their work about Fourier transformation of EXAFS data, by which a radial distribution function could be extracted from the experimental absorption spectra,[116] followed by several publications which proved the use of this technique for the determination of structural parameters such as distances or numbers of backscatters to the absorbing atom.[117–120] The development of synchrotrons in the 1970s (see chapter 1.3.1) and the possibilities of utilizing the high intense X-rays lead to further improvements of XAFS spectroscopy. Today it is an often used spectroscopic technique for the investigation of matter in diverse states of aggregation as well as under various sample conditions.[96]

1.3.3.2 Physical Principals of XAFS

XAFS experiments are based on the measurement of the so-called X-ray absorption coefficient μ(E) as a function of photon energy E.[95,96] μ(E) represents the basic physical quantity of XAFS spectroscopy

When an X-ray beam passes through a sample, the intensity of the incident beam will be reduced by a certain amount according to the absorbing properties of the sample. The decrease of intensity dI is proportional to the incident intensity I and the path length through the sample dx according to:

$$\mathrm{d}I = -\mu(E) I \mathrm{d}x \tag{2}$$

Integration of equation (2) with μ(E) as proportional factor gives Lambert-Beer's law:

$$\frac{I}{I_0} = e^{-\mu(E)x} \tag{3}$$

With I = transmitted intensity
I_0 = incident intensity
x = path length through sample
$\mu(E)$ = linear X-ray absorption coefficient

When an isolated atom is exposed to X-ray radiation, its absorption spectrum and therefore $\mu(E)$ decreases monotonically as a function of the photon energy. This behaviour is caused by the direct proportionality of $\mu(E)$ to the photoelectric absorption cross section σ and the scattering cross sections τ, according to $\mu(E)=\sigma+\tau$. In the energy range of interest for XAFS experiments, σ shows a strong energy dependence of approximately $1/E^3$ and the scattering cross sections are negligible.[95,96]

If the incident photon energy reaches a certain element specific threshold, the absorption coefficient increases abruptly. This sharp rise is caused by ejection of a photoelectron from a deep core level into higher levels or into the continuum and is called absorption edge or threshold energy.[121] After the respective absorption edge the absorption coefficient decreases monotonically again until the next absorption edge is reached, see Figure 1.9. The kinetic energy E_{kin} of the ejected electron is given by the difference of the photon energy and the binding energy of the electron $E_{kin} = h\nu - E_{binding}$, according to the photoelectric effect. Per definition, the kinetic energy of the ejected electron at the absorption edge is equal to E_0, which is also called zero-point energy or "inner potential".[121]

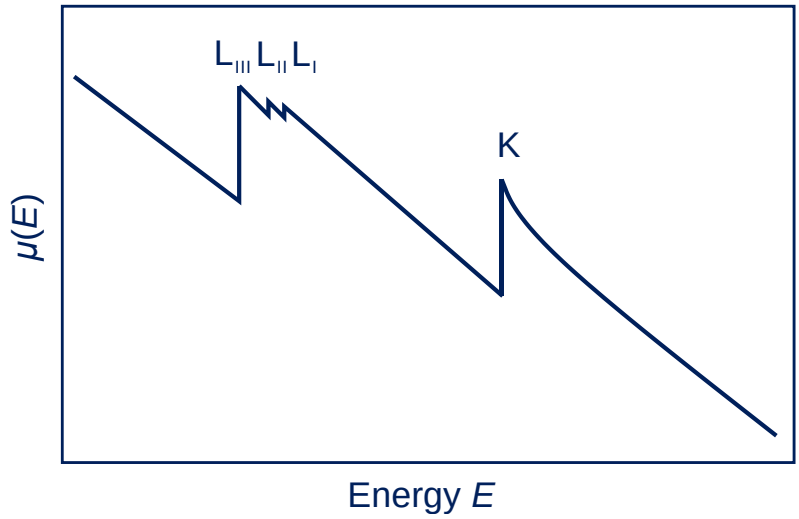

Figure 1.9: Schematic representation of the absorption coefficient $\mu(E)$ as function of the incident photon energy E. L_I-L_{III} and K indicate the origin of the ejected electron according to the Sommerfeld notification.

In case of a free atom, the absorption spectrum shows no further fine structure after the absorption edge (see Figure 1.10 left). If the absorbing atom is surrounded by other atoms, the ejected photoelectron, which possesses wave as well as particle characteristics, is scattered at the neighbouring atoms, producing a backscattered wave. Due to interference effects between the outgoing and the backscattered wave, the absorption spectrum shows sinusoidal oscillations after the absorption edge, also known as EXAFS (see Figure 1.10 right). The fine structure region is extended from around 50 eV to 1000 eV after the absorption edge and the oscillations typically have an amplitude of around 1-20% of the edge jump.[95]

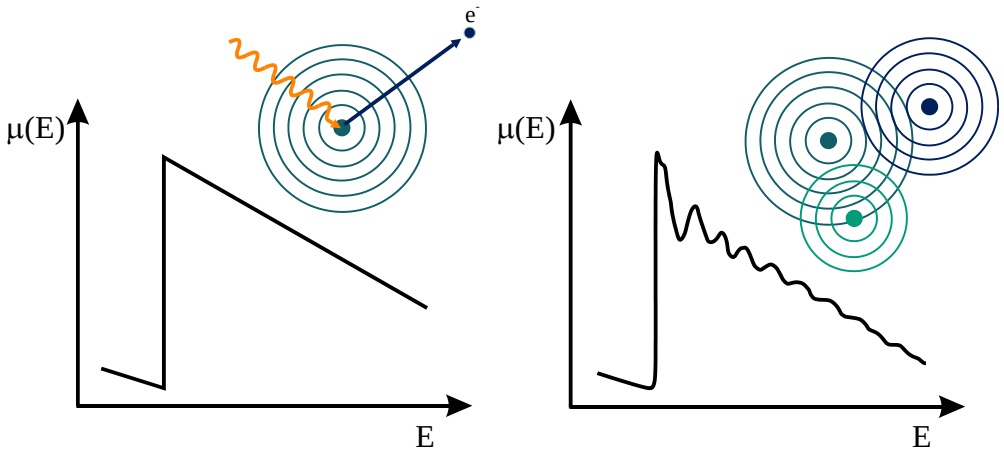

Figure 1.10: Schematic depiction of the influence of backscattering neighbouring atoms on the absorption coefficient $\mu(E)$ as a function of the photon energy. Left: Free atom without backscattering atoms. Right: Absorbing atom in condensed phase, surrounding atoms lead to interference effects of the outgoing and backscattered wave represented by the oscillations after the absorption edge.

An X-ray absorption spectrum can be divided into three parts, the X-ray absorption near edge structure region (XANES), divided into the prepeak and the rising edge, and the extended X-ray absorption fine structure region (EXAFS) which provide different types of information (Figure 1.11).

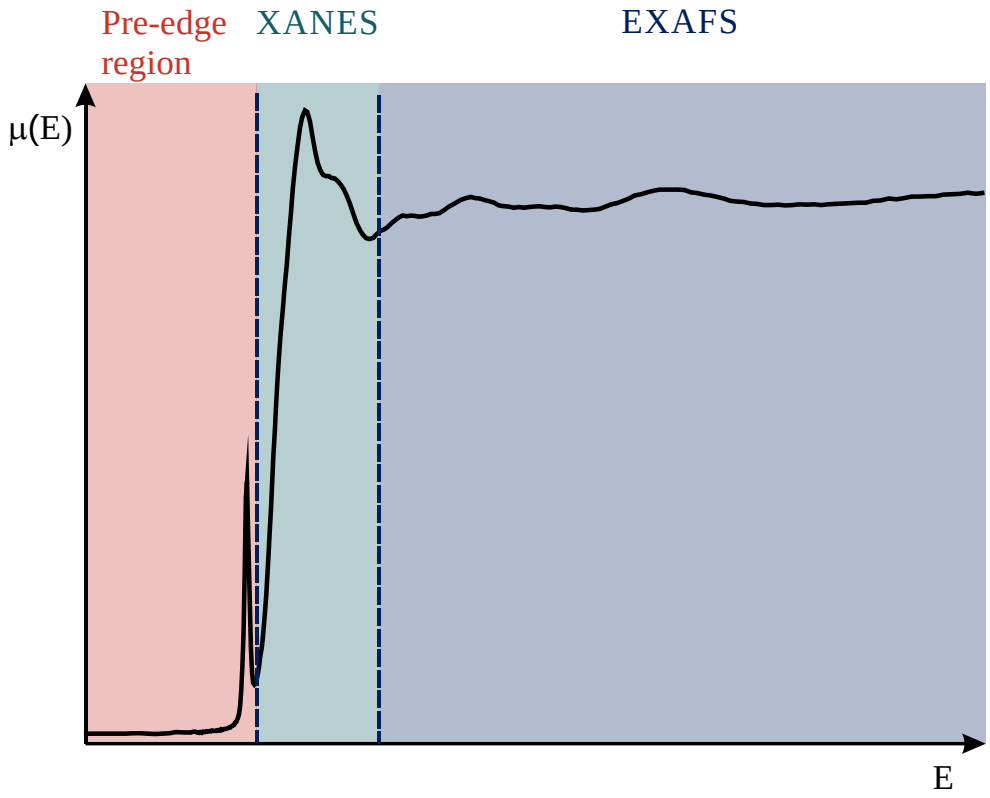

Figure 1.11: Classification of the different regions present in a XAFS spectrum. Shaded in red: pre-edge region; shaded in green: XANES region; shaded in blue: EXAFS region.

The pre-edge region is located at around 15-20 eV below the absorption edge and typically shows one or more signals.[122] These signals are caused either by 1s→nd transitions or by transitions from the 1s orbital into nd/(n+1)p hybridized orbitals, depending on the coordination geometry of the absorbing atom. The intensity of the prepeak is strongly influenced by the number of coordinating atoms and the coordination geometry.
Electric quadrupole transitions, like 1s→nd, are parity forbidden. Thus the transitions occur with only significant smaller probability than parity allowed electric dipole transitions, like 1s→np transitions. Due to this, the intensity of quadrupole transitions is only very low.
In case of a tetrahedral coordination (point group T_d), a hybridization between $p_{x,y,z}$ and $d_{xy,xz,yz}$ orbitals is possible, since these orbitals belong to the same irreducible representation in the character table.[123] Thus, transitions into the hybridized orbitals show a high intensity, since the transitions are dominated by the transition into the p-component of the

orbital, which again is parity-allowed. In contrast to this, in case of an octahedral coordination environment (O_h symmetry), which shows an inversion centre, no hybridization between p and d orbitals is possible, since no irreducible representation exists to which both types of orbitals belong to. As a result, octahedral systems show prepeak signals of very low intensity, since only quadrupole transitions are allowed.[123] Distortion of the perfect octahedral geometry allows mixing of p and d orbitals and thus leads to an increase of the prepeak intensity.

Summarizing, the pre-edge region offers information about the coordination geometry of the absorbing atom. Systems with high inversion symmetry, like octahedral systems, show only weak prepeak features, caused by parity-forbidden 1s→nd quadrupole transitions. Reduction of symmetry leads to a hybridization between p and d orbitals and therefore transitions into the p-component lead to significant increased intensities, like observed for tetrahedral systems. In addition to information about the coordinating environment, the prepeak region provides information about the spin and oxidation state, since the LUMOs (lowest unoccupied molecular orbitals) are influenced by the number of d electrons and their distribution to the different d orbitals.

Information about the oxidation state can be obtained by analysis of the XANES region, too. The absorption edge represents the photoionisation of a core electron into the continuum. With increasing oxidation state, the edge position is shifted to higher energies, since the electrons are attracted more strongly to the core due to the higher positive charge of the nucleus.[122] Therefore, photoionisation requires more energy resulting in the mentioned edge shift. The energetic position of the edge can further be influenced by the coordinating environment around the absorbing atom. Number and type of ligands bound to the central atom, as well as the respective bond lengths can affect the electron density of the orbitals involved into the transition and thus the energy required for the photoionisation.[96] A quantitative evaluation of the edge position of unknown samples is possible, if suitable reference compounds with similar coordination and known oxidation states are available. Furthermore, linear combination XANES fits provide the opportunity to determine for example the fraction of HS and LS centres in SCO compounds, assumed that spectra of the pure spin states are available.

The analysis of the oscillations in the EXAFS region provides element specific information about the local structure of the absorbing atom. Type and number of coordinating atoms around the absorber, as well as the distances between the absorber and the coordinating atoms can be obtained precisely.[118,119] Especially the determination of the metal ligand bond lengths offers great potential for the investigation of SCO processes.

Since XAFS requires no long-range order, the described techniques are applicable not only to crystalline samples, but also to diverse other systems like solutions, glasses, liquids, amorphous systems and many more. Due to this manifold applicability, XAFS can be used in a wide variety of disciplines such as physics, chemistry, biophysics, biology, medicine, geology and materials science.[95,96]

1.3.3.3 Experimental Modes

In principal, XAFS experiments can be performed in two different experimental modes, namely step scan and dispersive mode. Furthermore, various detection techniques like absorption or fluorescence detection are known. These different modes are described in more detail in the following section.

In transmission mode, the flux of the beam is monitored in so-called ionisation chambers before and after passing through the sample, as shown in Figure 1.12.[96] According to Lambert-Beer's law, the transmitted flux I is related to the incident flux I_0 by $\mu(E)x = \ln I_0/I$ (compare section 1.3.3.2). The signal detected by the ionisation chambers is not the original flux, but a generated current that is proportional to the flux. An ionisation chamber consists of a pair of electrodes with a fill gas (e.g. N_2, Ar, He…) and an electric field between them. If an X-ray beam passes through the chamber, some of the X-ray photons are absorbed by the fill gas and a part of the gas is ionised. The generated electrons and positive ions are accelerated towards the anode and cathode respectively, generating a current that is proportional to the amount of ionised gas atoms and therefore to the flux of the incident beam. Since the absorption step is correlated with the sample concentration, measurements in absorption mode require a minimum concentration to obtain a spectrum of reasonable quality. Measurements of a reference metal foil simultaneous to the sample measurement can be used to correct shifts of the energy calibration of the monochromator.[122]

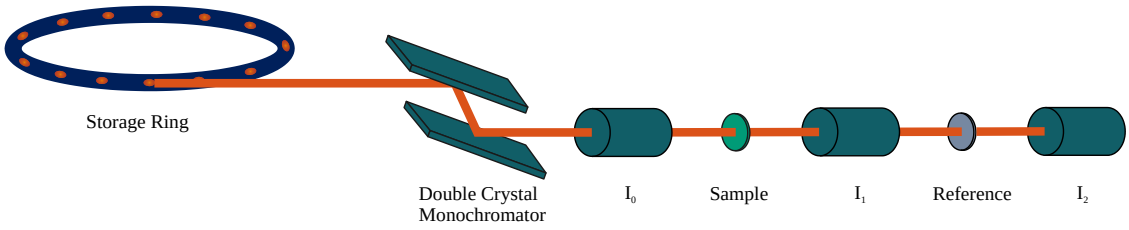

Figure 1.12: Schematic setup of a XAFS experiment in transmission mode. I_0, I_1 and I_2 depict the ionisation chambers before and after the sample and the reference.

For samples with very low concentration, measurements in fluorescence mode are preferred. In this mode, the signal is not detected by ionisation chambers but by a fluorescence detector, which is positioned at 90° to the incident beam. The sample is placed at 45° to the incident beam and to the detector respectively, see Figure 1.13.[96] All components are arranged in a horizontal plane. The fluorescence X-rays I_f, generated in course of the radiative annihilation of the core hole are detected with the fluorescence detector and normalized to the incident flux I_0, which is measured in the first ionisation chamber.

Since the radiative decay process is proportional to the absorption a similar spectrum can be obtained.[122]

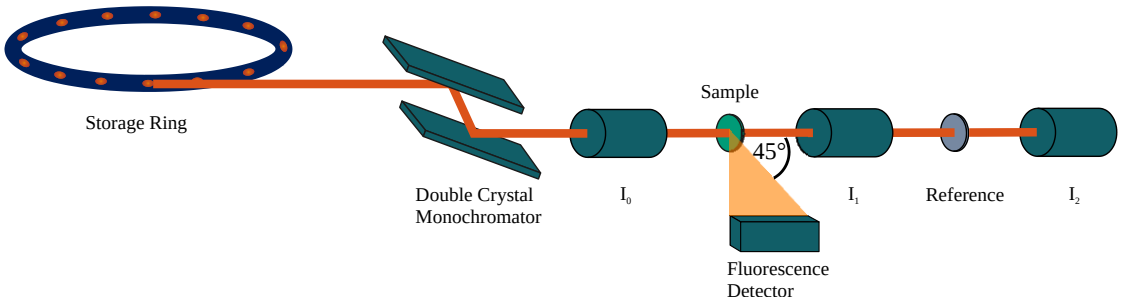

Figure 1.13: Schematic setup of a XAFS experiment in fluorescence mode.

Most XAFS experiments are performed in step scan mode, which means that the monochromator is moved to a certain energy, stays there for a defined acquisition time and then moves to the next energies step by step. In this mode a full scan can be obtained in minutes up to hours. If the monochromator is moved continuously, a spectrum can be obtained in a time range of seconds or even less. Therefore, this mode is called rapid scan or quick XAFS (QXAFS).[96] For time-dependent measurements on shorter time scales, these methods are even too slow, so other techniques are needed. One possible approach is energy dispersive XAFS, in which a complete spectrum can be recorded within one shot and without mechanical movements.[96] In principal, dispersive XAFS is based on the diffraction of a non-monochromatic X-ray beam by a bent polychromator crystal. Then the diffracted beam is focused on the sample and diverges in different directions onto a position-sensitive detector (compare Figure 1.14).

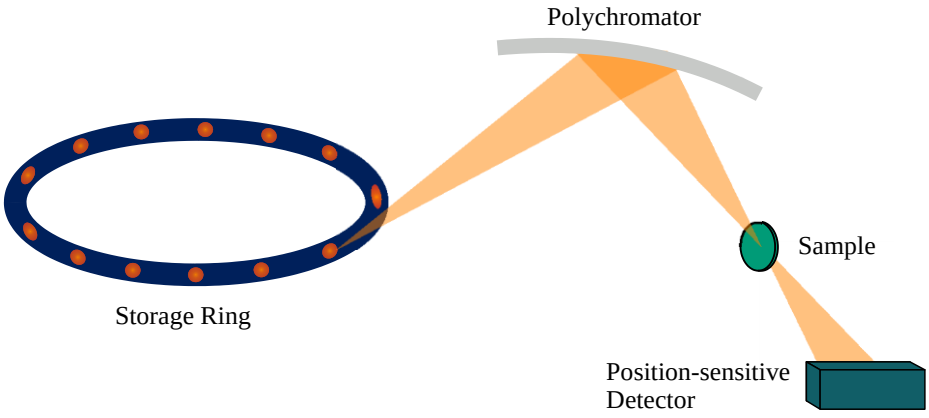

Figure 1.14: Schematic setup of a dispersive XAFS experiment with polychromator crystal and position-sensitive detector.

With sufficient X-ray flux and a fast enough detection system rapid measurements are possible allowing the exploration of time-dependent processes and fast reactions. Another possible technique is time resolved XAFS.[96] In time-slicing mode, the sample is perturbed for example by an intense laser pulse, by fast mixing with reactants or by variation of pressure and then the XAFS signal at one energy point is recorded in dependency of time. Repeating this process at different energies results in a time-dependent XAFS spectrum. Pump-probe XAFS is very similar to the time-slicing method with the difference that the signal is recorded during a defined time interval after the perturbation.[96] With respect to spin crossover research, these methods bear high potential for the investigation of short-lived spin states and spin dynamics, as already demonstrated in a few cases.[124,125]

1.3.3.4 Theory of EXAFS

As described in chapter 1.3.3.2 before, the fine structure in the EXAFS region is caused by interference between the ejected photoelectron wave and the backscattered photoelectron wave from neighbouring atoms. The interference pattern can vary between total construction (waves fully in phase) or total destruction (waves exactly out of phase). These interferences cause an energy-dependent variation of the X-ray absorption probability, which is proportional to the linear X-ray absorption coefficient $\mu(E)$. By analysis of the oscillations in the EXAFS region information about the structure, distances to and types of neighbouring atoms, as well as information about the static and thermal disorder can be extracted.[95,96,121,122]

Until today, a number of different derivations for the EXAFS theory with varying theoretical approaches were presented.[116,126,127] On the basis of the widely accepted *short-range single-electron single-scattering* theory the main aspects of EXAFS theory will be explained.[117,119,127–130] In this theoretical approach, the photoelectron is scattered only once before returning to the absorber atom, which is sufficient for the description and analysis of most EXAFS experiments. Therefore, multiple scattering events are not considered.

Prior to the EXAFS analysis, the fine structure oscillations need to be extracted from the experimental spectra and have to be normalized to the atomic background.[95,122] For this, the energy-dependent absorption coefficient $\mu(E)$ is subtracted by the atomic background $\mu_0(E)$. The difference is normalized to $\mu_0(E)$, resulting in the energy-dependent EXAFS function $\chi(E)$:[95,122]

$$\chi(E) = \frac{\mu(E) - \mu_0(E)}{\mu_0(E)} \tag{4}$$

With $\chi(E)$ = energy-dependent, isolated and normalized fine structure
$\mu(E)$ = linear X-ray absorption coefficient
$\mu_0(E)$ = linear X-ray absorption coefficient of atomic background

It should be noted that the atomic background is not the absorption coefficient of an isolated atom, but of an atom in its chemical environment with the effects of neighbouring atoms "switched off".[96,122] For the correlation of the EXAFS function $\chi(E)$ with structural parameters a transformation from E space to k space has to be performed by which the energy E is converted to the photoelectron wave vector k to achieve $\chi(k)$.
According to the photoelectric effect the kinetic energy of the photoelectron is given by equation (5):

$$E_{kin} = h\nu - E_{binding} \tag{5}$$

Using the de Broglie equation $\lambda = \frac{h}{p}$ and the definition of the wavevector $k = \frac{2\pi}{\lambda}$, the kinetic energy can be written as follows:[95]

$$E_{kin} = \frac{p^2}{2m} = \frac{h^2k^2}{8\pi^2m} = \frac{\hbar^2k^2}{2m} \tag{6}$$

With $\hbar = \frac{h}{2\pi}$
p = electron momentum
m = electron mass
h = Planck constant

Insertion into equation (5) and resolving to the wave-vector k gives:

$$k = \sqrt{\frac{2m}{\hbar^2}(E - E_{binding})} \tag{7}$$

With $E = h\nu$ = photon energy
E_{binding} = electron binding energy

The EXAFS signal $\chi(k)$ can be given as a summation over all interference patterns scattered off by all surrounding atoms:

$$\chi(k) = \sum_{j=1}^{Shells} A_j(k) \sin \Phi_{ij}(k) \quad (8)$$

With $A_j(k)$ = amplitude of scattering event at j^{th} shell

It can be seen that the EXAFS formula contains two main components for the description of the interference patterns, the sine functions and the amplitude *Aj(k)*. The sine functions account for the periodic oscillations in the fine structure and the amplitude reflects the scattering intensity of the photoelectron with the respective backscatterer.
The argument of the sine function $\Phi_{ij}(k)$ comprises the interatomic distances between the absorbing and scattering atoms and a factor that accounts for the phase shift:

$$\sin \Phi_{ij}(k) = \sin\left[2kr_j - \phi_{ij}(k)\right] \quad (9)$$

With r_j = distance absorbing atom – scattering atoms in j^{th} shell
$\phi_{ij}(k)$ = total phase shift

Since the argument of the sine function can be related to the time the photoelectron needs to travel to the neighbouring atom and back, $2kr_j$ can be interpreted as the electron travelling with constant speed the whole way to the scattering atom and back. But due to the attraction of the nuclei, the electron speeds up when it approaches the scattering atom or the absorbing atom again, resulting in a phase shift diminishing the total time required.[121]
The total phase shift $\phi_{ij}(k)$ can be expressed as twice the phase shift of the absorbing atom (outgoing and returning photoelectron) plus the phase shift of the backscattering atom:

$$\phi_{ij}(k) = 2\phi_i(k) + \phi_j(k) \quad (10)$$

With: $\phi_i(k)$ = phase shift of the absorbing atom
$\phi_j(k)$ = phase shift of the backscattering atoms in the j^{th} shell

The amplitude $A_j(k)$ contains several structural information and is expressed as follows:[95]

$$A_j(k) = \frac{N_j}{kr_j^2} S_i(k) F_j(k) e^{-2k^2\sigma_j^2} e^{-2r_j/\lambda(k)} \tag{11}$$

Insertion of equations (9) and (11) in (8) results in the so-called EXAFS formula:

$$\chi(k) = \sum_j N_j S_i(k) F_j(k) e^{-2\sigma_j^2 k^2} e^{-2r_j/\lambda_j(k)} \frac{\sin\left[2kr_j + \phi_{ij}(k)\right]}{kr_j^2} \tag{12}$$

In the following section the parameters contributing to the EXAFS formula are explained in more detail.

- $F_j(k)$: Backscattering amplitude of N_j neighbouring atoms in the j^{th} shell at distance r_j. Due to the resonant nature of the backscattering process, the intensity is enhanced at energies of the photoelectron that are equal to the orbital energies of the backscattering atom. Therefore, the backscattering amplitude is element specific, since each atom has a unique electronic configuration.[121]
- N_j: Number of neighbouring atoms of the j^{th} coordination shell. All atoms of the same type at the same distance r_j contribute to one coordination shell.
- σ_j: Debye-Waller-like factor which contains structural as well as chemical information. σ_j accounts for thermal vibrations (σ_{vib}) and static disorder (σ_{stat}), therefore, σ_j is expressed as summation of both components $\sigma_j = \sigma_{vib} + \sigma_{stat}$. These two components can be separated by temperature dependent studies, since the thermal vibrations can be diminished by measurements at low temperatures.[95]
- $\frac{1}{kr_j^2}$: Describes the distance dependence of the EXAFS oscillations. The larger the distances between absorbing and scattering atom, the weaker the corresponding EXAFS signal appears. The scattering amplitude of nearest neighbours is dominating the spectrum, while scatterers at larger distances contribute only weakly.[95]
- $\sin\left[2kr_j - \phi_{ij}(k)\right]$: Sinusoidal oscillations as a function of the interatomic distances ($2kr_j$) and the total phase shift $\phi_{ij}(k)$, as described above.[95,121]

The last two components of the EXAFS formula are attributed to inelastic scattering processes resulting in a reduction of the EXAFS amplitude.

- $e^{-2r_j/\lambda_j(k)}$: Accounts for inelastic losses due to excitations of neighbouring atoms and the intervening medium. Therefore, the photoelectron lifetime is reduced in dependence of its mean free path length $\lambda_j(k)$, leading to an amplitude reduction.
- $S_i(k)$: The amplitude reduction factor is the second contribution to inelastic losses, caused by multiple excitations of the absorbing atom *i*, such as many body effects like shake-up and shake-off processes. The photoelectron transfers a part of its kinetic energy to the other electrons of the absorbing atom, mainly localised in outer shells. These electrons are then excited to unoccupied bound states (shake-up) or into the continuum (shake-off). Since the total absorption rate has to be the same with or without multi-electron effects, these processes reduce the EXAFS amplitude due to loss of intensity of the primary channel.

1.3.3.5 Data Reduction and Evaluation

The determination of structural parameters from EXAFS data depends on the feasibility of resolving the experimental data into individual waves corresponding to the different backscattering neighbour atoms.[95] There are in general two different approaches to perform EXAFS analysis. One is the so-called curve fitting technique whereby the spectrum is fitted in k space. The refinement can be based on several different criteria like least squares or difference minimization.[95] The second technique is based on Fourier transformation of the data to obtain a radial distribution function in dependence of the distance *r*. Before the experimental data can be fitted or Fourier transformed, several steps of data reduction have to be performed to extract the oscillatory part of the absorption coefficient. Depending on which experimental mode was applied to perform the experiment, the obtained data need to be converted to a spectrum of the absorption coefficient $\mu(E)$ in dependence of energy *E*. For spectra collected in transmission mode, the Lambert-Beer's law is applied, since the absorption coefficient is proportional to the natural logarithm of the incident intensity referred to the transmitted intensity according to $\mu(E) \sim \ln I_0/I$. For spectra received in fluorescence mode, however, the absorption coefficient is proportional to the emitted fluorescence intensity which is normalized to the incident intensity, $\mu(E) \sim I_f/I_0$.[96]
Subsequent to the conversion of the experimental data to the spectrum, further steps of data reduction have to be performed:[95,121,122]

1) Pre-edge background removal
2) Atomic background removal and data normalization
3) Conversion into k space
4) Fourier transformation

1) Pre-edge background removal

In the first step, the contributions of lower-energy edges and Compton scattering to the absorption coefficient have to be subtracted since only the region above the absorption edge is of interest for EXAFS analysis. For this, usually a Victoreen-spline of the form $\mu_{pre-edge} = cE^{-3} - dE^{-4}$ is used to approximate the pre-edge region, alternatively simple linear or quadratic polynomials can be used. Extrapolation of this function beyond the edge (as shown in Figure 1.15) and subsequent subtraction from the measured absorption coefficient results in the "elemental" absorption coefficient of the investigated chemical element.[120,122]

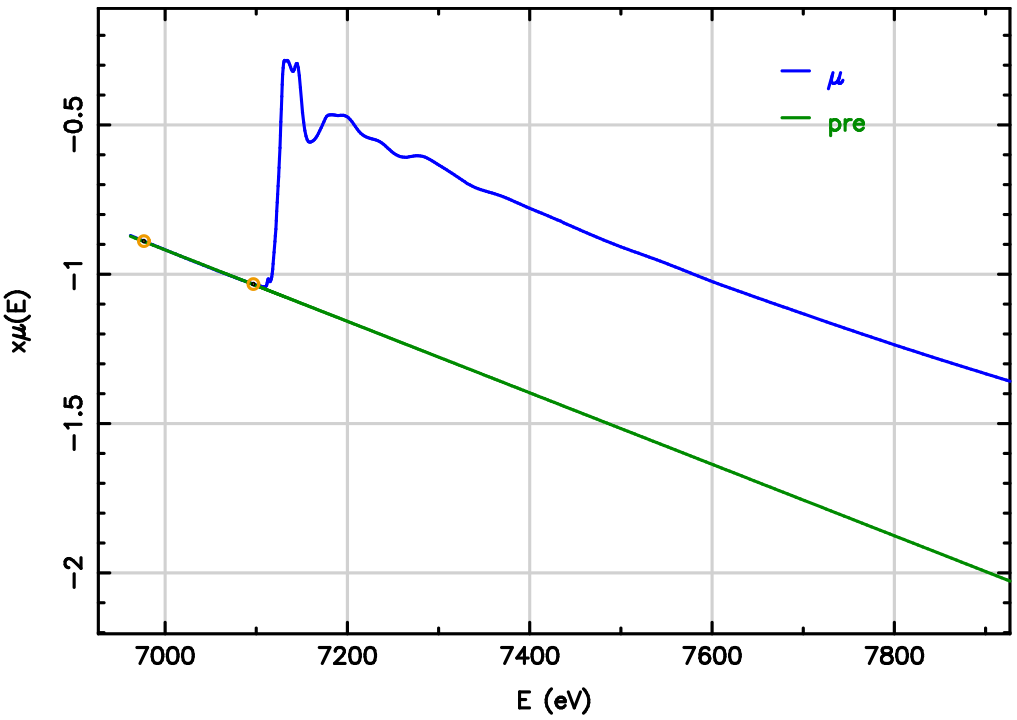

Figure 1.15: Experimental X-ray absorption coefficient $\mu(E)$ (μ, blue line) and adjusted pre-edge line (pre, green line).

2) Atomic background removal and data normalization

As already described in section 1.3.3.4, the EXAFS fine structure has to be extracted from the experimental spectrum before further analysis can be performed. For this, the absorption coefficient $\mu(E)$ has to be subtracted by the atomic background $\mu_0(E)$ and afterwards the resulting difference is normalized to $\mu_0(E)$. The atomic background, which is not the absorption coefficient of an isolated atom, but of an atom with effects of neighbouring atoms "switched off", is generally not known. Since it is influenced by different factors, like spectrometer baseline, beam harmonics or scattering of the photoelectron at valence electrons, it cannot be calculated or determined experimentally. Therefore, the atomic

background is assumed as the smooth part of the measured $\mu(E)$ (as shown in Figure 1.16), which can be approximated by different fitting procedures. The most common ones are least squares fits with polynomial splines or B-splines. A spline is a function defined over a series of polynomials (of same or different order) that are linked by knots. These knots are tied together in such a way that the function and at least the first derivative are continuous across the knots. The advantage of these spline functions is their high flexibility, obtained by varying the number of intervals and the order of the used polynomials. The applied least squares fit allows an effective removal of low frequency background contributions without affecting higher frequency EXAFS oscillations.

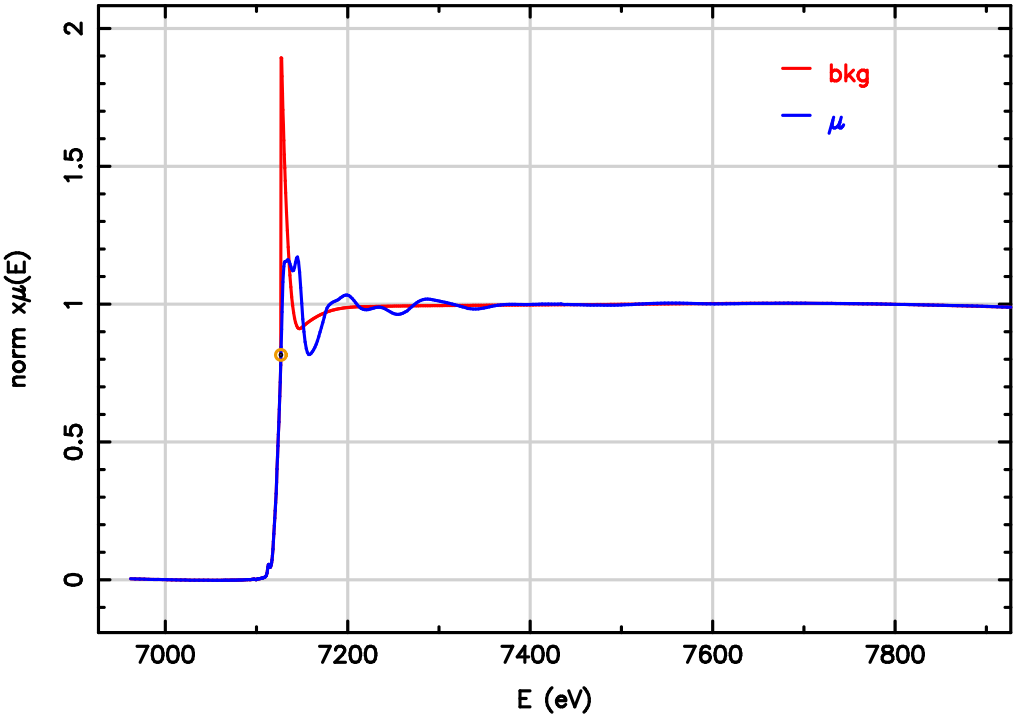

Figure 1.16: Background corrected and normalized "elemental" absorption coefficient (μ, blue line) with atomic background function $\mu_0(E)$ (bkg, red line).

3) Conversion to k space

After removal of the atomic background and normalization, the energy dependent $\chi(E)$ has to be converted from E space to k space according to $k = \sqrt{2m/\hbar^2(E - E_{binding})}$ (section 1.3.3.4, equation (7)). In this case, the threshold or electron binding energy $E_{binding}$ is equivalent to the edge energy of the spectrum. There are different ways to determine $E_{binding}$, probably the most common one is to use the first inflection point of the first derivative of the spectrum. Another possibility is to use the energetic position of half the edge jump, since in some cases the first method is difficult to apply. This is due to the

presence of resonances or electronic excitations which can cover up the exact edge position.[95,121,122]

4) Fourier transformation

Even though the spectrum can be analysed and interpreted in k space by fitting the function with theoretical models, usually a Fourier transformation (FT) is performed according to equation (13):[121,122]

$$\mathrm{FT}(r) = \frac{1}{\sqrt{2\pi}} \int_{k_{min}}^{k_{max}} k^n \chi(k) e^{i2kr}\, \mathrm{d}k \tag{13}$$

The Fourier transformation of $\chi(k)$ yields a pseudo radial distribution function with peaks at distances corresponding to the neighbouring shells. Due to the energy dependence of the phase factors in the sine function (compare equation (10)), the distances obtained by the transformation are usually about 0.2-0.5 Å shorter than the real distances. Fourier transformation results in a complex function, so a real and an imaginary part is obtained. The first one is mainly determined by the number of neighbouring atoms and disorder, while the latter can be used to determine the absorber-scatterer distances accurately.[121]

1.3.4 X-ray Emission Spectroscopy

After the detailed description of X-ray absorption spectroscopy, this chapter is focused on X-ray emission spectroscopy (XES). In principal, XES is based on recording of fluorescence X-rays that are emitted in course of the radiative decay of electrons of higher levels to a core hole. For this purpose, an instrument with an energy bandwidth on the order of the core hole lifetime broadening is used. The basic theoretical aspects of the different spectroscopic methods core-to-core (CtC) and valence-to-core (VtC) XES, high energy resolution fluorescence detected XANES (HERFD-XANES) and resonant inelastic scattering (RIXS) are explained, as well as the different types of instrumentation, which are mainly used.

1.3.4.1 History of XES

In the 1910s, the discovery and exploration of X-ray diffraction and especially the energy dependence of the diffraction angle over periodic crystal structures laid the foundation of X-ray emission spectroscopy in its today applied form.[131,132] In the first years after the discovery, the scientists tried to understand these fundamental physical processes and attempted to develop suitable instruments for related experimental investigations.[133] It was found out that the energy dependence of the diffraction angle could be utilised for the exact determination of the arrangement of atoms in crystals and vice versa for resolving

the energy distribution of X-rays.[133] The X-ray spectrometers used for these first experiments consisted of a rather simple setup based on a flat rotating plate the crystal was mounted on. The X-rays were produced by an X-ray tube and passed through several slits onto the crystal. The diffracted X-rays were collected on photographic plates.[133] By application of experimental studies on X-ray tube energy distributions, characteristic lines energies and X-ray scattering mechanisms, X-ray spectroscopy played an important role in the establishment of the atomic structure picture and quantum physics theories in the following years.[134–136] The periodic table, like it is known today, was established through the observations of the characteristic X-ray emission lines and their elemental wavelength dependence by *Henry Moseley*.[137] The steadily increasing research based on X-ray radiation lead to the necessity of highly efficient detection systems which provide a high energy resolution. For this purpose, mainly two different approaches were developed in the 1930s. Using curved diffraction optics, the first approach is based on reflecting geometry (Bragg optics), while the second one is used in transmission geometry (Laue optics). Different geometrical arrangements were developed by *Cauchois*, *DuMond*, *Johann*, *Johansson* and *von Hamos*, whereby most of them were based on the so-called Rowland circle geometry.[138–144] Even though there has been made great progress concerning the used technology – improved fabrication process of diffraction devices, X-ray detection systems, precise control of motorised stages and so on – modern X-ray spectrometers are based on the same geometrical arrangements developed in these early years. Today, X-ray emission is established in several different ways. For example, X-ray fluorescence spectrometry (XRF) based on the analysis of the characteristic lines can be used as a quantitative technique for elemental analysis of materials.[145] Furthermore, high energy resolution of emission lines is nowadays used to obtain information about the atomic species, atomic environment and the chemical state (oxidation or spin state).[134,146,147]

1.3.4.2 Theory of XES

Considering chapter 1.3.2, Interaction of X-rays with matter, it is obvious that X-ray emission is a two-step process. As described before, first an intermediate state with a vacancy in an inner-shell is created by photoionisation through the incoming photon. Afterwards, this intermediate state relaxes by emission of a fluorescence photon. Therefore, X-ray emission can be considered as a photon-in/photon-out process and thus an X-ray scattering phenomenon.[148] The incoming photon is characterised by an electro-magnetic field with vector field **A**, that is described by wave vector **k** and polarisation ε. The interaction of the photon with the sample can be described by a perturbation Hamiltonian with a linear ($\mathbf{p}\cdot\mathbf{A}$) and a quadratic term in **A**, whereby **p** is the electron momentum operator. In this treatment the interaction with the electron spin is neglected.[149] The quadratic term only contributes to the first order treatment of the perturbation, since it annihilates and

creates a photon in one single step, without a photon-less intermediate state. It can therefore be described as a one-step scattering process and accounts for Thomson, Compton and Raman scattering.[134,148] Contrary to this, the linear term **p**·**A** does only appear in the second order treatment and not in the first order. Starting from a ground state |g⟩, an intermediate state |n⟩ with lifetime τ_n is created by annihilation of a photon. Then, after creation of a photon, the final state |f⟩ with lifetime τ_f is reached. According to the Heisenberg uncertainty relation, the lifetimes can be translated into energy broadenings Γ. Even though cross-terms between **p**·**A** and $\mathbf{A^2}$ are possible, in case of element-specific spectroscopies these terms are not taken into account, so that only the **p**·**A** term is considered. The cross-section of this term is proportional to the resonant Kramers-Heisenberg term, which accounts for X-ray absorption and X-ray emission, as well as other resonant scattering processes:[134,150,151]

$$F_{HK}(\omega_{in},\omega_{out}) = \frac{\omega_{out}}{\omega_{in}}\sum_f\left|\sum_n \frac{\langle f|\hat{O}'^{\dagger}|n\rangle\langle n|\hat{O}|g\rangle}{E_n - E_g - \hbar\omega_{in} - i\Gamma_n}\right|^2 \frac{\frac{\Gamma_f}{\pi}}{\left(E_f - E_g - \hbar(\omega_{in}-\omega_{out})\right)^2 + \Gamma_f^2} \qquad (14)$$

With $\hat{O}'^{\dagger} = \sum_{j'}\left(\varepsilon_{out}^* \cdot \boldsymbol{p}_{j'}\right)e^{-i\boldsymbol{k}_{out}\boldsymbol{r}_{j'}}$ = transition operator

$\hat{O} = \sum_j(\varepsilon_{in}^* \cdot \boldsymbol{p}_j)e^{i\boldsymbol{k}_{in}\boldsymbol{r}_j}$ = transition operator

E_f, E_n, E_g = energy of final, intermediate and initial state

ω_{in}, ω_{out} = angular velocity of incoming and outgoing photon

Γ_n, Γ_f = energy broadening of intermediate and final state

In this equation, only one ground state is considered, while all intermediate and final states are summed up. Additionally, all electrons in the scattering system (*j*, *j*') are included in the transition operators. The denominator of the first fraction is a complex expression of a Lorentzian profile with the energy broadening Γ_n of the intermediate state appearing in the imaginary part. The second fraction describes a Lorentzian profile in which the energy transfer needs to be equal to an energy difference in the system within the energy bandwidth defined by the final state lifetime.[134]

Interference effects, which can occur according to equation (14) will affect only the intensities of the spectral features but not the transition energies. Therefore, these effects can be ignored, what leads to equation (15) with the cross-section being proportional to the product of absorption (first fraction) and emission (second fraction) probability.[134]

$$F_{HK}(\omega_{in}, \omega_{out}) \approx \frac{\omega_{out}}{\omega_{in}} \sum_f \sum_n \frac{\left|\langle f|\hat{O}'^{\dagger}|n\rangle\right|^2 \left|\langle n|\hat{O}|g\rangle\right|^2}{(E_n - E_g - \hbar\omega_{in})^2 + \Gamma_n^2} \times \frac{\frac{\Gamma_f}{\pi}}{\left(E_f - E_g - \hbar(\omega_{in} - \omega_{out})\right)^2 + \Gamma_f^2} \quad (15)$$

The resonant Kramers-Heisenberg equation can be used to explain several processes one may not consider as scattering processes at first look:

- The linear absorption coefficient $\mu(E)$ measured in X-ray absorption experiments is defined by the Lambert-Beer's law (see section 1.3.3.2, equation (3)). As mentioned above, it describes how strong a photon beam passing through a sample is attenuated. In general, this is also a photon-in/photon-out experiment, where the outgoing photon is scattered at an angle of 0 degrees (forward scattering). The scattering can be designated coherent, since the scattered photon is in phase with the incoming one. In addition, there is no energy change (elastic scattering) or polarisation. In this context, it is possible to describe absorption by the full Kramers-Heisenberg equation including the $\mathbf{A^2}$ term.[134,150]
- In principal, in XES there are two different ways how the incident energy can be tuned. If the energy is tuned well above an absorption edge (into the continuum) the method is called "non-resonant" XES. Contrary to this, tuning the incident energy close to an absorption edge leads to "resonant" XES. Since both types are based on X-ray emission after photoionisation, they can be described by the resonant Kramers-Heisenberg equation. In the non-resonant case, the intermediate state is described by an excited ion with a core hole and a photoelectron in the continuum. For calculations of non-resonant XES processes, an approximation can be made since it can be assumed that the interaction between the photoelectron and the excited ion is negligible. Therefore, in this simplification only the radiative decay from the excited ion into the ground state is considered, while the photoelectron is ignored. The situation is somewhat different in the resonant case. Here, the photoexcited electron is located in an orbital that is low enough in energy so that the electron can still interact with the other electrons of the excited ion. Even though a one-electron treatment may give satisfying results, one has to consider that multi-electron excitations can occur in both cases and description via the Kramers-Heisenberg formalism may be required.[134]
- Fluorescence or X-ray emission takes place after photoexcitation. Usually, the emitted radiation exhibits energies lower than the incident energy and so this process can be described by the Kramers-Heisenberg equation in form of an inelastic

X-ray scattering process. In fluorescence-detected absorption spectroscopy, the linear absorption coefficient $\mu(E)$ is detected in a second-order process according to the Kramers-Heisenberg formalism. Since the linear absorption coefficient $\mu(E)$ measured in true absorption experiments is defined for coherent elastic forward scattering (as described above), only an approximation of $\mu(E)$ can be measured in fluorescence-detected absorption spectroscopy. In case of hard X-ray experiments, like for 3d transition metal K-edges, this approximation is quite good. Unfortunately, this approximation fails for 3d transition metal L-edges, since the different excited states show different probabilities for radiative and non-radiative decay processes.[152] Unlike as in case of transition metal K-edges, the ejection of Auger electrons is the dominating decay process in 3d transition metal L-edge spectroscopy. Therefore, monitoring of the fluorescence detected absorption cannot result in the same linear absorption coefficient like in case of true absorption experiments.[134]

One- and multi-electron Description

The electronic transitions, described above, can be displayed in two different ways, either in a one- or a multi-electron diagram. Figure 1.17 depicts both varieties, each in the resonant as well as in the non-resonant case. The more vivid depiction is the one-electron diagram, since it shows transitions between the involved atomic orbitals. But this picture cannot provide information about interactions between electrons in open shells. In cases where the electron-electron interactions exhibit a magnitude in the order of or even larger than the experimental energy bandwidth and the lifetime broadening of the excited states, the spectral shape is influenced by these multi-electron effects. This leads to the fact that the one-electron picture bears only limited possibilities for a detailed understanding and analysis of the spectral features since it cannot cover multi-electron effects.[134]

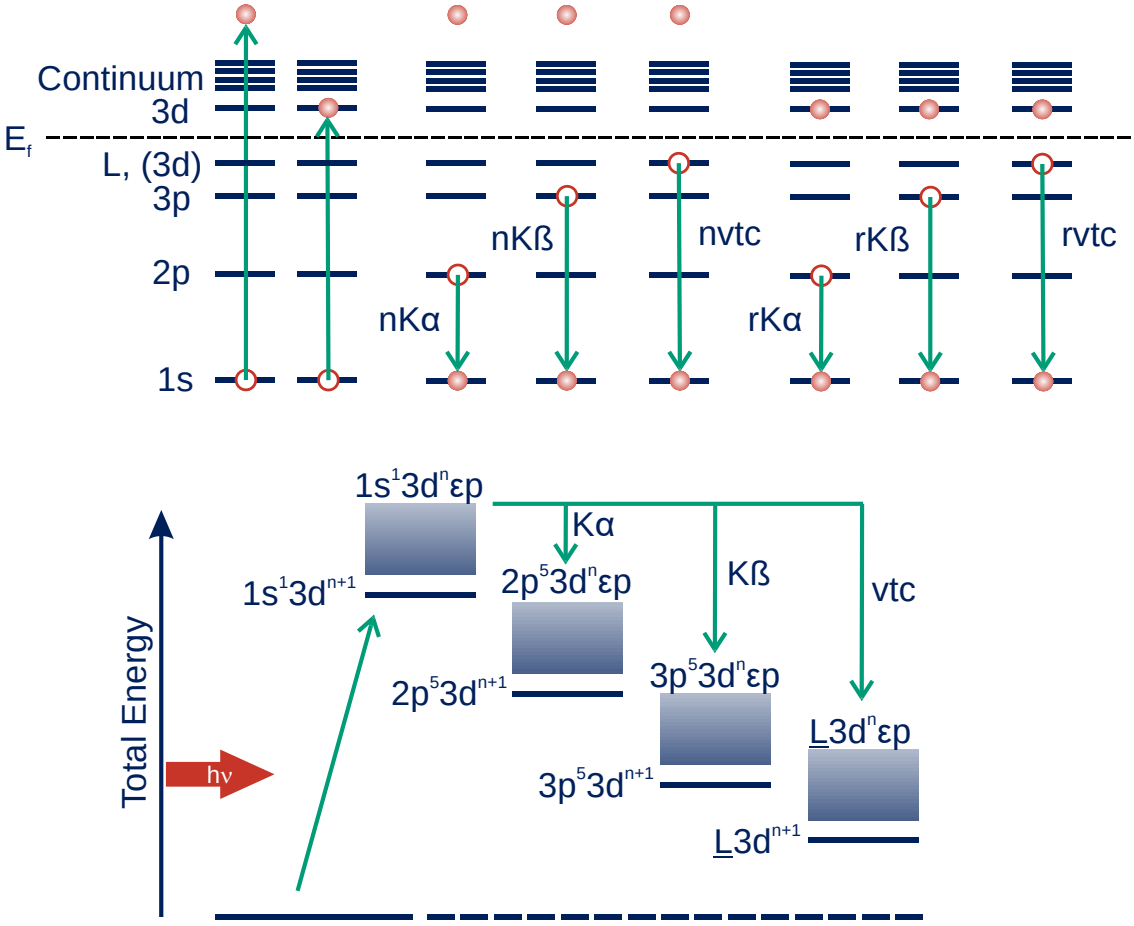

Figure 1.17: One-electron (top) and multi-electron description (bottom) of K emission in a 3d transition metal with ground state configuration $3d^n$. The resonant (r) as well as the non-resonant (n) case are shown. (L: hole in ligand orbital, ε: electron in continuum level, E_f: Fermi energy)

Contrary to the one-electron description, the multi-electron description is based on a total energy diagram, which considers all electrons of the excited atom, especially electrons in open shells, as well as the ejected photoelectron. Excited states at energies higher than the ground state can be reached by an external stimulus, like e.g. a photon, but it is not essential to know the nature of the transition exactly. In theory, all these states with the respective transition probabilities would result from an ideal calculation including all interactions between all nuclei and electrons. But up to today, such calculations are not feasible in reality due to the high demand of computing resources.[134] Since the dominant contribution to the transition and therefore to the electron configuration of the excited state is built by partially filled orbitals, the total energy diagram in Figure 1.17 bottom shows only configurations with partially filled orbitals.[134]

As mentioned before, the interaction between electrons can have a significant influence on the spectral shape, but in some cases the shape of the spectrum cannot be explained by

theses interactions solely. To elucidate this circumstance in more detail, the Kβ emission of 3d transition metals will be discussed. The fluorescence intensity of the Kβ main line results from transitions between populated 3p orbitals and the 1s core hole. The Kβ main line is also named $K\beta_{1,3}$ line to account for a line splitting caused by spin-orbit interactions of the electrons in the 3p shell which affects the shape of the strongest feature.[134,147] Whether this line splitting can be observed experimentally or not depends on the element of interest. While high Z elements like Uranium or Rhodium exhibit a visible line splitting, 3d transition metal complexes normally show no spin-orbit splitting. Only for free 3d metal atoms a line splitting can be observed.[134]

Due to the absence of this line splitting in 3d transition metal complexes, the spectral shape of the Kβ line needs to be explained by other effects. In general, the spin-orbit splitting needs to be larger than all other electron-electron interactions to be observable. Hence, the magnitude of the different interactions, such as spin-orbit splitting or electron-electron interactions, has to be determined for a detailed understanding. Today, several codes are available that can provide these values.[153,154] Looking at a $3p^5 3d^5$ configuration, the final state configuration of the Kβ emission of Mn(II), one can see, that the 3p spin-orbit interaction is about ten times smaller than the 3p-3d exchange interaction, but still about ten times larger than the 3d spin-orbit interaction. [134,147] Therefore, in case of the Kβ emission, the spectral shape is caused by the 3p-3d interactions, while the spin-orbit interactions can be neglected. For Kα emission 2p spin-orbit interaction is dominating, resulting in a visible line splitting ($K\alpha_1$, $K\alpha_2$).

1.3.4.3 Chemical Sensitivity of X-ray Emission

The chemical sensitivity and information content of XES spectra depends on the transitions which are observed. In general, XES probes occupied orbitals and whether the transition is a core-to-core (CtC, $K\alpha_1$, $K\alpha_2$ and Kβ main) or a valence-to-core (VtC, Kβ satellite) transition, different information can be extracted. The next two sections deal with the information content of CtC with focus on Kβ main line and VtC emission and how this information can be employed for the investigation of SCO processes.

Core-to-core Emission

CtC emission does not probe the valence electrons directly, since it originates from relaxation of 2p (Kα) or 3p (Kβ) core electrons to the 1s core hole. Therefore, the chemical sensitivity in this type of spectra is only indirect. Depending on the spin state of the probed metal ion the Kβ emission spectrum shows two prominent features, the intense $K\beta_{1,3}$ line at higher energies and at lower fluorescence energies the Kβ' signal. With decreasing valence spin state both features move towards each other as can be seen in Figure 1.18.

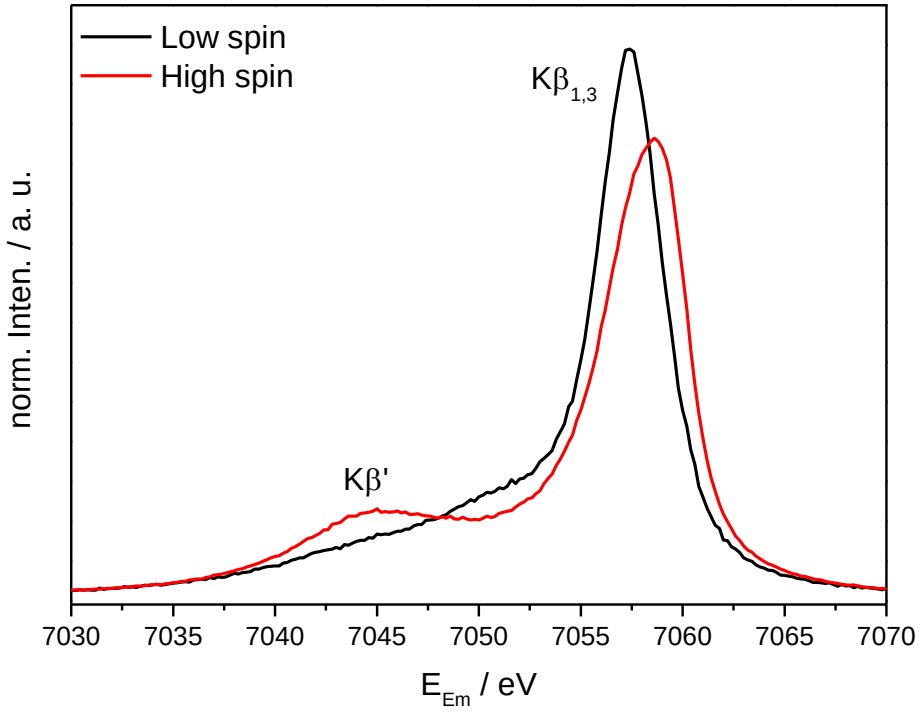

Figure 1.18: CtC emission spectra of an iron SCO compound in LS and HS state.

The shape of the CtC emission line is primarily influenced by the 3p-3d exchange interaction as already mentioned before, but the spectral features are affected by different effects depending on the valence electron configuration and thus the spin state, too. One effect is the screening of the core hole potential, that directly depends on the valence charge density. This density is influenced by the total number of 3d electrons and therefore by the oxidation state of the metal ion. Additionally, the effective number of 3d electrons is affected by the degree of covalency, since the electron cloud between the metal ion and the ligand is more delocalised for more covalent compounds. In the spectrum, a change of the valence charge density leads to a small but observable shift of the $K\beta_{1,3}$ line. Although it would be straightforward to attribute this shift to the changes of the nuclear screening following the changes of the valence charge density, *Glatzel* showed, that the shift can be ascribed to the variations in the 3p-3d exchange splitting.[155,156]

Therefore, the spectra are however shaped indirectly by changes of the nuclear screening, since this influences the 3p-3d exchange interaction as well.[134,147]

The 3p-3d exchange interaction has a second effect on the Kβ main line spectrum since it is responsible for the Kβ' signal at lower fluorescence energies.[155] A change of the spin state or the formal oxidation state results in a modified electron-electron interaction between the valence electrons and the unpaired 3p electron. With increasing number of unpaired 3d electrons the 3p-3d exchange interaction and therefore the intensity of the Kβ' signal increases, too.[134,147]

In the past years, several publications described the potential of the Kβ main line emission for determination of the spin state or for monitoring changes of the spin state of a system, more precisely the local magnetic moment on the 3d orbitals, even in a quantitative way.[88,89,157–161]

Since both features of the Kβ main line are sensitive to changes of the spin state, as already mentioned before, a number of different methods to quantify the spin state have been described. The approaches are either based on variations of intensity or energy shifts of the spectral features. *Vankó* gave a concise survey on the methods and tested their suitability on a set of simulated Kβ spectra.[88] A more detailed description of the different methods can be found in chapter 4 (Core-to-Core Emission Spectroscopy) of this thesis.

Valence-to-core Emission

Unlike CtC emission, VtC emission is directly influenced by the coordination environment of the metal centre, since it probes transitions from the valence orbitals (highest occupied molecular orbitals, HOMOs) into the metal 1s core hole. [134,147,162–165] Since the HOMOs are influenced by the ligand environment and the spin state at the metal centre there is a direct correlation with the spectral shape of the VtC spectra.

The typical structure of a VtC emission spectrum with the $K\beta_{2,5}$ line and the Kβ'' signal is depicted in the upper panel of Figure 1.19 using the example of Fe_2O_3. The Kβ'' signal can be used to identify different types of ligands like C, N or O since it is assigned to ligand 2s to metal 1s cross-over transitions. Therefore, it is also called cross-over transition. This signal generally appears at lower fluorescence energies compared to the $K\beta_{2,5}$ feature and it is shifted approximately by the ligand 2s binding energies of the atomic species.[147,162] Another interesting property of VtC emission spectra is the dependency of the spectral intensity on the metal-ligand distance. With increasing bond length, the intensity of the $K\beta_{2,5}$ feature is reduced due to a weaker overlap between the metal np orbitals and the ligand orbitals.[162,165,166] Consequently, this fact should also be a suitable probe for changes of the spin state during SCO processes. Since the metal-ligand bond length is elongated with increasing HS fraction, the strength of the overlap is reduced and therefore, the intensity of the VtC emission is lowered as well.

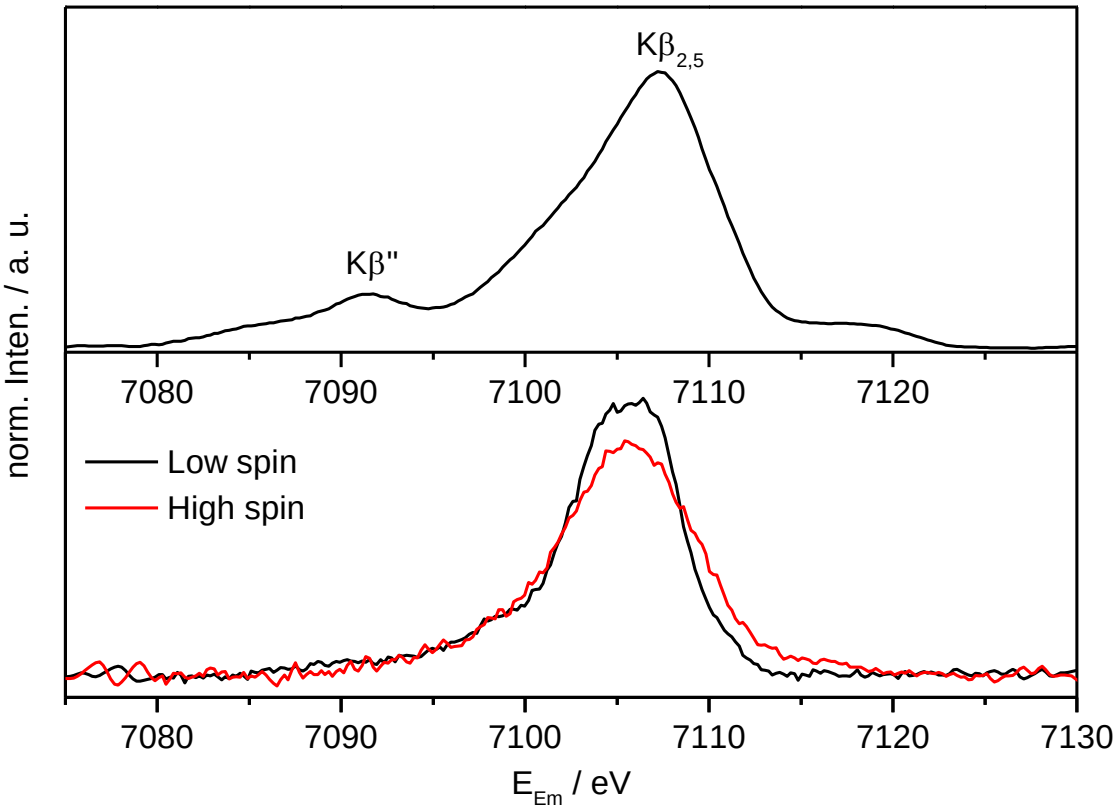

Figure 1.19: Top: Area normalized VtC emission spectrum of Fe_2O_3 with the $K\beta_{2,5}$ line at higher fluorescence energies and the Kβ'' signal at lower energies. Bottom: Area normalized VtC emission spectra of an iron SCO compound in the LS and HS state.

The lower panel of Figure 1.19 shows exemplarily the area-normalized VtC spectra of an iron SCO compound in the HS and LS state. It can be seen, that the spectrum of the HS species (red) with longer bond lengths shows a decreased intensity of the $K\beta_{2,5}$ feature and almost no intensity in the Kβ'' region compared to the spectrum of the LS species (black). Additionally, in relation to the LS spectrum the HS spectrum shows a broadening. In the results part of this thesis it will be evaluated in which way these different changes can be utilized to follow the changes of the spin state during the SCO process and if a quantification of the spin is possible.

1.3.4.4 HERFD-XANES and RIXS Spectroscopy

As already described in chapter 1.3.3 (X-ray Absorption Spectroscopy), XANES spectroscopy, especially the pre-edge region, offers information about the oxidation state, the local site symmetry and the spin state as well. Basically, the transitions into the LUMO states are 1s $\rightarrow$ 3d transitions in case of K-edge spectra, which are dipole forbidden. Only hybridization with p orbitals leads to dipole allowed transitions and therefore increased intensity. But in general, the pre-edge features are of quite low intensity. Due to the short lifetime of the 1s core hole, the lifetime broadening in conventional XAS limits the obtainable resolution according to Heisenberg's uncertainty principle. Therefore, it is often difficult to separate and resolve the prepeak features from the rising edge, which is assigned to 1s $\rightarrow$ 4p transitions. A possibility to circumvent this limitation is the application of the so-called partial fluorescence yield (PFY) or HERFD-XANES technique, [147,167,168] where the XAS spectra are collected in fluorescence mode. In contrast to conventional XAS, where the whole fluorescence intensity is collected, the spectra are recorded by monitoring a selected fluorescence decay channel with an energy resolution smaller than the natural lifetime broadening. In practice, the incident energy is scanned across the absorption edge with a double crystal monochromator and the fluorescence intensity of e.g. the Kα or Kβ main line is monitored with analyser crystals. The advantage of this procedure arises from the fact that fluorescence detected XAS is based on second-order process described by the Kramers-Heisenberg equation (cf. chapter 1.3.4.2).[151] Since the broadening of the spectrum is determined by the lifetime of the final state core hole, which is in this case either a 2p or 3p hole, the fluorescence detection results in a line sharpening effect, demonstrated in Figure 1.20. As can be seen, even though the fluorescence detected XAS is not exactly proportional to the linear absorption coefficient measured in true absorption experiments, in case of 3d transition metal K edge XAS the resulting signal is approximately the same.[134,147] Only in the pre-edge region significant differences are visible, since the prepeak features are much better separated from the rising edge and also the resolution of the signals is improved.

For the investigation of SCO compounds, the most interesting part of a XANES spectrum is the prepeak region, since it offers information about the distribution of the 3d electrons and so it can be used to determine the spin state of the system. Therefore, the improvement in resolution gained by the HERFD-XANES technique offers enhanced possibilities for quantitative analysis of the spin state, what will be elucidated in the results section in more detail.

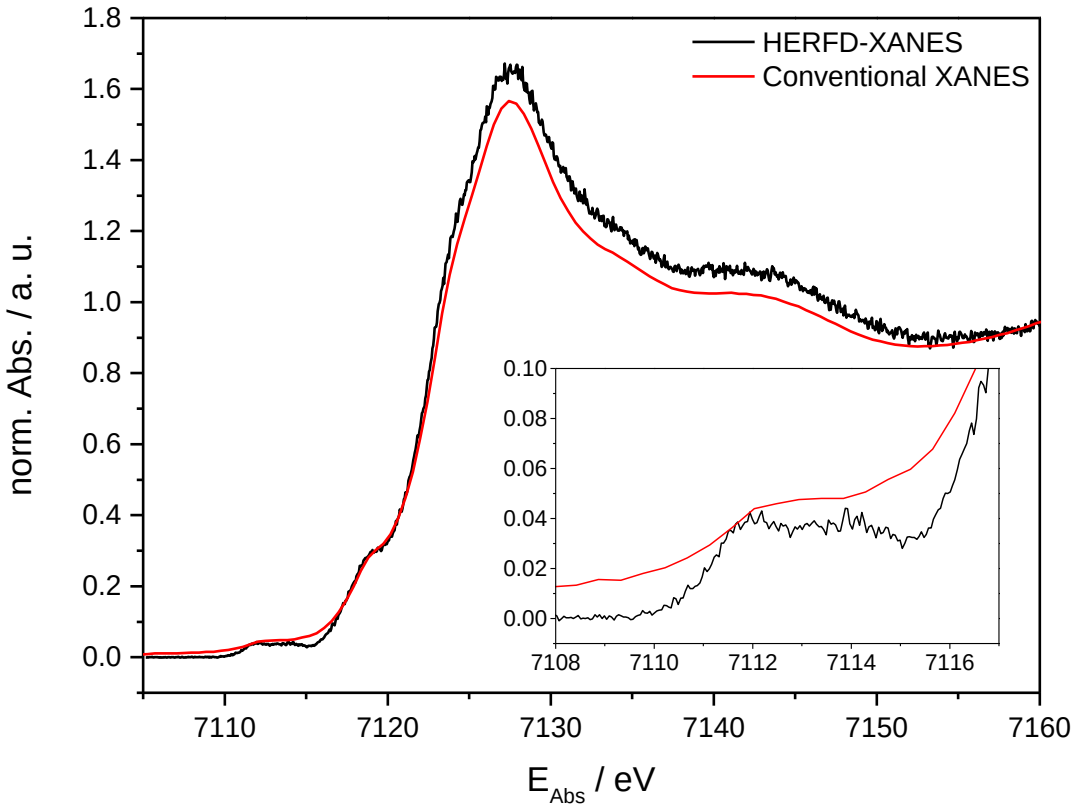

Figure 1.20: Comparison of conventional (red) and HERFD-XANES (black) of an iron(II) HS compound. The enlarged prepeak region is shown in the inset.

A correlated technique to facilitate the separation of the pre-edge from the main edge is the so-called RIXS spectroscopy,[147] which will only be discussed briefly. In general, it is based on the same principal as HERFD-XAS, with the difference that both the incident (Ω) as well as the emitted energy (ω) are scanned. Figure 1.21 shows a simulated RIXS plane together with different line scans that can be extracted from this 2D contour plot.[170] As can be seen, if the energy transfer Ω-ω is plotted versus the incident energy, the two lifetime broadenings of the intermediate and the final state extend perpendicular to each other. As already discussed, the lifetime broadening of the intermediate state is larger than that of the final state. Therefore, scans at constant incident energy (Figure 1.21, bottom right) are broadened by the final state lifetime and scans at constant energy transfer (Figure 1.21, top left) by that of the intermediate state, namely the 1s core hole lifetime. A diagonal cut through the RIXS plane corresponds to a constant emission energy scan equivalent to a HERFD-XAS scan (Figure 1.21, top right). In this case the broadening of the spectrum is smaller than that of both depicted lifetime broadenings, according to equation (16):[167]

$$\Gamma_{CEE} = \frac{1}{\sqrt{\left(\frac{1}{\Gamma_n^2}\right) + \left(\frac{1}{\Gamma_f^2}\right)}} \tag{16}$$

With Γ_{CEE} = lifetime broadening of constant emission energy scan
Γ_n = lifetime broadening of 1s core hole / intermediate state
Γ_f = lifetime broadening of either 2p or 3p core hole / final state

So altogether, RIXS as well as HERFD-XANES spectroscopy offer great possibilities for the investigation of SCO compounds. The high resolution that can be obtained by these

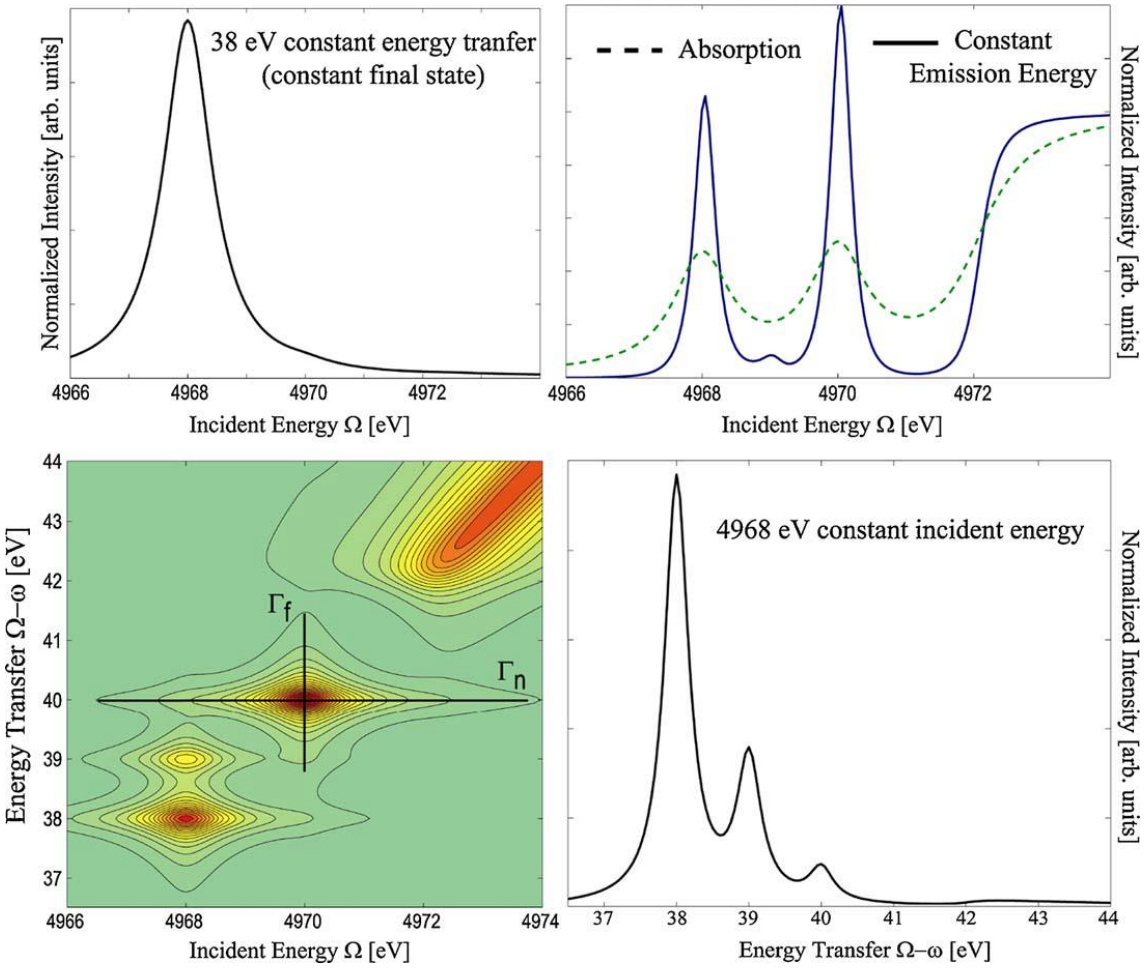

Figure 1.21: Bottom left: Simulated RIXS plane with lifetime broadenings of intermediate Γ_n and final state Γ_f. Extracted line scans for constant energy transfer (top left), constant incident energy (bottom right) and constant emission energy (top right) are shown as well. Figure reproduced with permission from Catalysis Today, Elsevier.[168]

methods can be used to resolve the pre-edge signals with their small intensity and furthermore, it can help to reveal further signals, which are not visible in conventional XAS spectroscopy as shown in Figure 1.21 (top right). The advantages of RIXS and HERFD-XANES for a quantitative determination of the spin state will be elucidated in the results section.

1.3.4.5 X-ray Emission Spectrometers

All the above described emission based techniques (CtC-XES, VtC-XES, HERFD-XANES and RIXS) are based on the diffraction of X-rays over perfect analyser crystals according to the Bragg equation:

$$n\lambda = 2d \sin\theta \tag{17}$$

With: d = lattice constant
θ = Bragg angle
n = diffraction order
λ =X-ray wavelength

The Bragg law describes that each photon with a given energy is diffracted at a given angle θ. In a real Bragg crystal, the X-ray radiation with wavelength λ will be dispersed to a range of angles near θ, meaning that there is an angular width $\Delta\theta$, so-called Darwin width, for which the above mentioned condition is fulfilled. The Darwin width depends on several factors, like quality and thickness of the crystal or lattice stress, and it contributes to the energy resolution dE according to the derivative of the Bragg law:[171]

$$\mathrm{d}E/E = \mathrm{d}\theta \cot\theta \tag{18}$$

For the so-called backscattering geometry θ = 90°, the angular width becomes zero and therefore, it is attempted to approximate this geometry in practical applications.
In general, one can distinguish between reflection (Bragg) and transmission (Laue) detection, but for photon energies below 20 keV usually reflection geometries are used.[134] XES spectrometers in reflective geometry can be grouped in two categories, namely scanning and dispersive setups. The first one uses scanning components to record the X-ray

intensity step by step in a certain energy range, while the second one utilises dispersing components which allow to detect a rather broad energy range simultaneously with a position sensitive 2D detector. Both types will be discussed shortly in the following sections, using the most common examples, like the Johann, Johansson and von Hamos geometries.

Point-to-Point Scanning Spectrometers

The most applied geometrical arrangement for scanning spectrometers is the so called Rowland circle geometry according to *Johann* and *Johansson*.[138,139] In this geometry the X-ray beam originating from a fixed point on the circle is reflected onto the detector with the same Bragg angle θ from any point of the circle. The most commonly used scheme is the *Johann* approach where the sample source, a bent analyser crystal with radius 2*R* and an X-ray detector are placed on a circle with radius *R*. Since the radius of the crystal surface is different from that of the Rowland circle, only the central point of the bent crystal is on the circle. This leads to the so-called Johann aberration, which is negligible if the surface of the crystal is not too extended and the Bragg angle is close to backscattering (θ = 90°). In the original Johann geometry,[138] the analyser crystal was bent cylindrically along the Rowland circle, while nowadays mainly spherically bent crystals are used. To increase the covered solid angle multiple analyser crystals on overlapping Rowland circles can be employed as depicted in Figure 1.22. In practice, usually the sample position is fixed, so that the analyser crystals and the detector are placed on motorised parts to move their position along the Rowland circle.

A slightly different setup was introduced by *Johansson* in 1933.[139] This setup is based on modified crystal analysers, which have their crystallographic planes bent to a radius of 2*R*, while the optical surface is ground to radius *R*. This modification allows that the entire surface of the crystal is exactly on the Rowland circle. Thus, the Johansson spectrometer is focusing precisely and it is not restricted to geometries near backscattering, since there is no variation of the incident angles across the crystal like in Johann-type spectrometers. Additionally, the Johansson geometry is advantageous for lower energies (1.5 – 4.5 keV), because in this energy range smaller Bragg angles are inevitable since no appropriate analyser crystals with Bragg angles above 70° are available.[134]

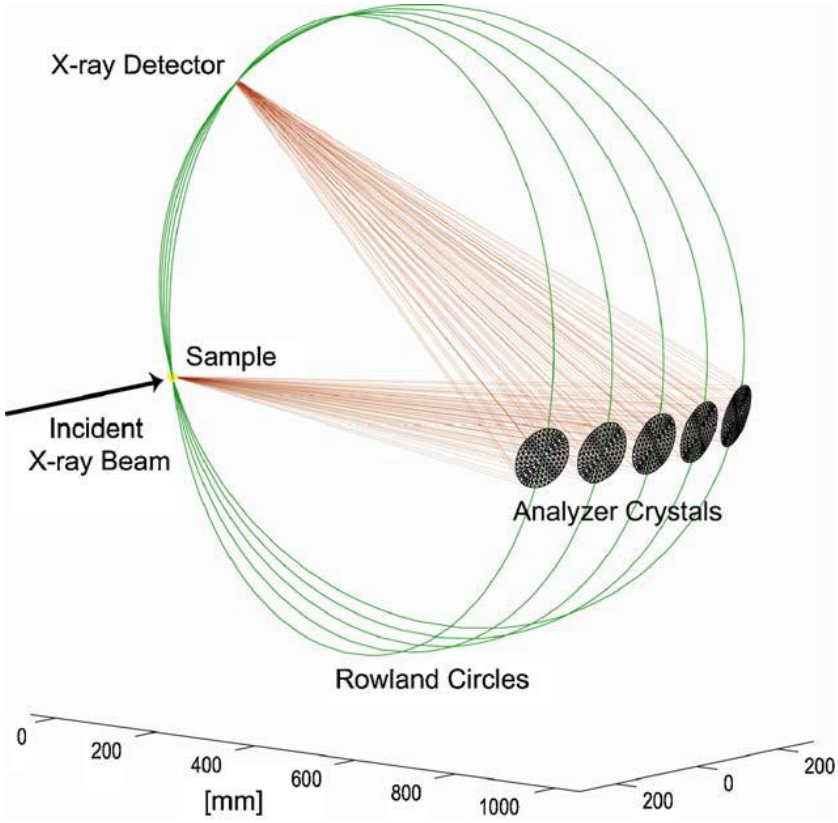

Figure 1.22: Johann-type X-ray emission spectrometer with five analyser crystals arranged with sample and detector on overlapping Rowland circles. Figure reproduced with permission from Catalysis Today, Elsevier.[168]

Wavelength Dispersive Setups

As already discussed, the second group of X-ray emission spectrometers are wavelength dispersive setups. Here, the X-rays are diffracted simultaneously by the optical element (crystal) over a range of Bragg angles and then the diffracted radiation is detected by a position sensitive detector.[134] The advantage of these setups is that there is no need for scanning to collect a full spectrum and since all intensities for all energies are recorded simultaneously no normalization to the incident beam is necessary. With this setup single shot measurements become possible, which are of great interest for time-dependent investigations, like for example pump-probe or catalytic experiments. Additionally, RIXS experiments are simplified significantly, since there is no more need to scan the emitted energy.

The simplest arrangement contains a flat crystal that diffracts the incident X-rays, which are then detected position sensitive. With this setup it is difficult to obtain a high resolution while collecting a large solid angle, so applications for XES are rather rare. Another possibility is the use of the von Hamos geometry.[140] As shown in Figure 1.23, this setup is based on cylindrically bent analyser crystals, which combine the advantages of planar crystals (high-energy resolution) and curved crystals (large solid angle). These crystals diffract and focus the emitted radiation from the sample to the 2D detector according to Bragg's law (cf. equation 17).

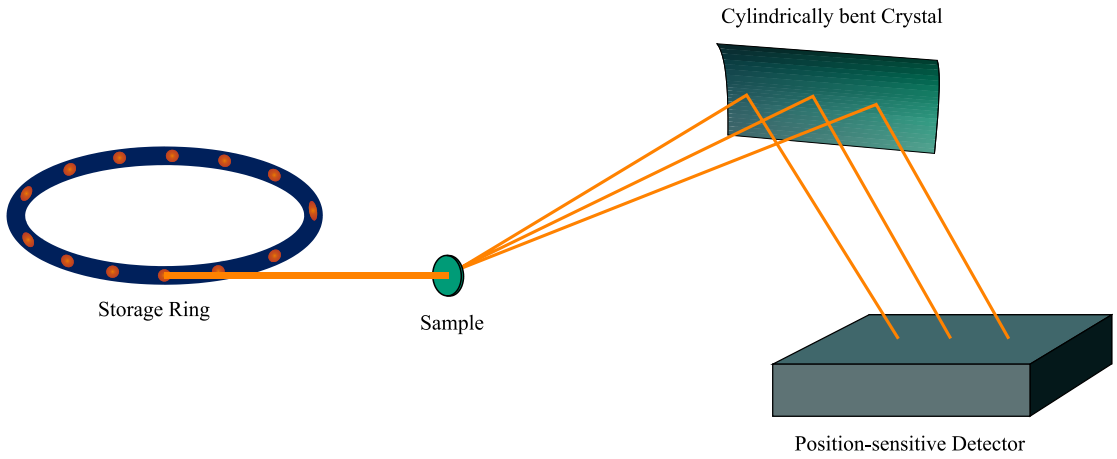

Figure 1.23: Schematic setup of a dispersive X-ray emission spectrometer in von Hamos geometry.

In recent years, some other dispersive setups based for example on the Rowland geometry have been developed, but will not be discussed here.

1.4 Motivation and Scope of this Work

The scope of this thesis is focused on the improvement of existing and development of new methods for the analysis of SCO processes with hard X-ray spectroscopic techniques. As already described in the introduction, there are a number of standard experimental techniques, which are mainly applied in SCO research, such as SQUID magnetometry, X-ray structural analysis, Mößbauer, IR, Raman, NMR, EPR or UV/Vis spectroscopy. But unfortunately, these methods bear several limitations: most of the techniques are restricted to defined working conditions or are limited to specific aggregation states or elements (e.g. Mößbauer spectroscopy). In addition, the mentioned techniques provide either electronic *or* structural information, so a combination of results from different techniques is necessary to obtain a complete picture of the effects occurring during the SCO process. At this point, the advantages of hard X-ray absorption and emission spectroscopy become important, since these methods offer the possibility to investigate samples under various conditions (e.g. cryogenic or elevated temperature, pressure etc.) and in all states of aggregation. Furthermore, these techniques provide structural as well as electronic information in one experiment without changing the experimental conditions.
There are only very few studies combining the advantages of some of the described X-ray spectroscopic techniques (EXAFS, VtC-XES, CtC-XES, HERFD-XANES, RIXS) which concentrate on the examination of the spin state or more precisely the change of the spin state during a SCO process. [80,88,89]
Therefore, all the above mentioned high resolution X-ray techniques shall be applied to a chosen SCO compound with a temperature-induced spin transition, which is described subsequently. The resulting temperature-dependent spectra are analysed by different methods to obtain a correlation of the spectral changes with the spin state. For this, already known analytical methods are tested with regard to their applicability for the investigation of SCO processes and if necessary, the methods shall be improved and refined. Additionally, new analytical methods are developed, that can be used to correlate the spectral features or the changes of the spectral features during the SCO process with the spin state.
The used SCO compound $[Fe(L\text{-}N_4Bn_2)(NCS)_2]$ (L-N_4Bn_2 = N,N′-Dibenzyl-2,11-diaza[3.3](2.6)pyridinophane) is an iron(II) complex with a substituted macrocyclic diaza[3.3](2.6)pyridinophane ligand (cf. Figure 1.24, left), that builds a cis-octahedral coordination geometry around the Fe centre completed by two monodentate NCS co-ligands (cf. Figure 1.24, right).[172] This type of complexes is already known for several metals with different substituents at the macrocycle and different mono- or bidentate co-ligands.[173] Depending on the used ligands, the ligand field strength can be tuned in such way that either LS, HS or SCO compounds are obtained. Therefore, it is possible to use compounds with very similar geometry as reference systems for the different spin states. The reference compounds used in this work are described in chapter 4.2.1 in more detail. All complexes used in this work (SCO and reference compounds) were provided by the

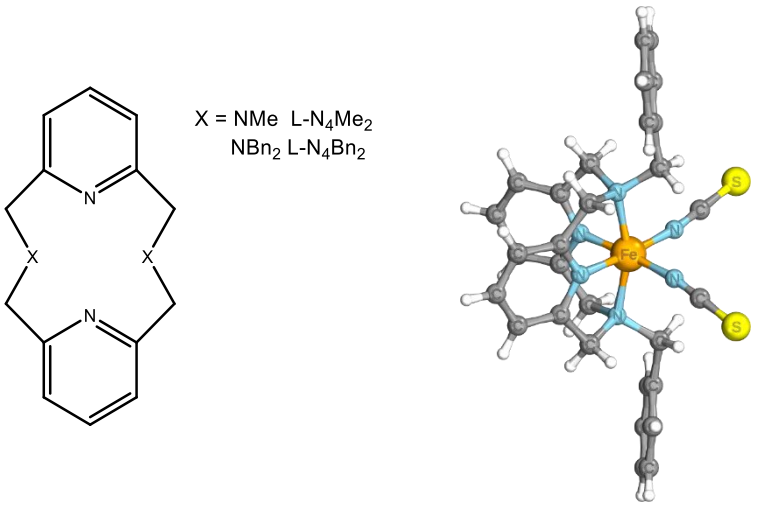

Figure 1.24: Left: Schematic structure of the 2,11-diaza[3.3](2,6)pyridinophane (L-N_4R_2) ligand system with R=Me, Bn. Right: Crystal structure of [Fe(L-N_4Bn_2)$(NCS)_2$] at 110 K.

group of Prof. Dr. Krüger (Inorganic Chemistry, Technische Universität Kaiserslautern), where the substances were synthesised and characterised.

The SCO behaviour of [Fe(L-N_4Bn_2)$(NCS)_2$] is already extensively investigated by several characterisation methods, like e.g. SQUID magnetometry, temperature-dependent X-ray crystallography, IR, Raman, Mößbauer and UV/Vis spectroscopy.[172] The magnetization measurements by SQUID magnetometry revealed a gradual SCO behaviour in a temperature range from around 150 K up to 250 K, where the transition is almost completed. Figure 1.25 shows the product of the molar susceptibility χ_M and temperature T plotted in dependence of temperature T.

The temperature-dependent X-ray crystallography data showed the same SCO behaviour as the magnetization obtained by SQUID and additionally, the data indicate that the SCO process is of an isotropic nature, since the different Fe-N bonds change simultaneously at almost the same temperature. These structural parameters will be used for the analysis of the EXAFS spectra and are shown in chapter 2.3.2.2.

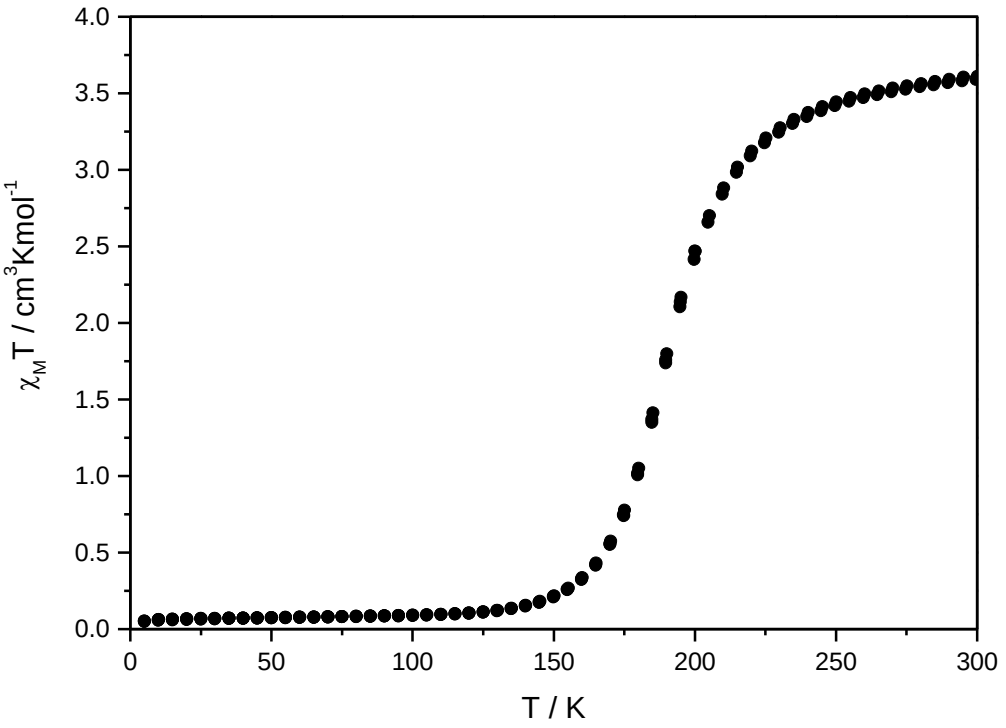

Figure 1.25: Plot of the product of the molar magnetic susceptibility with temperature $\chi_M T$ versus temperature T.

The occurrence of the SCO behaviour of this complex was proven with all other mentioned methods, as well. In case of Mößbauer spectroscopy, characteristic subspectra for HS and LS were detected at high and low temperature, as well as a mixture of both at the SCO temperature. For temperature-dependent IR and Raman spectroscopy the N-C stretching vibration of the NCS ligand was used as an indicator for the spin change. A spin transition curve could be derived by both techniques, but in each case the curve shape and the transition temperature showed significant deviations from the SQUID data. The increased transition temperature resulting from the analysis of the IR spectra, presumably could be attributed to the application of pressure to the sample during the measurements and sample preparation, leading to a preference of the LS state. In case of the Raman spectra, the lower transition temperature compared to the magnetization probably could be explained by the irradiation with laser light, leading to a local heating of the sample and therefore an increase of the HS fraction

The results obtained up to now clearly demonstrate the existing difficulties in SCO research, as described above. To obtain a complete view on the structural and electronic changes, the results of the different methods need to be combined, but the results are strongly influenced by the different measurement conditions. Therefore, it still remains unclear if the structural changes are induced by the electronic changes or vice versa.

2 EXAFS Spectroscopy

The following chapter is focused on the analysis of the temperature-dependent EXAFS experiments. In the investigated complex [Fe(L-N_4Bn_2)$(NCS)_2$] the iron centre is surrounded by six nitrogen atoms in the first sphere. Since the axial and equatorial Fe-N bond lengths show a difference of approx. 0.2 Å, it was tested if it is possible to distinguish the different nitrogen backscatterers by EXAFS spectroscopy and how the respective Fe-N bond lengths change during the SCO process. The obtained spectra were analysed with a number of different theoretical fit models using either one or two nitrogen shells. The resulting fit parameters were correlated with the spin state of the system and compared to the magnetization obtained by SQUID magnetometry. Additionally, the structural parameters were used to calculate the HS fraction at each temperature point. The chapter is finished with a summary of the obtained information and a comparison of the different models.

2.1 Experimental Section

EXAFS measurements were performed at the Swiss-Norwegian beamline (BM01B) at the European Synchrotron Radiation Facility (ESRF, Grenoble, France). A Si(111) double crystal monochromator was used for the measurements at the Fe K-edge (7.112 keV). Energy calibration was performed with an iron foil. The experiment was carried out in a temperature range of 10 – 293 K using a Helium cryostat under vacuum conditions. The spectra were recorded in transmission mode with ionisation chambers filled with nitrogen. The solid sample was diluted in boron nitride and pressed to a pellet. At each temperature point, temperature was allowed to stabilize and then several scans were averaged to obtain a good signal-to-noise ratio.

2.2 Data Analysis

Data analysis started with background absorption removal from the experimental absorption spectrum by subtracting a Victoreen-type polynomial.[174–177] The first maximum of the first derivative was set as E_0. Afterwards the smooth part of the spectrum, corrected for pre-edge absorption, was determined by use of a piecewise polynomial, which was adapted in a way that the low-R components of the resulting Fourier transform were minimal. The background-subtracted spectrum was divided by its smooth part and then the

photon energy was converted to photoelectron wavenumbers *k*. The resulting $\chi(k)$ was weighted with k^3 and Fourier transformed using a Hanning function window. According to the curved wave formalism data analysis was performed in *k*-space using the EXCURV98[178,179] program which calculates the EXAFS functions according to a formulation in terms of radial distribution functions:

$$\chi(k) = \sum_j S_0^2(k) F_j(k) \int P_j(r_j) \frac{e^{-2r_j/\lambda}}{kr_j^2} \sin\left[2kr_j + \delta_j(k)\right] \mathrm{d}r_j \tag{19}$$

To calculate the theoretical spectra XALPHA phase and amplitude functions [178,179] were used and the mean free path of the scattered electrons was calculated from the imaginary part of the potential (VPI set to -4.00). Additionally, a correction for the inner potential E_f was introduced to adjust the phase differences of the experimental and theoretical EXAFS functions.

The quality of the applied least-square fit is determined by the *R*-factor, which represents the percentage disagreement between experiment and theory and takes into account systematic and random errors according to [180,181]:

$$R = \sum_i^N \frac{k_i^n}{\sum_j^N k_j^n \left| \chi_j^{exp}(k_j) \right|} \left| \chi^{exp}(k_i) - \chi^{theo}(k_i) \right| \cdot 100\% \tag{20}$$

The accuracy of the determined distances is 1 %, of the Debye-Waller-like factor 10 % and of the coordination numbers depending of the distance 5–15 %.[121]

2.3 Results

For analysis of the temperature-dependent EXAFS measurements a number of different theoretical models was applied and compared to each other. According to the crystal structures at 110 K (LS) and 293 K (HS) the complex shows a quasi-octahedral coordination geometry with six nitrogen atoms in the first sphere around the iron centre (see Figure 2.1).

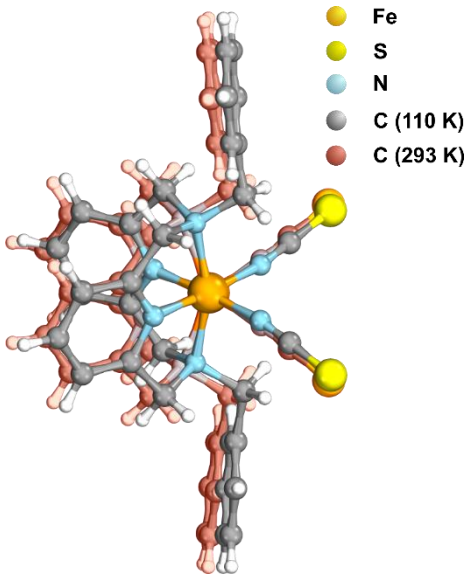

Figure 2.1: Crystal structures of $[Fe(L\text{-}N_4Bn_2)(NCS)_2]$ at 110 K (grey) and 293 K (red).

As a starting point for the EXAFS analysis two different approaches were applied. For the first one, the spectra of the LS (110 K) and the HS (293 K) state were fitted with parameters based on the crystal structure data of these temperatures. Then the resulting fit parameters were used as input structure for the spectra of the other temperature points. In case of the second approach, the Fe-N distances obtained from the temperature-dependent crystal structures were used as initial distances.

2.3.1 Fit Models with one Nitrogen Shell, unfiltered Data

For the first group of fits the unfiltered data were used and the fits were based on a model with one nitrogen shell with six N-atoms in the first coordination sphere. Additionally, three carbon shells at around 2.8 Å, 4.3 Å and 4.8 Å and a sulphur shell at 4.8 Å were fitted. The coordination numbers of the carbon shells were iterated freely, while the coordination number of nitrogen was fixed to 6 and of sulphur to 2 as obtained from the crystal structure. The distances were also based on the crystal structure data of the LS and the HS state (110 K and 293 K) and the Debye-Waller-like factors of all shells were iterated in the range of 0.032 – 0.112 $Å^{-1}$.

2.3.1.1 Fit Model 1A: Fit of unfiltered Data with one Nitrogen Shell based on HS and LS Distances and afac at 0.8000

In the first applied model with one nitrogen shell the amplitude reducing factor (afac) was held fix at the standard value 0.8000, while all other parameters were treated as explained above (cf. section 2.3.1).
The temperature-dependent EXAFS spectra with the resulting fit functions are displayed in k-space (top) and R-space (bottom) in Figure 2.2. In these figures, temperature increases from 10 K (bottom) to 293 K (top) and the spin transition temperature, as determined by SQUID magnetometry, is represented as the blue spectrum at 190 K.
Therefore, the spectra below the blue one depict the system with a predominant LS fraction while the spectra above the blue one depict the system mainly in the HS state. It is clearly visible, that the structure of the spectra is changing during the temperature induced SCO process, reflected by the shift of the signals to higher distances in the Fourier transformation according to an elongation of the Fe-N distances with increasing HS fraction (Figure 2.2, bottom).[8,11,68,75,76]
The resulting theoretical fit functions show a very good agreement with the experimental spectra from 10 K up to 150 K. In this temperature range the complex is almost completely present in the LS state. With beginning of the spin conversion from LS to HS the fit model with one nitrogen shell starts to fail, since it is not able to reproduce the intensity as well as the position of the first signal. The fit overestimates the intensity of this first signal corresponding to the nitrogen shell and additionally, the maximum of the signal is slightly shifted to higher distances compared to the experimental spectra. Especially at the spin transition temperature 190 K, where the system should consist of approximately 50% LS and 50% HS, the fit function is not able to reproduce the spectral shape, too. The experimental spectrum shows two signals at around 2.5 Å and 3 Å, which are assigned to carbon, whereas the theoretical fit function shows only one averaged signal at 2.85 Å.

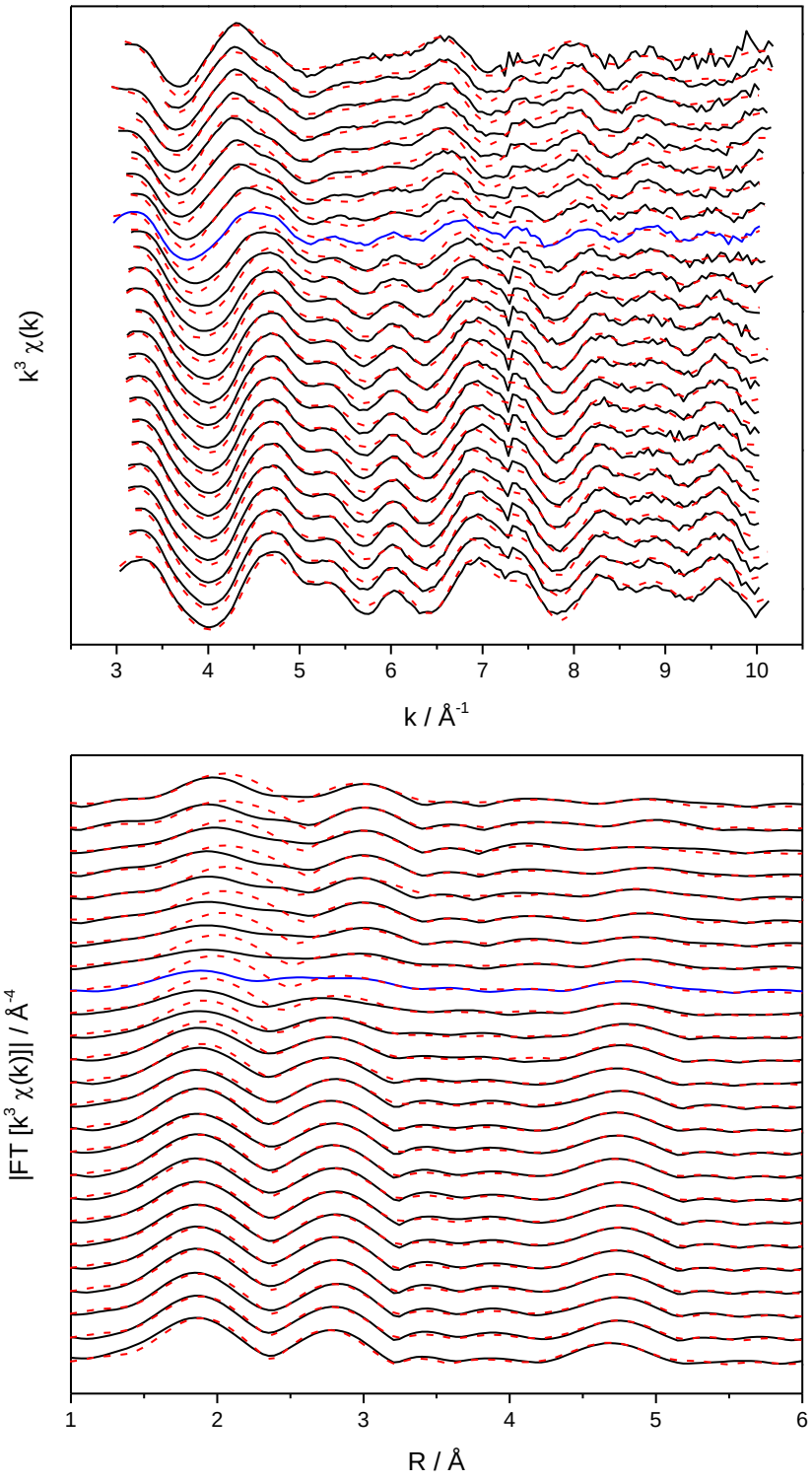

Figure 2.2: Fit model 1A: Temperature-dependent EXAFS spectra of [Fe(L-N_4Bn_2)$(NCS)_2$], blue spectrum: spin transition temperature (190 K), top: χ(k), bottom: Fourier transformation, (—) experimental data, (---) theoretical data.

To evaluate the quality of the fits, the fitting results of all temperatures are displayed in Table 1 as an overview.

Table 1: Fit model 1A: Neighbour atoms, coordination numbers and distances obtained by EXAFS analysis.

Sample	Abs-Bs [a]	N(Bs) [b]	R(Abs-Bs) [c] / Å	σ [d] / Å^{-1}	R [e] / % E_f [f] / eV Afac [g]
10 K	Fe-N Fe-C Fe-C Fe-S Fe-C	6.0 7.0±0.7 9.2±0.9 2.0 14.9±1.5	1.964±0.020 2.822±0.028 4.323±0.043 4.816±0.048 4.812±0.048	0.105±0.010 0.067±0.007 0.112±0.011 0.045±0.005 0.032±0.003	 24.19 4.449 0.8000
30 K	Fe-N Fe-C Fe-C Fe-S Fe-C	6.0 8.9±0.9 8.0±0.8 2.0 14.6±1.5	1.961±0.020 2.826±0.028 4.305±0.043 4.851±0.049 4.836±0.048	0.107±0.011 0.087±0.009 0.112±0.011 0.032±0.003 0.039±0.004	 21.13 3.887 0.8000
40 K	Fe-N Fe-C Fe-C Fe-S Fe-C	6.0 8.2±0.8 8.4±0.8 2.0 15.4±1.5	1.962±0.020 2.830±0.028 4.333±0.043 4.831±0.048 4.825±0.048	0.105±0.011 0.081±0.008 0.112±0.011 0.032±0.003 0.039±0.004	 23.11 3.840 0.8000
50 K	Fe-N Fe-C Fe-C Fe-S Fe-C	6.0 8.0±0.8 8.6±0.9 2.0 13.5±1.4	1.963±0.020 2.832±0.028 4.305±0.043 4.851±0.049 4.835±0.048	0.105±0.011 0.077±0.008 0.112±0.011 0.032±0.003 0.032±0.003	 22.21 3.627 0.8000
70 K	Fe-N Fe-C Fe-C Fe-S Fe-C	6.0 8.3±0.8 8.9±0.9 2.0 15.7±1.6	1.965±0.020 2.833±0.028 4.320±0.043 4.819±0.048 4.824±0.048	0.107±0.011 0.081±0.008 0.112±0.011 0.045±0.005 0.032±0.003	 21.13 3.581 0.8000
80 K	Fe-N Fe-C Fe-C Fe-S Fe-C	6.0 8.6±0.9 8.0±0.8 2.0 14.9±1.5	1.964±0.020 2.831±0.028 4.322±0.043 4.836±0.048 4.830±0.048	0.107±0.011 0.084±0.008 0.112±0.011 0.032±0.003 0.032±0.003	 20.34 3.730 0.8000
90 K	Fe-N Fe-C Fe-C Fe-S Fe-C	6.0 9.0±0.9 7.5±0.8 2.0 14.0±1.4	1.963±0.020 2.829±0.028 4.310±0.043 4.848±0.048 4.835±0.048	0.107±0.011 0.089±0.009 0.112±0.011 0.032±0.003 0.039±0.004	 21.57 3.854 0.8000
100 K	Fe-N Fe-C Fe-C Fe-S Fe-C	6.0 8.6±0.9 7.7±0.8 2.0 14.5±1.5	1.963±0.020 2.832±0.028 4.312±0.043 4.826±0.048 4.830±0.048	0.110±0.011 0.084±0.008 0.112±0.011 0.050±0.005 0.032±0.003	 23.08 3.875 0.8000

Sample	Abs-Bs [a]	N(Bs) [b]	R(Abs-Bs) [c] / Å	σ [d] / Å^{-1}	R [e] / % E_f [f] / eV Afac [g]
110 K	Fe-N Fe-C Fe-C Fe-S Fe-C	6.0 8.2±0.8 7.9±0.8 2.0 14.1±1.4	1.966±0.020 2.833±0.028 4.309±0.043 4.839±0.048 4.836±0.048	0.107±0.011 0.081±0.008 0.110±0.011 0.032±0.003 0.032±0.003	 21.06 3.830 0.8000
120 K	Fe-N Fe-C Fe-C Fe-S Fe-C	6.0 8.2±0.8 7.9±0.8 2.0 14.6±1.5	1.968±0.020 2.835±0.028 4.321±0.043 4.830±0.048 4.830±0.048	0.112±0.011 0.087±0.009 0.112±0.011 0.032±0.003 0.032±0.003	 22.65 3.763 0.8000
130 K	Fe-N Fe-C Fe-C Fe-S Fe-C	6.0 8.8±0.9 6.9±0.7 2.0 13.8±1.4	1.965±0.020 2.829±0.028 4.308±0.043 4.841±0.048 4.834±0.048	0.110±0.011 0.092±0.009 0.112±0.011 0.032±0.003 0.032±0.003	 20.99 4.080 0.8000
140 K	Fe-N Fe-C Fe-C Fe-S Fe-C	6.0 8.6±0.9 6.9±0.7 2.0 14.7±1.5	1.972±0.020 2.837±0.028 4.330±0.043 4.841±0.048 4.834±0.048	0.112±0.011 0.095±0.010 0.112±0.011 0.032±0.003 0.045±0.005	 24.00 3.940 0.8000
150 K	Fe-N Fe-C Fe-C Fe-S Fe-C	6.0 9.6±1.0 6.7±0.7 2.0 16.0±1.6	1.973±0.020 2.843±0.028 4.339±0.043 4.831±0.048 4.828±0.048	0.112±0.011 0.107±0.011 0.112±0.011 0.074±0.007 0.063±0.006	 25.76 3.975 0.8000
160 K	Fe-N Fe-C Fe-C Fe-S Fe-C	6.0 8.7±0.9 9.2±0.9 2.0 23.0±2.3	1.980±0.020 2.843±0.028 4.438±0.044 4.802±0.048 4.817±0.048	0.112±0.011 0.107±0.011 0.112±0.011 0.063±0.006 0.074±0.007	 28.88 4.509 0.8000
170 K	Fe-N Fe-C Fe-C Fe-S Fe-C	6.0 7.9±0.8 4.2±0.4 2.0 14.0±1.4	1.991±0.020 2.851±0.029 4.415±0.044 4.882±0.049 4.861±0.049	0.112±0.011 0.112±0.011 0.112±0.011 0.039±0.004 0.071±0.007	 39.03 4.424 0.8000
180 K	Fe-N Fe-C Fe-C Fe-S Fe-C	6.0 7.7±0.8 8.3±0.8 2.0 17.3±1.7	2.015±0.020 2.892±0.029 4.424±0.044 4.760±0.048 4.803±0.048	0.112±0.011 0.112±0.011 0.112±0.011 0.112±0.011 0.092±0.009	 49.30 5.111 0.8000
190 K	Fe-N Fe-C Fe-C Fe-S Fe-C	6.0 6.1±0.6 10.6±1.1 2.0 21.0±2.1	2.055±0.021 2.942±0.029 4.445±0.044 4.700±0.047 4.791±0.048	0.112±0.011 0.112±0.011 0.112±0.011 0.032±0.003 0.081±0.008	 60.68 4.316 0.8000
200 K	Fe-N Fe-C Fe-C Fe-S Fe-C	6.0 6.2±0.6 13.4±1.3 2.0 20.9±2.1	2.076±0.021 2.950±0.030 4.475±0.045 4.716±0.047 4.795±0.048	0.112±0.011 0.112±0.011 0.112±0.011 0.032±0.003 0.077±0.008	 56.59 5.042 0.8000

Sample	Abs-Bs [a]	N(Bs) [b]	R(Abs-Bs) [c] / Å	σ [d] / Å^{-1}	R [e] / % E_f [f] / eV Afac [g]
210 K	Fe-N Fe-C Fe-C Fe-S Fe-C	6.0 5.6±0.6 14.0±1.4 2.0 19.2±1.9	2.110±0.021 2.993±0.030 4.508±0.045 4.782±0.048 4.839±0.048	0.112±0.011 0.089±0.009 0.112±0.011 0.032±0.003 0.063±0.006	 53.42 3.872 0.8000
220 K	Fe-N Fe-C Fe-C Fe-S Fe-C	6.0 4.3±0.4 18.7±1.9 2.0 24.8±2.5	2.131±0.021 3.004±0.030 4.537±0.045 4.785±0.048 4.842±0.048	0.112±0.011 0.055±0.006 0.112±0.011 0.032±0.003 0.074±0.007	 50.95 3.612 0.8000
230 K	Fe-N Fe-C Fe-C Fe-S Fe-C	6.0 9.8±1.0 11.1±1.1 2.0 12.5±1.3	2.150±0.022 3.036±0.030 4.548±0.045 4.998±0.050 4.910±0.049	0.112±0.011 0.112±0.011 0.112±0.011 0.039±0.004 0.112±0.011	 48.52 2.636 0.8000
240 K	Fe-N Fe-C Fe-C Fe-S Fe-C	6.0 3.8±0.4 16.6±1.7 2.0 23.0±2.3	2.154±0.022 3.022±0.030 4.513±0.045 4.753±0.048 4.826±0.048	0.112±0.011 0.032±0.003 0.112±0.011 0.032±0.003 0.084±0.008	 40.33 3.232 0.8000
250 K	Fe-N Fe-C Fe-C Fe-S Fe-C	6.0 5.3±0.5 11.0±1.1 2.0 25.2±2.5	2.145±0.021 3.018±0.030 4.467±0.045 4.738±0.047 4.796±0.048	0.112±0.011 0.063±0.006 0.071±0.007 0.032±0.003 0.102±0.010	 37.53 3.864 0.8000
260 K	Fe-N Fe-C Fe-C Fe-S Fe-C	6.0 4.4±0.4 18.0±1.8 2.0 23.2±2.3	2.153±0.022 3.022±0.030 4.505±0.045 4.738±0.047 4.816±0.048	0.112±0.011 0.045±0.005 0.112±0.011 0.032±0.003 0.084±0.008	 38.37 3.779 0.8000
293 K	Fe-N Fe-C Fe-C Fe-S Fe-C	6.0 10.6±1.1 17.9±1.8 2.0 23.1±2.3	2.139±0.021 3.021±0.030 4.496±0.045 4.736±0.047 4.812±0.048	0.112±0.011 0.112±0.011 0.112±0.011 0.032±0.003 0.095±0.010	 40.97 4.2920 0.8000

a) Abs=X-ray absorbing atom, Bs=backscattering atom, b) number of backscattering atoms, c) distance of absorbing atom to backscattering atom, d) Debye-Waller-like factor, e) fit-index, f) Fermi energy, that accounts for the shift between theory and experiment, g) amplitude reducing factor

During the SCO process from the LS to the HS state the Fe-N bond lengths are usually elongated.[8,11,20,68,75,76] In case of [Fe(L-N_4Bn_2)$(NCS)_2$] the crossover occurs in a gradual way in a temperature range from around 150 K up to 250 K, where the transition is almost completed (cf. Figure 1.25).
In Table 2 the Fe-N bond lengths of all temperatures, resulting from the EXAFS fit functions, are listed separately for a better comparability. Additionally, the table displays values of the HS fraction γ_{HS}, which were calculated using the Fe-N distances according to a method which will be described subsequently.

Table 2: Fit model 1A: Fe-N distances obtained by EXAFS analysis and calculated γ_{HS} values.

T / K	Fe-N distance R(Abs-Bs) / Å	γ_{HS}(EXAFS) [a)]
10	1.964±0.020	0
30	1.961±0.020	-0.016
40	1.962±0.020	-0.011
50	1.963±0.020	-0.005
70	1.965±0.020	0.005
80	1.964±0.020	0
90	1.963±0.020	-0.005
100	1.963±0.020	-0.005
110	1.966±0.020	0.011
120	1.968±0.020	0.021
130	1.965±0.020	0.005
140	1.972±0.020	0.043
150	1.973±0.020	0.048
160	1.980±0.020	0.086
170	1.991±0.020	0.144
180	2.015±0.020	0.273
190	2.055±0.021	0.487
200	2.076±0.021	0.599
210	2.110±0.021	0.781
220	2.131±0.021	0.893
230	2.150±0.022	0.995
240	2.154±0.022	1.016
250	2.145±0.021	0.968
260	2.153±0.022	1.011
293	2.139±0.021	0.936

a) HS fraction calculated according to $\gamma_{HS} = (R_T - R_{LS})/(R_{HS} - R_{LS})$.[84] Applied procedure is described in this section.

As displayed in the second column of Table 2 the Fe-N distances change from 1.964 Å to 2.139 Å. To check if the structural changes occurring during the SCO process show the gradual behaviour of the magnetization curve, too, and to obtain a correlation of the fitting parameters, especially the bond lengths, with temperature, the fitted Fe-N distances were plotted versus temperature. The plot of the bond lengths (Figure 2.4) shows a gradual increase of the Fe-N distances in a sigmoidal shape. Therefore, the data points were fitted with a Boltzmann function that also produces a sigmoidal curve (cf. Figure 2.3 and equation (21)):

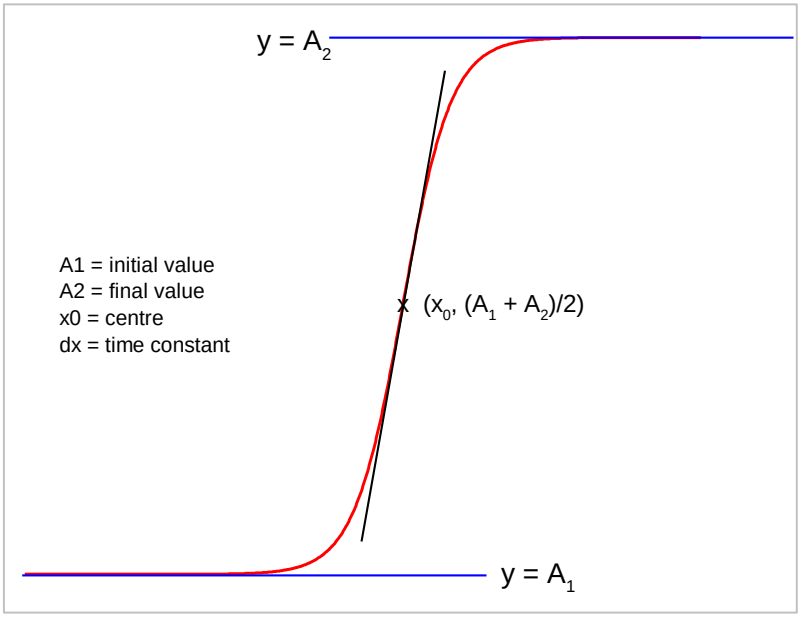

Figure 2.3: Sample curve of a Boltzmann function.

$$y = \frac{A_1 - A_2}{1 + e^{\frac{(x-x_0)}{dx}}} + A_2 \qquad (21)$$

The centre of the Boltzmann fit x_0, which corresponds to the inflection point, can be assigned to the spin transition temperature $T_{1/2}$. The fit of the Fe-N distances results in a spin transition temperature of $T_{1/2}$(EXAFS) = 192.6 ± 0.9 K and the fit curve with the corresponding parameters is shown in the appendix (cf. Figure A.1). Comparison of the magnetization curve obtained by SQUID magnetometry and the fit of the bond lengths shows that the structural changes clearly correlate with the magnetic changes, since the fit curve follows the fit of the magnetization within the error bar (Figure 2.4). Only in the SCO region the fit of the bond lengths shows a negligible shift to higher temperatures resulting in a spin transition temperature that is 0.6 K ($T_{1/2}$(EXAFS) = 192.6 K ± 0.9 K)

higher than the transition temperature obtained by SQUID magnetometry ($T_{1/2}$(SQUID) = 192.0 K ± 0.2 K).

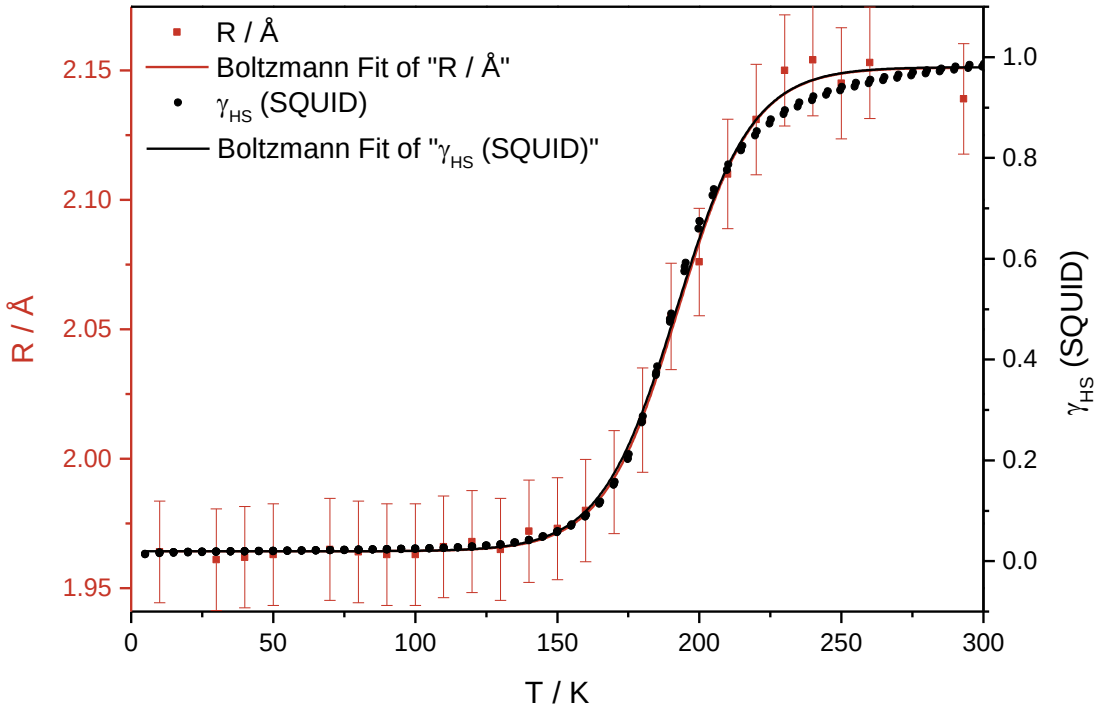

Figure 2.4: Fit model 1A: Comparison of HS fraction obtained by SQUID measurements (black) and fit of the Fe-N distance (red).

For a direct comparison of the results from the EXAFS analysis with the HS fraction obtained by SQUID magnetometry, the Fe-N distances were converted into HS fractions, too. According to Boča et al.,[84] the HS fraction is calculated as follows:

$$\gamma_{HS} = \frac{R_T - R_{LS}}{R_{Hs} - R_{LS}} \tag{22}$$

With R_T = Fe-N distance at temperature T
R_{LS} = Fe-N distance of LS state
R_{HS} = Fe-N distance of HS state

Since the distances obtained from the EXAFS fit functions show small variations in the LS region and rather large variations in the HS region, it is not reasonable to choose one of these values for R_{LS} and R_{HS}. Instead, the distances which were obtained by the Boltzmann fit in Figure A.1 were used. Here, the lower (A_1 = 1.964 Å) and upper (A_2 = 2.151 Å) limits correspond to the LS (R_{LS}) respective HS (R_{HS}) Fe-N distances. But since the system shows a very small HS fraction at low temperatures (10 – 120 K) and also a small LS fraction at high temperatures, these values are only approximations for the pure spin states. Nevertheless, the resulting calculated γ_{HS}(EXAFS) values are shown in Table 2 and a comparison with γ_{HS}(SQUID) is depicted in Figure 2.5.

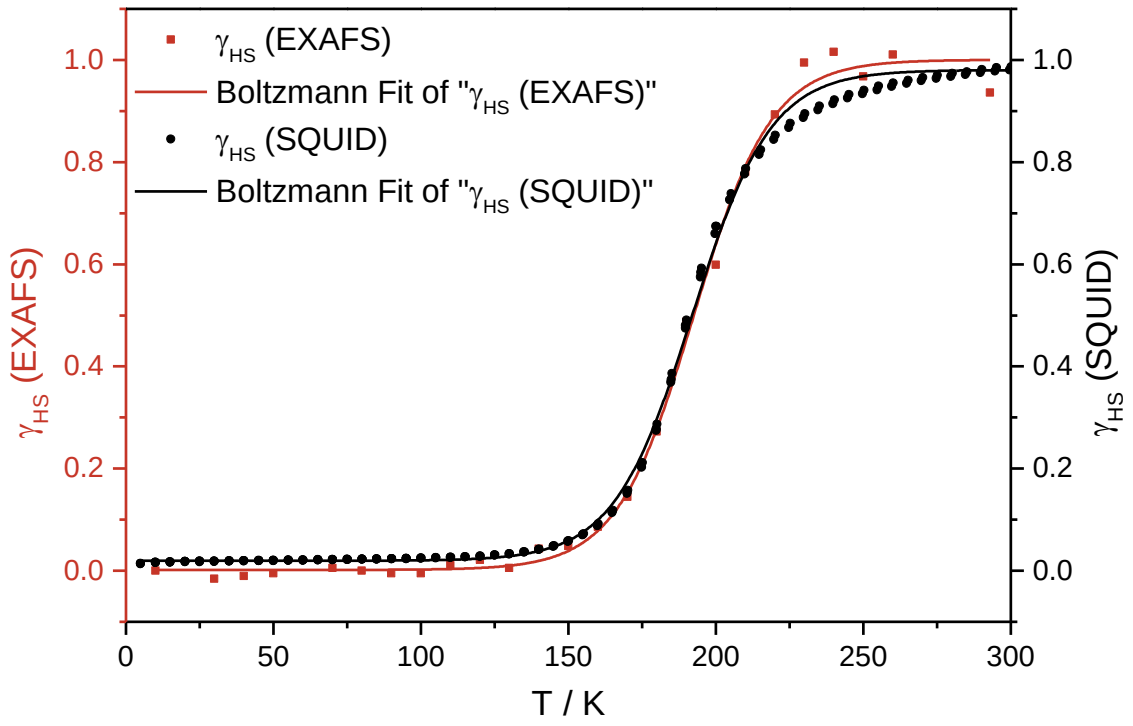

Figure 2.5: Fit model 1A: Comparison of HS fractions obtained by SQUID (black) and EXAFS measurements (red).

The fit of the γ_{HS}(EXAFS) values shows almost the same curve shape as that of γ_{HS}(SQUID). The small discrepancy of the lower and upper limits of the fits of the EXAFS and the SQUID data can be explained by the small HS respective LS contribution (as already described above), which distort the absolute values for pure LS and HS. However, the fit results in the same spin transition temperature $T_{1/2}$ like the fit of the Fe-N distances in Figure 2.4 ($T_{1/2}$(EXAFS) = 192.6 K ± 0.9 K) and is therefore in very good agreement with the SQUID data.

Summarising the results of fit model 1A, it can be said, that the obtained Fe-N bond length turned out to be a suitable quantity to follow the spin transition. The resulting γ_{HS} values are in very good agreement with the magnetization data by SQUID. But it has to be mentioned, that it is not possible to fit the experimental spectra in the SCO and HS region with this model reasonably, since number of signals as well as intensity cannot be reproduced. This can be partly explained by the existing correlation between the coordination number, the amplitude reducing factor and the Debye-Waller-like factor σ.[95,182] Since the coordination number of the nitrogen shell and the amplitude reducing factor were held fix in this fit model, it is obviously not possible to adjust the intensity of the signal properly only by variation of σ.

2.3.1.2 Fit Model 1B: Fit of unfiltered Data with one Nitrogen Shell based on HS and LS Distances and iterated afac

In the second applied fit model with one nitrogen shell, the amplitude reducing factor was iterated freely, since the previous model with the afac fixed at the standard value 0.8000 showed that a reproduction of the intensity of the first experimental signal only by iteration of the Debye-Waller-like factor is not possible.
In addition to the nitrogen shell, three carbon shells at around 2.8 Å, 4.3 Å and 4.8 Å and a sulphur shell at 4.8 Å were fitted. The coordination numbers of the carbon shells were iterated freely, while the coordination number of nitrogen was fixed to 6 and of sulphur to 2 according to the crystal structure. The distances were also based on the crystal structure data from the LS and the HS state (110 K and 293 K) and the Debye-Waller-like factors were iterated in the range of 0.032 – 0.112 $Å^{-1}$.
First, the temperature-dependent EXAFS spectra and the resulting fit functions are displayed in k-space (top) and R-space (bottom) in Figure 2.6. Again the blue spectrum depicts the spin transition temperature (190 K) and the spectra above the blue one can be assigned to the system in the HS state, while the spectra below the blue one illustrate the LS state.
As in the model with one nitrogen shell and fixed amplitude reducing factor, the fits in the LS region show a rather good agreement with the experimental spectra. In contrast to the previous model the fits up to 180 K show a good agreement, too. In the range from 190 - 293 K the fits with this model reproduce the experimental spectra much better in terms of intensity of the signals but the position of the first signal cannot be reproduced very well. The distances in the fit are shifted to higher values than in the experimental spectra. Additionaly, in case of the spin transition temperature (190 K) the experimental spectrum shows two signals at around 2.5 and 3.0 Å, while the fit functions show again only one signal at around 2.85 Å.

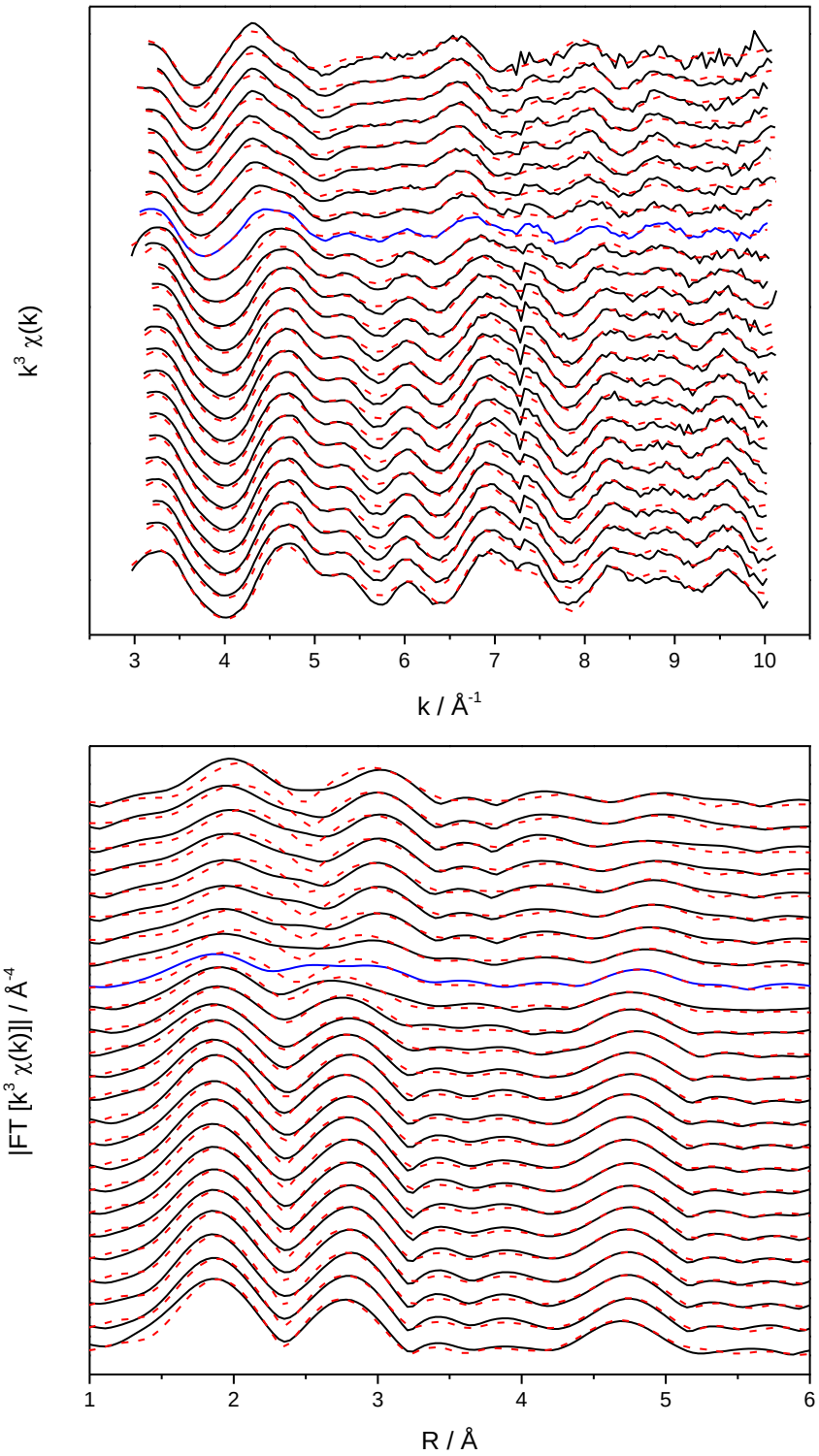

Figure 2.6: Fit model 1B: Temperature-dependent EXAFS spectra of [Fe(L-N_4Bn_2)$(NCS)_2$], blue spectrum: spin transition temperature (190 K), top: χ(k), bottom: Fourier transformation, (—) experimental data, (---) theoretical data.

The resulting EXAFS fitting parameters are displayed in Table 3 for all temperatures.

Table 3: Fit model 1B: Neighbour atoms, coordination numbers and distances obtained by EXAFS analysis.

Sample	Abs-Bs [a]	N(Bs) [b]	R(Abs-Bs) [c] / Å	σ [d] / Å^{-1}	R [e] / % E_f [f] / eV Afac [g]
10 K	Fe-N Fe-C Fe-C Fe-S Fe-C	6.0 8.7±0.9 9.5±1.0 2.0 16.5±1.7	1.962±0.020 2.821±0.028 4.317±0.043 4.825±0.048 4.815±0.048	0.100±0.010 0.074±0.007 0.112±0.011 0.039±0.004 0.032±0.003	 22.72 4.385 0.7059
30 K	Fe-N Fe-C Fe-C Fe-S Fe-C	6.0 10.0±1.0 8.5±0.9 2.0 17.2±1.7	1.959±0.020 2.827±0.028 4.309±0.043 4.816±0.048 4.823±0.048	0.097±0.010 0.084±0.009 0.110±0.011 0.045±0.005 0.032±0.003	 20.34 3.785 0.7028
40 K	Fe-N Fe-C Fe-C Fe-S Fe-C	6.0 10.6±1.1 9.4±0.9 2.0 17.6±1.8	1.957±0.020 2.829±0.028 4.334±0.043 4.825±0.048 4.820±0.048	0.092±0.009 0.081±0.008 0.112±0.011 0.032±0.003 0.032±0.003	 21.61 3.749 0.6596
50 K	Fe-N Fe-C Fe-C Fe-S Fe-C	6.0 9.9±1.0 9.3±0.9 2.0 15.9±1.6	1.960±0.020 2.831±0.028 4.307±0.043 4.843±0.048 4.829±0.048	0.097±0.010 0.081±0.008 0.110±0.011 0.032±0.003 0.032±0.003	 21.54 3.635 0.6972
70 K	Fe-N Fe-C Fe-C Fe-S Fe-C	6.0 9.1±0.9 9.3±0.9 2.0 15.7±1.6	1.962±0.020 2.833±0.028 4.318±0.043 4.835±0.048 4.829±0.048	0.100±0.010 0.077±0.008 0.112±0.011 0.032±0.003 0.032±0.003	 20.71 3.566 0.7323
80 K	Fe-N Fe-C Fe-C Fe-S Fe-C	6.0 10.3±1.0 8.6±0.9 2.0 16.5±1.7	1.962±0.020 2.832±0.028 4.324±0.043 4.834±0.048 4.827±0.048	0.100±0.010 0.087±0.009 0.112±0.011 0.032±0.003 0.032±0.003	 19.74 3.644 0.6977
90 K	Fe-N Fe-C Fe-C Fe-S Fe-C	6.0 10.3±1.0 8.4±0.8 2.0 16.2±1.6	1.960±0.020 2.830±0.028 4.315±0.043 4.831±0.048 4.827±0.048	0.100±0.010 0.087±0.009 0.112±0.011 0.032±0.003 0.032±0.003	 21.27 3.780 0.6944
100 K	Fe-N Fe-C Fe-C Fe-S Fe-C	6.0 10.3±1.0 8.0±0.8 2.0 15.9±1.6	1.960±0.020 2.832±0.028 4.307±0.043 4.838±0.048 4.835±0.048	0.102±0.010 0.087±0.009 0.112±0.011 0.032±0.003 0.032±0.003	 22.49 3.821 0.7011
110 K	Fe-N Fe-C Fe-C Fe-S Fe-C	6.0 10.3±1.0 8.7±0.9 2.0 16.2±1.6	1.962±0.020 2.832±0.028 4.309±0.043 4.832±0.048 4.830±0.048	0.100±0.010 0.087±0.009 0.110±0.011 0.032±0.003 0.032±0.003	 20.48 3.831 0.6903

Sample	Abs-Bs [a]	N(Bs) [b]	R(Abs-Bs) [c] / Å	σ [d] / Å^{-1}	R [e] / % E_f [f] / eV Afac [g]
120 K	Fe-N Fe-C Fe-C Fe-S Fe-C	6.0 9.7±1.0 8.3±0.8 2.0 16.0±1.6	1.965±0.020 2.835±0.028 4.321±0.043 4.834±0.048 4.830±0.048	0.105±0.011 0.087±0.009 0.112±0.011 0.032±0.003 0.039±0.004	 22.19 3.721 0.7132
130 K	Fe-N Fe-C Fe-C Fe-S Fe-C	6.0 11.8±1.2 7.8±0.8 2.0 16.6±1.7	1.961±0.020 2.828±0.028 4.310±0.043 4.834±0.048 4.827±0.048	0.097±0.010 0.097±0.010 0.112±0.011 0.032±0.003 0.032±0.003	 20.12 4.067 0.6526
140 K	Fe-N Fe-C Fe-C Fe-S Fe-C	6.0 10.8±1.1 7.4±0.7 2.0 17.9±1.8	1.957±0.020 2.832±0.028 4.341±0.043 4.831±0.048 4.825±0.048	0.100±0.010 0.089±0.009 0.112±0.011 0.032±0.003 0.045±0.005	 22.24 3.872 0.6427
150 K	Fe-N Fe-C Fe-C Fe-S Fe-C	6.0 13.9±1.4 6.9±0.7 2.0 17.7±1.8	1.964±0.020 2.830±0.028 4.329±0.043 4.819±0.048 4.821±0.048	0.100±0.010 0.107±0.011 0.112±0.011 0.032±0.003 0.039±0.004	 22.24 4.377 0.5958
160 K	Fe-N Fe-C Fe-C Fe-S Fe-C	6.0 14.3±1.4 6.0±0.6 2.0 18.1±1.8	1.974±0.020 2.840±0.028 4.374±0.044 4.817±0.048 4.822±0.048	0.102±0.010 0.112±0.011 0.112±0.011 0.050±0.005 0.032±0.003	 23.18 4.434 0.5650
170 K	Fe-N Fe-C Fe-C Fe-S Fe-C	6.0 13.4±1.3 7.4±0.7 2.0 24.8±2.5	1.990±0.020 2.854±0.029 4.441±0.044 4.823±0.048 4.827±0.048	0.112±0.011 0.112±0.011 0.112±0.011 0.063±0.006 0.067±0.007	 24.76 4.178 0.5562
180 K	Fe-N Fe-C Fe-C Fe-S Fe-C	6.0 12.5±1.3 17.0±1.7 2.0 34.8±3.5	2.000±0.020 2.854±0.029 4.459±0.045 4.788±0.048 4.808±0.048	0.112±0.011 0.112±0.011 0.112±0.011 0.059±0.006 0.089±0.009	 27.55 5.653 0.5085
190 K	Fe-N Fe-C Fe-C Fe-S Fe-C	6.0 12.8±1.3 7.0±0.7 2.0 20.1±2.0	2.041±0.020 2.927±0.029 4.463±0.045 4.977±0.050 4.843±0.048	0.112±0.011 0.112±0.011 0.089±0.009 0.032±0.003 0.107±0.011	 34.99 4.253 0.4697
200 K	Fe-N Fe-C Fe-C Fe-S Fe-C	6.0 13.2±1.3 14.2±1.4 2.0 43.4±4.3	2.080±0.021 2.955±0.030 4.489±0.045 4.726±0.047 4.813±0.048	0.112±0.011 0.112±0.011 0.112±0.011 0.032±0.003 0.102±0.010	 35.24 4.224 0.4914
210 K	Fe-N Fe-C Fe-C Fe-S Fe-C	6.0 14.3±1.4 19.3±1.9 2.0 28.4±2.8	2.107±0.021 2.991±0.030 4.506±0.045 4.767±0.048 4.837±0.048	0.112±0.011 0.112±0.011 0.110±0.011 0.032±0.003 0.074±0.007	 33.69 3.593 0.4817

Sample	Abs-Bs [a]	N(Bs) [b]	R(Abs-Bs) [c] / Å	σ [d] / Å^{-1}	R [e] / % E_f [f] / eV Afac [g]
220 K	Fe-N Fe-C Fe-C Fe-S Fe-C	6.0 13.2±1.3 18.0±1.8 2.0 24.8±2.5	2.125±0.021 3.003±0.030 4.532±0.045 4.765±0.048 4.842±0.048	0.112±0.011 0.102±0.010 0.112±0.011 0.032±0.003 0.067±0.007	 34.03 3.391 0.5058
230 K	Fe-N Fe-C Fe-C Fe-S Fe-C	6.0 11.9±1.2 29.3±2.9 2.0 38.1±3.8	2.139±0.021 3.014±0.030 4.531±0.045 4.763±0.048 4.839±0.048	0.112±0.011 0.102±0.010 0.112±0.011 0.032±0.003 0.089±0.009	 35.62 3.297 0.5605
240 K	Fe-N Fe-C Fe-C Fe-S Fe-C	6.0 8.9±0.9 20.8±2.1 2.0 28.0±2.8	2.128±0.021 3.003±0.030 4.500±0.045 4.741±0.047 4.818±0.048	0.112±0.011 0.087±0.009 0.112±0.011 0.032±0.003 0.089±0.009	 29.84 4.297 0.6139
250 K	Fe-N Fe-C Fe-C Fe-S Fe-C	6.0 10.5±1.1 14.3±1.4 2.0 32.3±3.2	2.134±0.021 3.009±0.030 4.460±0.045 4.732±0.047 4.790±0.048	0.112±0.011 0.095±0.010 0.071±0.007 0.032±0.003 0.112±0.011	 28.76 4.261 0.6051
260 K	Fe-N Fe-C Fe-C Fe-S Fe-C	6.0 8.7±0.9 20.5±2.1 2.0 23.8±2.4	2.136±0.021 3.012±0.030 4.519±0.045 4.768±0.048 4.833±0.048	0.112±0.011 0.084±0.008 0.112±0.011 0.032±0.003 0.074±0.007	 30.77 4.1480 0.6627
293 K	Fe-N Fe-C Fe-C Fe-S Fe-C	6.0 20.7±2.1 25.2±2.5 2.0 27.1±2.7	2.128±0.021 3.010±0.030 4.550±0.046 4.781±0.048 4.857±0.049	0.089±0.009 0.112±0.011 0.112±0.011 0.032±0.003 0.077±0.008	 37.54 4.186 0.4429

a) Abs=X-ray absorbing atom, Bs=backscattering atom, b) number of backscattering atoms, c) distance of absorbing atom to backscattering atom, d) Debye-Waller-like factor, e) fit-index, f) Fermi energy, that accounts for the shift between theory and experiment, g) amplitude reducing factor

To get a better view on the changes occurring during the SCO process, the Fe-N distances received by EXAFS analysis are displayed in Table 4 as an overview. Furthermore, the table shows the thereof calculated HS fractions according to equation (22).

Table 4: Fit model 1B: Fe-N distances obtained by EXAFS analysis and calculated γ_{HS} values.

T / K	Fe-N distance R(Abs-Bs) / Å	γ_{HS}(EXAFS) [a)]
10	1.962±0.020	0.006
30	1.959±0.020	-0.011
40	1.957±0.020	-0.023
50	1.960±0.020	-0.006
70	1.962±0.020	0.006
80	1.962±0.020	0.006
90	1.960±0.020	-0.006
100	1.960±0.020	-0.006
110	1.962±0.020	0.006
120	1.965±0.020	0.023
130	1.961±0.020	0
140	1.957±0.020	-0.023
150	1.964±0.020	0.017
160	1.974±0.020	0.075
170	1.990±0.020	0.167
180	2.000±0.020	0.224
190	2.041±0.020	0.460
200	2.080±0.021	0.684
210	2.107±0.021	0.839
220	2.125±0.021	0.943
230	2.139±0.021	1.023
240	2.128±0.021	0.960
250	2.134±0.021	0.994
260	2.136±0.021	1.006
293	2.128±0.021	0.960

a) HS fraction calculated according to $\gamma_{Hs} = (R_T - R_{LS})/(R_{HS} - R_{LS})$.[84] Applied procedure is described in section 2.3.1.1.

Again, the Fe-N bond lengths of all temperatures were plotted as a function of temperature to obtain the correlation between the changes of the distances and temperature. The distances with the resulting sigmoidal Boltzmann fit function that reveals a spin transition temperature of $T_{1/2}$(EXAFS) = 191.5 ± 0.7 K is shown in the appendix (cf. Figure A.2). The lower and upper limits of the Boltzmann fit, corresponding to the approximated distances of pure LS and HS, were determined as $A_1 = R_{LS}$ = 1.961 ± 0.001 Å and $A_2 = R_{HS}$ = 2.135 ± 0.002 Å. These values were used to calculate the HS fraction γ_{HS}(EXAFS) from the Fe-N distances in Table 4 according to equation (22).
In Figure 2.7 the fit of the Fe-N distances is adjusted and compared to the magnetization curve obtained by SQUID magnetometry.The fit of the distances shows the overall shape of the magnetization curve. Especially in the LS range, up to around 130 K, a very good agreement is observable. But the change of the bond lengths starts at slightly higher temperatures and the elongation finishes at lower temperatures compared to the change of the magnetization. Therefore, the fit curve of the distances exhibits a higher slope than the SQUID measurement. Altogether, despite the small deviation of the curve shape, the agreement between both compared techniques is really good and the fit of the bond lengths leads to essentially the same spin transition temperature as obtained by SQUID magnetometry ($T_{1/2}$(EXAFS) = 191.5 ± 0.7 K ↔ $T_{1/2}$(SQUID) = 192.0 K ± 0.2 K).

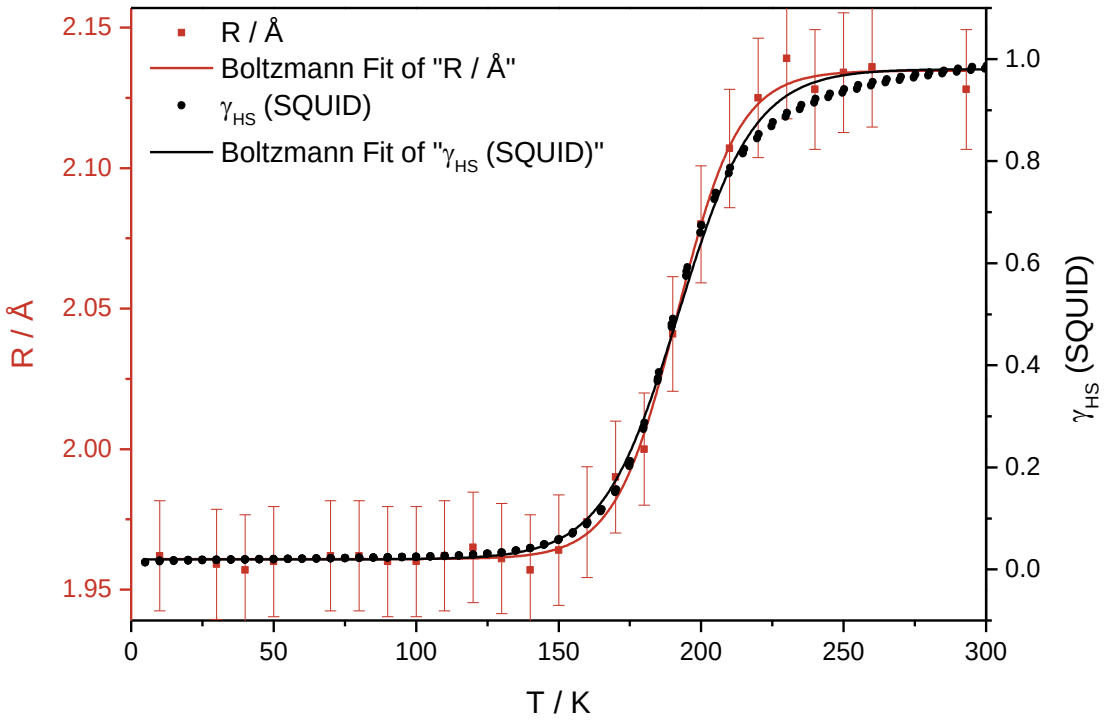

Figure 2.7: Fit model 1B: Comparison of HS fraction obtained by SQUID measurements (black) and fit of the Fe-N distance (red).

In the next step, the Fe-N distances were converted into HS fractions according to equation (22), as described in the last section. Like in the previous model, the limits of the Boltzmann fit (A_1 and A_2) were used as approximation for the pure LS and HS distances, since the distances obtained by the EXAFS fit show certain variations in the HS and LS region. The resulting γ_{HS}(EXAFS) values are shown in Table 4 and the comparison of the Boltzmann fit functions of the γ_{HS} values obtained by EXAFS and SQUID is depicted in Figure 2.8.

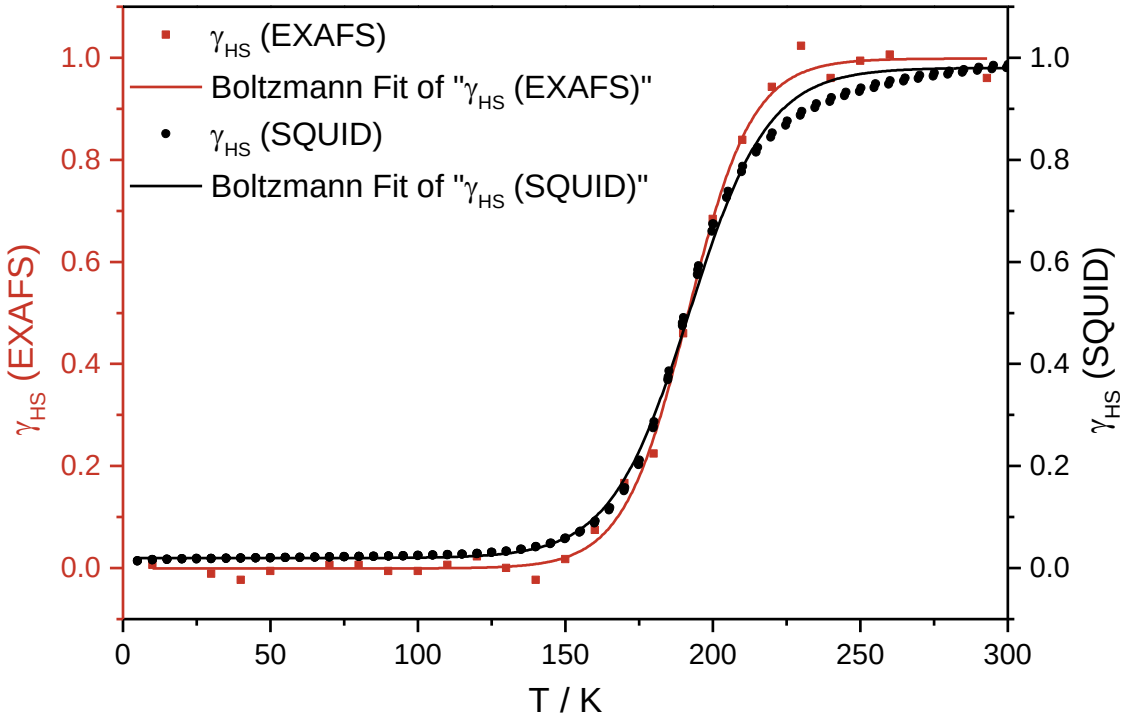

Figure 2.8: Fit model 1B: Comparison of HS fractions obtained by SQUID (black) and EXAFS measurements (red).

Since the γ_{HS}(EXAFS) values are calculated from the Fe-N distances, the fits of both values lead to essentially the same curve shape (cf. Figures 2.7 and 2.8). Additionally, both fits result in the same transition temperature $T_{1/2}$(EXAFS) = 191.5 ± 0.7 K. As can be seen in Figure 2.8, the Boltzmann fit of the γ_{HS}(EXAFS) values matches the fit of the γ_{HS}(SQUID) values quite well. Like in the fit of the distances, the γ_{HS}(EXAFS) values start to change at slightly higher temperatures and the conversion to the HS state is finished at lower temperatures than in case of the SQUID data. Apart from this, the lower and upper limits of the fit are again distorted, since the used distances for pure LS and HS are only approximations for the pure spin states. Actually, in each case a very small fraction of the other spin state is still present.

Furthermore, the Debye-Waller-like factor of the nitrogen shell and the amplitude reducing factor were plotted as functions of temperature to receive a correlation with temperature.

Figure 2.9 shows the plot of the Debye-Waller-like factor. At first glance, no clear correlation with temperature and therefore with the spin state is observable. In the temperature range from 10 to 160 K the Debye-Waller-like factor varies in the range from 0.092 to 0.105 $Å^{-1}$, while from 170 to 260 K σ takes the maximal allowed value of 0.112 $Å^{-1}$. At 293 K σ decreases to 0.089 $Å^{-1}$, what seems to be an outlier.

Since the Debye-Waller-like factor accounts for static disorder as well as thermal vibrations in the system, the jump to the maximum at 170 K can be attributed either to an increased disorder in the system due to the spin transition process or to the increase of temperature. But since the temperature increases linearly, the abrupt jump of σ presumably indicates the region where the transition from LS to HS starts.

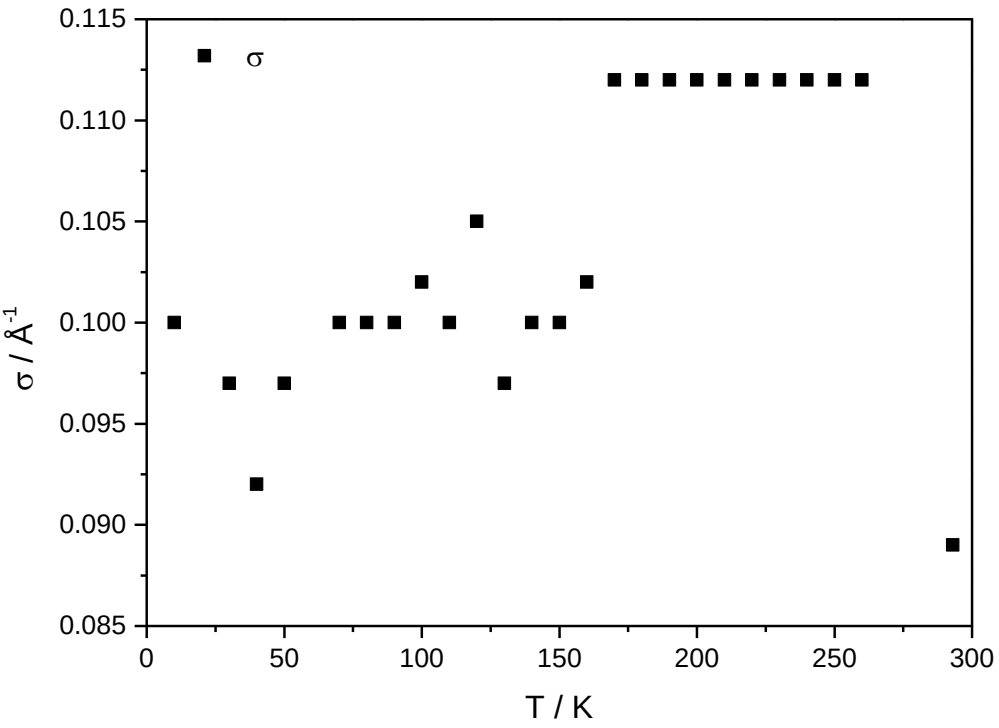

Figure 2.9: Fit model 1B: Plot of Debye-Waller like factor σ of the nitrogen shell vs. temperature.

In addition, the behaviour of σ reflects the observations discussed at the beginning of this section. In contrast to fit model 1A with fixed afac, which starts to fail at around 130 K, the actual model with iterated afac is able to fit the temperature-dependent spectra up to around 170 – 180 K quite good. At higher temperatures, the fit model starts to fail, represented in the high σ-values.

The plot of the amplitude reducing factor (Figure 2.10) shows a more or less constant value of 0.7 in the temperature range from 10 to 120 K, with increasing temperature the amplitude reducing factor decreases until it reaches a minimum of 0.4697 at the spin transition temperature 190 K. Further rise of temperature up to 260 K leads to an increase of the afac to 0.6627 again. At 293 K the amplitude reducing factor drops to its absolute minimum with a value of 0.4429. The course of the data points indicates a minimum in the region of the spin transition temperature. Therefore, the data, except of the point at 293 K, were fitted with a Gaussian function to receive the fitted minimum $x_c = T_{1/2}(\text{afac}) = 197.6 \pm 1.6$ K, that can be correlated with the transition temperature. Compared to the transition temperature obtained by SQUID ($T_{1/2}(\text{SQUID}) = 192.0 \text{ K} \pm 0.2$ K), it is shifted by around 5 K to higher temperatures, but still a good agreement is observable.

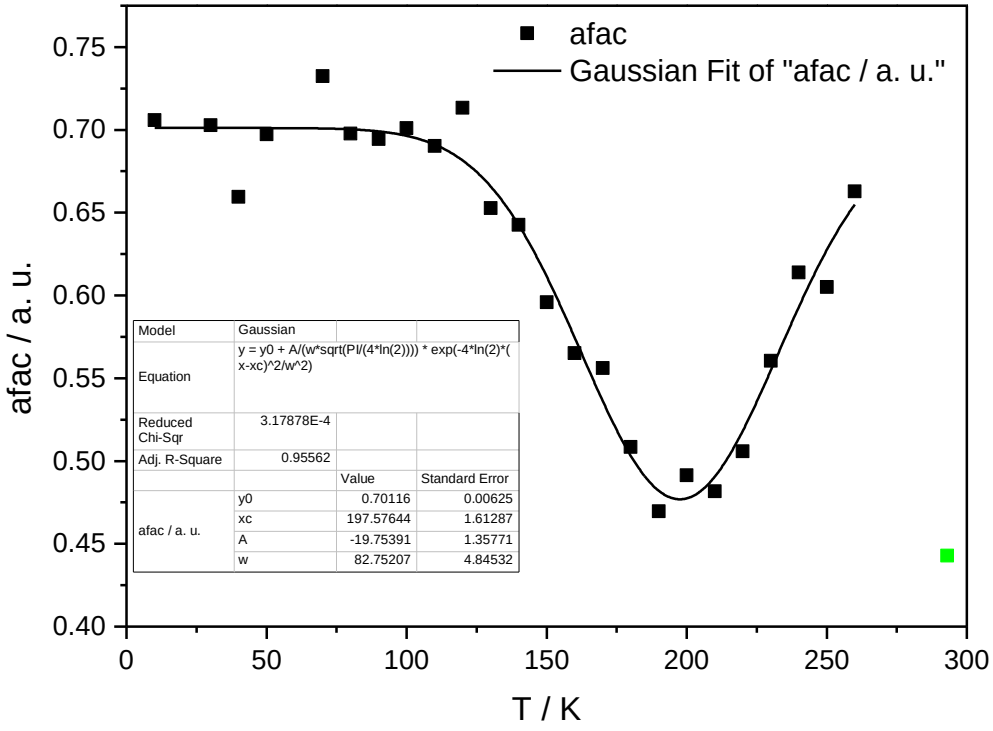

Figure 2.10: Fit model 1B: Plot of amplitude reducing factor of the EXAFS fits vs. temperature.

Since the afac is correlated with the coordination number and the Debye-Waller-like factor, it contains indirect structural information. The observed course of the afac could probably be explained by the structural disorder in the system during the SCO process. In case of the pure LS state, only one signal corresponding to the nitrogen shell is observable (cf. Figure 2.11, top left). In the SCO range, the amplitude of this signal is reduced visibly

and a shoulder or a second signal respectively becomes visible that could be assigned to the HS fraction (cf. Figure 2.11, middle left and right). Therefore, the afac is reduced in this temperature range to reproduce the lowered amplitudes. In the HS region, again only one signal at slightly higher distances is visible (cf. Figure 2.11, bottom right), which exhibits an increased amplitude compared to the SCO region, represented by the higher afac value.

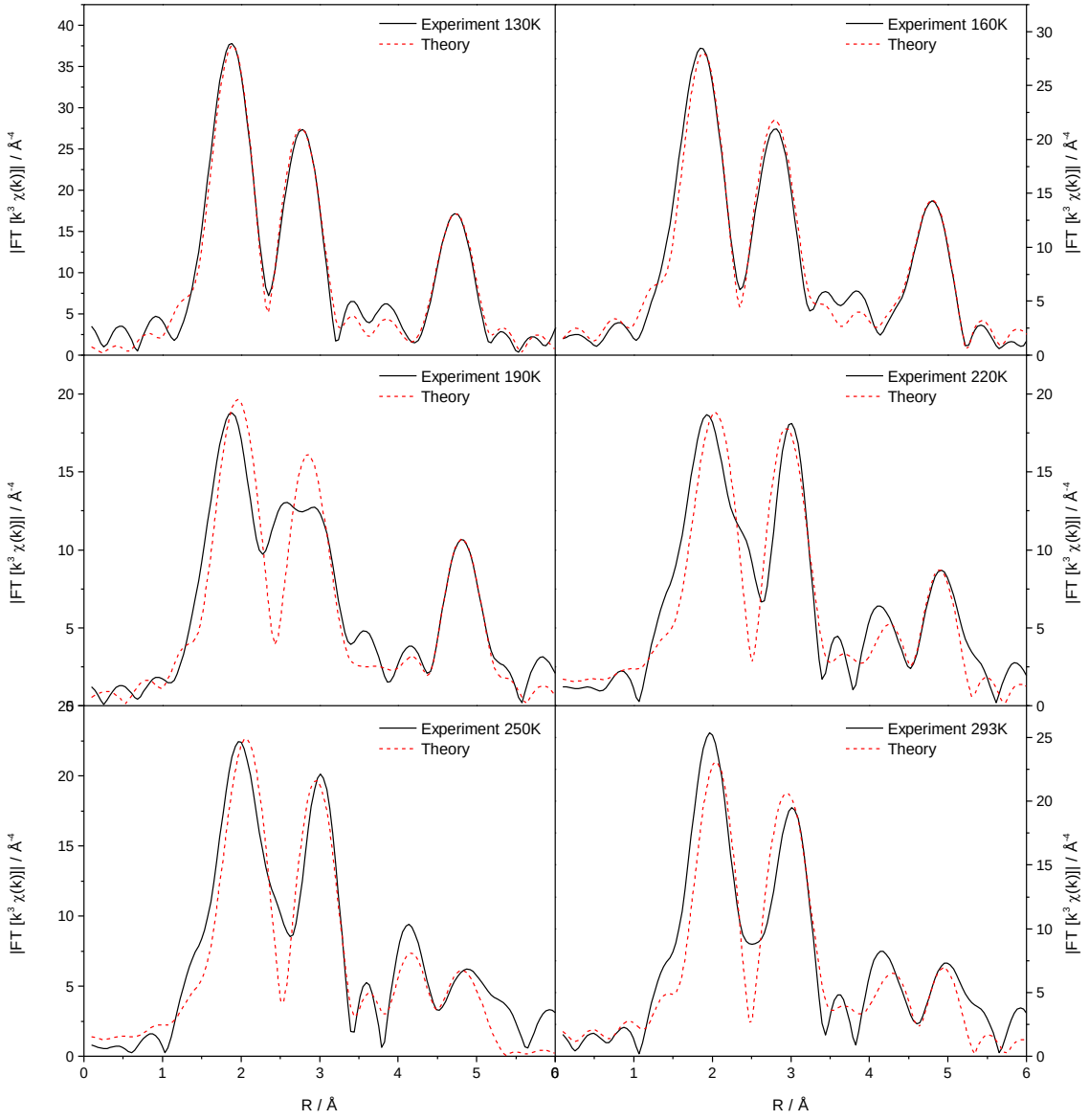

Figure 2.11: Depiction of amplitude changes of the Fourier transformed EXAFS spectra of [Fe(L-N_4Bn_2)$(NCS)_2$] at six different temperatures. (—) experimental data, (---) theoretical data.

In summary, it can be said that the second fit model, where the amplitude reducing factor was iterated freely, gives better fit results in the whole temperature range concerning the fit quality compared to fit model 1A with fixed afac. Especially in the range from 10 to 180 K, the fit model is able to reproduce the spectral shape quite good. At higher temperatures, the number of signals cannot be adjusted correctly. Despite these shortcomings, the changes of the bond lengths as well as the thereof calculated HS fractions lead to a spin transition curve that is in very good agreement with the SQUID data. Furthermore, the analysis of the temperature-dependent behaviour of the Debye-Waller-like factor and the amplitude reducing factor revealed interesting correlations with the SCO process. The temperature of the observed abrupt increase of the Debye-Waller-like factor can be roughly correlated with the start of the transition process from LS to HS, leading to an increased disorder in the system. In addition, the temperature-dependent afac showed a minimum, which can be used for a rough estimation of the SCO temperature.

2.3.2 Fit Models with two Nitrogen Shells, unfiltered Data

Since the axial and equatorial Fe-N distances in the investigated complex [Fe(L-N_4Bn_2)$(NCS)_2$] show a difference of around 0.2 Å in the crystal structure, it should be possible to distinguish the axial and equatorial nitrogen atoms by EXAFS spectroscopy. Therefore, different fit models with two nitrogen shells, one shell with four N-atoms in the equatorial positions (marked purple in Figure 2.12) and one with two N-atoms in the axial positions (marked green in Figure 2.12) were applied. The other shells remain the same as in the fit models with one nitrogen shell, three carbon shells and one sulphur shell (cf. chapter 2.3.1).

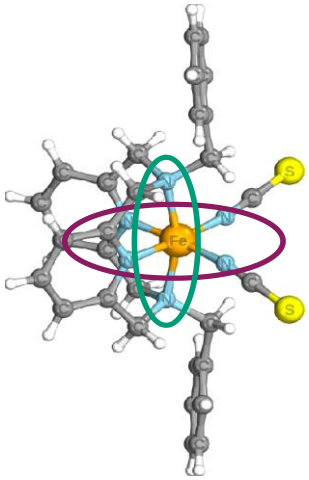

Figure 2.12: Axial (green) and equatorial (purple) nitrogen atoms of [Fe(L-N_4Bn_2)$(NCS)_2$].

2.3.2.1 Fit Model 2A: Fit of unfiltered Data with two Nitrogen Shells based on HS and LS Distances and afac at 0.6695

In the first fit model with two nitrogen shells the coordination numbers of both nitrogen shells and the sulphur shell were held fix, while the coordination numbers of the carbon shells were iterated freely. The initial distances of the backscattering atoms were based on the crystal structures of the LS and HS state at 110 K and 293 K and iterated freely. The Debye-Waller-like factors were iterated freely for all shells and the amplitude reducing factor was set to 0.6695 for all temperatures, corresponding to the afac obtained at 110 K.

Figure 2.13 shows the temperature-dependent EXAFS spectra with the resulting fit functions in k-space (top) and R-space (bottom). In these two figures temperature increases from 10 K (bottom) to 293K (top) and the blue spectrum is assigned to the spin transition

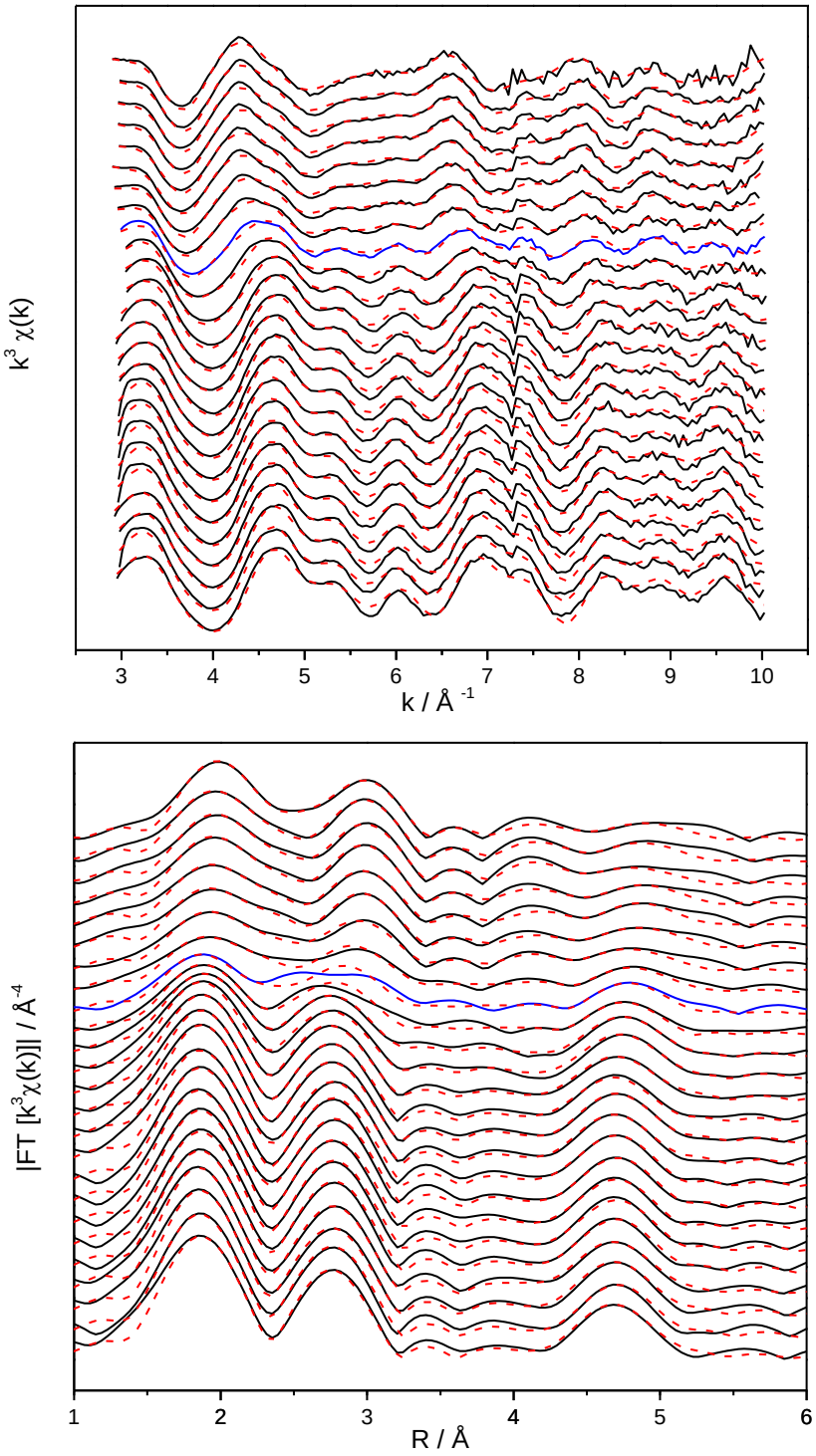

Figure 2.13: Fit model 2A: Temperature-dependent EXAFS spectra of [Fe(L-N_4Bn_2)$(NCS)_2$], blue spectrum: spin transition temperature (190 K), top: χ(k), bottom: Fourier transformation, (—) experimental data, (---) theoretical data.

temperature (190 K). The fit functions reproduce the experimental spectra quite well, except for the spectrum of the transition temperature (190 K). At this temperature the experimental spectrum shows two signals at around 2.5 – 3.0 Å whereas the fit function shows only one signal at around 2.9 Å.
The fitting results of the EXAFS analysis of all temperature points are shown in Table 5 as an overview.

Table 5: Fit model 2A: Neighbour atoms, coordination numbers and distances obtained by EXAFS analysis.

Sample	**Abs-Bs** [a]	**N(Bs)** [b]	**R(Abs-Bs)** [c] **/ Å**	**σ** [d] **/ Å^{-1}**	**R** [e] **/ %** **E_f** [f] **/ eV** **Afac** [g]
10 K	Fe-N Fe-N Fe-C Fe-C Fe-S Fe-C	4.0 2.0 9.2±0.9 10.4±1.0 2.0 17.5±1.7	1.921±0.019 2.074±0.021 2.823±0.028 4.324±0.043 4.821±0.048 4.818±0.048	0.059±0.006 0.050±0.005 0.074±0.007 0.112±0.011 0.032±0.003 0.032±0.003	21.73 3.993 0.6695
30 K	Fe-N Fe-N Fe-C Fe-C Fe-S Fe-C	4.0 2.0 10.4±1.0 8.3±0.8 2.0±0.2 18.3±1.8	1.922±0.019 2.083±0.021 2.830±0.028 4.322±0.043 4.856±0.049 4.840±0.049	0.055±0.006 0.055±0.006 0.081±0.008 0.112±0.011 0.032±0.003 0.050±0.005	20.50 3.178 0.6695
40 K	Fe-N Fe-N Fe-C Fe-C Fe-S Fe-C	4.0 2.0 9.3±0.9 11.5±1.2 2.0 17.3±1.7	1.924±0.019 2.083±0.021 2.824±0.028 4.326±0.043 4.809±0.048 4.815±0.048	0.055±0.006 0.055±0.006 0.077±0.008 0.112±0.011 0.055±0.006 0.032±0.003	20.61 3.927 0.6695
50 K	Fe-N Fe-N Fe-C Fe-C Fe-S Fe-C	4.0 2.0 8.6±0.9 10.8±1.1 2.0 17.8±1.8	1.927±0.019 2.096±0.021 2.830±0.028 4.323±0.043 4.847±0.048 4.834±0.048	0.050±0.005 0.045±0.005 0.067±0.007 0.112±0.011 0.032±0.003 0.050±0.005	21.15 3.382 0.6695
70 K	Fe-N Fe-N Fe-C Fe-C Fe-S Fe-C	4.0 2.0 10.0±1.0 9.8±1.0 2.0 19.4±1.9	1.925±0.019 2.088±0.021 2.836±0.028 4.335±0.043 4.857±0.049 4.841±0.048	0.055±0.006 0.050±0.005 0.077±0.008 0.112±0.011 0.032±0.003 0.059±0.006	20.30 2.877 0.6695
80 K	Fe-N Fe-N Fe-C Fe-C Fe-S Fe-C	4.0 2.0 10.2±1.0 9.3±0.9 2.0 24.3±2.4	1.928±0.019 2.091±0.021 2.837±0.028 4.352±0.044 4.894±0.049 4.855±0.049	0.059±0.006 0.059±0.006 0.081±0.008 0.112±0.011 0.032±0.003 0.092±0.009	20.83 2.987 0.6695

Sample	Abs-Bs [a]	N(Bs) [b]	R(Abs-Bs) [c] / Å	σ [d] / Å^{-1}	R [e] / % E_f [f] / eV Afac [g]
90 K	Fe-N Fe-N Fe-C Fe-C Fe-S Fe-C	4.0 2.0 10.1±1.0 9.2±0.9 2.0 24.5±2.5	1.928±0.019 2.091±0.021 2.837±0.028 4.352±0.044 4.894±0.049 4.855±0.049	0.059±0.006 0.059±0.006 0.081±0.008 0.112±0.011 0.032±0.003 0.095±0.010	21.49 2.987 0.6695
100 K	Fe-N Fe-N Fe-C Fe-C Fe-S Fe-C	4.0 2.0 10.1±1.0 8.4±0.8 2.0 21.1±2.1	1.926±0.019 2.096±0.021 2.838±0.028 4.336±0.043 4.888±0.049 4.858±0.049	0.055±0.006 0.050±0.005 0.081±0.008 0.112±0.011 0.032±0.003 0.081±0.008	20.92 2.92 0.6695
110 K	Fe-N Fe-N Fe-C Fe-C Fe-S Fe-C	4.0 2.0 10.0±1.0 9.2±0.9 2.0 24.0±2.4	1.928±0.019 2.091±0.021 2.837±0.028 4.348±0.043 4.894±0.049 4.855±0.046	0.059±0.006 0.059±0.006 0.081±0.008 0.112±0.011 0.032±0.003 0.092±0.009	20.03 2.987 0.6695
120 K	Fe-N Fe-N Fe-C Fe-C Fe-S Fe-C	4.0 2.0 8.9±0.9 9.7±1.0 2.0 16.3±1.6	1.926±0.019 2.087±0.021 2.830±0.028 4.320±0.043 4.847±0.048 4.831±0.048	0.063±0.006 0.055±0.006 0.074±0.007 0.112±0.011 0.032±0.003 0.045±0.005	22.64 3.913 0.6695
130 K	Fe-N Fe-N Fe-C Fe-C Fe-S Fe-C	4.0 2.0 9.5±1.0 10.7±1.1 2.0 17.2±1.7	1.925±0.019 2.072±0.021 2.823±0.028 4.306±0.043 4.668±0.047 4.772±0.048	0.067±0.007 0.067±0.007 0.087±0.009 0.110±0.011 0.032±0.003 0.032±0.003	21.14 4.316 0.6695
140 K	Fe-N Fe-N Fe-C Fe-C Fe-S Fe-C	4.0 2.0 8.6±0.9 7.8±0.8 2.0 20.3±2.0	1.934±0.019 2.095±0.021 2.831±0.028 4.339±0.043 4.895±0.049 4.855±0.049	0.067±0.007 0.067±0.007 0.081±0.008 0.112±0.011 0.032±0.003 0.092±0.009	21.73 3.741 0.6695
150 K	Fe-N Fe-N Fe-C Fe-C Fe-S Fe-C	4.0 2.0 9.8±1.0 7.8±0.8 2.0 13.2±1.3	1.926±0.019 2.072±0.021 2.821±0.028 4.310±0.043 4.846±0.048 4.801±0.048	0.081±0.008 0.081±0.008 0.095±0.010 0.112±0.011 0.112±0.011 0.045±0.005	23.07 5.03 0.6695
160 K	Fe-N Fe-N Fe-C Fe-C Fe-S Fe-C	4.0 2.0 10.0±1.0 7.7±0.8 2.0 9.3±0.9	1.933±0.019 2.094±0.021 2.821±0.028 4.343±0.043 4.971±0.050 4.782±0.048	0.081±0.008 0.087±0.009 0.105±0.011 0.112±0.011 0.089±0.009 0.032±0.003	23.72 5.764 0.6695

Sample	Abs-Bs [a]	N(Bs) [b]	R(Abs-Bs) [c] / Å	σ [d] / Å^{-1}	R [e] / % E_f [f] / eV Afac [g]
170 K	Fe-N Fe-N Fe-C Fe-C Fe-S Fe-C	4.0 2.0 10.0±1.0 5.4±0.5 2.0 8.4±0.8	1.949±0.019 2.091±0.021 2.833±0.028 4.359±0.044 4.977±0.050 4.789±0.048	0.100±0.010 0.110±0.010 0.112±0.011 0.112±0.011 0.089±0.009 0.032±0.003	23.67 5.466 0.6695
180 K	Fe-N Fe-N Fe-C Fe-C Fe-S Fe-C	4.0 2.0 8.7±0.9 8.4±0.8 2.0 24.3±2.4	1.976±0.020 2.169±0.022 2.864±0.028 4.444±0.044 4.898±0.049 4.847±0.048	0.097±0.010 0.110±0.011 0.112±0.011 0.110±0.011 0.089±0.009 0.112±0.011	26.25 4.796 0.6695
190 K	Fe-N Fe-N Fe-C Fe-C Fe-S Fe-C	4.0 2.0 8.0±0.8 11.0±1.1 2.0 21.8±2.2	2.006±0.020 2.217±0.022 2.915±0.029 4.467±0.045 4.735±0.047 4.806±0.048	0.097±0.010 0.089±0.009 0.112±0.011 0.112±0.011 0.032±0.003 0.063±0.006	29.73 4.197 0.6695
200 K	Fe-N Fe-N Fe-C Fe-C Fe-S Fe-C	4.0 2.0 8.1±0.8 12.0±1.2 2.0 19.6±2.0	2.045±0.020 2.242±0.022 2.966±0.030 4.494±0.045 4.760±0.048 4.827±0.048	0.097±0.010 0.081±0.008 0.112±0.011 0.112±0.011 0.032±0.003 0.059±0.006	26.69 3.424 0.6695
210 K	Fe-N Fe-N Fe-C Fe-C Fe-S Fe-C	4.0 2.0 9.0±0.9 10.5±1.1 2.0 26.6±2.7	2.064±0.021 2.265±0.023 2.991±0.030 4.459±0.045 4.732±0.047 4.800±0.048	0.089±0.009 0.067±0.007 0.112±0.011 0.067±0.007 0.032±0.003 0.100±0.010	26.41 3.352 0.6695
220 K	Fe-N Fe-N Fe-C Fe-C Fe-S Fe-C	4.0 2.0 7.3±0.7 14.9±1.5 2.0 19.3±1.9	2.087±0.021 2.288±0.023 3.007±0.030 4.526±0.045 4.785±0.048 4.847±0.048	0.077±0.008 0.045±0.005 0.087±0.009 0.112±0.011 0.032±0.003 0.059±0.006	25.24 2.853 0.6695
230 K	Fe-N Fe-N Fe-C Fe-C Fe-S Fe-C	4.0 2.0 7.8±0.8 15.5±1.6 2.0 19.7±2.0	2.090±0.021 2.289±0.023 3.007±0.030 4.536±0.045 4.805±0.048 4.859±0.049	0.074±0.007 0.045±0.005 0.089±0.009 0.110±0.010 0.032±0.003 0.055±0.006	23.80 3.059 0.6695
240 K	Fe-N Fe-N Fe-C Fe-C Fe-S Fe-C	4.0 2.0 8.1±0.8 16.2±1.6 2.0 24.0±2.4	2.089±0.021 2.286±0.023 3.006±0.030 4.503±0.045 4.753±0.048 4.825±0.048	0.067±0.007 0.039±0.004 0.087±0.009 0.102±0.010 0.032±0.003 0.084±0.008	23.09 3.581 0.6695

Sample	Abs-Bs [a]	N(Bs) [b]	R(Abs-Bs) [c] / Å	σ [d] / Å^{-1}	R [e] / % E_f [f] / eV Afac [g]
250 K	Fe-N Fe-N Fe-C Fe-C Fe-S Fe-C	4.0 2.0 8.4±0.8 9.6±1.0 2.0 27.5±2.8	2.196±0.022 2.292±0.023 3.011±0.030 4.457±0.045 4.730±0.047 4.788±0.048	0.067±0.007 0.039±0.004 0.089±0.009 0.045±0.005 0.032±0.003 0.112±0.011	24.88 3.554 0.6695
260 K	Fe-N Fe-N Fe-C Fe-C Fe-S Fe-C	4.0 2.0 8.4±0.8 16.7±1.7 2.0 26.3±2.6	2.091±0.021 2.286±0.023 3.004±0.030 4.488±0.045 4.744±0.047 4.810±0.048	0.063±0.007 0.032±0.003 0.087±0.009 0.095±0.010 0.032±0.003 0.089±0.009	23.70 3.956 0.6695
293 K	Fe-N Fe-N Fe-C Fe-C Fe-S Fe-C	4.0 2.0 9.2±.09 15.6±1.6 2.0 20.5±2.1	2.101±0.021 2.300±0.023 3.011±0.030 4.526±0.045 4.781±0.048 4.847±0.048	0.059±0.006 0.039±0.004 0.095±0.010 0.100±0.010 0.032±0.003 0.074±0.007	24.88 3.554 0.6695

a) Abs=X-ray absorbing atom, Bs=backscattering atom, b) number of backscattering atoms, c) distance of absorbing atom to backscattering atom, d) Debye-Waller-like factor, e) fit-index, f) Fermi energy, that accounts for the shift between theory and experiment, g) amplitude reducing factor

The most interesting information obtained by this analysis is the variation of the Fe-N distances of the axial and equatorial nitrogen backscatterers within the SCO process shown in Table 6. From these distances, the respective HS fractions were calculated.

Table 6: Fit model 2A: Fe-N distances of the axial and equatorial nitrogen atoms obtained by EXAFS analysis and thereof calculated γ_{HS} values.

T / K	R_{eq}(Abs-Bs) / Å	$\gamma_{HS}(R_{eq})$ [a]	R_{ax}(Abs-Bs) / Å	$\gamma_{HS}(R_{ax})$ [a]
10	1.921±0.019	-0.026	2.074±0.021	-0.054
30	1.922±0.019	-0.020	2.083±0.021	-0.010
40	1.924±0.019	-0.008	2.083±0.021	-0.010
50	1.927±0.019	0.010	2.096±0.021	0.054
70	1.925±0.019	-0.002	2.088±0.021	0.015
80	1.928±0.019	0.016	2.091±0.021	0.030
90	1.928±0.019	0.016	2.091±0.021	0.030
100	1.926±0.019	0.004	2.096±0.021	0.054
110	1.928±0.019	0.016	2.091±0.021	0.030
120	1.926±0.019	0.004	2.087±0.021	0.010
130	1.925±0.019	-0.002	2.072±0.021	-0.064
140	1.934±0.019	0.051	2.095±0.021	0.049
150	1.926±0.019	0.004	2.072±0.021	-0.064
160	1.933±0.019	0.045	2.094±0.021	0.044
170	1.949±0.019	0.139	2.091±0.021	0.030
180	1.976±0.020	0.298	2.169±0.022	0.412
190	2.006±0.020	0.474	2.172±0.022	0.648
200	2.045±0.020	0.703	2.242±0.022	0.771
210	2.064±0.021	0.815	2.265±0.023	0.884
220	2.087±0.021	0.950	2.288±0.023	0.997
230	2.090±0.021	0.968	2.289±0.023	1.001
240	2.089±0.021	0.962	2.286±0.023	0.987
250	2.096±0.021	1.003	2.292±0.023	1.016
260	2.091±0.021	0.974	2.286±0.023	0.987
293	2.101±0.021	1.032	2.300±0.023	1.055

a) HS fraction calculated according to $\gamma_{Hs} = (R_T - R_{LS})/(R_{HS} - R_{LS})$.[84] Applied procedure is described in section 2.3.1.1.

As displayed in Table 6, the equatorial Fe-N distances change from 1.921 Å to 2.101 Å and the axial Fe-N distances change from 2.074 Å to 2.300 Å. To obtain a correlation of the fitting parameters, especially the bond lengths with temperature, all parameters were plotted versus temperature. The plots of the bond lengths (cf. Appendix, Figure A3 and Figure A4) show a gradual increase of the equatorial and axial distances as in the models with one nitrogen shell. Therefore, the data were fitted again with a sigmoidal Boltzmann function. The fit of the equatorial Fe-N distances results in a spin transition temperature of $T_{1/2}$(eq) = 190.8 ± 0.6 K, while the fit of the axial Fe-N distances yields a transition temperature of $T_{1/2}$(ax) = 186.6 ± 1.3 K. Comparison of the magnetization curve obtained by SQUID magnetometry and the fits of the bond lengths reveals that the structural changes do not clearly correlate with the magnetic changes since the fit curves do not follow the magnetization exactly (Figure 2.14). Especially the fit of the axial Fe-N distances diverges from the magnetization curve since the bonds start to elongate at lower temperatures and therefore the HS state is reached at lower temperatures, too. The fit of the equatorial Fe-N distances slightly differs from the magnetization; only small deviations from the SQUID curve are observable in the spin transition region resulting in a small difference of the spin transition temperatures $T_{1/2}$ ($T_{1/2}$(eq) = 190.8 ± 0.6 K, $T_{1/2}$(SQUID) = 192.0 ± 0.2 K). But it has to be considered, that the changes of the axial and the equatorial distances mix up within the respective error bars and therefore the interpretation of the curve shapes need to be treated with caution.

Nevertheless, the different curve shapes for the axial and equatorial distances can lead to the assumption that the axial distances start to change at lower temperature, what does not seem to affect the magnetic properties of the whole system. Only when the equatorial Fe-N bonds start to elongate, the system starts to change its spin state from LS to HS. However, the temperature-dependent X-ray structure analysis indicates that the different Fe-N bonds change more or less simultaneously in the same temperature range.[172]

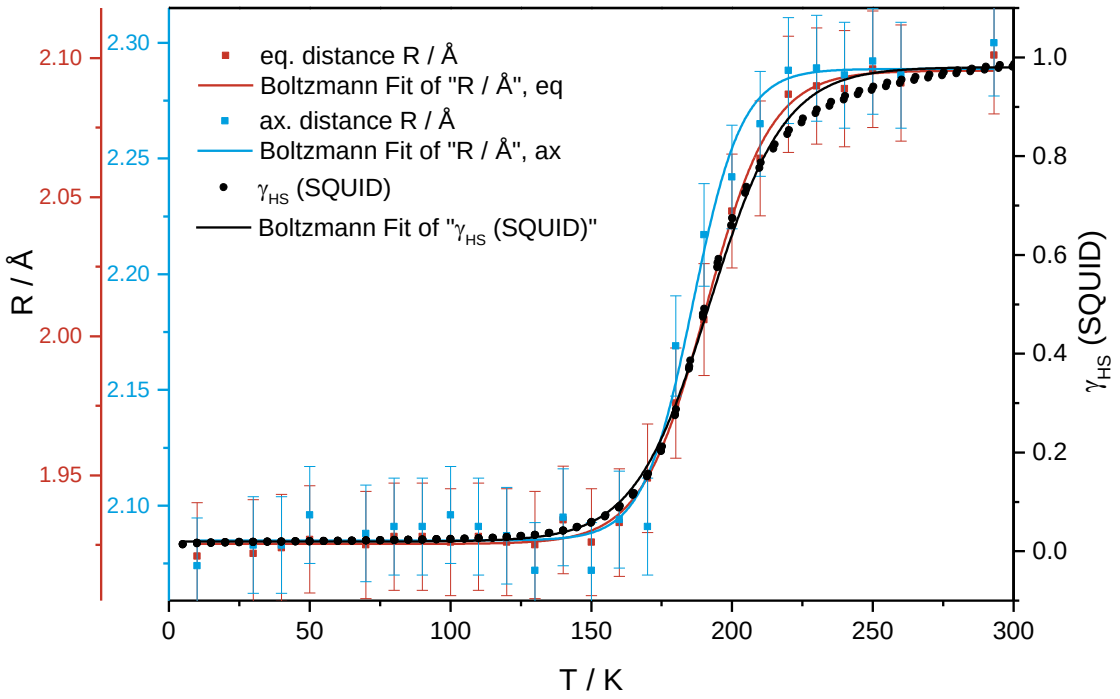

Figure 2.14: Fit model 2A: Comparison of HS fraction obtained by SQUID measurements and fits of the equatorial (red) and axial (blue) Fe-N distances.

For a direct comparison with the HS fractions obtained by SQUID magnetometry, the equatorial and axial Fe-N distances were converted to HS fractions, too. According to the procedure described in chapter 2.3.1.1, the limits of the Boltzmann fits (A_1 and A_2) were used as approximations for the pure LS and HS distances, which were inserted into equation (22) to calculate $\gamma_{HS}(R_{eq})$ and $\gamma_{HS}(R_{ax})$. In the equatorial case the limits were determined as $A_1(eq) = R_{eq,LS} = 1.925 \pm 0.001$ Å and $A_2(eq) = R_{eq,HS} = 2.096 \pm 0.002$ Å, whereas in the axial case the LS distance was determined as $A_1(ax) = R_{ax,LS} = 2.085 \pm 0.003$ Å and the HS distance as $A_2(ax) = R_{ax,HS} = 2.289 \pm 0.004$ Å. The resulting $\gamma_{HS}(R_{eq})$ and $\gamma_{HS}(R_{ax})$ values are shown in Table 6 and the comparison with the γ_{HS}(SQUID) data and the respective Boltzmann fits is displayed in Figure 2.15.

As already discussed in the previous sections, dealing with the fit models with only one nitrogen shell, the course of the γ_{HS} values is the same as the course of the Fe-N distances, since these quantities are directly correlated. Therefore, the Boltzmann fits of the HS fractions and the Fe-N bond lengths yield the same transition temperatures. Even though the absolute values for LS and HS are distorted, due to the small remaining fraction of HS respective LS, the agreement with the fit curve obtained from the SQUID data is quite good.

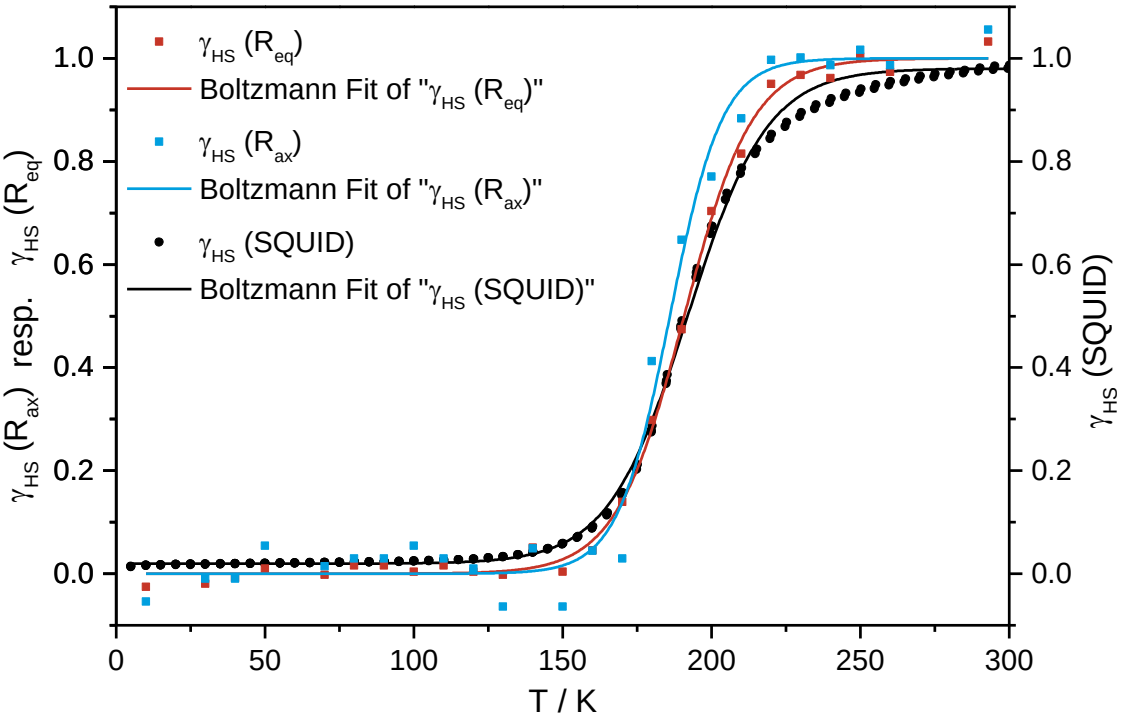

Figure 2.15: Fit model 2A: Comparison of HS fractions obtained by SQUID (black) and EXAFS measurements (red and blue).

Additionally, the plots of the Debye-Waller-like factors σ_{eq} and σ_{ax} versus temperature are shown in Figure 2.16 and Figure 2.17. The equatorial Debye-Waller-like factor shows an increase up to 170 K, stays more or less constant up to 200 K and then it is decreasing again (Figure 2.16). The axial Debye-Waller-like factor shows its maximum at 170 K and 180 K, at higher temperatures it is decreasing again (Figure 2.17). Due to the visible peak structure in both cases, a Gaussian fit was applied to obtain the temperatures of the maxima, which were used to check for a possible correlation with the spin transition temperature. In the equatorial case, the maximum of the fit is determined at T(eq) = 186.7 ± 1.5 K, compared to the spin transition temperature determined for this shell, it is shifted by around 4 K to lower temperatures. The fit of the axial Debye-Waller-like factor leads to a maximum at T(ax) = 173.7 ± 2.2 K. In this case the shift to lower temperatures is even more pronounced with about 13 K. In general, it seems that the fits can give an indication for the SCO region of the system, but a precise determination of the transition temperature is not possible.

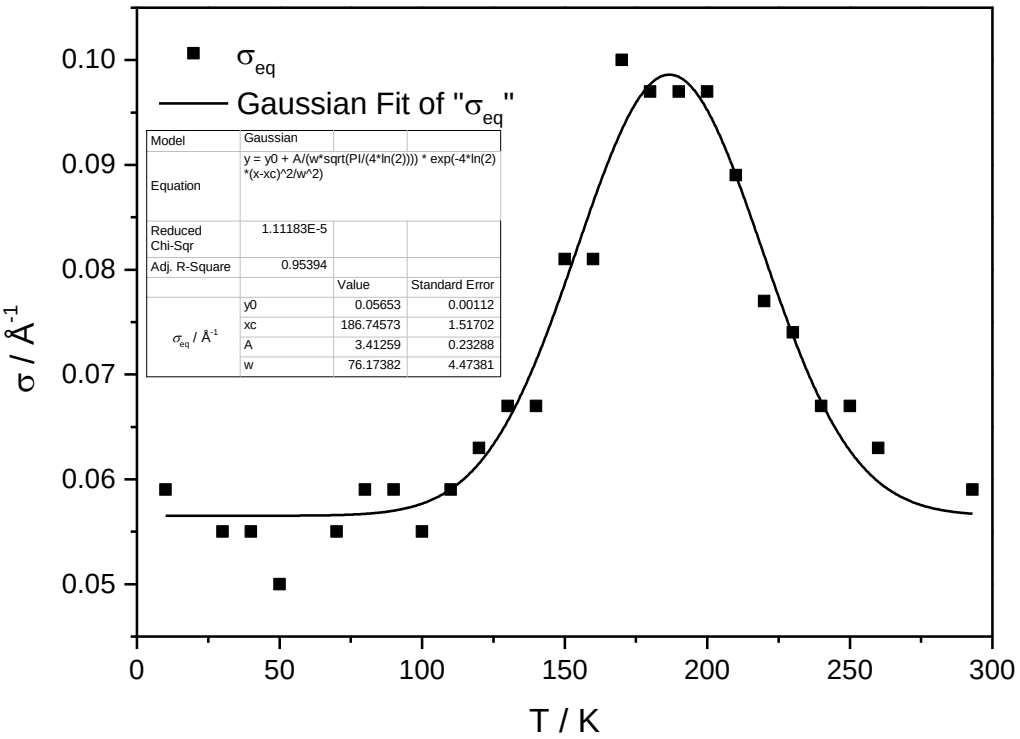

Figure 2.16: Fit model 2A: Plot of Debye-Waller like factor σ_{eq} of the equatorial nitrogen shell vs. temperature with resulting Gaussian fit.

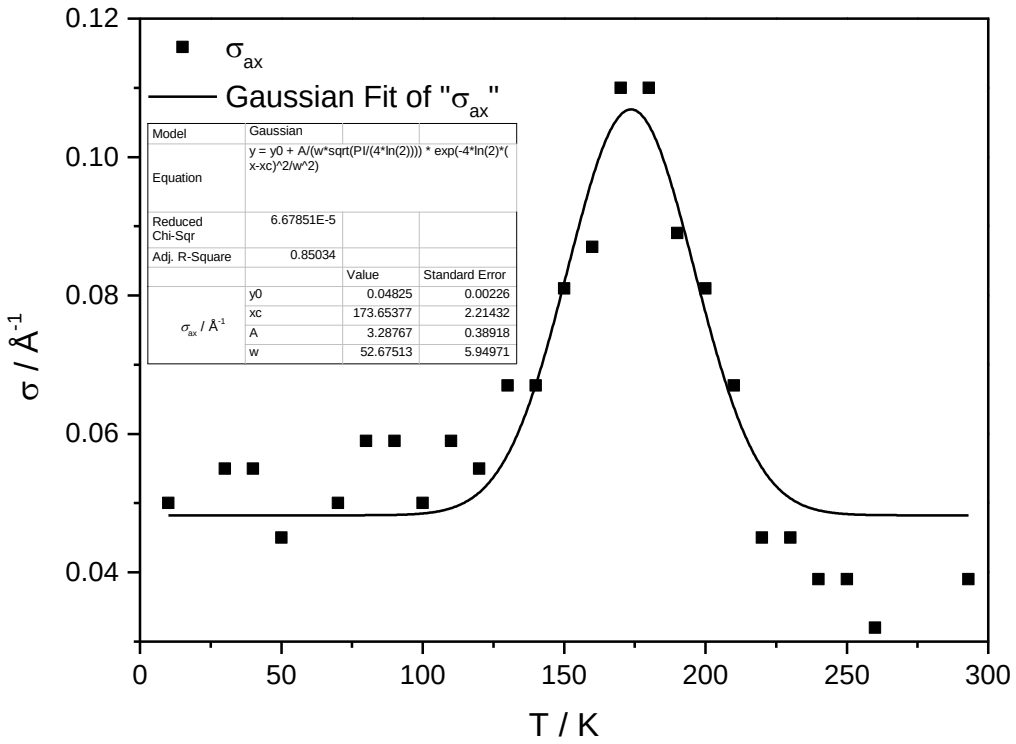

Figure 2.17: Fit model 2A: Plot of Debye-Waller like factor σ_{ax} of the axial nitrogen shell vs. temperature with resulting Gaussian fit.

Despite this, the Debye-Waller-like factors lead to the suggestion that the axial Fe-N bonds start to elongate at slightly lower temperature and that the maximum value corresponding to the HS state is reached earlier than in the equatorial case. In addition, the narrower peak structure can probably be correlated with a more abrupt change of the axial Fe-N bonds compared to the equatorial ones, where a broader peak is observable. These findings are in good agreement with the resulting plots of the Fe-N distances obtained by the EXAFS analysis, which also show a more abrupt SCO behaviour in case of the axial distances.

To understand the overall course of the σ values it is useful to recapitulate the different components of the Debye-Waller-like factor. As already described in chapter 1.3.3.4, σ accounts for thermal vibrations and static disorder in the system. At low and high temperatures, the system mainly consists of one species, namely LS at low T or HS at high T, so the static disorder should be more or less constant in these regions. But in the region of the spin transition, the disorder should increase due to a supposed mixture of LS and HS centres, resulting in the observable peak structures.

Summarising the results of the first fit model with two nitrogen shells, it can be said that it is obviously possible to distinguish the equatorial and axial nitrogen backscatterers. The EXAFS fit functions result in two N shells with $\Delta R \approx 0.2$ Å. In general, the experimental spectra are reproduced by the fit functions really good, only the spectrum at the spin transition temperature cannot be adjusted properly, since the fit cannot reproduce the number of signals between 2.5 – 3 Å correctly. The changes of the bond lengths as well as the thereof calculated HS fractions result in spin transition curves, which are in satisfying to good agreement with the SQUID data. Considering the curve shapes, it can be assumed, that the axial Fe-N bonds start to elongate at lower temperatures than the equatorial ones, what influences the magnetic properties only to a minor extend, since the magnetization rather follows the changes of the equatorial bonds. But since the error bars of both distances are overlapping in the whole temperature range, this observation has to be treated with caution. Additionally, the behaviour of the Debye-Waller-like factor with increasing temperature was analysed, resulting in a peak structure, which can be used for the qualitative determination of the SCO region and can probably give indications for the existing kind of SCO transition (e.g. gradual or abrupt).

2.3.2.2 Fit Model 2B: Fit of unfiltered Data with two Nitrogen Shells, Fe-N distances fixed at values from temperature-dependent Crystal Structures and afac at 0.8000

In the second fit model with two nitrogen shells the Fe-N distances were held fix at values obtained by temperature-dependent crystal structure analysis. In Table 7 the Fe-N distances of the different nitrogen atoms are displayed, which were obtained by X-ray crystallography.[172] For this fit model the equatorial distances (*Fe-$N_{Pyridine}$* and *Fe-N_{NCS}*) were averaged and the average value was used. For the temperatures without available crystal structure data, the data of the next temperature point was used. Additionally, the coordination numbers of the nitrogen shells were held fix at four (equatorial) and two (axial), the coordination number of sulphur was held fix at two and the amplitude reducing factor was fixed at 0.8000. The coordination numbers of the carbon shells, the Fe-C and Fe-S distances, the Fermi energy E_f and the Debye-Waller-like factors σ of all shells were iterated freely.

Table 7: Fe-N distances of the different nitrogen atoms obtained by temperature-dependent X-ray crystallography.

T / K	Fe-N_{Amin} / Å	Fe-$N_{Pyridine}$ / Å	Fe-N_{NCS} / Å	Fe-N_{eq} (av.) / Å
103	2.0849±0.0045	1.8982±0.0048	1.9495±0.0051	1.9238±0.0051
140	2.0891±0.0036	1.9016±0.0036	1.9466±0.0042	1.9241±0.0042
150	2.0941±0.0048	1.9065±0.0048	1.9505±0.0057	1.9285±0.0057
160	2.1027±0.0054	1.9153±0.0054	1.9530±0.0060	1.9340±0.0060
170	2.1180±0.0060	1.9390±0.0060	1.9530±0.0090	1.9460±0.0090
180	2.1520±0.0057	1.9890±0.0057	1.9650±0.0090	1.9770±0.0090
190	2.1989±0.0048	2.0544±0.0048	1.9980±0.0090	2.0260±0.0090
200	2.2329±0.0057	2.0990±0.0060	2.0220±0.0090	2.0610±0.0090
200	2.2330±0.0060	2.1020±0.0060	2.0250±0.0090	2.0640±0.0090
210	2.2550±0.0060	2.1240±0.0060	2.0370±0.0090	2.0810±0.0090
220	2.2655±0.0054	2.1370±0.0060	2.0380±0.0150	2.0880±0.0150
240	2.2817±0.0051	2.1506±0.0054	2.0460±0.0060	2.0980±0.0060
280	2.2940±0.0048	2.1624±0.0051	2.0460±0.0060	2.1042±0.0060
298	2.2972±0.0048	2.1636±0.0054	2.0440±0.0060	2.1040±0.0060

In Figure 2.18 the temperature-dependent EXAFS spectra with the resulting fit functions in k-space (top) and R-space (bottom) are displayed. Again the blue spectrum indicates

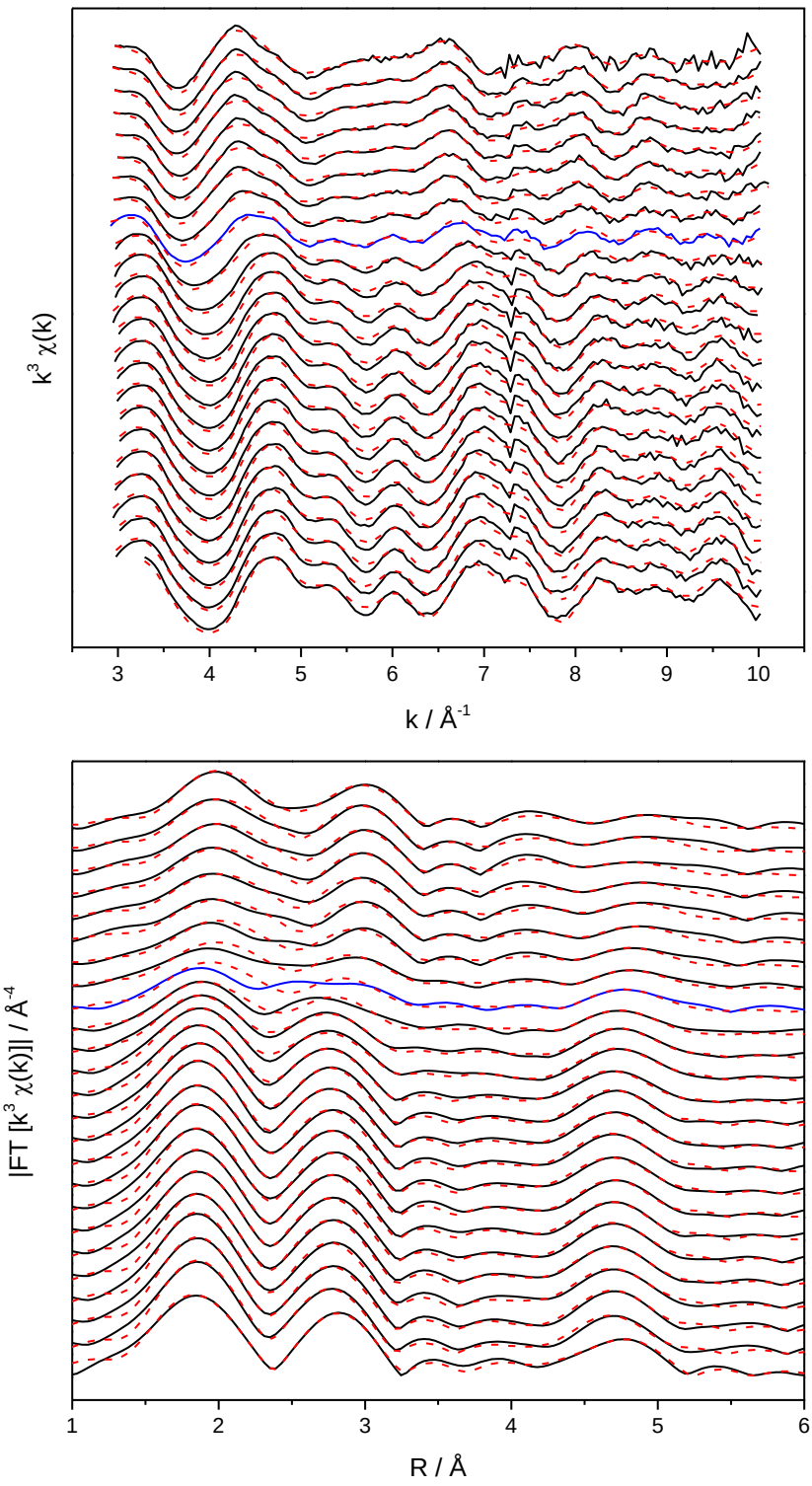

Figure 2.18: Fit model 2B: Temperature-dependent EXAFS spectra of [Fe(L-N_4Bn_2)$(NCS)_2$], blue spectrum: spin transition temperature (190 K), top: χ(k), bottom: Fourier transformation, (—) experimental data, (---) theoretical data.

the spin transition temperature (190 K) and temperature decreases from top (293 K) to bottom (10 K). The experimental spectra are reproduced quite well by the fit functions. But compared to the previous model with two N shells (cf. chapter 2.3.2.1), the quality of the fit is generally worse, what can be explained by the reduced number of iterated parameters. Only the spectrum at the spin transition temperature shows visible discrepancies with the fit function, since the experimental spectrum at 190 K shows two signals in the range from 2.5 – 3.0 Å, while the fit function gives only one signal in between.

The parameters resulting from the EXAFS analysis are shown in Table 8 for all temperatures as an overview.

Table 8: Fit model 2B: Neighbour atoms, coordination numbers and distances obtained by EXAFS analysis.

Sample	**Abs-Bs** [a]	**N(Bs)** [b]	**R(Abs-Bs)** [c] **/ Å**	**σ** [d] **/ Å^{-1}**	**R** [e] **/ %** **E_f** [f] **/ eV** **Afac** [g]
10 K	Fe-N Fe-N Fe-C Fe-C Fe-S Fe-C	4.0 2.0 7.4±0.7 9.0±0.9 2.0 16.2±1.6	1.924 2.085 2.831±0.028 4.344±0.043 4.856±0.049 4.838±0.048	0.074±0.007 0.074±0.007 0.071±0.007 0.112±0.011 0.032±0.003 0.055±0.006	22.35 3.365 0.8000
30 K	Fe-N Fe-N Fe-C Fe-C Fe-S Fe-C	4.0 2.0 6.7±0.7 9.6±1.0 2.0 15.4±1.5	1.924 2.085 2.824±0.028 4.328±0.043 4.873±0.049 4.849±0.048	0.071±0.007 0.077±0.008 0.067±0.007 0.112±0.011 0.032±0.003 0.067±0.007	22.42 3.883 0.8000
40 K	Fe-N Fe-N Fe-C Fe-C Fe-S Fe-C	4.0 2.0 7.0±0.7 9.1±0.9 2.0 14.6±1.5	1.924 2.085 2.823±0.028 4.325±0.043 4.828±0.048 4.826±0.048	0.071±0.007 0.077±0.008 0.071±0.007 0.112±0.011 0.039±0.004 0.032±0.003	22.25 4.091 0.8000
50 K	Fe-N Fe-N Fe-C Fe-C Fe-S Fe-C	4.0 2.0 6.7±0.7 9.2±0.9 2.0 14.9±1.5	1.924 2.085 2.825±0.028 4.318±0.043 4.813±0.048 4.819±0.048	0.071±0.007 0.074±0.007 0.063±0.006 0.110±0.011 0.055±0.006 0.032±0.003	22.94 3.926 0.8000
70 K	Fe-N Fe-N Fe-C Fe-C Fe-S Fe-C	4.0 2.0 6.8±0.7 12.2±1.2 2.0 17.7±1.8	1.924 2.085 2.825±0.028 4.312±0.043 4.641±0.046 4.760±0.048	0.074±0.007 0.074±0.007 0.067±0.007 0.112±0.011 0.032±0.003 0.059±0.006	21.79 4.019 0.8000

Sample	Abs-Bs [a]	N(Bs) [b]	R(Abs-Bs) [c] / Å	σ [d] / Å^{-1}	R [e] / % E_f [f] / eV Afac [g]
80 K	Fe-N Fe-N Fe-C Fe-C Fe-S Fe-C	4.0 2.0 7.1±0.7 9.3±0.9 2.0 15.2±1.5	1.924 2.085 2.825±0.028 4.330±0.043 4.807±0.048 4.816±0.048	0.074±0.007 0.077±0.008 0.071±0.007 0.112±0.011 0.050±0.005 0.032±0.003	22.32 4.096 0.8000
90 K	Fe-N Fe-N Fe-C Fe-C Fe-S Fe-C	4.0 2.0 7.0±0.7 9.0±0.9 2.0 14.0±1.4	1.924 2.085 2.825±0.028 4.326±0.043 4.825±0.048 4.828±0.048	0.074±0.007 0.077±0.008 0.071±0.007 0.112±0.011 0.039±0.004 0.032±0.003	23.49 4.093 0.8000
100 K	Fe-N Fe-N Fe-C Fe-C Fe-S Fe-C	4.0 2.0 7.0±0.7 9.1±0.9 2.0 13.1±1.3	1.924 2.085 2.826±0.028 4.307±0.043 4.773±0.048 4.805±0.048	0.077±0.008 0.081±0.008 0.071±0.007 0.112±0.011 0.112±0.011 0.039±0.004	23.59 4.233 0.8000
110 K	Fe-N Fe-N Fe-C Fe-C Fe-S Fe-C	4.0 2.0 6.6±0.7 10.0±1.0 2.0 18.7±1.9	1.924 2.085 2.826±0.028 4.336±0.043 4.918±0.049 4.839±0.048	0.074±0.007 0.077±0.008 0.067±0.007 0.112±0.011 0.039±0.004 0.112±0.011	23.30 4.198 0.8000
120 K	Fe-N Fe-N Fe-C Fe-C Fe-S Fe-C	4.0 2.0 6.9±0.7 8.7±0.9 2.0 14.2±1.4	1.924 2.085 2.826±0.028 4.321±0.043 4.816±0.048 4.820±0.048	0.077±0.008 0.077±0.008 0.074±0.007 0.112±0.011 0.045±0.005 0.032±0.003	24.23 4.295 0.8000
130 K	Fe-N Fe-N Fe-C Fe-C Fe-S Fe-C	4.0 2.0 6.9±0.7 8.4±0.8 2.0 17.7±1.8	1.924 2.085 2.822±0.028 4.340±0.043 4.909±0.049 4.846±0.048	0.077±0.008 0.077±0.008 0.077±0.008 0.112±0.011 0.032±0.003 0.105±0.010	24.02 4.293 0.8000
140 K	Fe-N Fe-N Fe-C Fe-C Fe-S Fe-C	4.0 2.0 6.7±0.7 7.6±0.8 2.0 13.1±1.3	1.924 2.089 2.821±0.028 4.308±0.043 4.735±0.047 4.792±0.048	0.081±0.008 0.077±0.008 0.077±0.008 0.112±0.011 0.095±0.010 0.032±0.003	24.06 4.637 0.8000
150 K	Fe-N Fe-N Fe-C Fe-C Fe-S Fe-C	4.0 2.0 7.0±0.7 7.2±0.7 2.0 19.6±2.0	1.929 2.094 2.824±0.028 4.358±0.044 4.904±0.049 4.847±0.048	0.089±0.009 0.089±0.009 0.087±0.009 0.112±0.011 0.045±0.005 0.112±0.011	25.83 4.553 0.8000

Sample	Abs-Bs [a]	N(Bs) [b]	R(Abs-Bs) [c] / Å	σ [d] / Å^{-1}	R [e] / % E_f [f] / eV Afac [g]
160 K	Fe-N Fe-N Fe-C Fe-C Fe-S Fe-C	4.0 2.0 8.4±0.8 5.7±0.6 2.0 12.1±1.2	1.934 2.103 2.828±0.028 4.360±0.044 4.849±0.048 4.812±0.048	0.095±0.010 0.095±0.010 0.112±0.011 0.112±0.011 0.112±0.011 0.050±0.005	25.89 5.114 0.8000
170 K	Fe-N Fe-N Fe-C Fe-C Fe-S Fe-C	4.0 2.0 7.8±0.8 6.0±0.6 2.0 17.5±1.8	1.946 2.118 2.838±0.028 4.420±0.044 4.918±0.049 4.847±0.048	0.105±0.011 0.110±0.011 0.112±0.011 0.112±0.011 0.050±0.005 0.112±0.011	26.83 4.971 0.8000
180 K	Fe-N Fe-N Fe-C Fe-C Fe-S Fe-C	4.0 2.0 6.6±0.7 8.8±0.9 2.0 20.2±2.0	1.977 2.152 2.877±0.029 4.445±0.044 4.904±0.049 4.834±0.048	0.112±0.011 0.112±0.011 0.112±0.011 0.112±0.011 0.102±0.010 0.112±0.011	28.45 4.541 0.8000
190 K	Fe-N Fe-N Fe-C Fe-C Fe-S Fe-C	4.0 2.0 6.1±0.6 8.1±0.8 2.0 16.8±1.7	2.026 2.199 2.939±0.029 4.480±0.045 4.781±0.048 4.840±0.048	0.112±0.011 0.110±0.011 0.112±0.011 0.112±0.011 0.032±0.003 0.050±0.005	34.72 3.284 0.8000
200 K	Fe-N Fe-N Fe-C Fe-C Fe-S Fe-C	4.0 2.0 6.4±0.6 10.5±1.1 2.0 17.8±1.8	2.060 2.233 2.970±0.030 4.498±0.045 4.765±0.048 4.833±0.048	0.112±0.011 0.110±0.011 0.112±0.011 0.112±0.011 0.032±0.003 0.063±0.006	30.14 3.396 0.8000
210 K	Fe-N Fe-N Fe-C Fe-C Fe-S Fe-C	4.0 2.0 6.8±0.7 9.4±0.9 2.0 19.9±2.0	2.081 2.255 2.997±0.030 4.485±0.045 4.755±0.048 4.826±0.048	0.112±0.011 0.112±0.011 0.105±0.011 0.087±0.009 0.032±0.003 0.077±0.008	28.61 3.103 0.8000
220 K	Fe-N Fe-N Fe-C Fe-C Fe-S Fe-C	4.0 2.0 5.4±0.5 13.9±1.4 2.0 18.8±1.9	2.088 2.266 3.003±0.030 4.516±0.045 4.772±0.048 4.836±0.048	0.110±0.011 0.102±0.010 0.077±0.008 0.112±0.011 0.032±0.003 0.063±0.006	26.24 3.546 0.8000
230 K	Fe-N Fe-N Fe-C Fe-C Fe-S Fe-C	4.0 2.0 5.9±0.6 15.9±1.6 2.0 18.9±1.9	2.088 2.266 3.000±0.030 4.527±0.045 4.790±0.048 04.846±0.048	0.105±0.011 0.102±0.010 0.081±0.008 0.112±0.011 0.032±0.003 0.059±0.006	25.46 3.92 0.8000

Sample	Abs-Bs [a]	N(Bs) [b]	R(Abs-Bs) [c] / Å	σ [d] / Å^{-1}	R [e] / % E_f [f] / eV Afac [g]
240 K	Fe-N Fe-N Fe-C Fe-C Fe-S Fe-C	4.0 2.0 5.7±0.6 13.4±1.3 2.0 20.7±2.1	2.098 2.282 3.013±0.030 4.511±0.045 4.767±0.048 4.834±0.048	0.095±0.010 0.084±0.008 0.074±0.007 0.102±0.010 0.032±0.003 0.077±0.008	24.19 3.284 0.8000
250 K	Fe-N Fe-N Fe-C Fe-C Fe-S Fe-C	4.0 2.0 5.8±0.6 8.1±0.8 2.0 25.0±2.5	2.098 2.282 3.016±0.030 4.454±0.045 4.729±0.047 4.788±0.048	0.092±0.009 0.081±0.008 0.074±0.007 0.045±0.005 0.032±0.003 0.112±0.011	25.24 3.538 0.8000
260 K	Fe-N Fe-N Fe-C Fe-C Fe-S Fe-C	4.0 2.0 6.1±0.6 14.4±1.4 2.0 23.2±2.3	2.098 2.282 3.009±0.030 4.495±0.045 4.752±0.048 4.818±0.048	0.089±0.009 0.081±0.008 0.074±0.007 0.095±0.010 0.032±0.003 0.087±0.009	24.55 3.788 0.8000
293 K	Fe-N Fe-N Fe-C Fe-C Fe-S Fe-C	4.0 2.0 6.9±0.7 15.9±1.6 2.0 20.6±2.1	2.104 2.297 3.012±0.030 4.523±0.045 4.776±0.048 4.843±0.048	0.081±0.008 0.071±0.007 0.089±0.009 0.107±0.011 0.032±0.003 0.081±0.008	30.15 3.608 0.8000

a) Abs=X-ray absorbing atom, Bs=backscattering atom, b) number of backscattering atoms, c) distance of absorbing atom to backscattering atom, d) Debye-Waller-like factor, e) fit-index, f) Fermi energy, that accounts for the shift between theory and experiment, g) amplitude reducing factor

Since in this fit model the coordination numbers of the nitrogen atoms and the Fe-N distances were fixed, only the Debye-Waller-like factors σ of the nitrogen shells were iterated freely. The values of the equatorial and the axial nitrogen shell were plotted as function of temperature and are displayed in Figure 2.19 and Figure 2.20, together with the resulting Gaussian fit functions. The equatorial Debye-Waller-like factor varies between 0.071 $Å^{-1}$ and 0.077 $Å^{-1}$ up to 140 K. With rising temperature, it increases up to 0.112 $Å^{-1}$ (180 to 210 K) and further rising temperature leads to a decrease of σ_{eq} to 0.081 $Å^{-1}$ at 293 K again. The Debye-Waller-like factor of the axial nitrogen shell shows a similar trend, the maximum value is reached in the range from 170 to 210 K, at higher temperatures it decreases again.

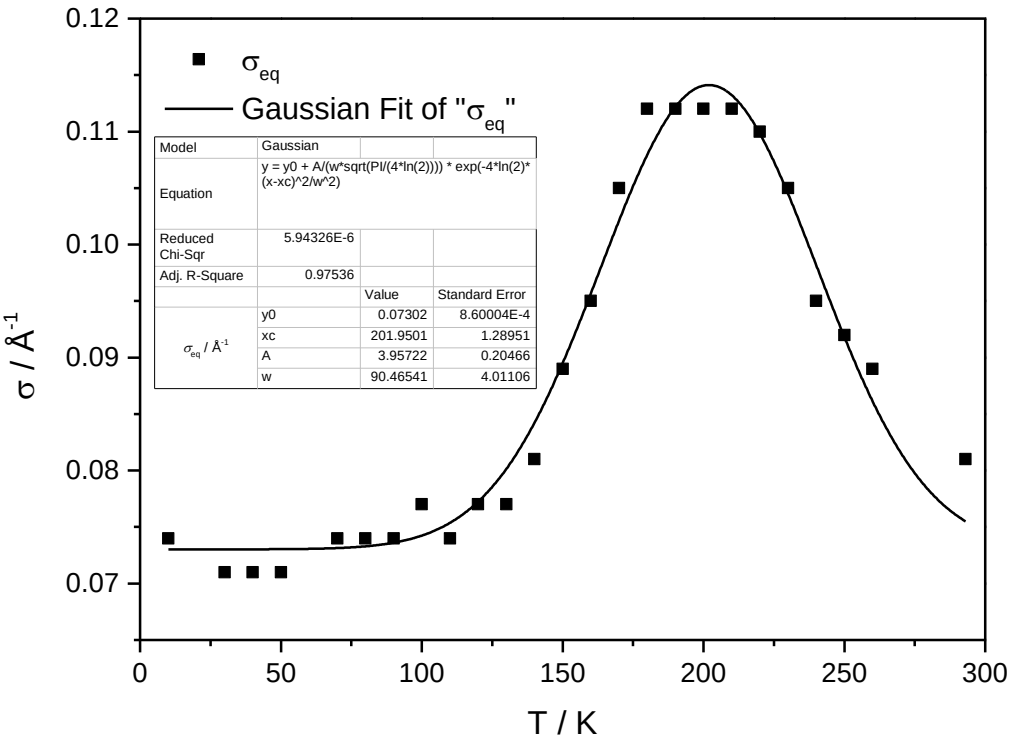

Figure 2.19: Fit model 2B: Plot of Debye-Waller like factor σ_{eq} of the equatorial nitrogen shell vs. temperature.

The fit of the equatorial Debye-Waller-like factor leads to a maximum at T(eq) = 202.0 ± 1.3 K. Compared to the spin transition temperature obtained by SQUID magnetometry $T_{1/2}$(SQUID) = 192.0 K ± 0.2 K, a shift to higher temperatures by around 10 K can be observed. In the axial case, the maximum of the fit is located at T(ax) = 194.7 ± 1.7 K, what is only shifted by 2 K to higher temperatures compared to the SQUID data.

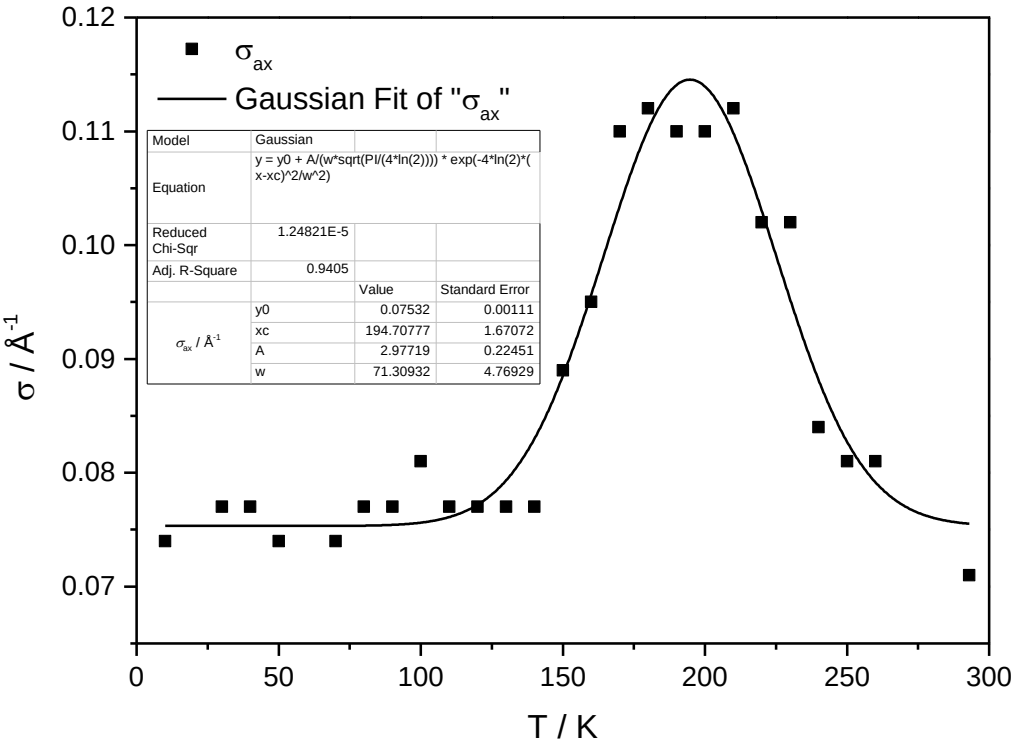

Figure 2.20: Fit model 2B: Plot of Debye-Waller like factor σ_{ax} of the axial nitrogen shell vs. temperature.

In comparison with the previous model with two nitrogen shells and iterated Fe-N distances (cf. chapter 2.3.2.1), it can be said that the overall course of the Debye-Waller-like factors is very similar. Both fit models result in a peak structure, which can be explained by the increasing static disorder in the SCO range, presumably caused by a mixture of LS and HS centres. But the maxima of the fits show no obvious trend, since in Fit Model 2A the maxima are shifted significantly to lower temperatures compared to the SQUID transition temperature, while in the actual fit model (Fit Model 2B) they are shifted to higher temperatures.

2.3.2.3 Fit Model 2C: Fit of unfiltered Data with two Nitrogen Shells, Fe-N distances iterated based on values from temperature-dependent Crystal Structures and afac at 0.8000

In the third fit model with two nitrogen shells the initial Fe-N distances were again based on the values obtained by temperature-dependent crystal structure analysis (Table 7). In contrast to Fit Model 2B the distances were iterated freely. All other parameters were treated equally as in Fit Model 2B. Thus, the coordination numbers of the nitrogen shells were held fix at four (equatorial) and two (axial), the coordination number of sulphur was held fix at two and the amplitude reducing factor was fixed at 0.8000. The coordination numbers of the carbon shells, the Fe-C and Fe-S distances, the Fermi energy E_f and the Debye-Waller-like factors σ of all shells were iterated freely.
The temperature-dependent EXAFS spectra with the resulting fit functions in k-space (top) and R-space (bottom) are displayed in Figure 2.21. The spin transition temperature (190 K) is depicted by the blue line and temperature decreases from top (293 K) to bottom (10 K). The experimental spectra are reproduced well by the fit functions, with exception of the spectrum at the transition temperature. As in the two models before, the experimental spectrum shows two signals at 2.5 Å and 3.0 Å, while the fit function shows only one signal at 2.9 Å. The overall fit quality is comparable to Fit Model 2A, where the Fe-N distances were iterated freely, too.

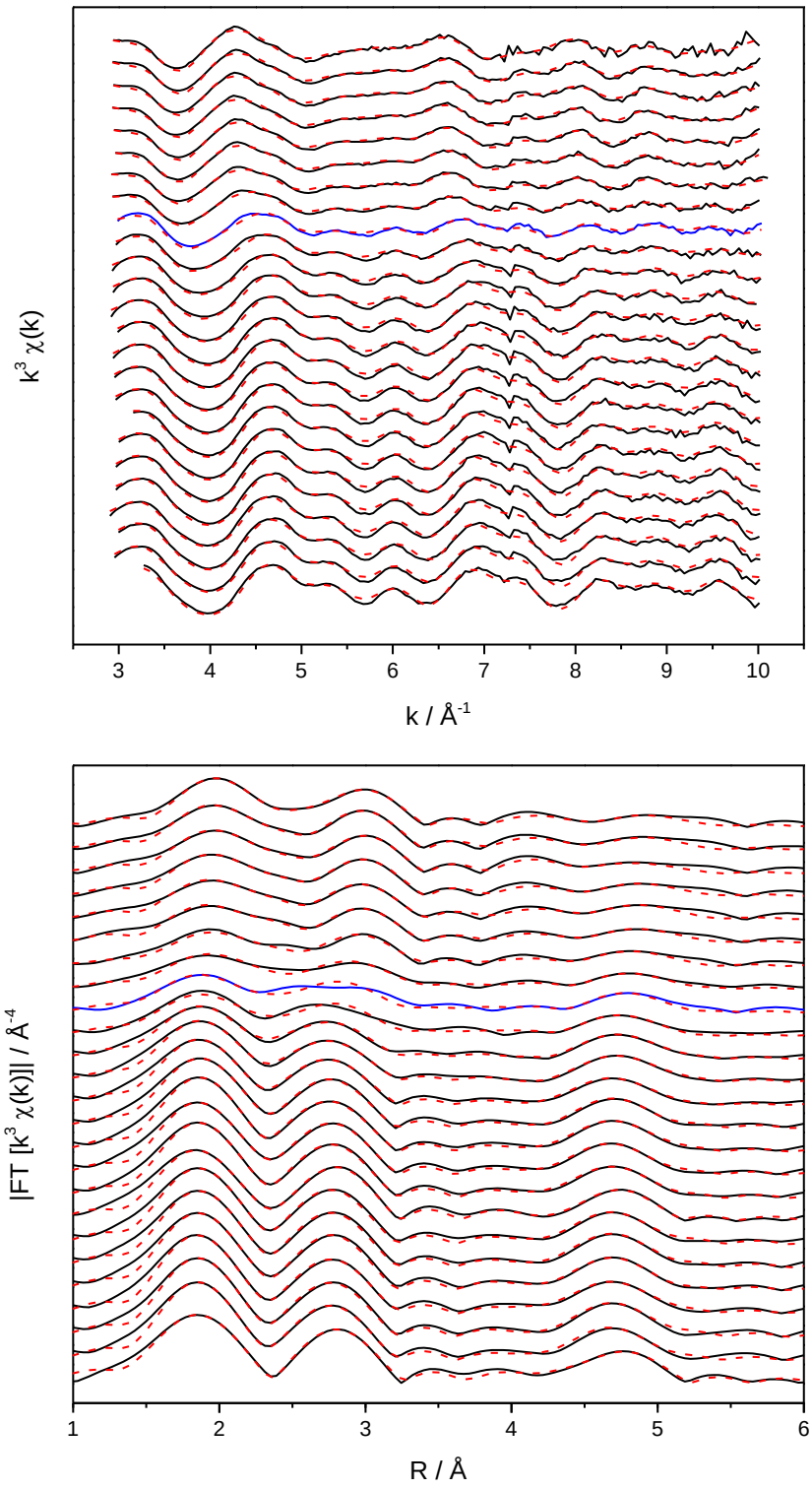

Figure 2.21: Fit Model 2C: Temperature-dependent EXAFS spectra of [Fe(L-N_4Bn_2)$(NCS)_2$], blue spectrum: spin transition temperature (190 K), top: χ(k), bottom: Fourier transformation, (—) experimental data, (---) theoretical data.

The resulting fit parameters obtained by temperature-dependent EXAFS analysis are displayed in Table 9.

Table 9: Fit Model 2C: Neighbour atoms, coordination numbers and distances obtained by EXAFS analysis.

Sample	Abs-Bs [a]	N(Bs) [b]	R(Abs-Bs) [c] / Å	σ [d] / Å^{-1}	R [e] / % E_f [f] / eV Afac [g]
10 K	Fe-N Fe-N Fe-C Fe-C Fe-S Fe-C	4.0 2.0 7.0±0.7 9.4±0.9 2.0 17.2±1.7	1.938±0.019 2.097±0.021 2.832±0.028 4.358±0.044 4.855±0.049 4.843±0.048	0.077±0.008 0.095±0.010 0.067±0.007 0.112±0.011 0.032±0.003 0.059±0.006	21.15 2.919 0.8000
30 K	Fe-N Fe-N Fe-C Fe-C Fe-S Fe-C	4.0 2.0 6.6±0.7 9.6±1.0 2.0 15.7±1.6	1.937±0.019 2.113±0.021 2.828±0.028 4.333±0.043 4.873±0.049 4.849±0.048	0.071±0.007 0.089±0.009 0.063±0.006 0.112±0.011 0.032±0.003 0.067±0.007	21.05 3.335 0.8000
40 K	Fe-N Fe-N Fe-C Fe-C Fe-S Fe-C	4.0 2.0 6.7±0.7 9.1±0.9 2.0 14.6±1.5	1.935±0.019 2.104±0.021 2.827±0.028 4.334±0.043 4.828±0.048 4.826±0.048	0.071±0.007 0.089±0.009 0.067±0.007 0.112±0.011 0.039±0.004 0.032±0.003	21.18 3.648 0.8000
50 K	Fe-N Fe-N Fe-C Fe-C Fe-S Fe-C	4.0 2.0 6.3±0.6 9.8±1.0 2.0 15.5±1.6	1.940±0.019 2.123±0.021 2.833±0.028 4.336±0.043 4.837±0.048 4.839±0.048	0.067±0.007 0.081±0.008 0.055±0.006 0.112±0.011 0.032±0.003 0.039±0.004	21.68 2.946 0.8000
70 K	Fe-N Fe-N Fe-C Fe-C Fe-S Fe-C	4.0 2.0 6.7±0.7 12.4±1.2 2.0 17.7±1.8	1.933±0.019 2.097±0.021 2.828±0.028 4.317±0.043 4.641±0.046 4.760±0.048	0.074±0.007 0.087±0.009 0.063±0.006 0.112±0.011 0.032±0.003 0.063±0.006	20.81 3.692 0.8000
80 K	Fe-N Fe-N Fe-C Fe-C Fe-S Fe-C	4.0 2.0 6.8±0.7 9.8±1.0 2.0 15.7±1.6	1.930±0.019 2.096±0.021 2.829±0.028 4.338±0.043 4.801±0.048 4.818±0.048	0.077±0.008 0.095±0.010 0.067±0.007 0.112±0.011 0.050±0.005 0.032±0.003	21.48 3.692 0.8000
90 K	Fe-N Fe-N Fe-C Fe-C Fe-S Fe-C	4.0 2.0 6.8±0.7 9.0±0.9 2.0 14.1±1.4	1.934±0.019 2.099±0.021 2.828±0.028 4.326±0.043 4.825±0.048 4.828±0.048	0.077±0.008 0.092±0.009 0.067±0.007 0.112±0.011 0.039±0.004 0.032±0.003	22.53 3.725 0.8000

Sample	Abs-Bs [a]	N(Bs) [b]	R(Abs-Bs) [c] / Å	σ [d] / Å^{-1}	R [e] / % E_f [f] / eV Afac [g]
100 K	Fe-N Fe-N Fe-C Fe-C Fe-S Fe-C	4.0 2.0 6.7±0.7 8.4±0.8 2.0 14.8±1.9	1.933±0.019 2.112±0.021 2.832±0.028 4.323±0.043 4.884±0.049 4.856±0.049	0.071±0.007 0.077±0.008 0.067±0.007 0.112±0.011 0.032±0.003 0.071±0.007	23.18 3.547 0.8000
110 K	Fe-N Fe-N Fe-C Fe-C Fe-S Fe-C	4.0 2.0 6.3±0.6 10.0±1.0 2.0 19.5±2.0	1.938±0.019 2.110±0.021 2.830±0.028 4.340±0.043 4.918±0.049 4.844±0.048	0.074±0.007 0.092±0.009 0.063±0.006 0.112±0.011 0.039±0.004 0.112±0.011	21.79 3.614 0.8000
120 K	Fe-N Fe-N Fe-C Fe-C Fe-S Fe-C	4.0 2.0 6.5±0.7 8.6±0.9 2.0 15.2±1.5	1.940±0.019 2.115±0.021 2.835±0.028 4.337±0.043 4.858±0.049 4.845±0.048	0.077±0.008 0.087±0.009 0.071±0.007 0.112±0.011 0.032±0.003 0.059±0.006	23.08 3.348 0.8000
130 K	Fe-N Fe-N Fe-C Fe-C Fe-S Fe-C	4.0 2.0 6.8±0.7 8.4±0.8 2.0 18.4±1.8	1.944±0.019 2.108±0.021 2.828±0.028 4.344±0.043 4.914±0.049 4.846±0.048	0.081±0.008 0.112±0.011 0.074±0.007 0.112±0.011 0.032±0.003 0.105±0.011	22.15 3.692 0.8000
140 K	Fe-N Fe-N Fe-C Fe-C Fe-S Fe-C	4.0 2.0 6.7±0.7 7.6±0.8 2.0 13.1±1.3	1.944±0.019 2.098±0.021 2.827±0.028 4.312±0.043 4.735±0.047 4.797±0.048	0.087±0.009 0.110±0.011 0.077±0.008 0.112±0.011 0.095±0.010 0.032±0.003	22.26 4.124 0.8000
150 K	Fe-N Fe-N Fe-C Fe-C Fe-S Fe-C	4.0 2.0 6.9±0.7 7.2±0.7 2.0 19.6±2.0	1.948±0.019 2.126±0.021 2.831±0.028 4.362±0.044 4.909±0.049 4.847±0.048	0.089±0.009 0.112±0.011 0.084±0.008 0.112±0.011 0.045±0.005 0.112±0.011	23.77 3.899 0.8000
160 K	Fe-N Fe-N Fe-C Fe-C Fe-S Fe-C	4.0 2.0 7.2±0.7 5.7±0.6 2.0 12.6±1.3	1.953±0.020 2.133±0.021 2.836±0.028 4.374±0.044 4.849±0.048 4.817±0.048	0.092±0.009 0.110±0.011 0.097±0.010 0.112±0.011 0.112±0.011 0.055±0.006	23.83 4.397 0.8000
170 K	Fe-N Fe-N Fe-C Fe-C Fe-S Fe-C	4.0 2.0 7.3±0.7 6.0±0.6 2.0 17.7±1.8	1.965±0.020 2.161±0.022 2.847±0.028 4.420±0.044 4.923±0.049 4.852±0.049	0.100±0.010 0.112±0.011 0.107±0.011 0.112±0.011 0.050±0.005 0.112±0.011	24.75 4.169 0.8000

Sample	Abs-Bs [a]	N(Bs) [b]	R(Abs-Bs) [c] / Å	σ [d] / Å^{-1}	R [e] / % E_f [f] / eV Afac [g]
180 K	Fe-N Fe-N Fe-C Fe-C Fe-S Fe-C	4.0 2.0 6.7±0.7 8.8±0.9 2.0 20.4±2.0	1.981±0.020 2.182±0.022 2.877±0.029 4.445±0.045 4.906±0.049 4.834±0.048	0.112±0.011 0.112±0.011 0.112±0.011 0.112±0.011 0.102±0.010 0.112±0.011	26.98 4.373 0.8000
190 K	Fe-N Fe-N Fe-C Fe-C Fe-S Fe-C	4.0 2.0 6.6±0.7 9.6±1.0 2.0 18.5±1.9	2.004±0.020 2.222±0.022 2.901±0.029 4.468±0.045 4.747±0.047 4.813±0.048	0.112±0.011 0.110±0.011 0.112±0.011 0.112±0.011 0.032±0.003 0.059±0.006	31.27 4.795 0.8000
200 K	Fe-N Fe-N Fe-C Fe-C Fe-S Fe-C	4.0 2.0 6.4±0.6 8.6±0.9 2.0 15.8±1.6	2.061±0.021 2.269±0.023 2.974±0.030 4.507±0.045 4.786±0.048 4.847±0.048	0.112±0.011 0.110±0.011 0.112±0.011 0.105±0.011 0.032±0.003 0.050±0.005	26.42 2.893 0.8000
210 K	Fe-N Fe-N Fe-C Fe-C Fe-S Fe-C	4.0 2.0 6.2±0.6 9.4±0.9 2.0 20.1±2.0	2.080±0.021 2.283±0.023 3.004±0.030 4.490±0.045 4.760±0.048 4.831±0.048	0.112±0.011 0.100±0.010 0.097±0.010 0.089±0.009 0.032±0.003 0.081±0.008	27.26 2.574 0.8000
220 K	Fe-N Fe-N Fe-C Fe-C Fe-S Fe-C	4.0 2.0 5.2±0.5 13.9±1.4 2.0 19.1±1.9	2.091±0.021 2.297±0.023 3.008±0.030 4.520±0.045 4.777±0.048 4.841±0.048	0.092±0.009 0.067±0.007 0.074±0.007 0.112±0.011 0.032±0.003 0.067±0.007	24.71 2.821 0.8000
230 K	Fe-N Fe-N Fe-C Fe-C Fe-S Fe-C	4.0 2.0 5.6±0.6 15.9±1.6 2.0 19.5±2.0	2.093±0.021 2.297±0.023 3.006±0.030 4.532±0.045 4.795±0.048 4.851±0.049	0.089±0.009 0.067±0.007 0.077±0.008 0.112±0.011 0.032±0.003 0.059±0.006	23.43 3.181 0.8000
240 K	Fe-N Fe-N Fe-C Fe-C Fe-S Fe-C	4.0 2.0 5.5±0.6 10.9±1.1 2.0 19.3±1.9	2.104±0.021 2.310±0.023 3.014±0.030 4.515±0.045 4.775±0.048 4.840±0.048	0.084±0.008 0.063±0.006 0.071±0.007 0.092±0.009 0.032±0.003 0.074±0.007	22.81 2.782 0.8000
250 K	Fe-N Fe-N Fe-C Fe-C Fe-S Fe-C	4.0 2.0 5.8±0.6 8.1±0.8 2.0 25.0±2.5	2.106±0.021 2.310±0.023 3.017±0.030 4.459±0.045 4.734±0.047 4.793±0.048	0.084±0.008 0.063±0.006 0.077±0.008 0.045±0.005 0.032±0.003 0.112±0.011	24.90 3.069 0.8000

Sample	Abs-Bs [a]	N(Bs) [b]	R(Abs-Bs) [c] / Å	σ [d] / Å^{-1}	R [e] / % E_f [f] / eV Afac [g]
260 K	Fe-N Fe-N Fe-C Fe-C Fe-S Fe-C	4.0 2.0 5.9±0.6 14.4±1.4 2.0 23.4±2.3	2.100±0.021 2.302±0.023 3.009±0.030 4.499±0.045 4.752±0.048 4.818±0.048	0.081±0.008 0.063±0.006 0.074±0.007 0.095±0.010 0.032±0.003 0.087±0.009	23.36 3.564 0.8000
293 K	Fe-N Fe-N Fe-C Fe-C Fe-S Fe-C	4.0 2.0 6.7±0.7 13.7±1.4 2.0 19.6±2.0	2.112±0.021 2.322±0.023 3.017±0.030 4.530±0.045 4.785±0.048 4.850±0.049	0.077±0.008 0.063±0.007 0.087±0.009 0.100±0.010 0.032±0.003 0.077±0.008	29.61 3.030 0.8000

a) Abs=X-ray absorbing atom, Bs=backscattering atom, b) number of backscattering atoms, c) distance of absorbing atom to backscattering atom, d) Debye-Waller-like factor, e) fit-index, f) Fermi energy, that accounts for the shift between theory and experiment, g) amplitude reducing factor

Since the structural changes during the SCO process, especially the elongation of the bond lengths between the central iron atom and the equatorial and axial nitrogen atoms, is the most important information that can be obtained by the analysis of the EXFAS spectra, the Fe-N distances are displayed in Table 10. Additionally, the HS fractions calculated from the Fe-N distances according to equation (22) are shown.

Table 10: Fit Model 2C: Fe-N distances of the axial and equatorial nitrogen atoms obtained by EXAFS analysis and thereof calculated γ_{HS} values.

T / K	R_{eq}(Abs-Bs) / Å	$\gamma_{HS}(R_{eq})$ a)	R_{ax}(Abs-Bs) / Å	$\gamma_{HS}(R_{ax})$ a)
10	1.938±0.019	0.000	2.097±0.021	-0.044
30	1.937±0.019	-0.006	2.113±0.021	0.034
40	1.935±0.019	-0.018	2.104±0.021	-0.010
50	1.940±0.019	0.012	2.123±0.021	0.083
70	1.933±0.019	-0.030	2.097±0.021	-0.044
80	1.930±0.019	-0.048	2.096±0.021	-0.049
90	1.934±0.019	-0.024	2.099±0.021	-0.034
100	1.933±0.019	-0.030	2.112±0.021	0.029
110	1.938±0.019	0.000	2.110±0.021	0.020
120	1.940±0.019	0.012	2.115±0.021	0.044
130	1.944±0.019	0.036	2.108±0.021	0.010
140	1.944±0.019	0.036	2.098±0.021	-0.039
150	1.948±0.019	0.060	2.126±0.021	0.098
160	1.953±0.020	0.089	2.133±0.021	0.132
170	1.965±0.020	0.161	2.161±0.022	0.268
180	1.981±0.020	0.256	2.182±0.022	0.371
190	2.004±0.020	0.393	2.222±0.022	0.566
200	2.061±0.021	0.732	2.269±0.023	0.795
210	2.080±0.021	0.845	2.283±0.023	0.863
220	2.091±0.021	0.911	2.297±0.023	0.932
230	2.093±0.021	0.923	2.297±0.023	0.932
240	2.104±0.021	0.988	2.310±0.023	0.995
250	2.106±0.021	1.000	2.310±0.023	0.995
260	2.100±0.021	0.964	2.302±0.023	0.956
293	2.112±0.021	1.036	2.322±0.023	1.054

a) HS fraction calculated according to $\gamma_{HS} = (R_T - R_{LS})/(R_{HS} - R_{LS})$.[84] Applied procedure is described in section 2.3.1.1.

As shown in Table 10, the equatorial Fe-N bond lengths change from 1.938 Å to 2.112 Å, while the axial distances change from 2.097 Å to 2.322 Å. To correlate the Fe-N bond lengths with temperature the distances were plotted as a function of temperature. The plots show again a gradual increase and therefore a fit with a sigmoidal Boltzmann function was carried out in both cases.

The fit of the equatorial Fe-N bond lengths results in a spin transition temperature of $T_{1/2}$(eq) = 191.6 ± 1.1 K (cf. Appendix, Figure A.5), while the fit of the axial distances leads to a spin transition temperature of $T_{1/2}$(ax) = 185.3 ±1.4 K (cf. Appendix, Figure A.6). Comparison of the magnetization curve obtained by SQUID magnetometry and the fits of the Fe-N distances illustrates that the structural changes do not follow the magnetization exactly and therefore cannot be clearly correlated with the magnetic changes (Figure 2.22). In general, the changes of both distances show nearly the same gradual behaviour, but the fit of the axial Fe-N distances diverges from the magnetization curve. The bonds start to elongate at lower temperatures than the magnetization and therefore the transition temperature is shifted to lower temperatures by around 7 K compared to the SQUID data. The fit of the equatorial bond lengths shows only negligible differences compared to the magnetization curve, so that the transition temperature is essentially the same within tolerance in both cases.

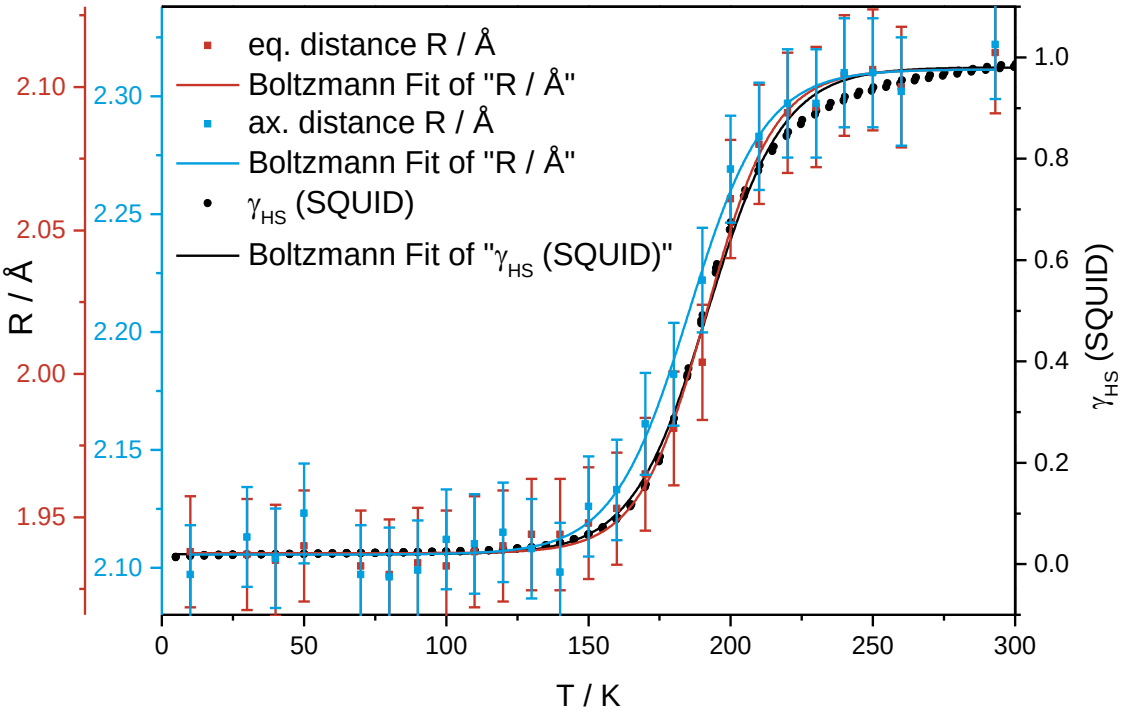

Figure 2.22: Fit Model 2C: Comparison of HS fraction obtained by SQUID measurements and fits of the equatorial (red) and axial (blue) Fe-N distances.

As in Fit Model 2A, where the Fe-N distances were also iterated freely, it can be assumed again, that the changes of the axial bonds do not affect the magnetization of the system, since the HS fraction rather follows the changes of the equatorial Fe-N bonds than the axial ones. Furthermore, the fits of the Fe-N distances obtained by EXAFS indicate, that the axial bonds start to change at lower temperature than the equatorial ones.
But comparison with the Fe-N distances from the temperature-dependent crystal structures reveals certain differences. According to an isotropic SCO behaviour as proposed for this complex,[172] all distances change in nearly the same temperature range as can be seen in Figure 2.23. Contrary to the EXAFS results, the fits of both distances, axial as well as equatorial, result in transition temperatures, which are slightly shifted to lower temperatures compared to the SQUID data ($T_{1/2}$(eq) = 187.7 ± 0.6 K, $T_{1/2}$(ax) = 188.6 ± 1.0 K, $T_{1/2}$(SQUID) = 192.0 ± 0.2 K). In addition, the fit of the equatorial distances changes in a more abrupt way than that of the axial bonds and so the HS distance is reached at lower temperature. But as in the case of the EXAFS data, the error bars of both shells are overlapping, therefore the significance of these findings has to be questioned. Especially in the temperature range from 190 K to 220 K, where the difference between the curve shape of the axial and equatorial distances shows the most pronounced differences, the error is quite high.

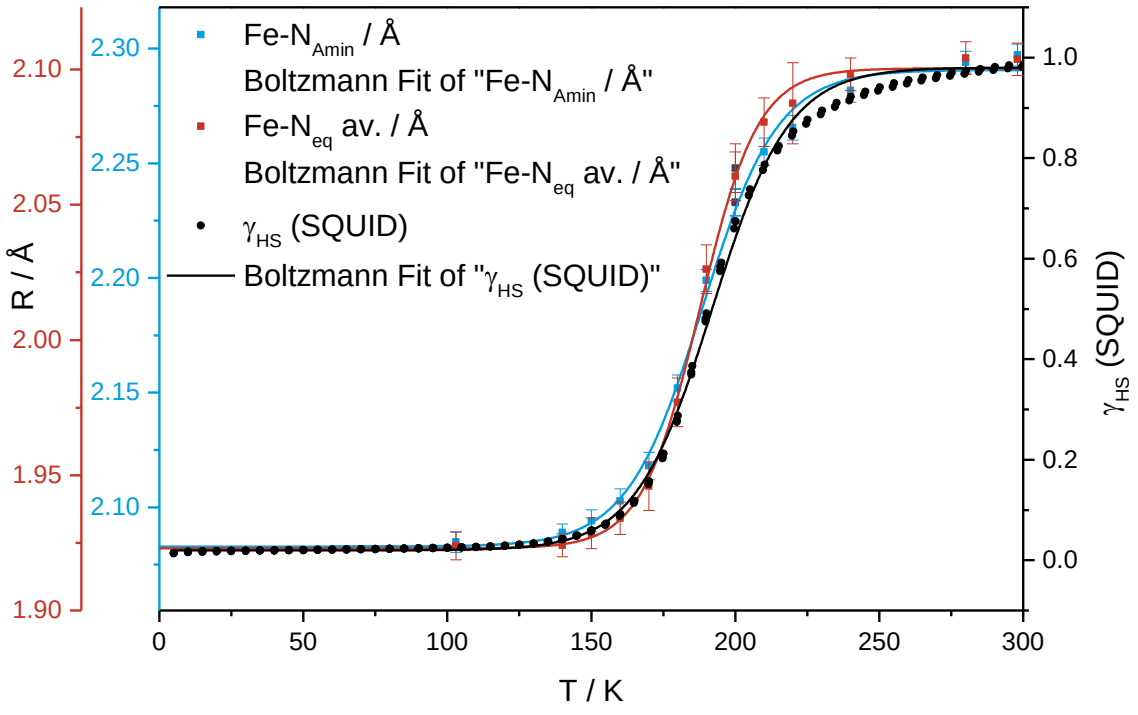

Figure 2.23: Comparison of HS fraction obtained by SQUID measurements and fits of the equatorial (red) and axial (blue) Fe-N distances obtained by temperature-dependent X-ray crystallography.

For a direct comparison with the HS fractions obtained by SQUID magnetometry, the equatorial and axial Fe-N distances obtained by this fit model were converted to HS fractions as well. According to the procedure described in chapter 2.3.1.1, the limits of the Boltzmann fits were determined and used as approximations for the pure LS and HS distances. For the calculation of $\gamma_{HS}(R_{eq})$ and $\gamma_{HS}(R_{ax})$, these values were inserted into equation (22). The fit limits of the equatorial bonds were identified as $A_1(eq) = R_{eq,LS} = 1.938 \pm 0.002$ Å and $A_2(eq) = R_{eq,HS} = 2.106 \pm 0.003$ Å, while in the axial case the LS distance was determined as $A_1(ax) = R_{ax,LS} = 2.106 \pm 0.003$ Å and the HS distance as $A_2(ax) = R_{ax,HS} = 2.311 \pm 0.004$ Å. The calculated HS fractions are listed in Table 10 and Figure 2.24 shows the comparison of the HS fractions obtained by EXAFS and SQUID magnetometry plotted versus temperature. Due to the direct correlation between the Fe-N distances and the $\gamma_{HS}(R_{eq})$ and $\gamma_{HS}(R_{ax})$ values, the fits of the HS fractions show the same course and therefore the same transition temperatures like the plots of the bond lengths. As already discussed in the previous models, the absolute values of the LS and HS are sligthly distorted due to a remaining small number of HS respective LS centres, but the overall agreement with the SQUID data is quite good.

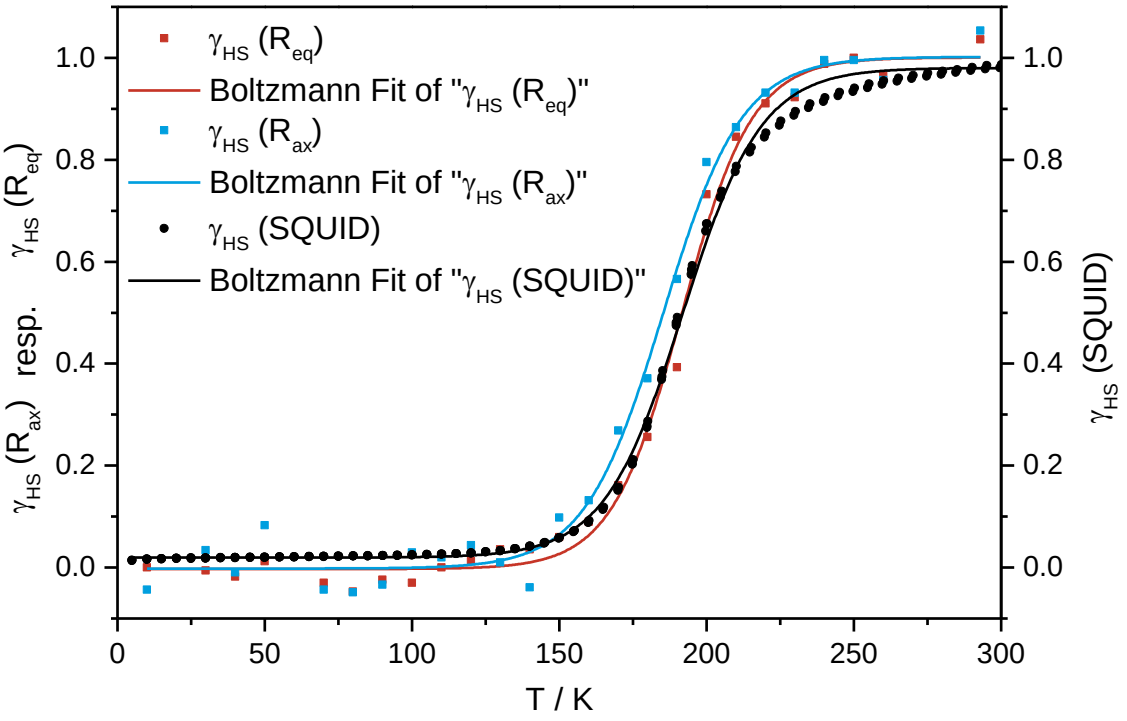

Figure 2.24: Fit model 2C: Comparison of HS fractions obtained by SQUID (black) and EXAFS measurements (red and blue).

Additionally, the Debye-Waller-like factors were plotted versus temperature to obtain a correlation of the thermal and structural disorder in the system within the SCO process with rising temperature. Figure 2.25 shows the Debye-Waller-like factor of the equatorial nitrogen shell which stays more or less constant up to around 120 K. With rising temperatures, it starts to increase until it reaches a maximum (0.112 $Å^{-1}$) in the temperature range from 180 – 210 K. With further increasing temperature σ_{eq} decreases again. The Debye-Waller-like factor of the axial nitrogen shell varies between 0.077 $Å^{-1}$ and 0.095 $Å^{-1}$ in the temperature range from 10 K to 120 K (Figure 2.26). Further rise of temperature leads to a maximum of σ_{ax} of 0.112 $Å^{-1}$ (130 - 200 K) and then it is decreasing again. Both parameters were fitted with a Gaussian function to obtain the temperatures of the maxima. In case of the equatorial Debye-Waller-like factor, the maximum is determined at T(eq) = 192.0 ± 1.8 K, which is in perfect agreement with $T_{1/2}$(SQUID) = 192.0 ± 0.2 K and also in very good agreement with the transition temperature, which was determined by the changes of the equatorial Fe-N distances $T_{1/2}$(eq) = 191.6 ± 1.1 K. Unfortunately, the data points in the axial case do not show such a nice peak structure like in the equatorial case, indicating a higher disorder. Therefore, the quality of the fit is less good. The fit results in a maximum at T(ax) = 160.6 ± 5.9 K and with a shift of around 32 K to lower temperatures it is far off the transition temperature obtained by SQUID magnetometry.

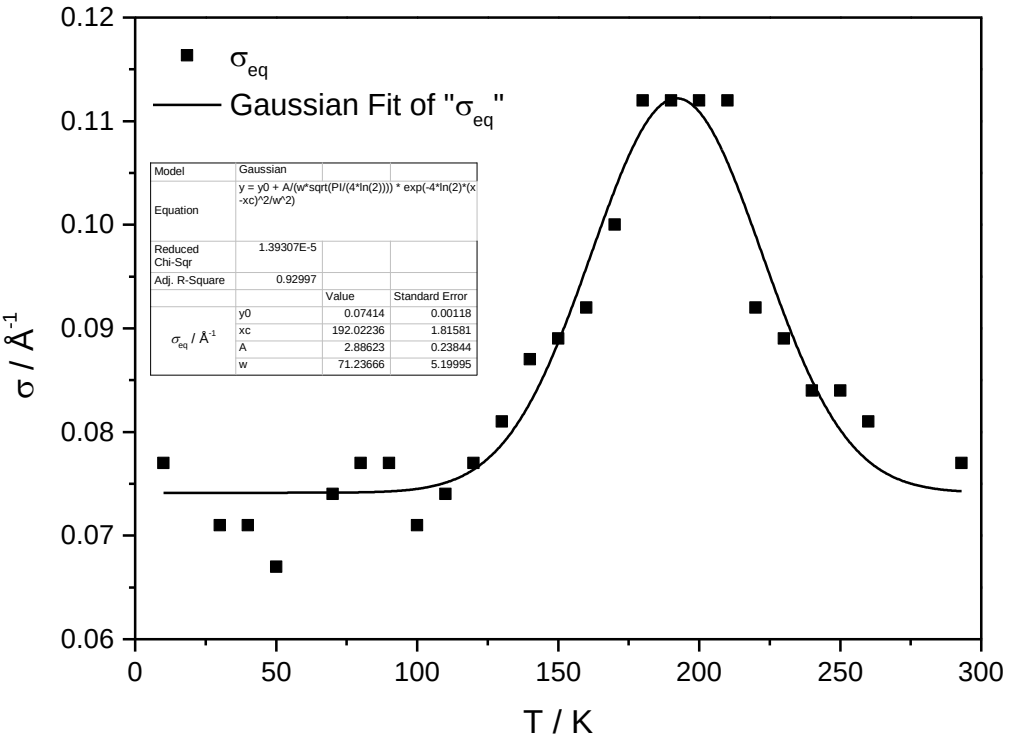

Figure 2.25: Fit Model 2C: Plot of Debye-Waller like factor σ_{eq} of the equatorial nitrogen shell vs. temperature.

Compared to the transition temperature resulting from the fit of the axial Fe-N distances it is shifted by around 25 K to lower temperatures. As a consequence, it can be concluded that the parameters of the equatorial nitrogen shell, Fe-N distance as well as Debye-Waller-like factor, can be used as a good indicator for the transition temperature, whereas the fits of the axial parameters show significant deviations compared to the magnetization.

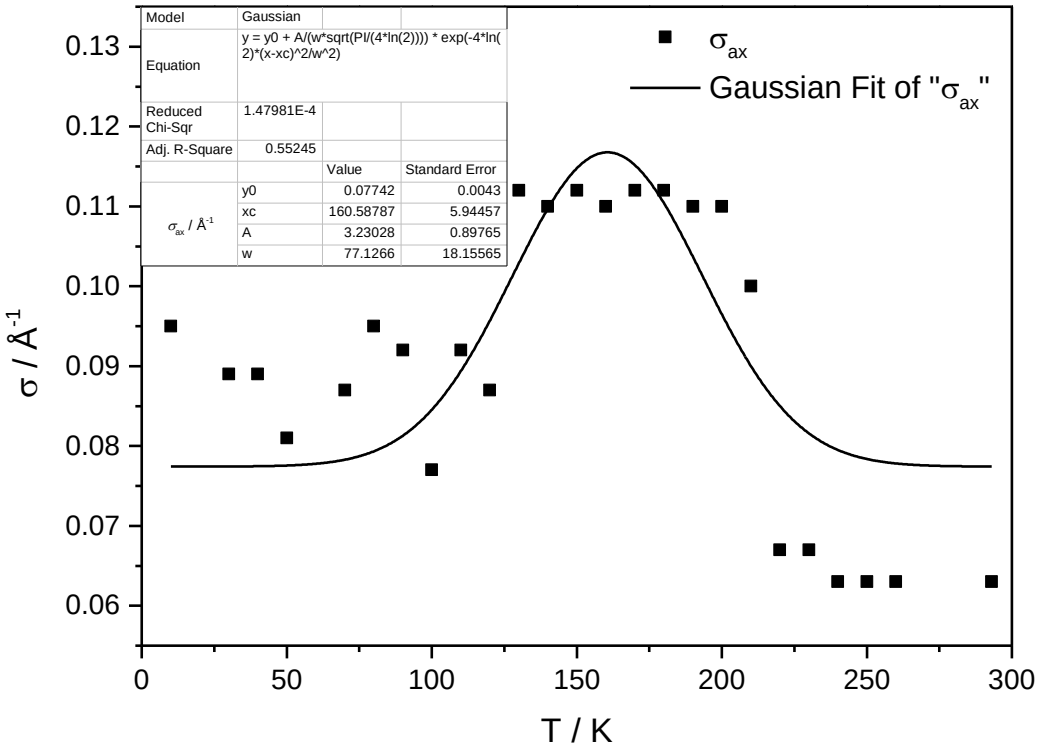

Figure 2.26: Fit Model 2C: Plot of Debye-Waller like factor σ_{ax} of the axial nitrogen shell vs. temperature..

To sum up the outcomes of the third fit model with two nitrogen shells, which is based on temperature-dependent crystal structure data, it can be said, that the changes of the Fe-N bond lengths and the thereof calculated HS fractions are in nice agreement with the changes of the magnetization within the error bar. Especially, the equatorial changes can be clearly correlated with the changes of the magnetization, whereas the axial bonds start to change at slightly lower temperature than the changes of the magnetization, represented by the shift of the transition curve to lower temperatures. Even though the error bars of both fit curves are overlapping, these observations strengthen the assumption already discussed for Fit Model 2A: Only the changes of the equatorial Fe-N bonds seem to affect the magnetization, whereas the changes of the axial distances seem to have no effect on the magnetization. Additionally, the temperature dependence of the equatorial Debye-Waller-like factor results in a peak structure leading to a maximum that is perfectly

matching the transition temperature of the SQUID data, thus this parameter seems to be a promising tool for the determination of the transition temperature. In case of the axial Debye-Waller-like factor, the data points are spread a bit more, so the quality of the fit is less good and the results less meaningful.

2.3.3 Fit Models with two Nitrogen Shells, Fourier filtered Data

Due to the low signal to noise ratio of the data and the insignificance of the carbon and sulphur shells at around 4 Å for the SCO process, the data were Fourier filtered in the range from 0 to 3.5 Å. Therefore, fit models with two nitrogen shells and only one carbon shell were applied. Two different fits were carried out where different parameters were held fix. The initial Fe-N distances were based on temperature-dependent crystal structure data (cf. Table 7).

2.3.3.1 Fit Model 2D: Fit of Fourier filtered Data with two Nitrogen Shells, Fe-N distances fixed at values from temperature-dependent Crystal Structures and afac at 0.8000

In the first model with two nitrogen shells and Fourier filtered data, the coordination numbers of the two nitrogen shells were held fix at four (equatorial) and two (axial), the Fe-N distances were held fix at the distances obtained by the temperature-dependent crystal structure data (cf. Table 7) and the amplitude reducing factor was fixed at 0.8000. The Fe-C distance, the coordination number of the carbon shell, the Fermi energy E_f and the Debye-Waller-like factors of all shells were iterated freely.
The temperature-dependent EXAFS spectra with the resulting fit functions are displayed in k-space (top) and R-space (bottom) in Figure 2.27. Temperature increases from bottom (10 K) to top (293 K). The blue spectrum depicts the spin transition temperature (190 K) and therefore the spectra above can be assigned to the HS state and the spectra below to the LS state. The fit functions reproduce the experimental spectra quite well, except of the spectrum of the transition temperature, since the experimental spectrum in R-space shows two signals between 2.5 Å and 3.0 Å, whereas the theoretical fit function shows only one signal.

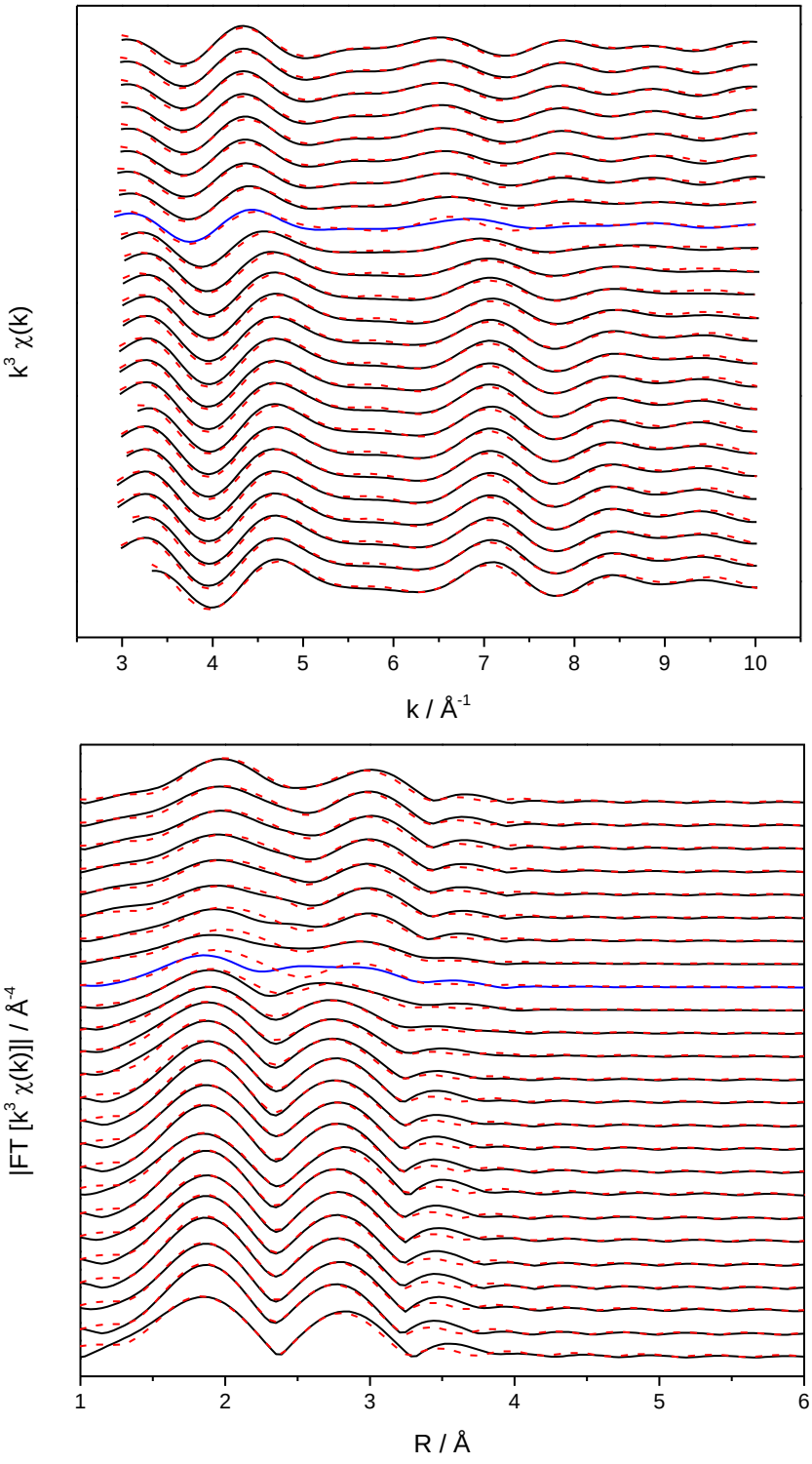

Figure 2.27: Fit Model 2D: Temperature-dependent EXAFS spectra of [Fe(L-N_4Bn_2)$(NCS)_2$], blue spectrum: spin transition temperature (190 K), top: χ(k), bottom: Fourier transformation, (—) experimental data, (---) theoretical data.

The fitting results of the temperature-dependent EXAFS analysis are shown in Table 11 as an overview.

Table 11: Fit Model 2D: Neighbour atoms, coordination numbers and distances obtained by EXAFS analysis.

Sample	Abs-Bs [a]	N(Bs) [b]	R(Abs-Bs) [c] / Å	σ [d] / Å^{-1}	R [e] / % E_f [f] / eV Afac [g]
10 K	Fe-N Fe-N Fe-C	4.0 2.0 6.3±0.6	1.924 2.085 2.823±0.028	0.074±0.007 0.074±0.007 0.063±0.006	21.93 3.787 0.8000
30 K	Fe-N Fe-N Fe-C	4.0 2.0 7.9±0.8	1.924 2.085 2.829±0.028	0.074±0.007 0.077±0.008 0.081±0.008	18.41 3.268 0.8000
40 K	Fe-N Fe-N Fe-C	4.0 2.0 7.7±0.8	1.924 2.085 2.828±0.028	0.074±0.007 0.074±0.007 0.077±0.008	19.04 3.322 0.8000
50 K	Fe-N Fe-N Fe-C	4.0 2.0 7.7±0.8	1.924 2.085 2.832±0.028	0.071±0.007 0.071±0.007 0.074±0.007	19.41 3.083 0.8000
70 K	Fe-N Fe-N Fe-C	4.0 2.0 7.9±0.8	1.924 2.085 2.833±0.028	0.074±0.007 0.074±0.007 0.077±0.008	19.74 3.051 0.8000
80 K	Fe-N Fe-N Fe-C	4.0 2.0 8.0±0.8	1.924 2.085 2.833±0.028	0.074±0.007 0.071±0.007 0.081±0.008	18.92 3.189 0.8000
90 K	Fe-N Fe-N Fe-C	4.0 2.0 8.0±0.8	1.924 2.085 2.831±0.028	0.077±0.008 0.074±0.007 0.081±0.008	19.21 3.322 0.8000
100 K	Fe-N Fe-N Fe-C	4.0 2.0 7.1±0.7	1.924 2.085 2.831±0.028	0.077±0.008 0.081±0.008 0.074±0.007	21.79 3.492 0.8000
110 K	Fe-N Fe-N Fe-C	4.0 2.0 7.7±0.8	1.924 2.085 2.832±0.028	0.077±0.008 0.074±0.007 0.081±0.008	19.50 3.417 0.8000
120 K	Fe-N Fe-N Fe-C	4.0 2.0 7.8±0.8	1.924 2.085 2.834±0.028	0.081±0.008 0.074±0.007 0.084±0.008	20.60 3.404 0.8000
130 K	Fe-N Fe-N Fe-C	4.0 2.0 7.9±0.8	1.924 2.085 2.828±0.028	0.081±0.008 0.077±0.008 0.087±0.009	21.10 3.609 0.8000
140 K	Fe-N Fe-N Fe-C	4.0 2.0 7.4±0.7	1.924 2.089 2.828±0.028	0.081±0.008 0.077±0.008 0.084±0.008	21.52 3.803 0.8000
150 K	Fe-N Fe-N Fe-C	4.0 2.0 7.1±0.7	1.929 2.094 2.820±0.028	0.089±0.009 0.092±0.009 0.089±0.009	24.42 4.912 0.8000
160 K	Fe-N Fe-N Fe-C	4.0 2.0 7.2±0.7	1.934 2.103 2.826±0.028	0.092±0.009 0.095±0.010 0.097±0.010	25.61 5.274 0.8000
170 K	Fe-N Fe-N Fe-C	4.0 2.0 7.4±0.7	1.946 2.118 2.833±0.028	0.105±0.011 0.112±0.011 0.107±0.011	24.90 5.326 0.8000

Sample	Abs-Bs [a]	N(Bs) [b]	R(Abs-Bs) [c] / Å	σ [d] / Å^{-1}	R [e] / % E_f [f] / eV Afac [g]
180 K	Fe-N Fe-N Fe-C	4.0 2.0 6.5±0.7	1.977 2.152 2.869±0.029	0.110±0.011 0.112±0.011 0.112±0.011	29.07 4.674 0.8000
190 K	Fe-N Fe-N Fe-C	4.0 2.0 6.2±0.6	2.026 2.199 2.991±0.030	0.112±0.011 0.105±0.011 0.112±0.011	44.05 2.233 0.8000
200 K	Fe-N Fe-N Fe-C	4.0 2.0 5.9±0.6	2.060 2.233 2.979±0.030	0.112±0.011 0.102±0.010 0.112±0.011	31.25 2.828 0.8000
210 K	Fe-N Fe-N Fe-C	4.0 2.0 5.5±0.6	2.081 2.255 3.003±0.030	0.112±0.011 0.105±0.011 0.092±0.009	28.91 2.606 0.8000
220 K	Fe-N Fe-N Fe-C	4.0 2.0 5.3±0.5	2.088 2.266 3.006±0.030	0.110±0.011 0.095±0.010 0.081±0.008	23.97 3.129 0.8000
230 K	Fe-N Fe-N Fe-C	4.0 2.0 5.7±0.6	2.088 2.266 3.003±0.030	0.105±0.010 0.092±0.009 0.084±0.008	22.17 3.546 0.8000
240 K	Fe-N Fe-N Fe-C	4.0 2.0 5.6±0.6	2.098 2.282 3.012±0.030	0.097±0.010 0.084±0.008 0.077±0.008	21.24 3.252 0.8000
250 K	Fe-N Fe-N Fe-C	4.0 2.0 5.9±0.6	2.098 2.282 3.015±0.030	0.095±0.010 0.081±0.008 0.081±0.008	3.497 0.8000 22.04
260 K	Fe-N Fe-N Fe-C	4.0 2.0 5.9±0.6	2.098 2.282 3.008±0.030	0.092±0.009 0.084±0.008 0.077±0.008	21.02 3.717 0.8000
293 K	Fe-N Fe-N Fe-C	4.0 2.0 6.8±0.7	2.104 2.297 3.010±0.030	0.084±0.008 0.077±0.008 0.092±0.009	19.84 3.570 0.8000

a) Abs=X-ray absorbing atom, Bs=backscattering atom, b) number of backscattering atoms, c) distance of absorbing atom to backscattering atom, d) Debye-Waller-like factor, e) fit-index, f) Fermi energy, that accounts for the shift between theory and experiment, g) amplitude reducing factor

Since all parameters, except of the Debye-Waller-like factors, were held fix in this fit model, only these parameters can be correlated with the temperature-dependent SCO behaviour. Therefore, the Debye-Waller-like factor of the equatorial and the axial nitrogen shell were plotted as function of temperature and a Gaussian fit was applied.
In Figure 2.28 the Debye-Waller-like factor of the equatorial nitrogen shell is plotted versus temperature. As in the fit models shown before, σ_{eq} shows only small variations in the temperature region from 10 K to 140 K (σ_{eq} = 0.071 – 0.081 Å^{-1}). With increasing temperature, σ_{eq} reaches a maximum of 0.112 Å^{-1} at 190 – 210 K and then drops again. The maximum of the Gaussian fit function is determined at T(eq) = 204.3 ± 1.5 K. Compared to the SQUID transition temperature, it is shifted by around 12 K to higher temperatures.
The plot of the axial Debye-Waller-like factor is shown in Figure 2.29. The overall trend of the temperature dependency of the parameter is very similar to the equatorial Debye-Waller-like factor. It stays more or less constant in the low temperature region (10 – 140 K), increases to a maximum of 0.112 Å^{-1} at 170 K and 180 K and decreases again at higher temperatures. In the axial case, the maximum of the Gaussian fit is located at T(ax) = 189.8 ± 2.2 K, showing a shift of around 2 K to lower temperatures compared to the transition temperature received by SQUID magnetometry.

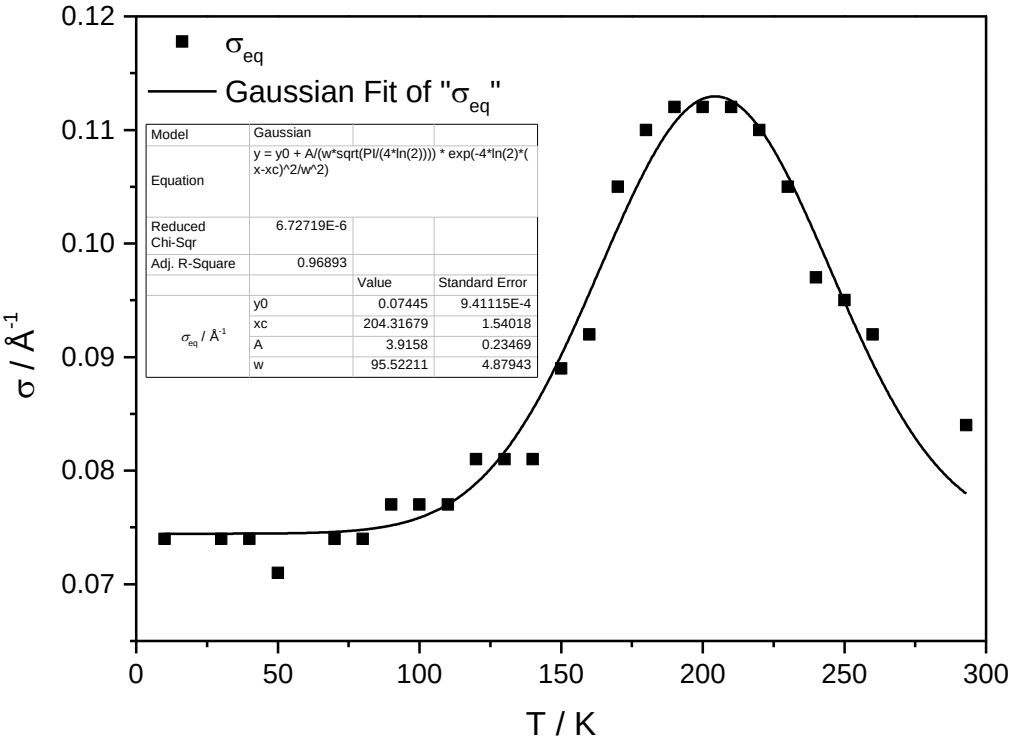

Figure 2.28: Fit Model 2D: Plot of Debye-Waller like factor σ_{eq} of the equatorial nitrogen shell vs. temperature.

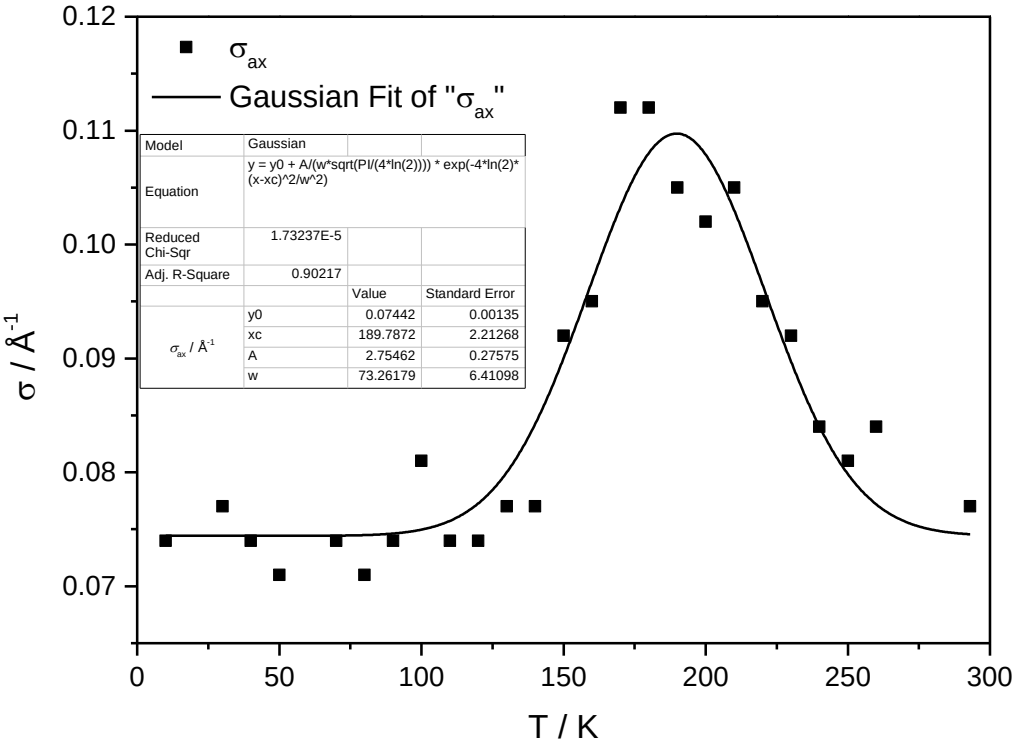

Figure 2.29: Fit Model 2D: Plot of Debye-Waller like factor σ_{ax} of the axial nitrogen shell vs. temperature.

In summary it can be said, that the first fit model with Fourier filtered data, two nitrogen shells and fixed Fe-N distances gives quite good fit results, which are comparable to the equivalent fit model with unfiltered data (Fit Model 2B). The experimental spectra are reproduced with a good fit quality, only the spectrum at 190 K cannot be reproduced satisfactorily, since there is a discrepancy between the number of experimental and fitted signals. The temperature dependence of the Debye-Waller-like factors shows a peak structure in case of the axial and equatorial nitrogen shell and the applied Gaussian fits can give an indication of the temperature range of the SCO process, since in this range the disorder in the system increases due to a supposed mixture of LS and HS centres. Comparison of the temperatures of the fit maxima of Fit Model 2B and the actual model reveals, that for both models the temperature of the equatorial shell is shifted by about 10 K to higher temperatures compared to the transition temperature by SQUID. In case of the axial shell, the temperature is shifted by 2 K to lower values in case of the actual model, whereas it is shifted by around 3 K to higher values in case of Fit Model 2B. Therefore, it seems that a precise determination of the transition temperature with use of the fit maxima of the Debye-Waller-like factors is actually not possible with the fit models with fixed Fe-N distances, since the determined temperatures show a rather large variation and no clear trend concerning the shift to lower or higher temperatures is observable.

2.3.3.2 Fit Model 2E: Fit of Fourier filtered Data with two Nitrogen Shells, Fe-N distances iterated based on values from temperature-dependent Crystal Structures and afac at 0.8000

In the second fit model with Fourier filtered data and two nitrogen shells only the coordination numbers of the two nitrogen shells (4 + 2) and the amplitude reducing factor (0.8000) were held fix. The Fe-N distances were based on the temperature-dependent crystal structure data (Table 7) and iterated freely, as well as the Fe-C distance, the coordination number of the carbon shell, the Debye-Waller-like factors of all shells and the Fermi energy E_f.

Figure 2.30 shows the temperature-dependent EXAFS spectra and the theoretical fit functions in k-space (top) and R-space (bottom). The blue spectrum is assigned to the spin transition temperature (190 K) again, the spectra above the blue one to a predominant HS state and the spectra below to a predominant LS state. Like in the other fit models, the fits reproduce the experimental spectra really well, except of the spectrum at 190 K. Once more, the experimental spectrum shows two signals between 2.5 Å and 3.0 Å, while the theoretical fit function gives only one signal at around 3.0 Å.

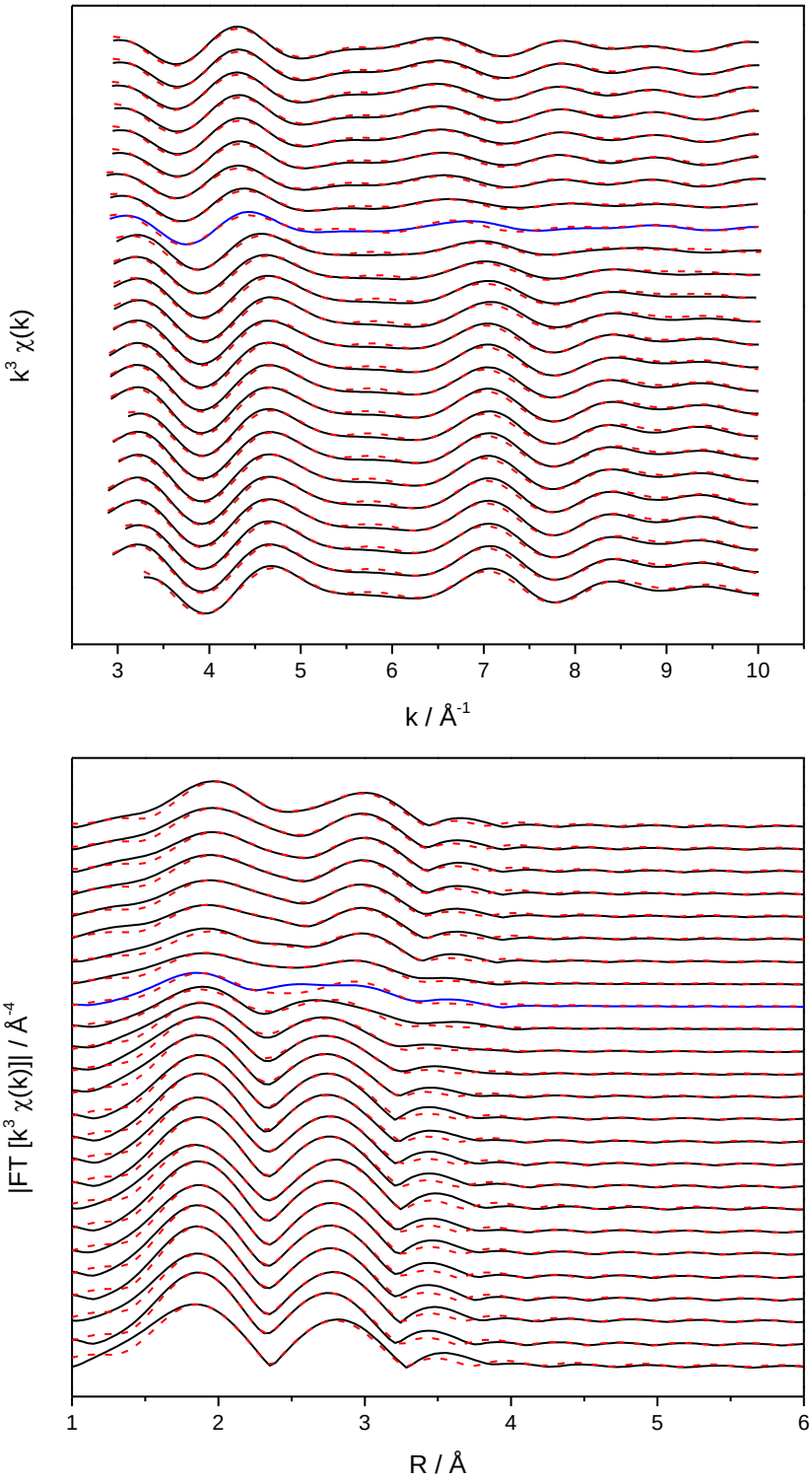

Figure 2.30: Fit Model 2E: Temperature-dependent EXAFS spectra of $[Fe(L\text{-}N_4Bn_2)(NCS)_2]$, blue spectrum: spin transition temperature (190 K), top: χ(k), bottom: Fourier transformation, (—) experimental data, (---) theoretical data.

The fit results of the temperature-dependent EXAFS spectra are shown in Table 12 as an overview.

Table 12: Fit Model 2E: Neighbour atoms, coordination numbers and distances obtained by EXAFS analysis.

Sample	Abs-Bs [a]	N(Bs) [b]	R(Abs-Bs) [c] / Å	σ [d] / Å^{-1}	R [e] / % E_f [f] / eV Afac [g]
10 K	Fe-N Fe-N Fe-C	4.0 2.0 6.0±0.6	1.947±0.019 2.113±0.021 2.832±0.028	0.081±0.008 0.112±0.011 0.059±0.006	20.61 2.731 0.8000
30 K	Fe-N Fe-N Fe-C	4.0 2.0 7.4±0.7	1.944±0.019 2.114±0.021 2.838±0.028	0.077±0.008 0.102±0.010 0.074±0.007	16.12 2.279 0.8000
40 K	Fe-N Fe-N Fe-C	4.0 2.0 7.0±0.7	1.949±0.019 2.128±0.021 2.840±0.028	0.077±0.008 0.102±0.010 0.071±0.007	16.62 2.004 0.8000
50 K	Fe-N Fe-N Fe-C	4.0 2.0 7.0±0.7	1.946±0.019 2.126±0.021 2.843±0.028	0.074±0.007 0.089±0.009 0.067±0.007	15.99 1.807 0.8000
70 K	Fe-N Fe-N Fe-C	4.0 2.0 7.2±0.7	1.946±0.019 2.119±0.021 2.843±0.028	0.077±0.008 0.097±0.010 0.071±0.007	16.98 1.955 0.8000
80 K	Fe-N Fe-N Fe-C	4.0 2.0 7.5±0.8	1.947±0.019 2.109±0.021 2.842±0.028	0.081±0.008 0.107±0.011 0.074±0.007	16.72 2.217 0.8000
90 K	Fe-N Fe-N Fe-C	4.0 2.0 7.6±0.8	1.945±0.019 2.109±0.021 2.840±0.028	0.081±0.008 0.107±0.010 0.077±0.008	17.07 2.395 0.8000
100 K	Fe-N Fe-N Fe-C	4.0 2.0 6.6±0.7	1.945±0.019 2.132±0.021 2.842±0.028	0.077±0.008 0.089±0.009 0.067±0.007	18.83 2.126 0.8000
110 K	Fe-N Fe-N Fe-C	4.0 2.0 7.2±0.7	1.948±0.019 2.120±0.021 2.842±0.028	0.081±0.008 0.105±0.011 0.074±0.007	16.48 2.280 0.8000
120 K	Fe-N Fe-N Fe-C	4.0 2.0 7.2±0.7	1.948±0.019 2.120±0.021 2.845±0.028	0.084±0.008 0.100±0.010 0.077±0.008	17.69 2.223 0.8000
130 K	Fe-N Fe-N Fe-C	4.0 2.0 7.4±0.7	1.952±0.020 2.128±0.021 2.841±0.028	0.084±0.008 0.112±0.011 0.081±0.008	17.27 2.268 0.8000
140 K	Fe-N Fe-N Fe-C	4.0 2.0 7.0±0.7	1.954±0.020 2.128±0.021 2.842±0.028	0.087±0.009 0.112±0.011 0.081±0.008	16.88 2.413 0.8000
150 K	Fe-N Fe-N Fe-C	4.0 2.0 6.9±0.7	1.948±0.019 2.121±0.021 2.830±0.028	0.089±0.009 0.112±0.011 0.087±0.009	22.67 3.945 0.8000
160 K	Fe-N Fe-N Fe-C	4.0 2.0 7.0±0.7	1.956±0.020 2.140±0.021 2.839±0.028	0.092±0.009 0.112±0.011 0.095±0.010	23.64 4.079 0.8000
170 K	Fe-N Fe-N Fe-C	4.0 2.0 7.2±0.7	1.970±0.020 2.172±0.022 2.851±0.029	0.100±0.010 0.112±0.011 0.112±0.011	22.69 3.812 0.8000

Sample	Abs-Bs [a]	N(Bs) [b]	R(Abs-Bs) [c] / Å	σ [d] / Å^{-1}	R [e] / % E_f [f] / eV Afac [g]
180 K	Fe-N Fe-N Fe-C	4.0 2.0 6.7±0.7	1.981±0.020 2.186±0.022 2.869±0.029	0.110±0.011 0.112±0.011 0.112±0.011	27.03 4.674 0.8000
190 K	Fe-N Fe-N Fe-C	4.0 2.0 6.2±0.6	2.035±0.020 2.263±0.023 2.991±0.030	0.112±0.011 0.105±0.011 0.112±0.011	35.10 2.233 0.8000
200 K	Fe-N Fe-N Fe-C	4.0 2.0 5.8±0.6	2.072±0.021 2.287±0.023 2.986±0.030	0.110±0.011 0.092±0.009 0.112±0.011	23.19 1.767 0.8000
210 K	Fe-N Fe-N Fe-C	4.0 2.0 5.1±0.5	2.102±0.021 2.317±0.023 3.019±0.030	0.112±0.011 0.092±0.009 0.087±0.009	23.48 1.061 0.8000
220 K	Fe-N Fe-N Fe-C	4.0 2.0 4.9±0.5	2.100±0.021 2.305±0.023 3.011±0.030	0.097±0.010 0.074±0.007 0.077±0.008	21.13 2.224 0.8000
230 K	Fe-N Fe-N Fe-C	4.0 2.0 5.3±0.5	2.102±0.021 2.306±0.023 3.010±0.030	0.095±0.010 0.074±0.007 0.081±0.008	19.36 2.582 0.8000
240 K	Fe-N Fe-N Fe-C	4.0 2.0 5.4±0.5	2.106±0.021 2.309±0.023 3.014±0.030	0.089±0.009 0.071±0.007 0.074±0.007	19.19 2.677 0.8000
250 K	Fe-N Fe-N Fe-C	4.0 2.0 5.5±0.6	2.117±0.021 2.323±0.023 3.024±0.030	0.089±0.009 0.071±0.007 0.074±0.007	20.04 2.336 0.8000
260 K	Fe-N Fe-N Fe-C	4.0 2.0 5.6±0.6	2.109±0.021 2.312±0.023 3.012±0.030	0.087±0.009 0.074±0.007 0.074±0.007	19.59 3.010 0.8000
293 K	Fe-N Fe-N Fe-C	4.0 2.0 6.2±0.6	2.119±0.021 2.330±0.023 3.019±0.030	0.081±0.008 0.071±0.007 0.084±0.008	19.25 2.619 0.8000

a) Abs=X-ray absorbing atom, Bs=backscattering atom, b) number of backscattering atoms, c) distance of absorbing atom to backscattering atom, d) Debye-Waller-like factor, e) fit-index, f) Fermi energy, that accounts for the shift between theory and experiment, g) amplitude reducing factor

The most interesting parameters to get a view on the structural changes during the SCO process are the equatorial and axial Fe-N bond lengths, which are shown in Table 13. Furthermore, these distances were used to calculate the respective HS fractions according to equation (22), which are also shown in the following table.

Table 13: Fit Model 2E: Fe-N distances of the axial and equatorial nitrogen atoms obtained by EXAFS analysis and thereof calculated γ_{HS} values.

T / K	R_{eq}(Abs-Bs) / Å	$\gamma_{HS}(R_{eq})$ [a]	R_{ax}(Abs-Bs) / Å	$\gamma_{HS}(R_{ax})$ [a]
10	1.947±0.019	-0.006	2.113±0.021	-0.036
30	1.944±0.019	-0.025	2.114±0.021	-0.030
40	1.949±0.019	0.006	2.128±0.021	0.041
50	1.946±0.019	-0.012	2.126±0.021	0.030
70	1.946±0.019	-0.012	2.119±0.021	-0.005
80	1.947±0.019	-0.006	2.109±0.021	-0.056
90	1.945±0.019	-0.018	2.109±0.021	-0.056
100	1.945±0.019	-0.018	2.132±0.021	0.061
110	1.948±0.019	0.000	2.120±0.021	0.000
120	1.948±0.019	0.000	2.120±0.021	0.000
130	1.952±0.020	0.025	2.128±0.021	0.041
140	1.954±0.020	0.037	2.128±0.021	0.041
150	1.948±0.019	0.000	2.121±0.021	0.005
160	1.956±0.020	0.049	2.140±0.021	0.102
170	1.970±0.020	0.135	2.172±0.022	0.264
180	1.981±0.020	0.202	2.186±0.022	0.335
190	2.035±0.020	0.534	2.263±0.023	0.726
200	2.072±0.021	0.761	2.287±0.023	0.848
210	2.102±0.021	0.945	2.317±0.023	1.000
220	2.100±0.021	0.933	2.305±0.023	0.939
230	2.102±0.021	0.945	2.306±0.023	0.944
240	2.106±0.021	0.969	2.309±0.023	0.959
250	2.117±0.021	1.037	2.323±0.023	1.030
260	2.109±0.021	0.988	2.312±0.023	0.975
293	2.119±0.021	1.049	2.330±0.023	1.066

a) HS fraction calculated according to $\gamma_{Hs} = (R_T - R_{LS})/(R_{HS} - R_{LS})$.[84] Applied procedure is described in section 2.3.1.1.

As displayed in Table 13, both Fe-N distances show significant changes with increasing temperature. The equatorial bond lengths change from 1.947 Å to 2.119 Å and the axial Fe-N distances change from 2.113 Å to 2.330 Å. The distances were plotted as a function of temperature to correlate the changes of the bond lengths during the SCO process with temperature again.

The Boltzmann fit of the equatorial Fe-N bond lengths (cf. Appendix Figure A.7) results in a spin transition temperature of $T_{1/2}$(eq) = 189.5 ± 0.8 K, whereas the fit of the axial Fe-N distances (cf. Appendix Figure A.8) results in a transition temperature of $T_{1/2}$(ax) = 182.9 ± 1.3 K. The comparison of the fits of the Fe-N distances with the magnetization curve obtained by SQUID magnetometry (Figure 2.31) shows that the structural changes cannot be clearly correlated with the magnetic changes in this fit model, since the deviations from the SQUID curve are much larger than in the case of the unfiltered data (cf. Fit Model 2C). The spin transition temperature obtained by the fit of the equatorial bond lengths differs from the one obtained by SQUID magnetometry only by 2.5 K, but the fit curve shows a much higher slope. Therefore, the spin transition starts at higher temperatures and the HS state is reached at lower temperatures than in the SQUID curve.

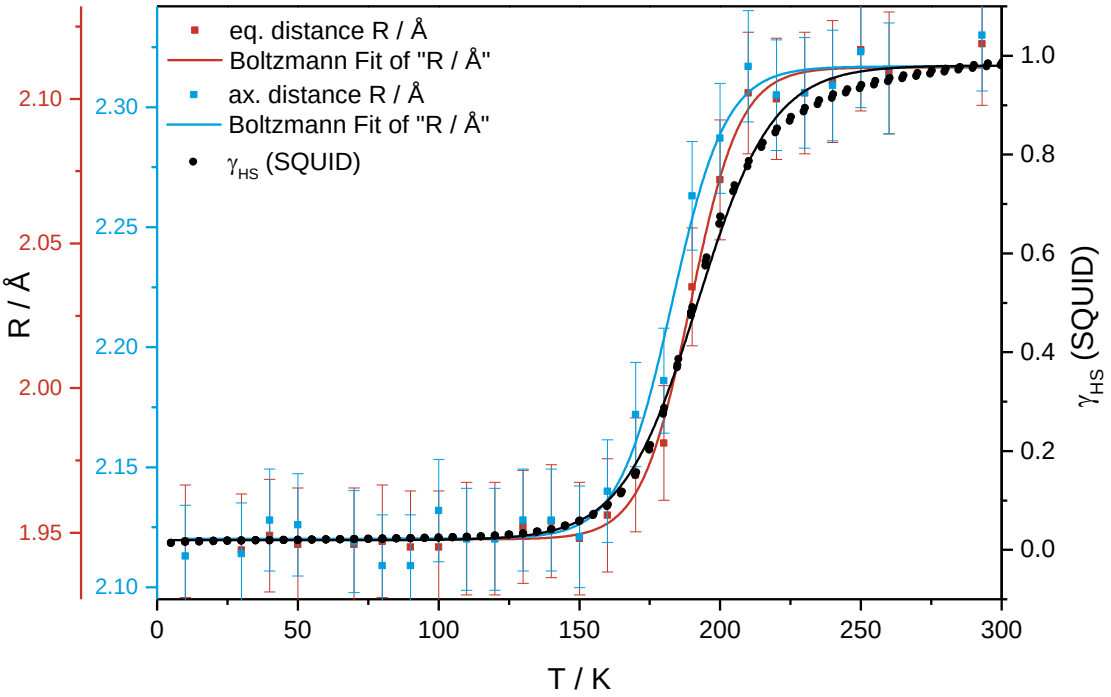

Figure 2.31: Fit Model 2E: Comparison of HS fraction obtained by SQUID measurements and fits of the equatorial (red) and axial (blue) Fe-N distances.

In case of the axial bond lengths the spin transition temperature deviates by nearly 10 K from the value obtained by SQUID magnetometry. The spin transition process starts at almost the same temperature but since the fit curve of the axial distances shows a more abrupt behaviour than the magnetization curve the HS state is reached at lower temperatures like in the equatorial case, too.

As in the previous fit models with iterated Fe-N distances, the equatorial and axial bond lengths were converted to HS fractions for a direct comparison with the HS fractions obtained by SQUID magnetometry. Following the procedure described in chapter 2.3.1.1, the lower and upper limits (A_1 and A_2) of the Boltzmann fits were determined and used as approximations for the pure LS respective HS distance. The fit limits of the equatorial bonds were identified as $A_1(\text{eq}) = R_{\text{eq,LS}} = 1.948 \pm 0.001$ Å and $A_2(\text{eq}) = R_{\text{eq,HS}} = 2.111 \pm 0.002$ Å, while in the axial case the LS distance was determined as $A_1(\text{ax}) = R_{\text{ax,LS}} = 2.120 \pm 0.003$ Å and the HS distance as $A_2(\text{ax}) = R_{\text{ax,HS}} = 2.317 \pm 0.004$ Å. These limits were inserted into equation (22) yielding the $\gamma_{\text{HS}}(R_{\text{eq}})$ and $\gamma_{\text{HS}}(R_{\text{ax}})$ values listed in Table 13. The plots of the HS fractions obtained by EXAFS spectroscopy and SQUID magnetometry versus temperature are shown in Figure 2.32. As already mentioned in the previous sections, the HS fractions are directly correlated to the Fe-N distances and therefore, the curve shapes and the resulting transition temperatures are essentially the same. Since there are small fractions of HS centres in the LS region

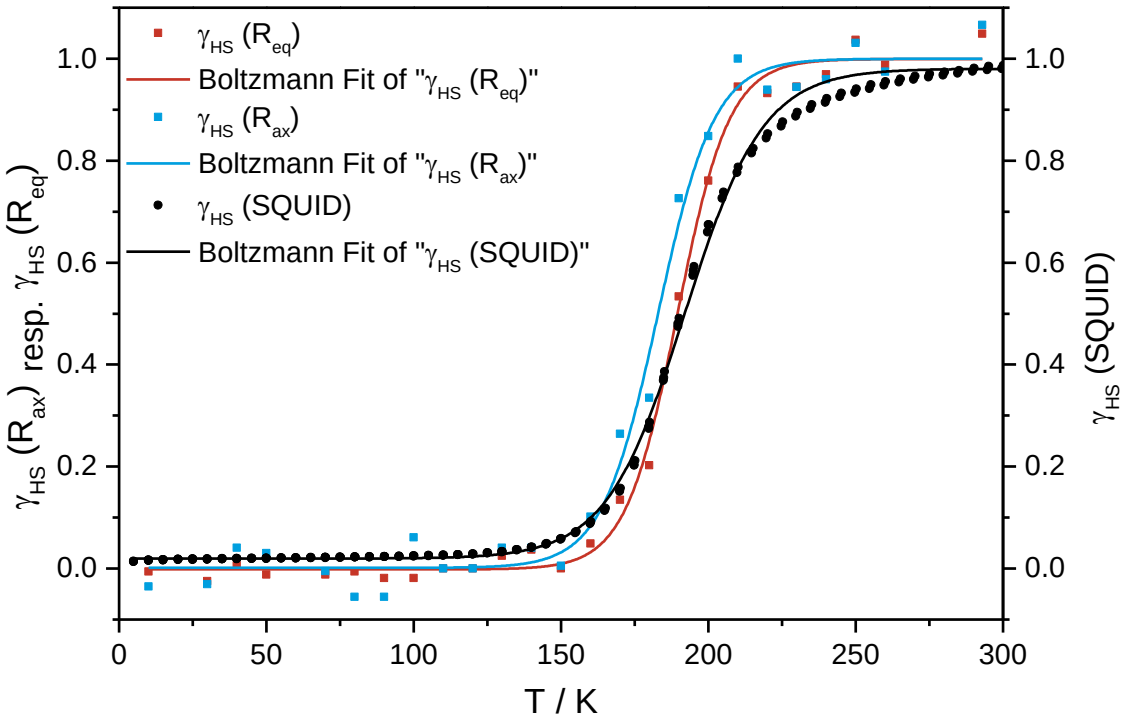

Figure 2.32: Fit model 2E: Comparison of HS fractions obtained by SQUID (black) and EXAFS measurements (red & blue).

and LS centres in the HS region, the absolute values are slightly distorted, but this does not influence the determination of the transition temperature.

The Debye-Waller-like factors of the equatorial and the axial nitrogen shell were plotted versus temperature to get a correlation with the temperature-dependent SCO behaviour. Figure 2.33 displays the plot of the equatorial parameter versus temperature, which shows the same trend like in the models discussed before. That means, σ_{eq} stays nearly constant in the low temperature region, with increasing temperature a maximum is reached at around the spin transition temperature and with further rising temperature σ_{eq} decreases again. To obtain the temperature of the maximum, a Gaussian fit was applied, which shows its maximum at T(eq) = 195.6 ± 1.8 K. Compared to $T_{1/2}$(SQUID) = 192.0 ± 0.2 K a shift of around 4 K to higher temperatures is observable. In contrast to the equatorial case, the values of the axial Debye-Waller-like factor show a bit different behaviour (Figure 2.34). In the low temperature region σ_{ax} is widely spread (0.089 – 0.112 Å^{-1}) and much higher than in the equatorial case. Since the maximum allowed value for the Debye-Waller-like factor is 0.112 Å^{-1}, no distinct maximum in the spin transition region is observable. With reaching the HS state, σ_{ax} is decreasing to 0.071 – 0.074 Å^{-1}. Due to the distribution of the data points no Gaussian fit was applied in this case.

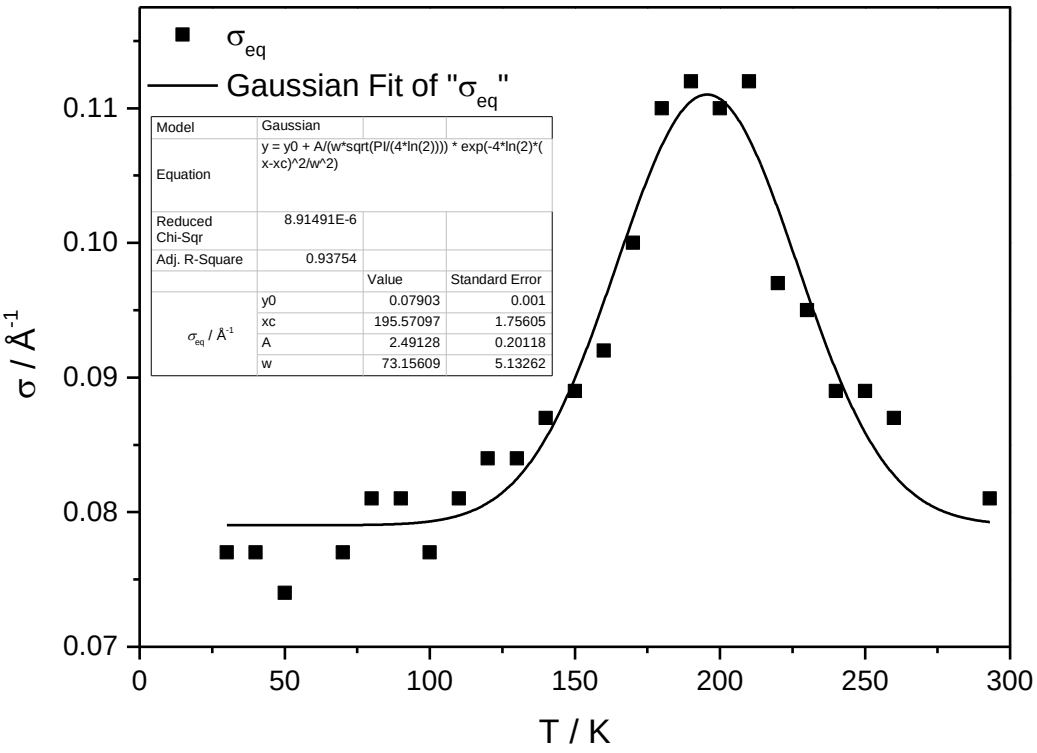

Figure 2.33: Fit Model 2E: Plot of Debye-Waller like factor σ_{eq} of the equatorial nitrogen shell vs. temperature.

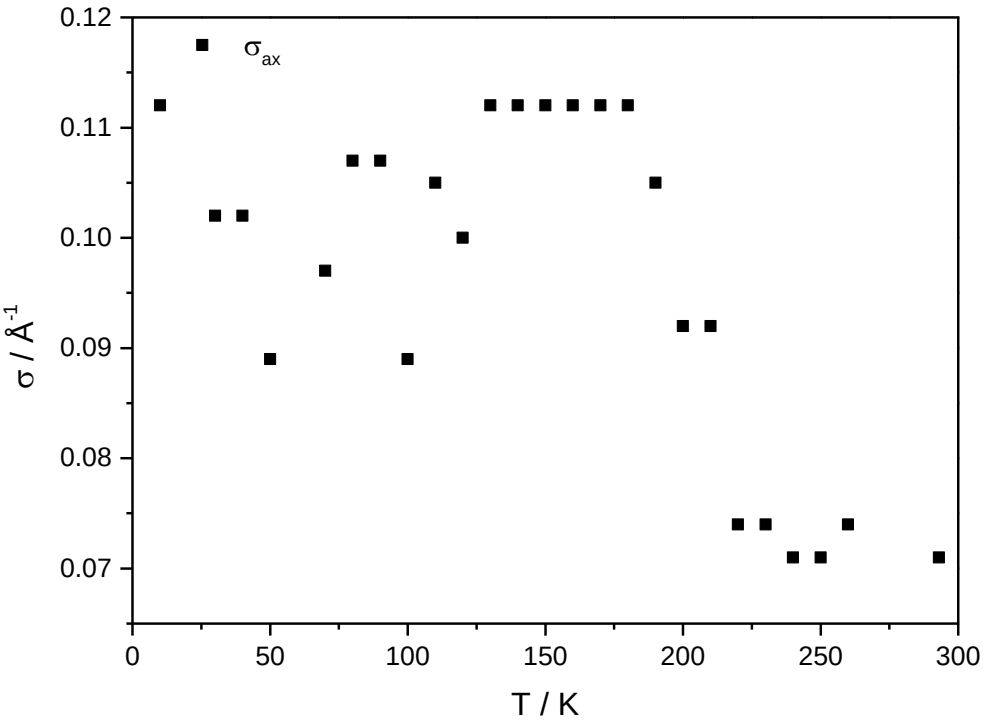

Figure 2.34: Fit Model 2E: Plot of Debye-Waller like factor σ_{ax} of the axial nitrogen shell vs. temperature.

The second fit model with Fourier filtered data gives improved results compared to the previous fit model with fixed Fe-N distances (Fit Model 2D). The free iteration of the Fe-N distances allows a better adjustment of the theoretical fit functions to the experimental spectra. Even though it is possible to distinguish between equatorial and axial backscatterers, the curve shapes of the distance versus temperature plots show larger deviations from the magnetization curve than in case of the unfiltered data. Both determined transition temperatures are shifted to lower temperatures compared to the SQUID data and both fits show a more abrupt behaviour than the magnetization curve. But due to the overlapping error bars of the Fe-N distances, the discussion of the curve shape is of minor significance. Evaluation of the temperature dependence of the Debye-Waller-like factors showed, that in case of σ_{eq} a rough determination of the SCO region is possible, since it results in a peak structure due to an increasing disorder in the system before and decreasing disorder after the transition temperature. The maximum of the peak can be roughly correlated with the transition temperature obtained by SQUID magnetometry. In case of σ_{ax}, no further information can be obtained because of the widely spread data points. So similar to the other fit models with two nitrogen shells and iterated Fe-N distances (Fit Model 2A and 2C), it seems that the parameters of the equatorial Fe-N shell are more suitable for the prediction of the SCO region and the transition temperature than the axial parameters.

2.4 Summary

This chapter was focused on the analysis of the temperature-dependent EXAFS data. Different fit models with one or two nitrogen shells were tested, using either unfiltered or Fourier filtered data. In general, it can be said, that all applied models gave satisfying to good results concerning the prediction of the SCO range and the transition temperature compared to the magnetization by SQUID.

The fit models with one nitrogen shell basically showed poorer results in terms of the adjustment of the theoretical fit functions to the experimental spectra compared to the two-shell models. With Fit Model 1A, where the amplitude reducing factor was held fix at the standard value 0.8000, it was not possible to adjust the number of signals as well as the intensity of the first signal properly. Free iteration of the amplitude reducing factor in Fit Model 1B resulted in a better adjustment of the intensity, but the number of signals still could not be reproduced by the fit function. But despite this, the resulting spin transition curves as well as the determined transition temperatures were in very good agreement with the magnetization data obtained by SQUID magnetometry for both models. The temperature dependence of the Debye-Waller-like factor of the nitrogen shell and the afac were evaluated, too. The Debye-Waller-like factor showed in both fit models no clear trend, so no direct correlation with the spin state was possible with these models. In case of Fit Model 1B, an abrupt increase of σ was observed, which could probably indicate the temperature at which the spin transition from LS to HS starts. The afac, however, resulted in a curve shape with a minimum that can be roughly correlated with the spin transition temperature.

An improvement of the fit quality could be achieved by adding the second nitrogen shell to the fit models. Free iteration of the Fe-N distances yielded a very good agreement between experimental and theoretical data, whereas the fit models with fixed distances (Fit Model 2B and 2D) gave just a satisfying agreement and a poorer fit quality. In case of the spectrum at the transition temperature all applied fit models showed deficiencies, since the number of signals could not be reproduced correctly. Basically, all models allowed the distinction between equatorial and axial nitrogen backscatterers, since the two fitted nitrogen shells showed a difference of around 0.2 Å in the Fe-N distance. Both nitrogen shells revealed a clear temperature dependence resulting in spin transition curves that were in rather good agreement within the error bars with the SQUID data for all fit models.

In all models, the axial Fe-N distances tended to start the elongation at lower temperatures than the equatorial ones, represented by the lower transition temperatures (cf. column two and three of Table 14). This led to the assumption, that the change of the axial distances does not affect the magnetization of the system, since the course of the magnetization rather follows the changes of the equatorial distances. In general, the equatorial distances showed a better agreement with the course of the magnetization. The average transition

temperature of the equatorial shell is in very good agreement with the transition temperature determined by SQUID magnetometry, while the axial temperature shows a larger deviation.

The Debye-Waller-like factors of both nitrogen shells exhibited an interesting behaviour with increasing temperature. Due to a presumed higher static disorder in the SCO region, a peak structure is observable, which could be used for a rough determination of the SCO region. Furthermore, the broadening of the peak could probably be used as an indicator of the degree of cooperativity, since a broader peak could be associated with a more gradual transition, while an abrupt transition should give a narrower peak structure.

Table 14: Comparison of the temperatures obtained by the fits of the Fe-N distances and the Debye-Waller-like factors of the equatorial and axial nitrogen shell.

Fit Model	$T_{1/2}$(eq) / K [a)]	$T_{1/2}$(ax) / K [a)]	T(eq) / K [b)]	T(ax) / K [b)]
2A	190.8±0.6	186.6±1.3	186.7±1.5	173.7±2.2
2B	--	--	202.0±1.3	194.7±1.7
2C	191.6±1.1	185.3±1.4	192.0±1.8	160.5±5.9
2D	--	--	204.3±1.5	189.8±2.2
2E	189.5±0.8	182.9±1.3	195.6±1.8	--
Av(2A, 2C, 2E) [c)]	190.6±0.8	184.9±1.3	191.4±1.7	167.1±4.0 [d)]

a) Transition temperatures obtained from Boltzmann fits of the Fe-N distances, b) Temperatures of fit maxima of the Gaussian fits of the Debye-Waller-like-factors, c) Averaged temperature of fit models with iterated Fe-N distances, d) Averaged temperature of fit models 2A and 2C, since no temperature could be determined for fit model 2E.

At first glance, the maximum of the peaks could not be clearly correlated with the transition temperature, since no clear trend could be observed. But if the fit models were grouped in fits with fixed Fe-N distances on the one hand (Fit Model 2B and 2D) and iterated distances (Fit Models 2A, 2C, and 2E) on the other hand, it could be observed, that the average temperature of the equatorial shell is in very good agreement with the SQUID data in case of the iterated distances, whereas the temperature of the fixed distances shows a clear shift to higher temperatures. In case of the axial distances, the temperatures reveal a much larger deviation compared to the SQUID data in case of the iterated distances than in case of the fixed distances.

Taking all this information together, it can be concluded, that analysis of the changes of the Fe-N distances is a well suited tool to follow the structural changes during the SCO process. Due to the overlapping error bars it is not possible to determine which Fe-N bond changes first reliably. But despite this, all fit models indicated, that the axial distances start to change at lower temperatures than the equatorial ones. In addition, the analysis of the afac and the Debye-Waller-like factors showed, that the afac as well as the Debye-

Waller-like factor of the equatorial nitrogen shell could be a good indicator for the determination of the SCO region. Especially the equatorial Debye-Waller-like factor seems to be suited for the determination of the transition temperature as well.

3 HERFD-XANES Spectroscopy

This chapter addresses the evaluation of the temperature-dependent HERFD-XANES spectra. Since the analysis of the EXAFS region gives information about the structural changes of the investigated complex occurring during the SCO process, the XANES region can provide electronic as well as structural information. First, a comparison of conventional and HERFD-XANES spectra is shown, discussing the observable spectral differences and the advantages of the HERFD technique. Because the prepeak features are caused by transitions from 1s into the 3d or 3d/4p hybridized orbitals, these features provide useful information about the distribution of the d electrons and therefore of the spin state of the system. To obtain these information, the HERFD-XANES data were background corrected to extract the prepeak features, which were then analysed by different methods. The resulting parameters were correlated with temperature to receive a spin transition curve that was compared to the magnetization curve obtained by SQUID magnetometry.

3.1 Experimental Section

HERFD-XANES measurements were carried out at beamline ID26 at the European Synchrotron Radiation Facility (ESRF, Grenoble, France). The ring current varied between 180 and 200 mA and the electron energy was 6.0 GeV. A cryogenically cooled Si(111) double-crystal monochromator was used for the measurements at the iron K-edge (7.112 keV). Energy calibration was performed using an iron foil. On the sample position the incident X-ray beam had a flux of approximately 2 x 10^{13} photons/s. The HERFD-XANES spectra were measured at a scattering angle of 90° with a 1 m diameter Rowland-circle spectrometer arranged in horizontal plane with spherically bent Ge(620) analyser crystals. The spectra were recorded by monitoring the intensity of the maximum of the $K\beta_{1,3}$ line in dependence of the incident energy, so-called $K\beta_{1,3}$-detection. The sample was diluted in boron nitride and pressed to a pellet to avoid self-absorption effects. Measurements were carried out using a closed cycle helium cryostat in a temperature range of 30 to 260 K. To avoid radiation damages several quick HERFD scans were performed at one sample spot to calculate the time in which the sample was stable, what means no changes in the spectrum were observable during this time span. Several scans were averaged to obtain a reasonable signal-to-noise ratio.

3.2 Data Analysis and Results

Figure 3.1 shows the comparison of the normalized conventional XANES spectra (top) in the temperature range from 10 to 293 K and the HERFD-XANES spectra (bottom) of [Fe(L-N_4Bn_2)$(NCS)_2$] in the temperature range from 30 to 260 K. The most significant differences between the conventional and the high resolution XANES are shown in the prepeak region, while the remaining spectral parts are only slightly affected by the high resolution measurement mode. The prepeak of the conventional XANES spectra shows just one broad signal, whereas the HERFD-XANES spectra show two overlapping signals. This nicely demonstrates the advantages of the high energy resolution spectra as already described in chapter 1.3.4.4; the prepeak features are separated better from the absorption edge than in case of the conventional XANES spectra and the resolution is visibly increased.[134,147]

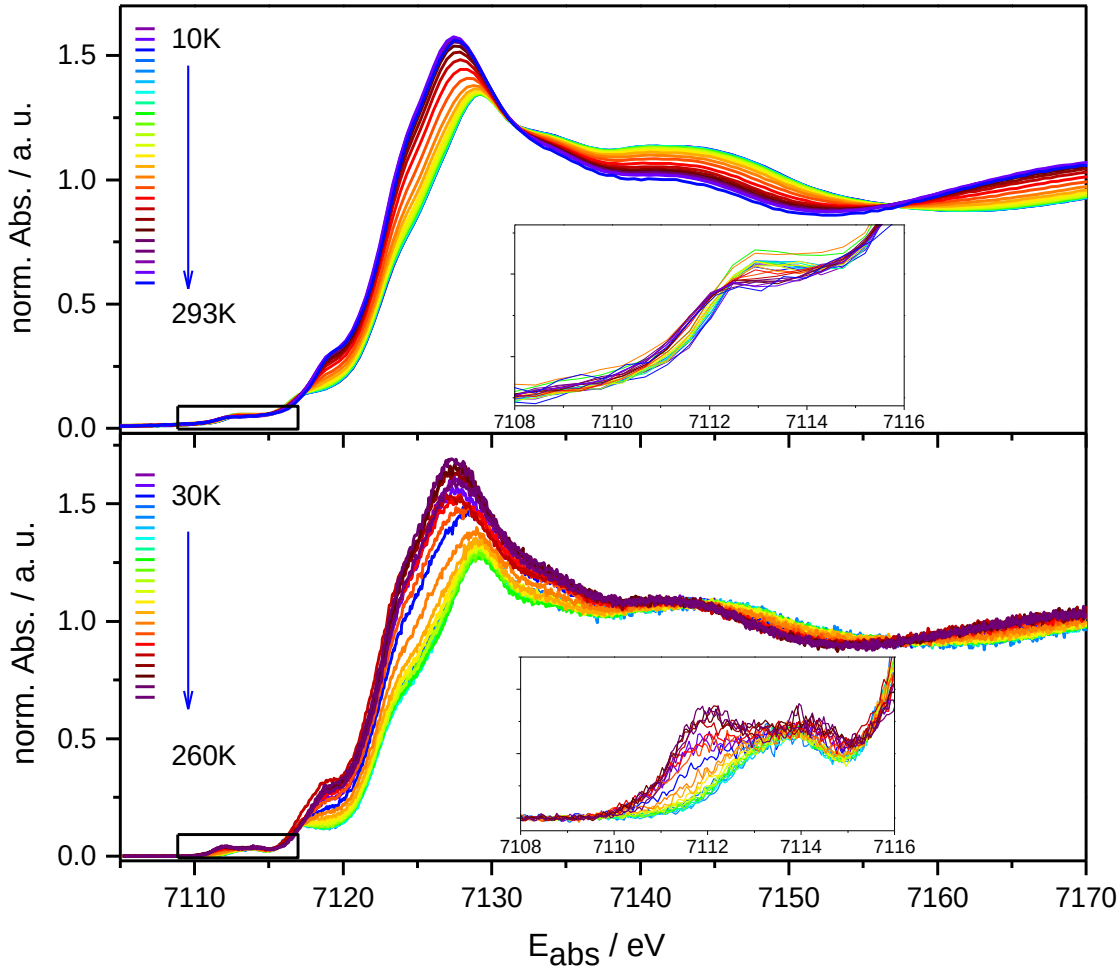

Figure 3.1: Comparison of normalized conventional XANES (top) and K$\beta_{1,3}$ -detected HERFD-XANES spectra (bottom) of [Fe(L-N_4Bn_2)$(NCS)_2$] in the respective temperature range, including the enlarged prepeak area.

Looking at the changes occurring with the rise of temperature, an increase of the white line and a shift of the absorption edge to lower energies is observable. Additionally, with rising temperature a second prepeak feature appears and increases in intensity. So therefore, this feature somehow seems to be correlated with the HS fraction.
A simplified qualitative explanation for the distribution of the signals can be given by looking at the occupation of the orbitals of an ideal octahedral $3d^6$ system. In the LS case the three t_{2g} orbitals are fully occupied, since the ligand field splitting Δ_O is bigger than the energy required for spin pairing P. In contrast to this, the ligand field splitting in the HS case is smaller than the energy for spin pairing and therefore all d-orbitals are occupied singly (e_g^* and t_{2g}) and only one t_{2g} orbital is doubly occupied (cf. Scheme 3.1). Considering that the prepeak features result from 1s → 3d transitions, it is apparently that the HS spectrum shows additional transitions at lower energies, since the core electron can be excited into the lower lying t_{2g} orbitals as well as into the e_g^* orbitals. In the LS case only excitations into the empty e_g^* orbitals are possible.[88] Of course, in real systems the situation is a bit more complicated since the number of possible transitions and therefore the spectral shape is influenced by effects like multiplet splitting.

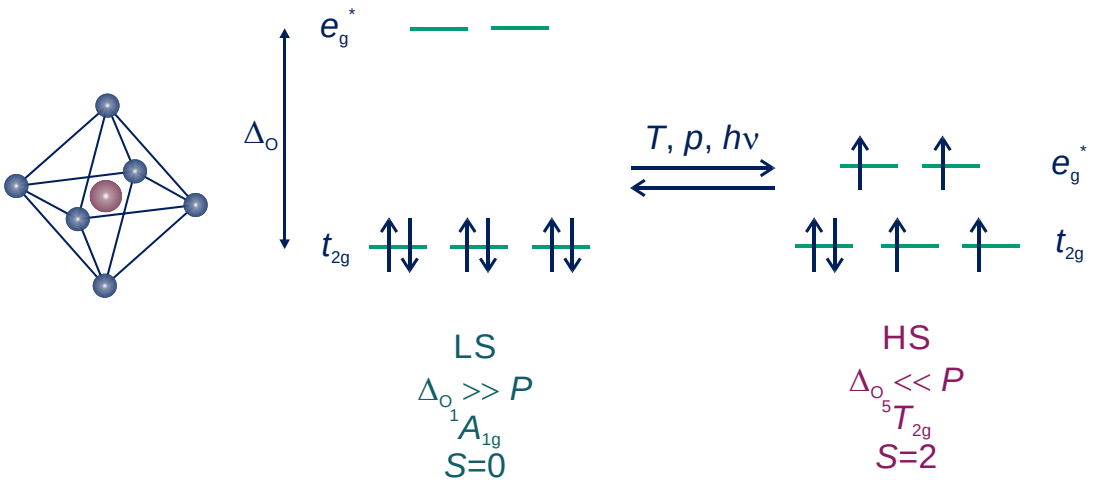

Scheme 3.1: Simplified scheme of the d-orbital splitting for an octahedral $3d^6$ configuration.

3.2.1 Background Correction

For a more detailed analysis of the temperature-dependent behaviour of the prepeak features a background correction according to the procedure described in the following was performed to extract the prepeak. First, the prepeak feature was masked in the energy range from 7110 to 7115 eV, what means that the data points in this energy region were excluded from the subsequent performed fit. The HERFD-XANES spectra were fitted with a sigmoidal Boltzmann function. At all temperatures, the fit was performed in the energy range from 7108 to 7118 eV, except for the spectra at 30, 40 and 220 to 260 K, which were fitted in the energy range from 7108 to 7120 eV.
The different energy regions for the fitting are caused by the shoulder at around 7118 eV, which becomes more pronounced in the HS case. The resulting Boltzmann fit function was subtracted from the experimental spectrum afterwards to obtain the background corrected prepeak region. The background corrections of the spectra at 110 K (LS) and 260 K (HS) are shown exemplarily in Figure 3.2 and Figure 3.3, where the upper figure depicts the applied Boltzmann fit function, while the lower figure shows the comparison of the uncorrected and background corrected prepeak area.

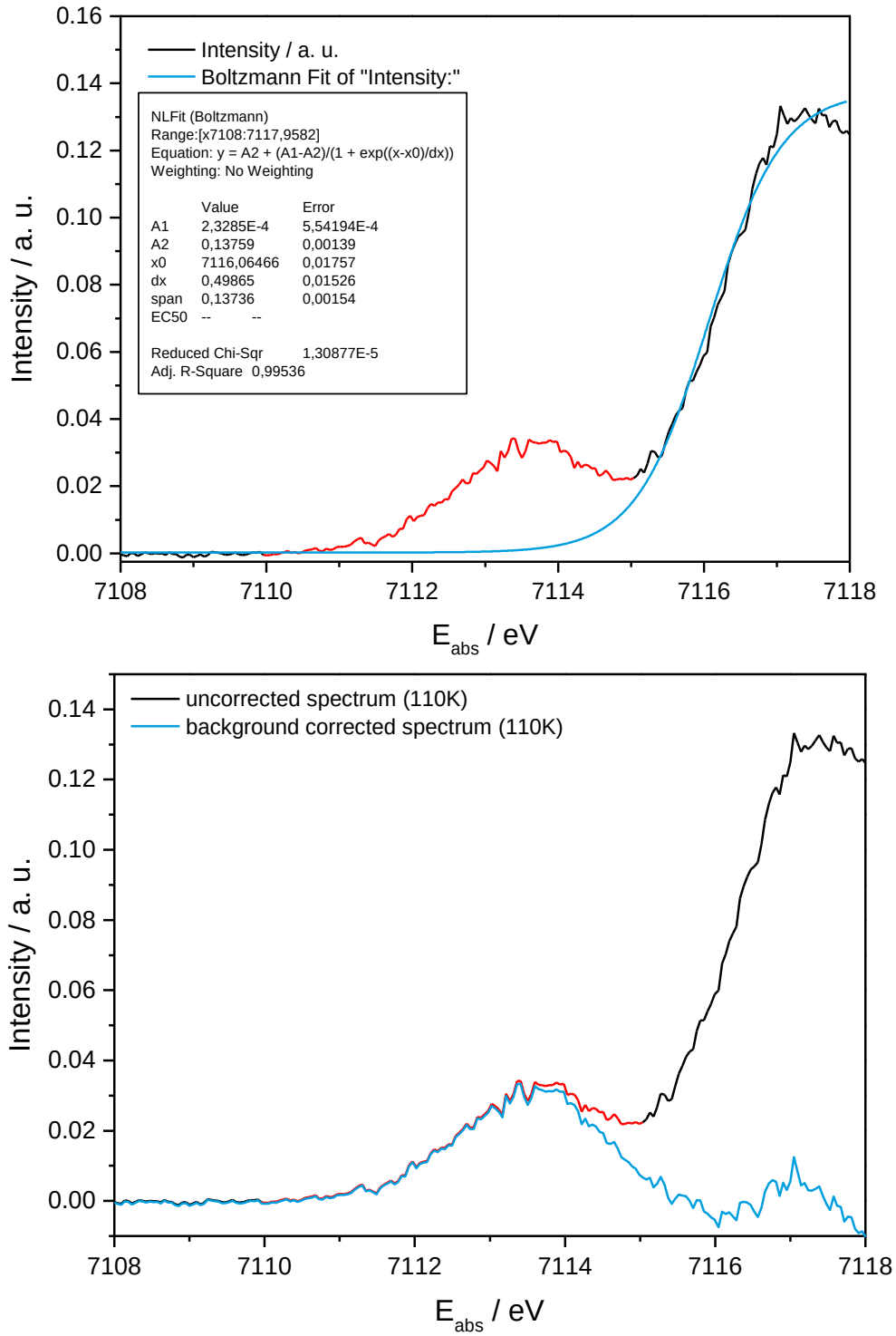

Figure 3.2: Top: Background fit (blue) of the experimental prepeak region of the HERFD-XANES spectrum at 110 K. Bottom: Uncorrected and background corrected HERFD-XANES prepeak region at 110 K (red: masked data range).

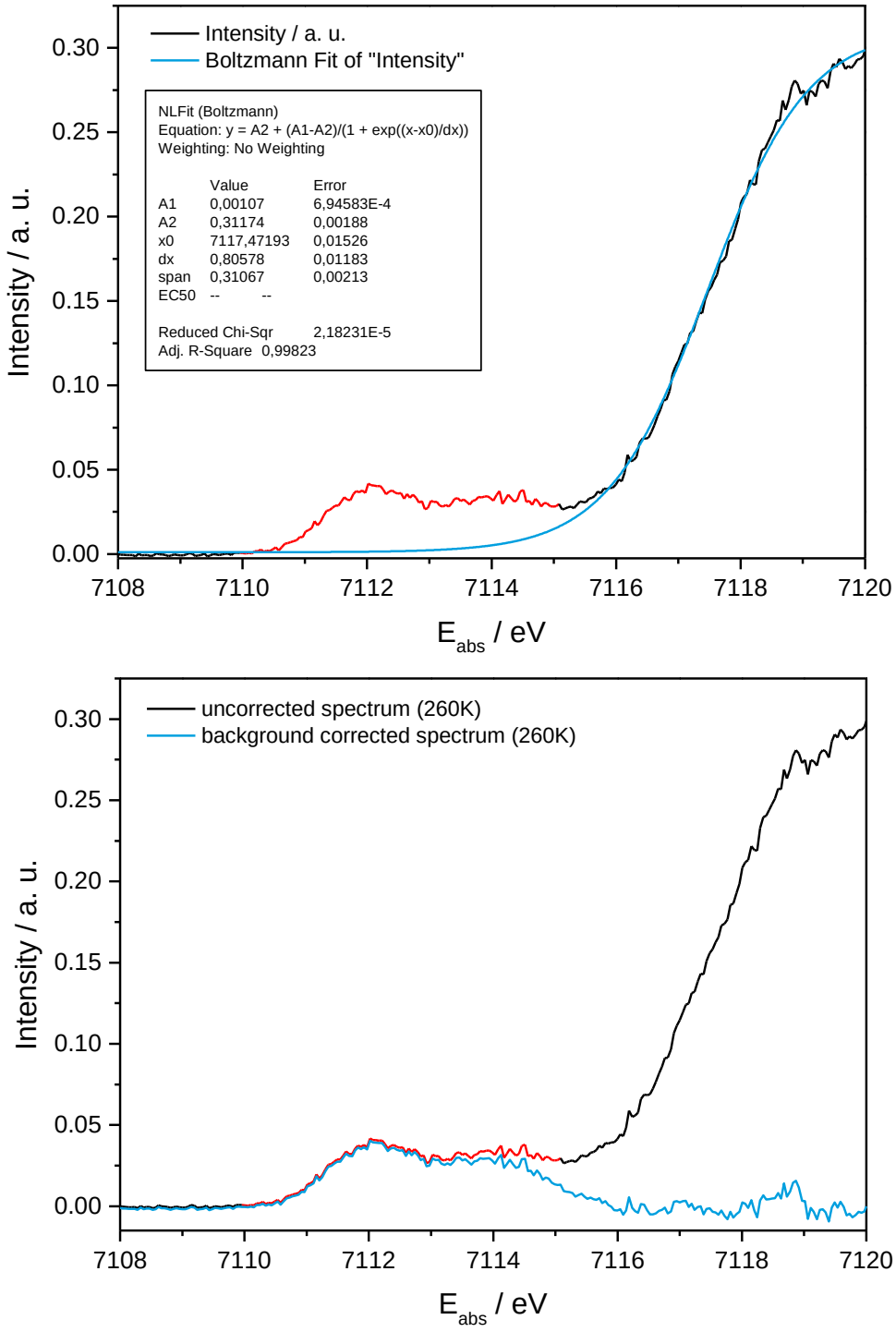

Figure 3.3: Top: Background fit (blue) of the experimental prepeak region of the HERFD-XANES spectrum at 260 K. Bottom: Uncorrected and background corrected HERFD-XANES prepeak region at 260 K (red: masked data range).

The background corrected prepeak region is displayed in Figure 3.4 for all temperatures. In the low temperature region, except for the spectra at 30 – 50 K, only one asymmetric signal with a maximum at around 7113.5 eV is observable. According to the brief explanation in section 3.2, this signal should correspond to transitions into the higher lying e_g^* orbitals. In case of the spectra at 30 – 50 K, a second signal with decreasing intensity is observable with a maximum at around 7112.0 eV. Since this second feature is also observable at high temperatures, it might be assigned to transitions into the lower lying t_{2g} orbitals. As already discussed, these orbitals are partly empty in the HS case and therefore this feature can be correlated somehow with the HS fraction. Obviously, irradiation with the high energetic X-rays leads to conversion of the system into a metastable HS state at very low temperatures, caused by the so-called HAXIESST effect (cf. chapter 1.2.1).[50] With increasing temperature, the feature at lower energy gains intensity. Therefore, in the following sections it is tested if these spectral changes can be correlated quantitatively with the spin state of the system.

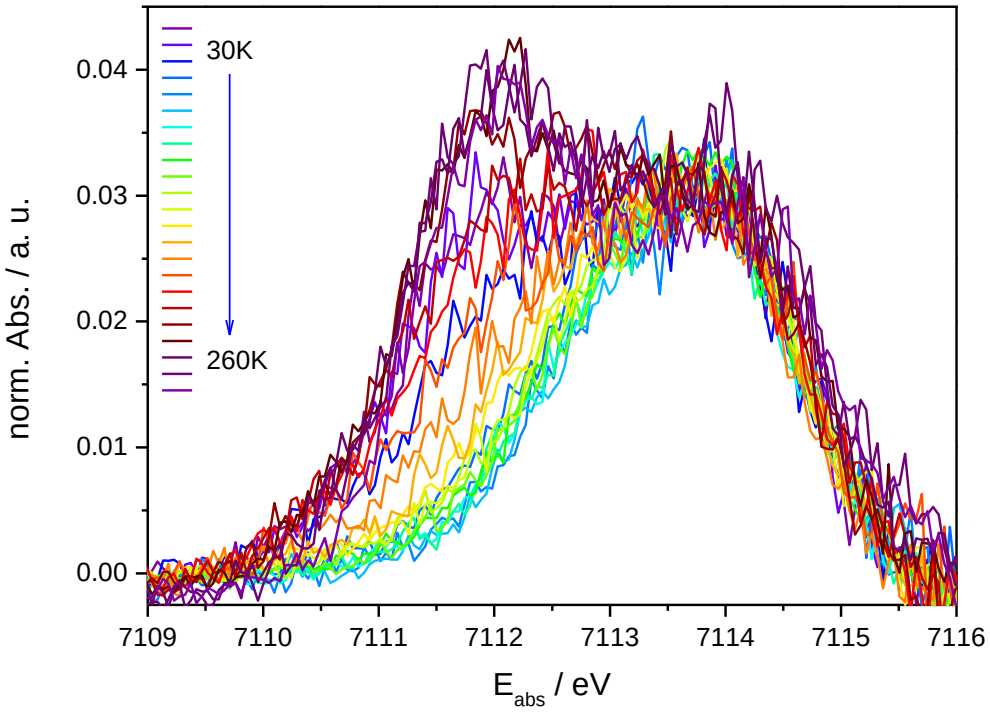

Figure 3.4: Background corrected prepeak area of the temperature-dependent HERFD-XANES spectra of $[Fe(L\text{-}N_4Bn_2)(NCS)_2]$ in the temperature range from 30 to 260 K.

3.2.2 Correlation of HERFD-XANES Spectra and 1s3p RIXS Planes

RIXS spectroscopy, which is directly correlated with the HERFD-XANES technique, is a further useful method to facilitate the separation of the pre-edge from the main edge and to improve the resolution of the spectra, as discussed in chapter1.3.4.4.[134] Since the obtained HERFD-XANES spectra are very noisy, it is not possible to determine the exact number of underlying transitions. Therefore, 1s3p RIXS planes of $[Fe(L\text{-}N_4Bn_2)(NCS)_2]$ were collected at three different temperatures, corresponding to the LS and HS state, as well as to the metastable HS state in the HAXIESST region, shown in Figure 3.5. According to the literature, in the LS case only one resonance at an incident energy of around 7113.5 eV corresponding to a ^2E_g state is visible. In case of the HS state, three resonances at incident energies of 7111.9 eV, 7112.4 eV and 7113.8 eV are observable, assigned to $^4T_{1g}$, $^4T_{2g}$ and $^4T_{1g}$ states.[88] At a temperature of 50 K, the RIXS plane exhibits two features at around 7111.9 eV and 7113.5eV (Figure 3.5, bottom). Comparison of all three measured RIXS planes leads to the assumption, that the system is only partly converted to the metastable HS state at 50 K. The RIXS plane at 50 K is obviously not identical with the one obtained at 293 K and also not with that at 100 K, instead it is rather a combination of both. The feature at lower energies can be correlated with the first resonance in the RIXS plane of the HS state, while the signal at higher energies matches the feature of the LS state. The third resonance, which is visible in the HS state cannot be identified at 50 K.

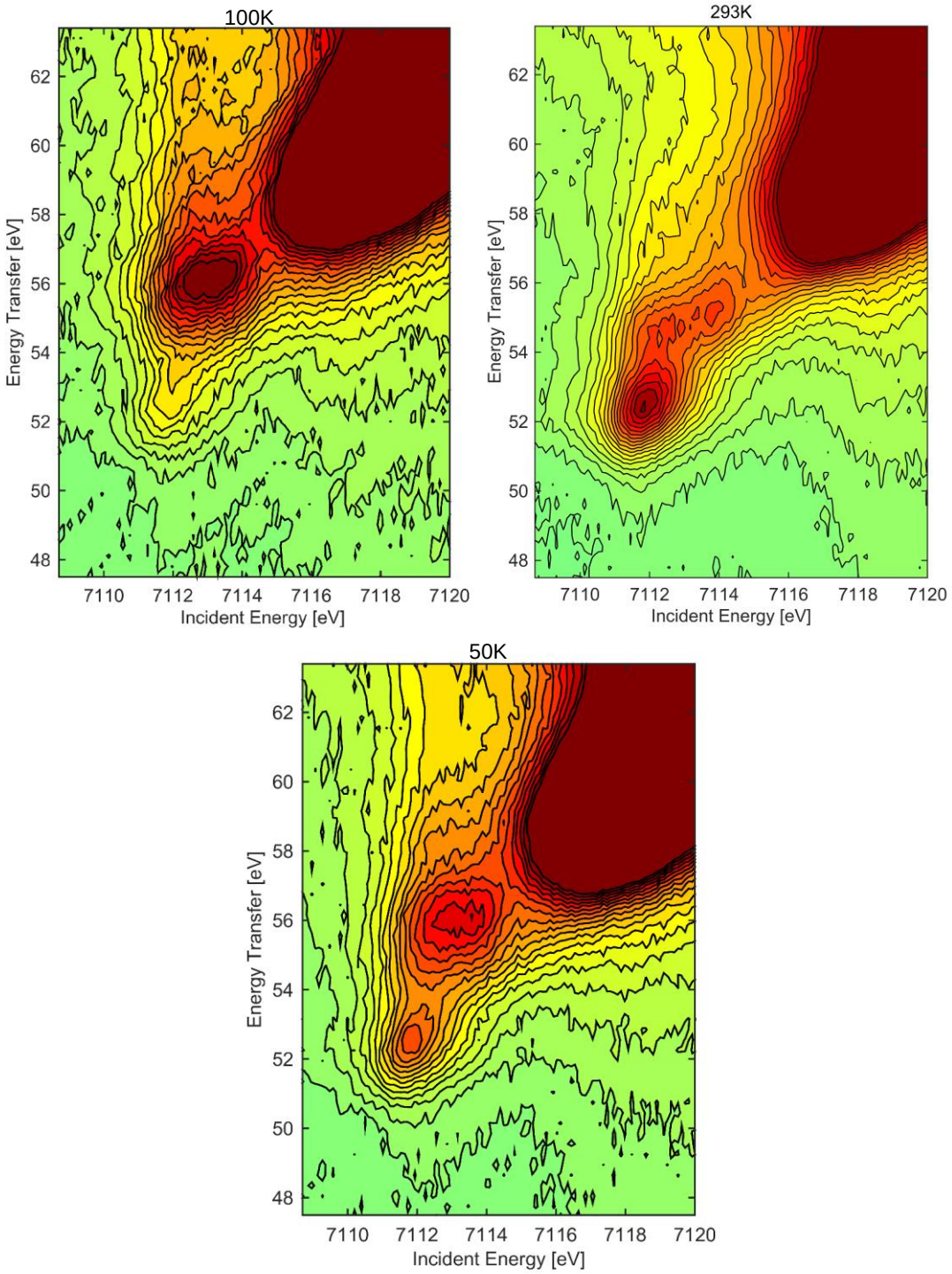

Figure 3.5: $K\beta_{1,3}$ detected RIXS planes of LS state at 100 K (top left), HS state at 293 K (top right) and in the HAXIESST region at 50 K (bottom).

3.2.3 Spin Determination with Use of the HERFD-XANES Prepeak

For the correlation of the changes in the HERFD-XANES prepeak region with the spin state, the spectral changes need to be quantified. Therefore, the background corrected prepeak features were fitted with two Gaussian type curves, as already described by Vankó *et al.*,[89] since there are at least two distinct features observable at most of the temperature points. The curve at lower absorption energies was fixed at a position of 7112.052 eV and a FWHM of 1.609953 eV. All other parameters were iterated freely (intensity of both fit curves, energetic position and FWHM of the second curve). The fitted spectra of all temperatures are shown in Figure 3.6 to Figure 3.9. The position of

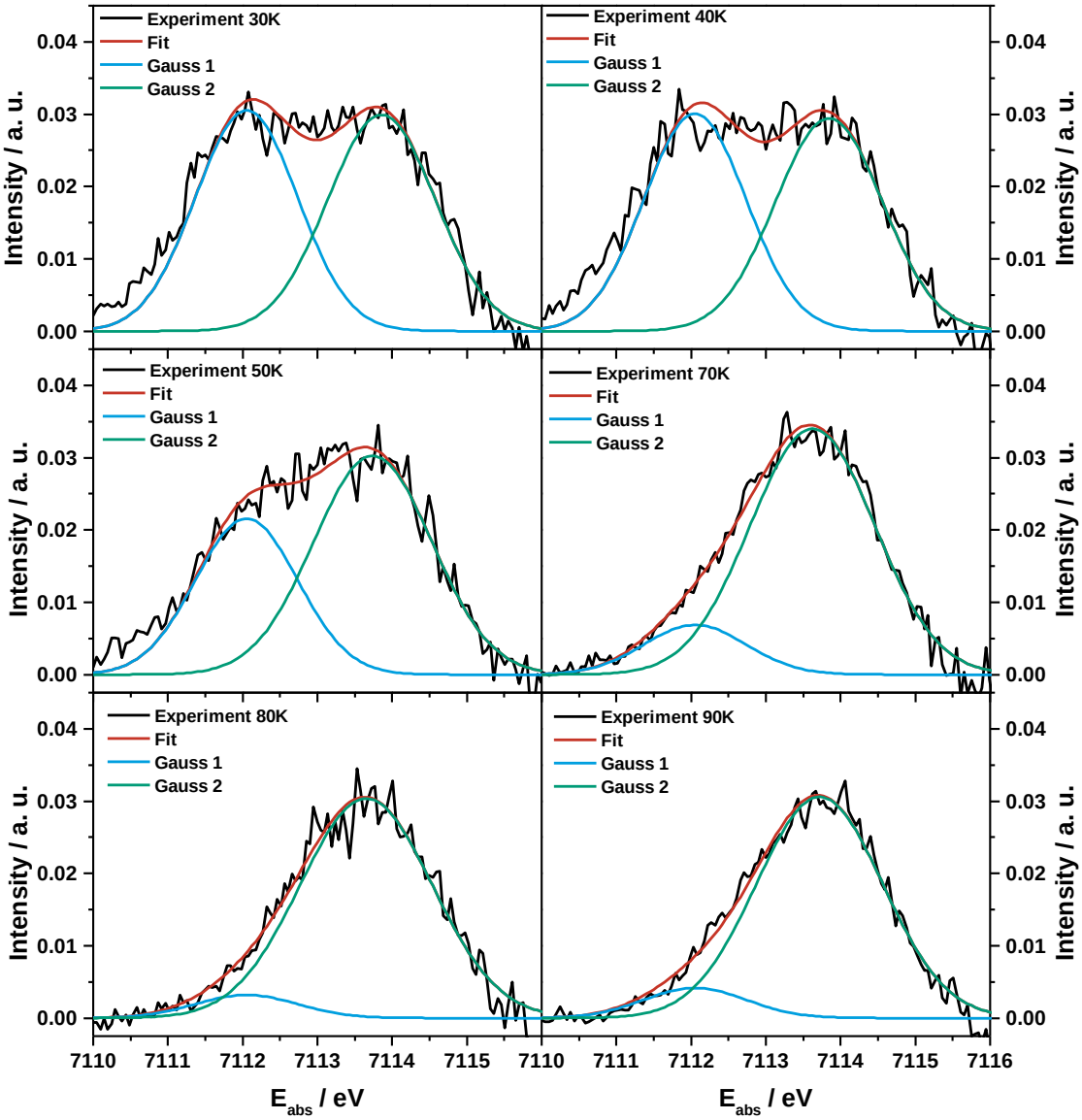

Figure 3.6: HERFD-XANES prepeak region at 30 to 90 K (top left to bottom right), fitted with two Gaussian type curves.

the feature at higher energies, which was iterated freely, stays more or less constant at around 7113.6 to 7114.0 eV for all temperature points. The same tendency is observable for the intensity of this signal, which varies only in a very small range from 0.028 to 0.034 arbitrary units. The situation is somewhat different for the signal at lower energies. During the iterations the energetic position was fixed, while the intensity was iterated freely to account for the changes occurring with increasing temperature. At low temperatures (30 to 70 K), where the system is partially trapped in the metastable HS state (HAXIESST effect, as discussed before) the intensity shows decreasing values of around

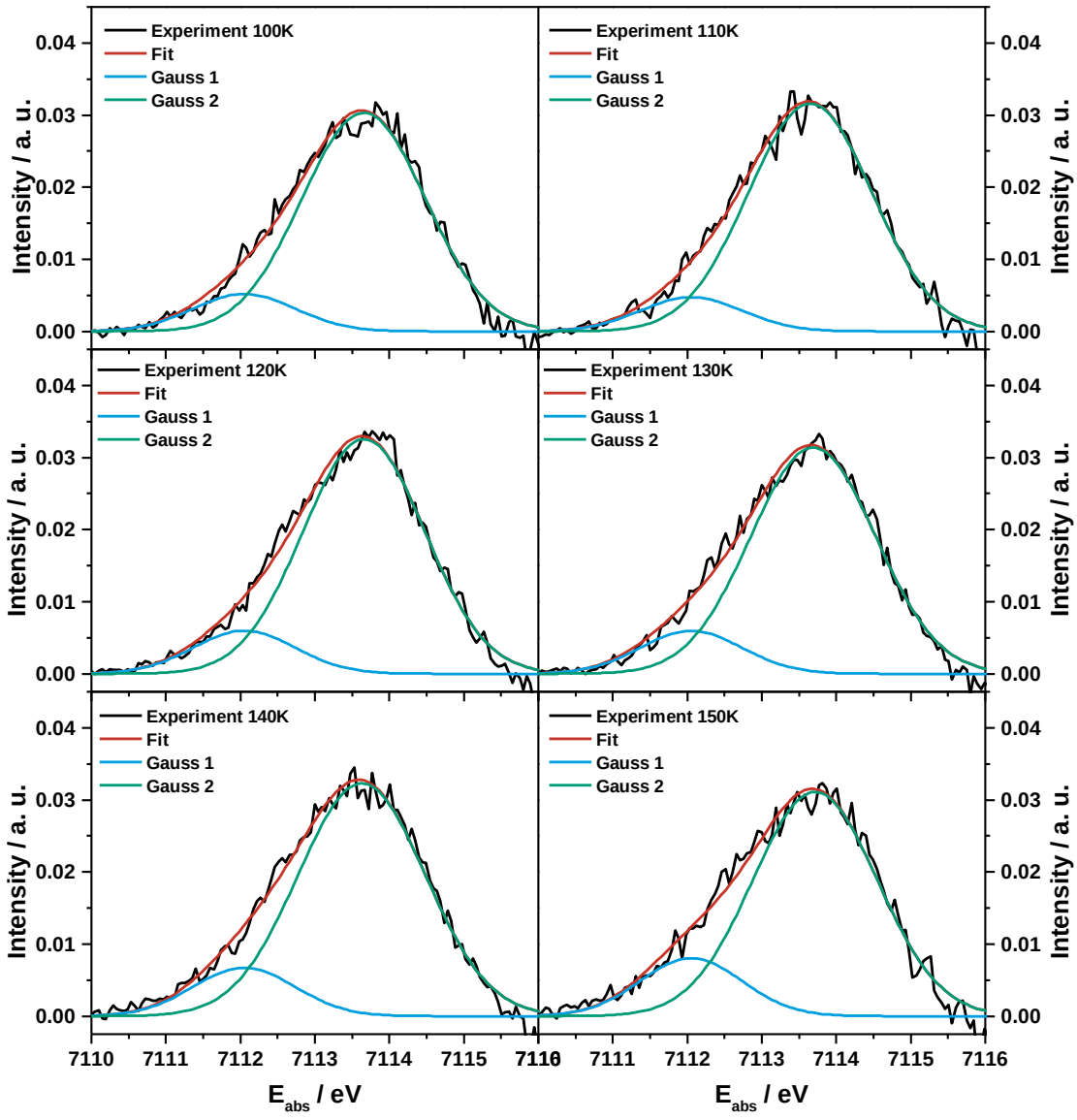

Figure 3.7: HERFD-XANES prepeak region at 100 to 150 K (top left to bottom right), fitted with two Gaussian type curves.

0.031 to 0.007 a. u. with increasing temperature. At 80 K the intensity reaches a minimum value of 0.003 a. u. and with increasing temperature the intensity rises continuously, until it reaches its maximum of around 0.040 a. u. at 250 K. Since the signal-to-noise ratio of the experimental spectra is rather poor, the fit curves can over- or underestimate the maximum intensity. Therefore, the absolute intensity shows some variations, demonstrated for example by the reduced intensity of both fitted signals in case of the spectrum at 260 K compared to that at 250 K.

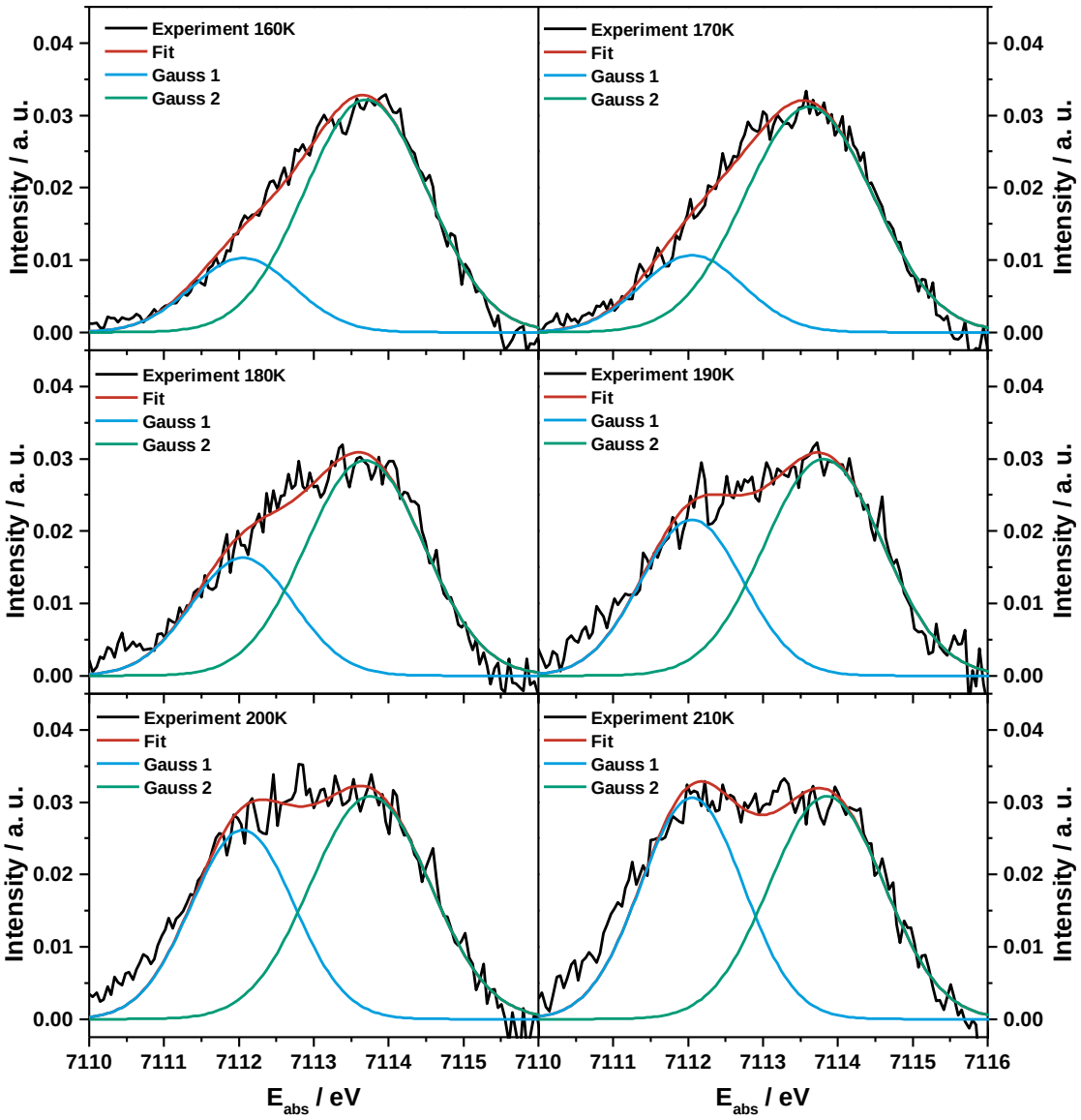

Figure 3.8: HERFD-XANES prepeak region at 160 to 210 K (top left to bottom right), fitted with two Gaussian type curves.

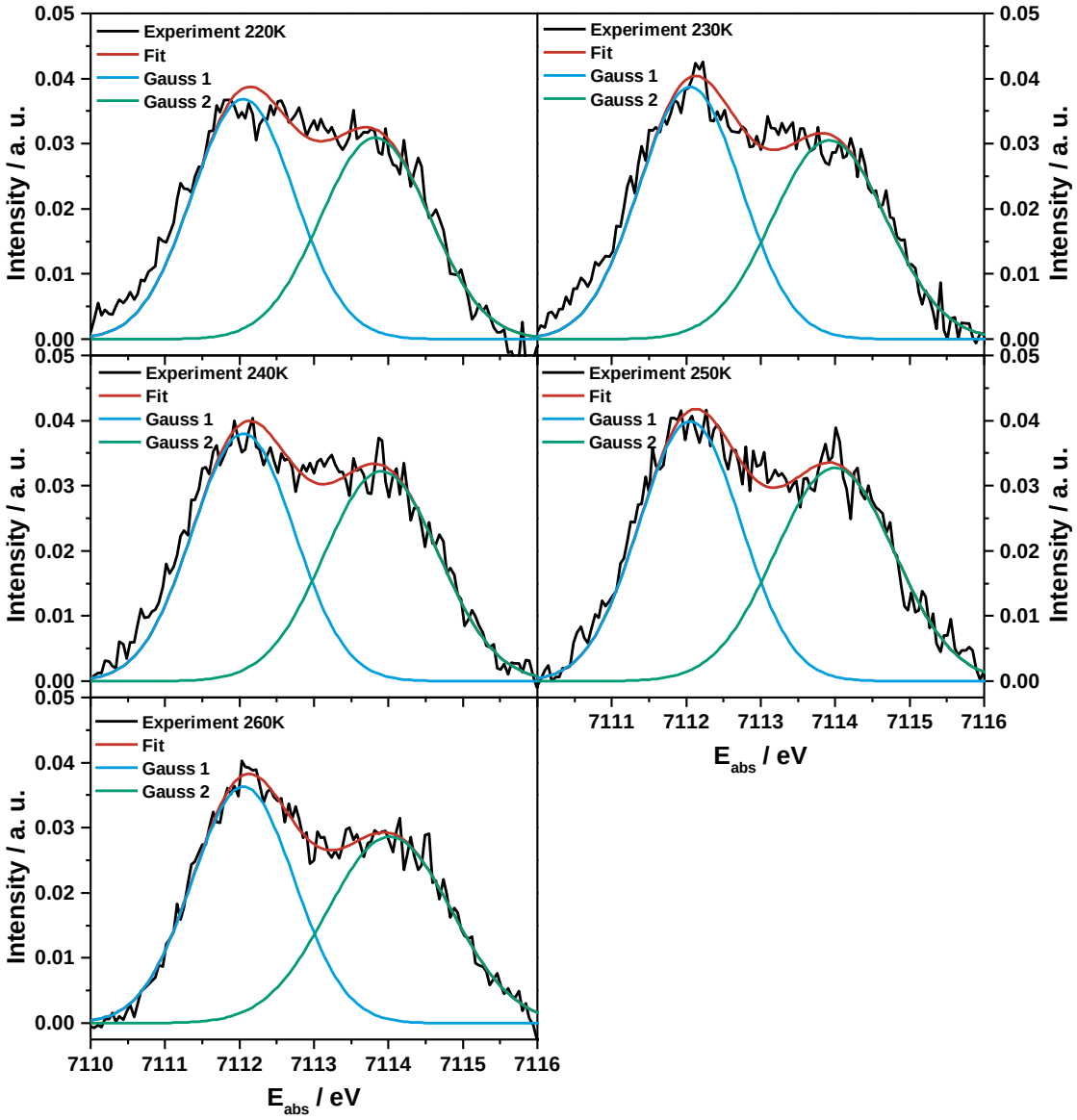

Figure 3.9: HERFD-XANES prepeak region at 220 to 260 K (top left to bottom left), fitted with two Gaussian type curves.

To correlate the experimental, or more specific the resulting fit parameters with the spin state, two different methods were tested. For the first approach, the intensities of the fit functions were plotted versus temperature to receive the temperature-dependent behaviour, which was then compared with the spin transition curve obtained by SQUID magnetometry. For the second method, the areas of the two Gaussian type fit curves and the resulting envelope were read out and then the HS fraction of the total area was determined and plotted versus temperature. The energetic positions and intensities of the fit curves used for method 1 are shown in Table 15.

Table 15: Energetic positions and intensities of applied Gaussian fit functions.

T / K	Maximum 1 / eV	Maximum 2 / eV	Intensity 1 / a. u.	Intensity 2 / a. u.
30	7112.052	7113.858	0.0305	0.0299
40	7112.052	7113.843	0.0301	0.0294
50	7112.052	7113.740	0.0216	0.0302
70	7112.052	7113.624	0.0069	0.0340
80	7112.052	7113.653	0.0032	0.0304
90	7112.052	7113.718	0.0042	0.0306
100	7112.052	7113.655	0.0052	0.0303
110	7112.052	7113.651	0.0047	0.0316
120	7112.052	7113.658	0.0060	0.0326
130	7112.052	7113.690	0.0059	0.0314
140	7112.052	7113.629	0.0067	0.0323
150	7112.052	7113.715	0.0080	0.0311
160	7112.052	7113.697	0.0103	0.0322
170	7112.052	7113.614	0.0107	0.0312
180	7112.052	7113.683	0.0163	0.0298
190	7112.052	7113.811	0.0216	0.0300
200	7112.052	7113.754	0.0261	0.0308
210	7112.052	7113.852	0.0306	0.0308
220	7112.052	7113.823	0.0369	0.0309
230	7112.052	7113.919	0.0387	0.0305
240	7112.052	7113.907	0.0380	0.0322
250	7112.052	7113.993	0.0399	0.0327
260	7112.052	7114.015	0.0363	0.0286

The plot of the intensities versus temperature reveals that the intensity of the higher energetic band remains constant within the temperature-dependent measurements, only small variations in intensity are observable, which can be ascribed to the signal-to-noise ratio (Figure 3.10).

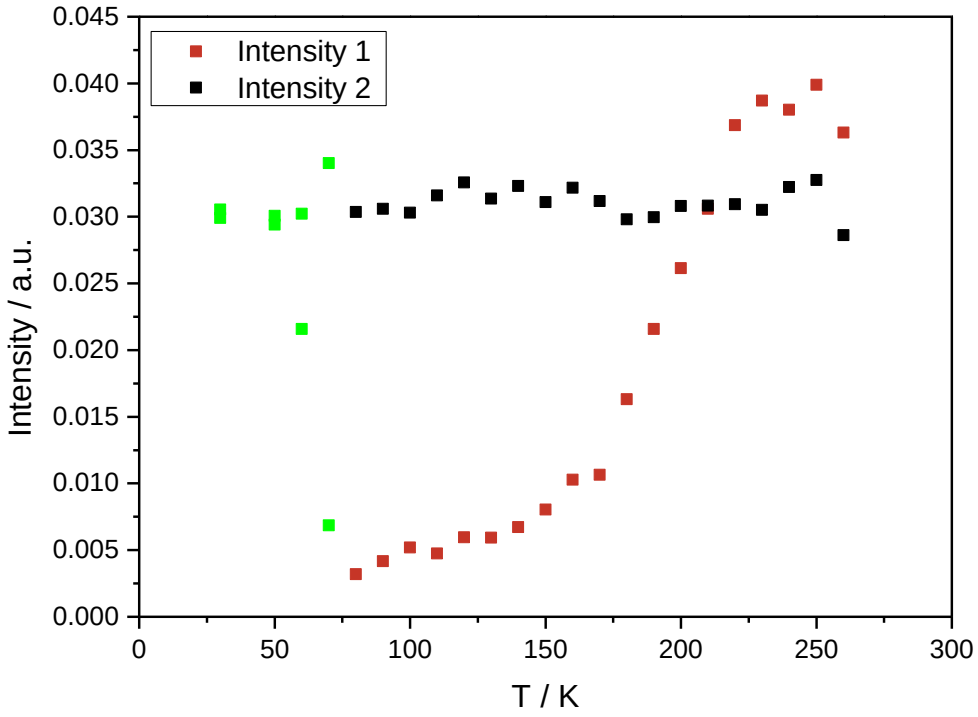

Figure 3.10: Plot of intensity versus temperature for both applied Gaussian fit curves.

In contrast to this, the signal at lower energies shows an increase with a sigmoidal shape with rising temperature. Since this signal can be assigned to the HS state, as explained above, the intensity values were fitted with a sigmoidal Boltzmann function and the fit with the resulting parameters is shown in the appendix (cf. Appendix, Figure A.9). The green marked data points depict the intensity at temperatures with HAXIESST effect and therefore, these values were excluded from the fit. The applied Boltzmann fit results in a transition temperature of $T_{1/2}$(Intensity 1) = 191.2 ± 1.7 K which is in very good agreement with the transition temperature obtained by SQUID magnetometry ($T_{1/2}$(SQUID) = 192.0 ± 0.2 K).
In addition, the comparison of the Boltzmann fit function resulting from the fit of the HS intensities and the magnetization curve obtained by SQUID magnetometry reveals that the fit curve of the intensity matches the magnetization curve nearly perfectly (cf. Figure 3.11).

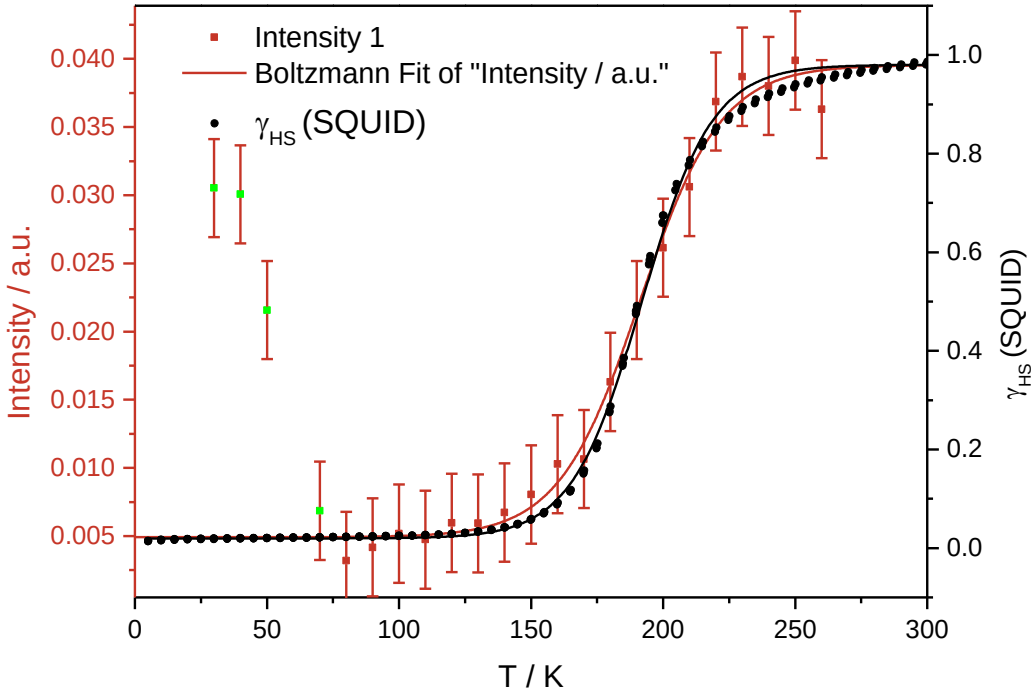

Figure 3.11: Comparison of magnetization curve obtained by fitting the intensity of the HS signal of the HERFD prepeak with the HS fraction obtained by SQUID magnetometry.

Even though the first applied method gives really good results, the second described approach was tested, too. For this method, the area of the fitted signals and the total area of the background corrected prepeak were determined and then the ratio between the two features and the total area was calculated and plotted versus temperature. The obtained values are listed in Table 16.

Table 16: Areas of total fit, fit curve 1, fit curve 2 and ratios of the respective curves and total area.

T / K	A_{total} / a.u.	A_1 / a.u.	A_2 / a.u.	$\frac{A_1}{A_{total}}$ / %	$\frac{A_2}{A_{total}}$ / %
30	0.10627	0.05224	0.05403	49.16	50.84
40	0.10421	0.05147	0.05275	49.39	50.61
50	0.09683	0.03692	0.05991	38.13	61.87
70	0.08260	0.01173	0.07087	14.20	85.80
80	0.07237	0.00544	0.06693	7.52	92.48
90	0.07176	0.00713	0.06464	9.93	90.07
100	0.07173	0.00886	0.06286	12.36	87.64
110	0.07397	0.00811	0.06586	10.96	89.04
120	0.07684	0.01021	0.06663	13.29	86.71
130	0.07597	0.01015	0.06581	13.37	86.63
140	0.08045	0.01151	0.06894	14.31	85.69
150	0.07880	0.01377	0.06503	17.48	82.52
160	0.08365	0.01758	0.06607	21.02	78.98
170	0.08494	0.01823	0.06671	21.46	78.54
180	0.08666	0.02791	0.05876	32.20	67.80
190	0.09613	0.03693	0.05920	38.41	61.59
200	0.10619	0.04475	0.06144	42.14	57.86
210	0.11115	0.05237	0.05878	47.12	52.88
220	0.11977	0.06310	0.05667	52.68	47.32
230	0.12451	0.06622	0.05829	53.18	46.82
240	0.12672	0.06505	0.06167	51.33	48.67
250	0.13343	0.06827	0.06517	51.16	48.84
260	0.12125	0.06215	0.05910	51.26	48.74

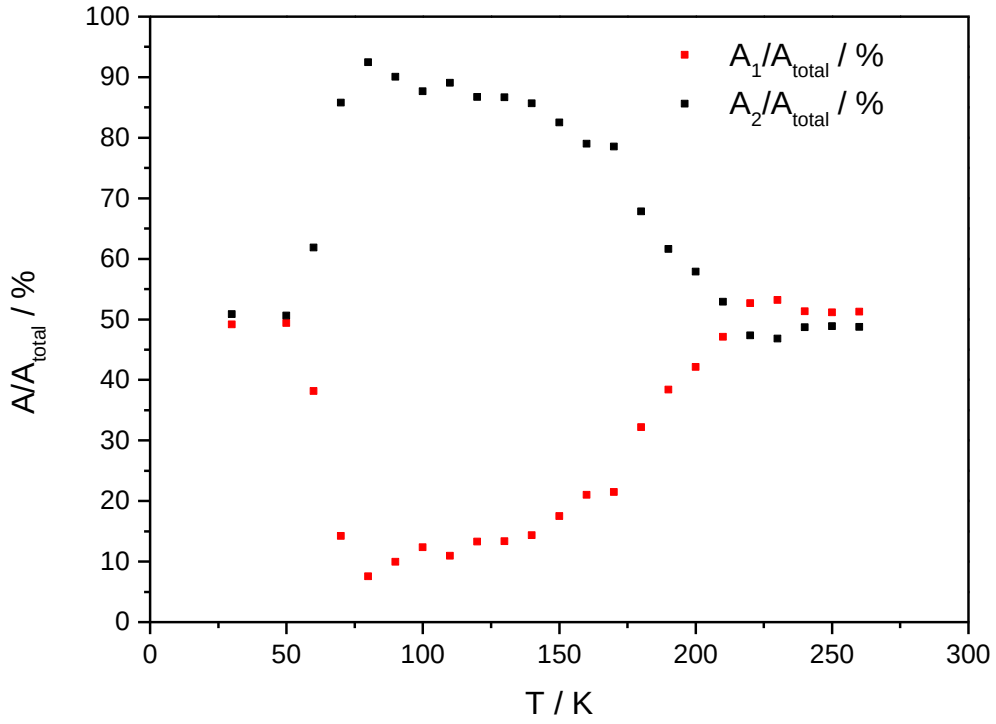

Figure 3.12: Ratio between area of signal 1 (7112 eV) and total prepeak area (red) and between area of signal 2 (7113.6 – 7114.0 eV) and total area (black).

The ratios between the areas of the two signals and the total area show a reverse temperature-dependent behaviour, as can be seen in Figure 3.12. At low temperatures, except for the HAXIESST region from 30-50 K, the prepeak is dominated by the signal at around 7113.5 to 7114 eV, which can be assigned to transitions into the e_g^* states. With increasing temperature, the fraction of the LS signal decreases while the fraction of the HS signal at 7112 eV increases. From around 200 K up to 260 K, the two signals reach almost the same constant values.

Since the variation of the signal at 7112 eV shows the typical sigmoidal shape, a Boltzmann fit was applied, which results in a transition temperature of $T_{1/2}(A_1) = 180.8 \pm 2.0$ K (cf. Appendix, Figure A.10). The data points at 30 to 70 K (marked green in Figure 3.13) were excluded from the fit because of the HAXIESST effect. In general, the variation of signal 2, which can be assigned to the LS state, results in an inverse Boltzmann fit function with the same transition temperature (cf. Appendix, Figure A.11).

Comparison of the spin transition curve obtained by analysis of the prepeak area referred to the area of the HS signal and the magnetization curve obtained by SQUID magnetometry (Figure 3.13) shows that the area fraction of signal 1 starts to increase at lower temperatures than the magnetization. Additionally, the plot of the prepeak area shows a smaller slope than the SQUID curve. Therefore, the transition temperature is shifted by around 10 K to lower temperatures and the overall curve shape is more gradual compared to the magnetization obtained by SQUID.

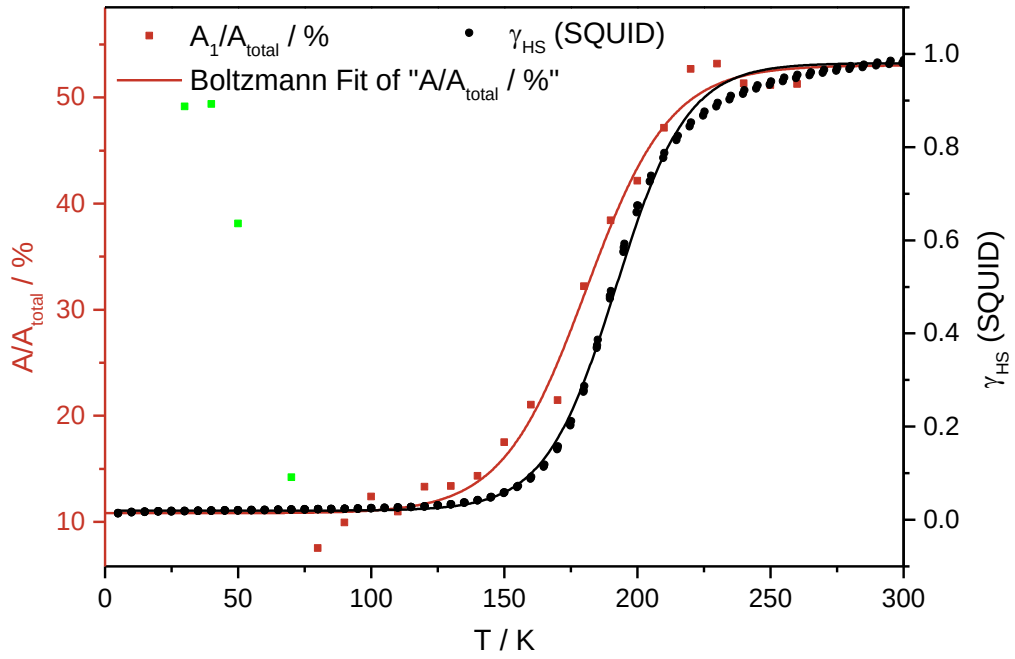

Figure 3.13: Comparison of magnetization curve obtained by analysis of the prepeak area (red) and by SQUID magnetometry (black)

3.3 Summary

Focus of this chapter was the analysis of the temperature-dependent HERFD-XANES spectra. First, the conventional XANES data were compared with the high energy resolution data to demonstrate the improved resolution and the better separation of the prepeak features from the main edge. For the evaluation of the temperature dependence, it was necessary to extract the prepeak from the spectra. Therefore, a method for background correction was established, which is applicable for all temperature points with only minor variations. All spectra were fitted with a Boltzmann function in a defined energy region and the resulting fit was subtracted afterwards, yielding the extracted prepeak region. In the LS region, except of the temperature range from 30 to 70 K, there is only one asymmetric signal observable. At the very low temperatures (HAXIESST effect) and in the HS region, a second signal arises and increases in intensity. Since this second signal is obviously correlated somehow with the HS fraction, the prepeak region was fitted with two Gaussian curves and the temperature dependence of the resulting fit parameters (intensity and area) was analysed. The first approach, based on the intensity changes of the lower energetic signal, corresponding to transitions into the partly empty t_{2g} orbitals in the HS case, gave very good results compared to the magnetization data from SQUID magnetometry. The determined transition temperature is in good accordance with the SQUID data and the course of the obtained spin transition curve follows the magnetization almost exactly. The second applied method used the area fraction of the HS signal referred to the total prepeak area as a measure for the HS fraction. The resulting spin transition curve showed significant variations compared to the SQUID data, since the area starts to increase at lower temperatures and reaches its maximum before the magnetization reaches the HS state. Therefore, the obtained transition temperature differs by around 10 K from that obtained by SQUID magnetometry.

The deviations from the SQUID data in the second method could probably be explained by the very simplified procedure for deconvolution of the spectra. Even though the RIXS planes of the HS state revealed at least three signals, the fit was performed with only two signals due to the signal-to-noise ratio. Therefore, the area of the feature at lower energy may perhaps be overestimated, leading to a larger HS fraction and a shift of the transition temperature to lower values.

In contrast to this, the intensity of the first fit curve corresponding to the HS state, seems to be a very good tool to follow the changes of the magnetization. A possible explanation for the good agreement with the magnetization data may be given by the nature of the probed transitions. In general, the prepeak transitions are assigned to $1s \rightarrow 3d$ or $1s \rightarrow 3d/4p$ transitions, as described in chapter 1.3.3.2. In case of the HS state of [Fe(L-

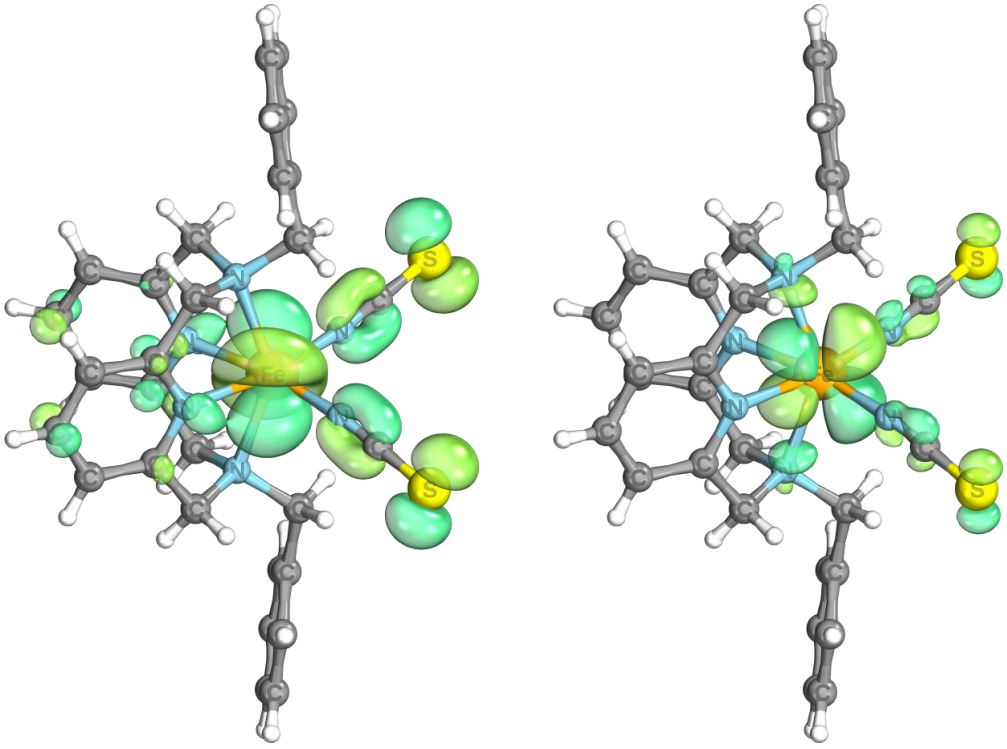

Figure 3.14: Molecular orbitals of LUMO (left) and LUMO+1 state (right).

N_4Bn_2)$(NCS)_2$], the acceptor orbitals (LUMO states) can be assigned to almost pure ligand field states, according to DFT calculations, which are described in chapter 5.2. Figure 3.14 shows the molecular orbitals of the LUMO and LUMO+1 state, which are the acceptor orbitals of the lowest lying transitions in the HERFD-XANES prepeak region. It can be seen, that these two orbitals show a very dominant Fe d-character, while only weak contributions of C, N and S are observable (cf. Appendix, Table A.1). Therefore, these transitions directly probe the changes in the distribution of the 3d electrons and thus are directly correlated with the magnetization.

4 Core-to-Core Emission Spectroscopy

The following chapter is focused on the analysis of the temperature-dependent CtC emission experiments. As already described in chapter 1.3.4.3., the spectral shape of the CtC emission spectra is changing significantly with a change of the spin state from LS to HS. The $K\beta_{1,3}$ line is shifted to higher emission energies and reduced in intensity. Additionally, a second feature, the Kβ' satellite arises with increasing HS fraction. These spectral changes are therefore analysed with different methods to quantify the spin state or more precisely the effective number of 3d electrons. The different approaches are either based on experimental parameters, such as the intensity of the Kβ' satellite or the energetic position of the $K\beta_{1,3}$ main line, or on parameters obtained by fitting of the experimental data. All parameters are correlated with temperature and if possible, the HS fractions are determined and compared with the magnetization obtained by SQUID magnetometry.

4.1 Experimental Section

CtC emission experiments were performed at beamline ID26 at the European Synchrotron Radiation Facility (ESRF, Grenoble, France). The ring current varied between 180 and 200 mA and the electron energy was 6.0 GeV. A cryogenically cooled Si(111) double-crystal monochromator was used for the measurements at the iron K-edge (7.112 keV). Energy calibration was performed using an iron foil. On the sample position the incident X-ray beam had a flux of approximately 2×10^{13} photons/s. The emission spectra were measured at a scattering angle of 90°with a 1 m diameter Rowland-circle spectrometer arranged in horizontal plane with spherically bent Ge(620) analyser crystals. The sample was diluted in boron nitride and pressed to a pellet to avoid self-absorption effects. Measurements were carried out using a closed cycle helium cryostat in a temperature range of 30 to 260 K. To avoid radiation damages several quick HERFD scans were performed at one sample spot to calculate the time in which the sample was stable, what means no changes in the spectrum were observable during this time span.

4.2 Data Analysis and Results

According to Vankó and de Groot, several approaches for the analysis of the CtC emission spectra are known, which allow a correlation of the XES data with the 3d spin momentum.[88] Therefore, the different known methods were tested for the complex [Fe(L-N_4Bn_2)$(NCS)_2$] and compared to each other. All applied approaches are explained in detail in the following sections. Due to the predominant 3p-3d exchange interaction, the spectral shape of the CtC emission spectra is very spin-selective. Therefore, the spectral changes represent the changes of the number of unpaired 3d electrons, which can be directly correlated with the magnetic changes. But it has to be mentioned, that the effective number of 3d electrons is influenced by the degree of covalency, so this might have an effect on the spectral shape and therefore the determined spin state, too. Thus, the approaches were modified to improve the agreement of the results with the magnetization data obtained by SQUID magnetometry.

4.2.1 Reference Compounds

Some of the methods presented in the following chapter require the use of reference systems with a known spin state to create a calibration curve whereby the unknown spin states of the different temperature points can be received. The used reference compounds show similar structure motifs compared to the SCO complex [Fe(L-N_4Bn_2)$(NCS)_2$] (Figure 4.1). The first LS reference [Fe(L-N_4Bn_2)(phen)]$(ClO_4)_2$·MeCN (**OS2**) is built up

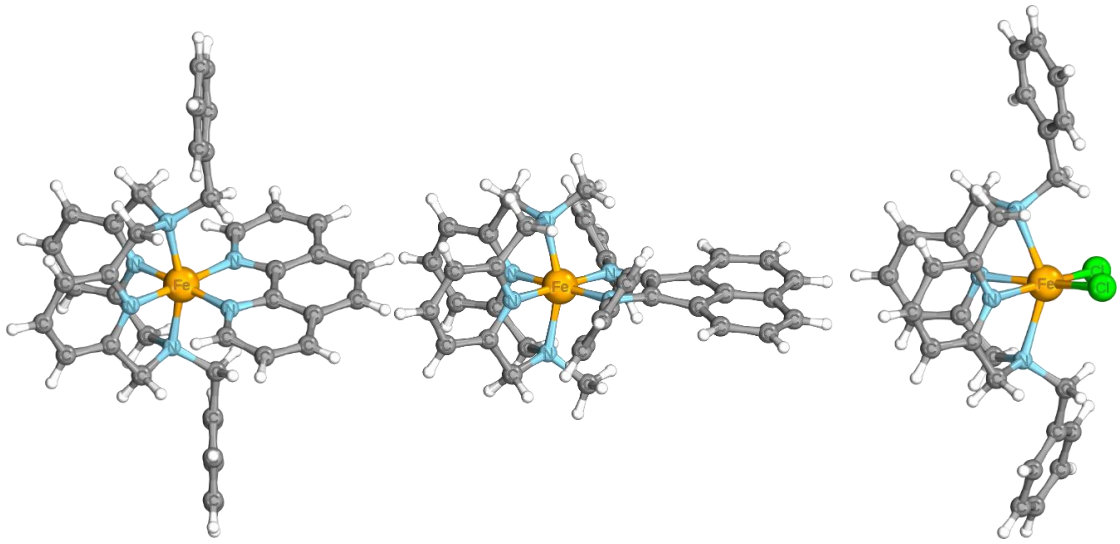

[Fe(L-N_4Bn_2)(phen)]$(ClO_4)_2$·MeCN	[Fe(L-N_4Me_2)(bian)]$(ClO_4)_2$	[Fe(L-N_4Bn_2)(Cl_2)]·MeCN
OS2	**OS7**	**OS1**
LS, S = 0	LS, S = 0	HS, S = 2

Figure 4.1: Crystal structures of the LS and HS reference compounds used for calibration.

with the same macrocyclic ligand (L-N_4Bn_2) but the two isothiocyanato ligands are replace by a bidentate phenanthroline ligand that enhances the ligand field strength of the complex, so it remains in the LS state at all temperatures. The second LS reference is built with the L-N_4Me_2 ligand and the two NCS ligands are replace by a bidentate bis(phenyl)iminoacenaphtene (bian) ligand (**OS7**). The HS reference [Fe(L-N_4Bn_2)(Cl_2)]·MeCN (**OS1**) has the same structural motif like the SCO complex. Only the two isothiocyanato ligands are replaced by two chloro ligands. Therefore, the ligand field strength is reduced so that the complex remains in the HS state at all temperatures. In addition, potassium hexacyanoferrate (III) (**K_3[Fe(CN)$_6$]**) was used as reference. In contrast to the other three reference compounds K_3[Fe(CN)$_6$] has an oxidation state of +III instead of +II and only one unpaired electron, leading to a spin state of S = 0.5.

Figure 4.2 displays the CtC emission spectra of the reference compounds **OS1**, **OS2** and **OS7**. The complex **OS7** was measured at 20 K and 200 K to check if there were any differences in the spectra observable at different temperatures. Since this was not the case, the other references were measured only at 200 K. The displayed spectra were normalized to area, what means that the spectra were integrated in the energy range from 7030 to 7070 eV and then the intensity values were divided by the resulting area. The Kβ main line and the Kβ' signal show a characteristic behaviour for HS or LS systems.[88,147] With increasing valence spin the two signals move away from each other, so the Kβ main line of **OS1** is shifted to higher emission energies (7059.0 eV) compared to the Kβ main line of the two LS complexes **OS2** and **OS7** (7057.4 eV). Furthermore, the Kβ' signal is

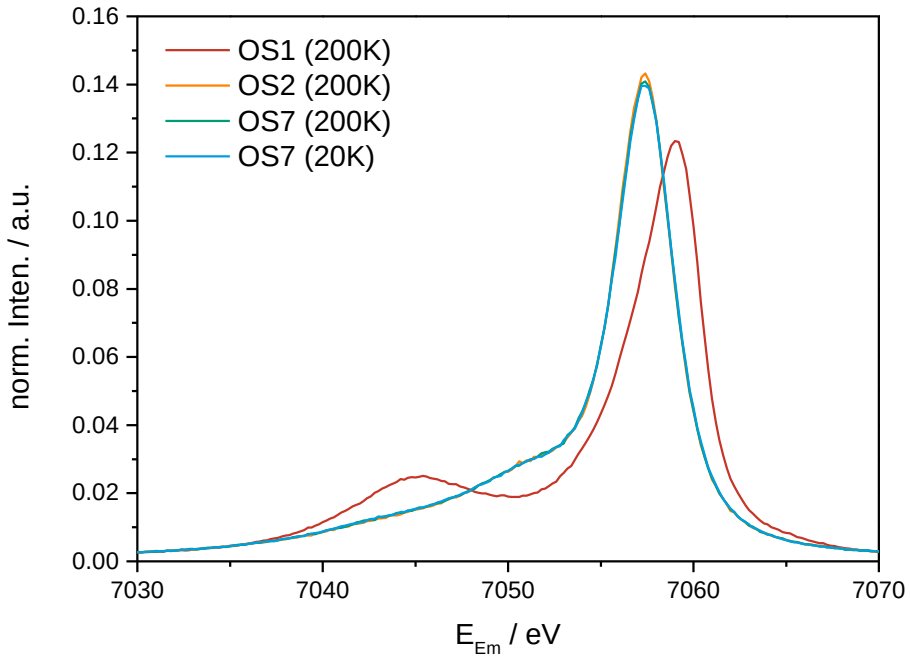

Figure 4.2: CtC emission spectra of the HS and LS reference compounds.

shifted to lower energies (7045.1 eV) and the intensity is increased with a higher number of unpaired 3d electrons, leading to an increased 3p-3d exchange interaction compared to the LS state (shoulder at 7050.7 eV).

4.2.2 Correlation between experimental / fitting Parameters and Spin State

The first described approach is based on the correlation of experimental parameters, like the emission energy of the Kβ main line or the intensity of the Kβ' signal, with the spin state of the system. For the second approach the fitting parameters obtained by deconvolution of the emission spectra, like area, energetic position and intensity of the underlying fit functions, were correlated with the spin state.

4.2.2.1 Creation of Calibration Curves by Use of Reference Compounds

For evaluation of the reference spectra and the construction of different possible calibration curves, the spectra were deconvolved first. Figure 4.3 displays the deconvolution of the complexes **OS1**, **OS2** and **OS7**, while Figure 4.4 shows the deconvolution of **$K_3[Fe(CN)_6]$**. The spectrum of the HS complex **OS1** was fitted with only two components, namely one Voigt function and one asymmetric Lorentz function, whereas the

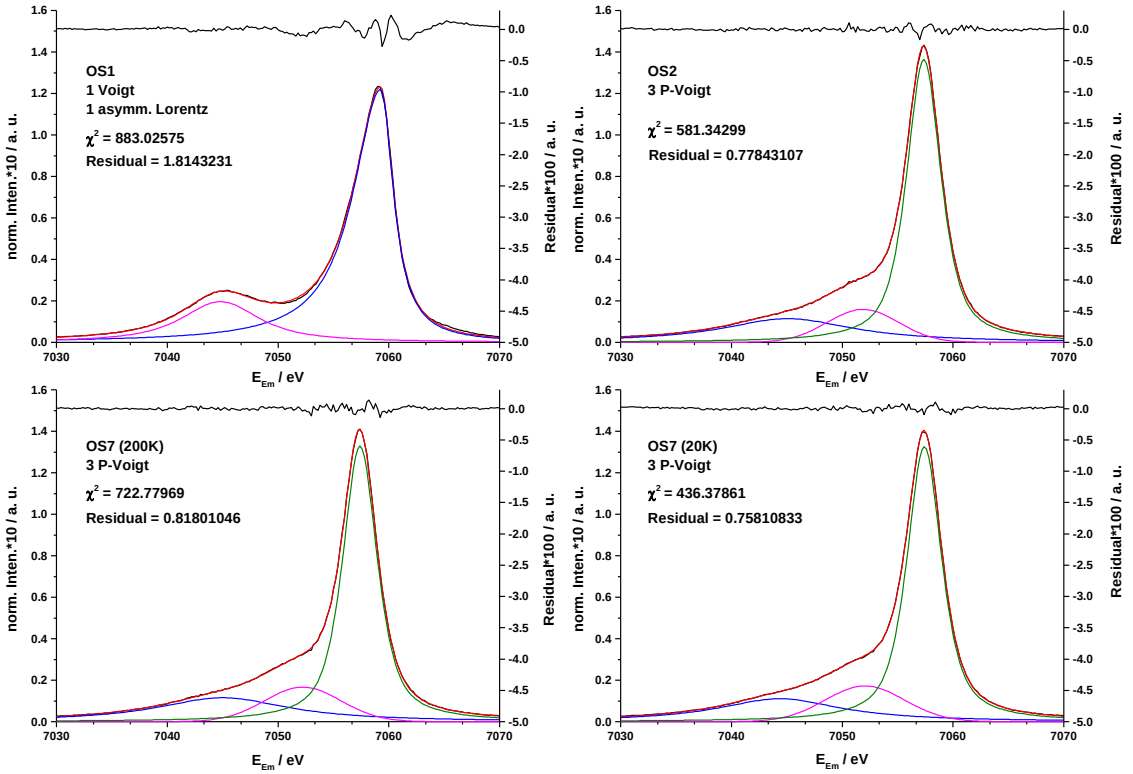

Figure 4.3: Deconvolved CtC emission spectra of the reference compounds **OS1** (top left), **OS2** (top right) and **OS7** (200 K bottom left, 20 K bottom right).

spectra of the LS references were fitted with three components. In case of **$K_3[Fe(CN)_6]$** two Pseudo-Voigt functions and one asymmetric Voigt function were used for deconvolution, while for the remaining complexes three Pseudo-Voigt functions were used.[160]

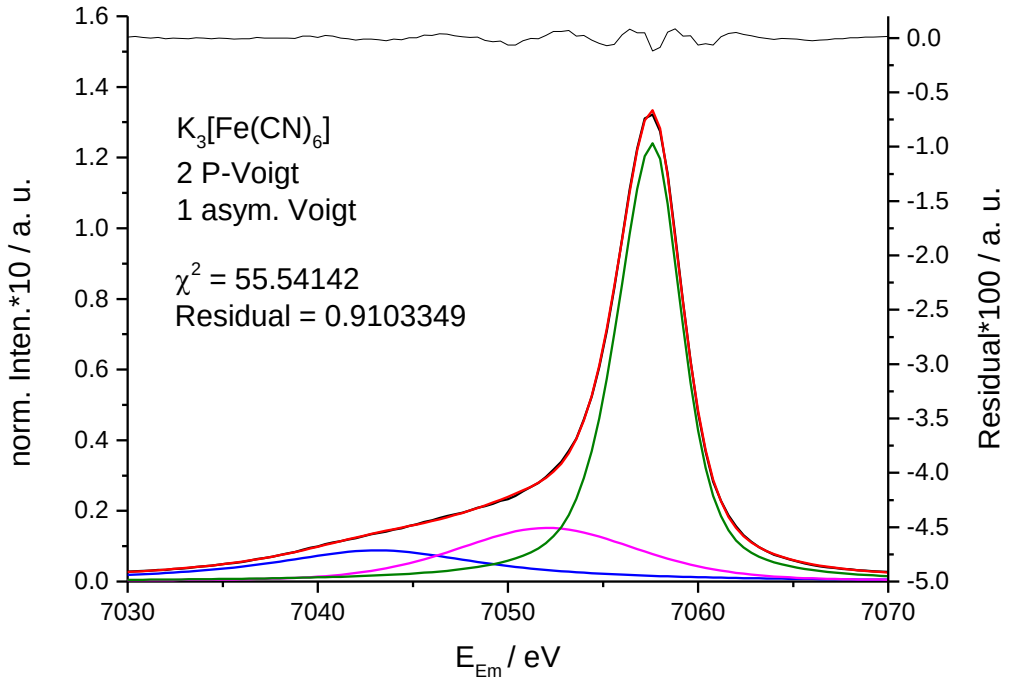

Figure 4.4: Deconvolved CtC emission spectrum of the reference compound **$K_3[Fe(CN)_6]$**.

The different calibration curves were constructed with use of several parameters that were read out and plotted versus the known spin states of the reference compounds. A linear fit of the data results in the respective calibration curves. The used parameters are listed in Table 17. Here, the emission energy of the Kβ main line $E_{Em}(K\beta_{1,3})$ and the intensity of the Kβ' signal *Inten.(Kβ')* are experimental parameters, while *E* (energy), *Inten.* (peak intensity) and *A* (peak area) are the parameters of the fit curves (FC) 1 to 3. Fit curve 1 corresponds to the Kβ main line, fit curve 2 is assigned to the Kβ' signal, while the third one represents the fit curve in the middle energy range.

Table 17: Parameters of experimental spectra and fit functions of the reference compounds.

	OS2	**OS7 (20K)**	**OS7 (200K)**	**$K_3[Fe(CN)_6]$**	**OS1**
Spin	0	0	0	0.5	2
$E_{Em}(K\beta_{1,3})$ / eV	7057.4	7057.4	7057.4	7057.6	7059.0
Inten.(Kβ') / a. u.	0.01555	0.01583	0.01583	0.01653	0.02513
E(FC 1) / eV	7057.4	7057.4	7057.4	7057.6	7059.2
Inten.(FC 1) / a. u.	0.1364	0.1329	0.1326	0.1240	0.1220
A(FC 1) / a. u.	0.67286	0.66205	0.65562	0.65807	0.78122
E(FC 2) / eV	7045.0	7044.4	7045.0	7043.1	7044.8
Inten.(FC 2) / a. u.	0.01142	0.01106	0.01155	0.00882	0.01965
A(FC 2) / a. u.	0.19885	0.18217	0.19987	0.14521	0.21588
E(FC 3) / eV	7051.8	7052.1	7052.2	7052.1	--
Inten.(FC 3) / a. u.	0.01589	0.01723	0.01665	0.01519	--
A(FC 3) / a. u.	0.12847	0.15453	0.14425	0.19684	--

Using the experimental parameters, the following calibration curves (Figure 4.5) were constructed, leading to equations (23) and (24).

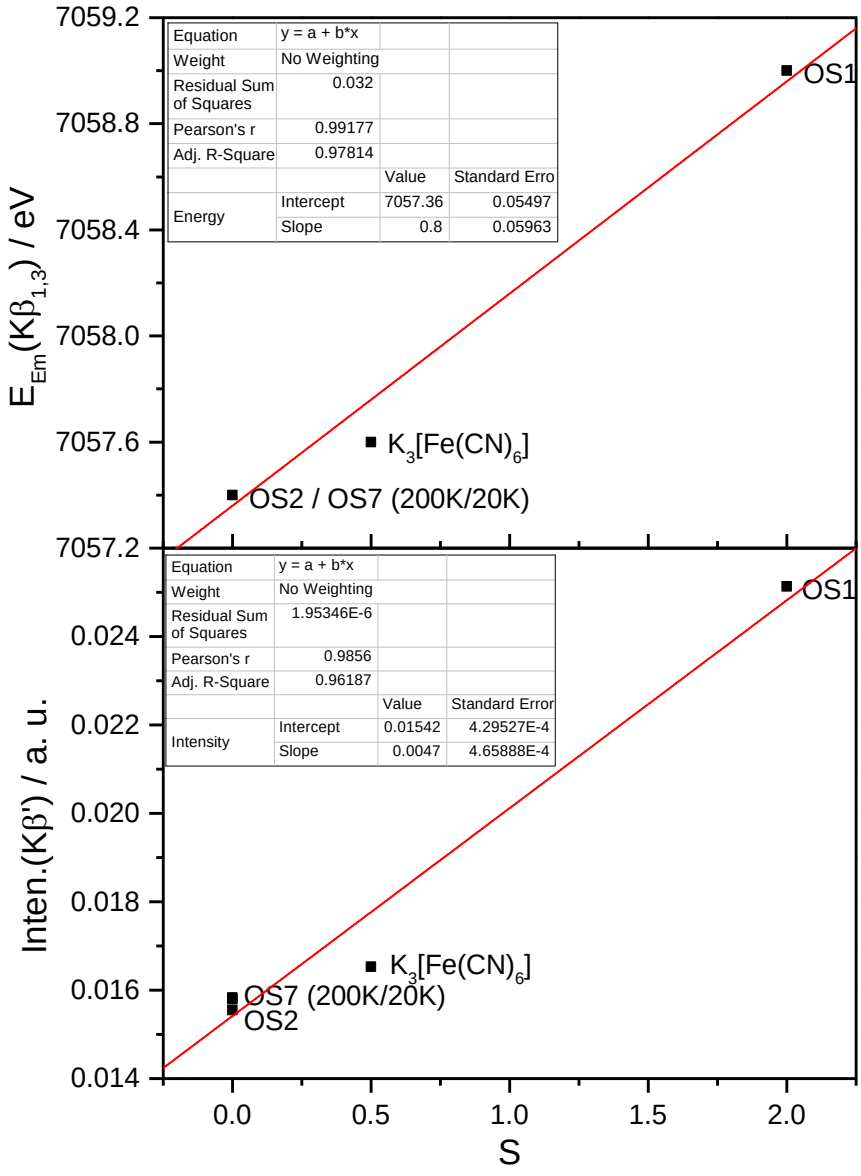

Figure 4.5: Calibration curves based on the experimental emission energy $E_{Em}(K\beta_{1,3})$ (top) and the intensity *Inten.(Kβ')* (bottom).

$$S = \frac{E_{Em}(K\beta_{1,3}) - 7057.36}{0.8} \tag{23}$$

$$S = \frac{Inten.(K\beta') - 0.01542}{0.0047} \tag{24}$$

The parameters of the three fit curves obtained by deconvolution of the reference spectra were plotted versus the spin *S* and used for construction of further calibration curves as well. Figure 4.6 shows the different calibration curves of the energetic position, intensity and area of fit curve 1. The linear fits of the data lead to equations (25) – (27).

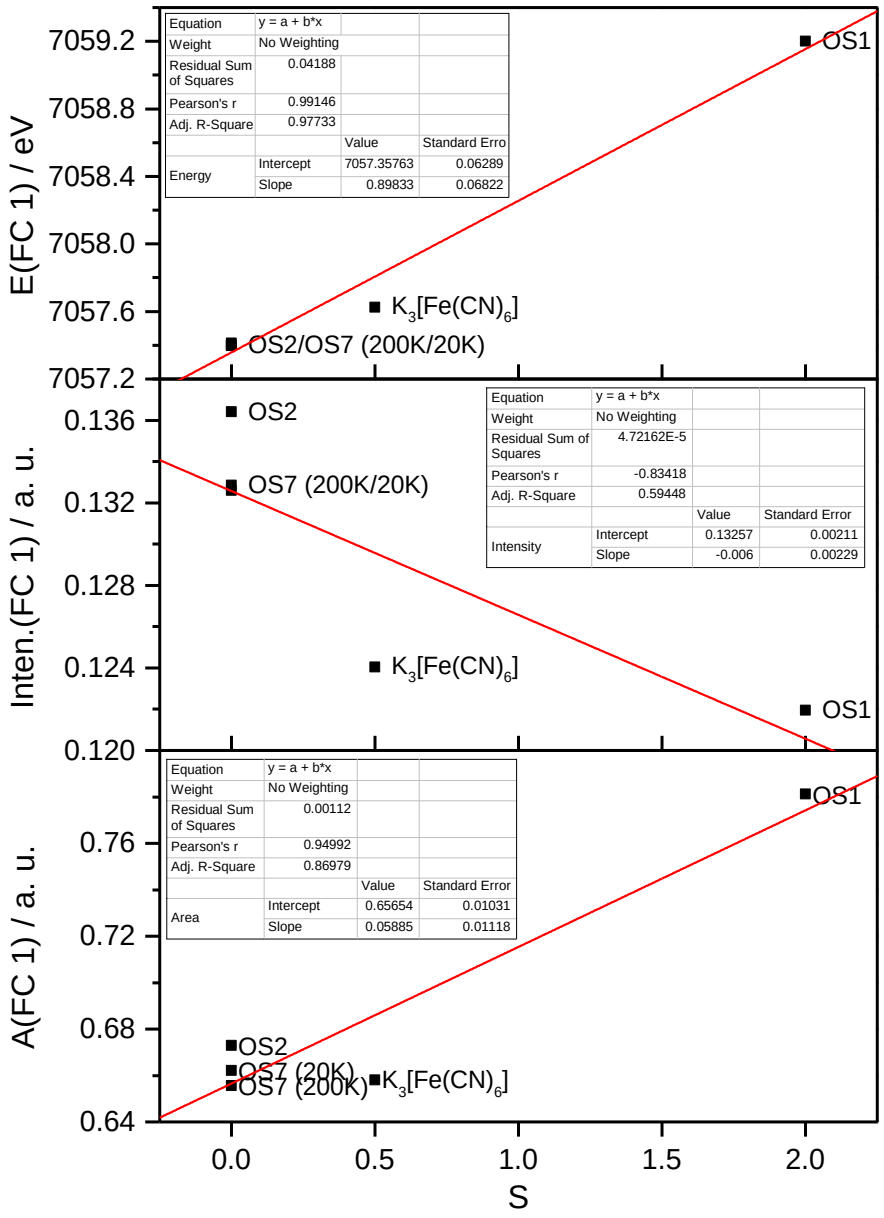

Figure 4.6: Calibration curves based on energetic position (top) , intensity (middle) and area (bottom) of fit curve 1.

$$S = \frac{E(FC1) - 7057.35763}{0.89833} \tag{25}$$

$$S = -\frac{Inten.(FC1) - 0.13257}{0.006} \tag{26}$$

$$S = \frac{A(FC1) - 0.65654}{0.05885} \tag{27}$$

The calibration curves resulting from the parameters of fit curve 2, corresponding to the Kβ' signal, are displayed in Figure 4.7. The linear fits of the data give equations (28) to (30).

$$S = \frac{E(FC2) - 7044.4578}{0.006} \tag{28}$$

$$S = \frac{Inten.(FC2) - 0.01042}{0.00415} \tag{29}$$

$$S = \frac{A(FC2) - 0.18283}{0.01113} \tag{30}$$

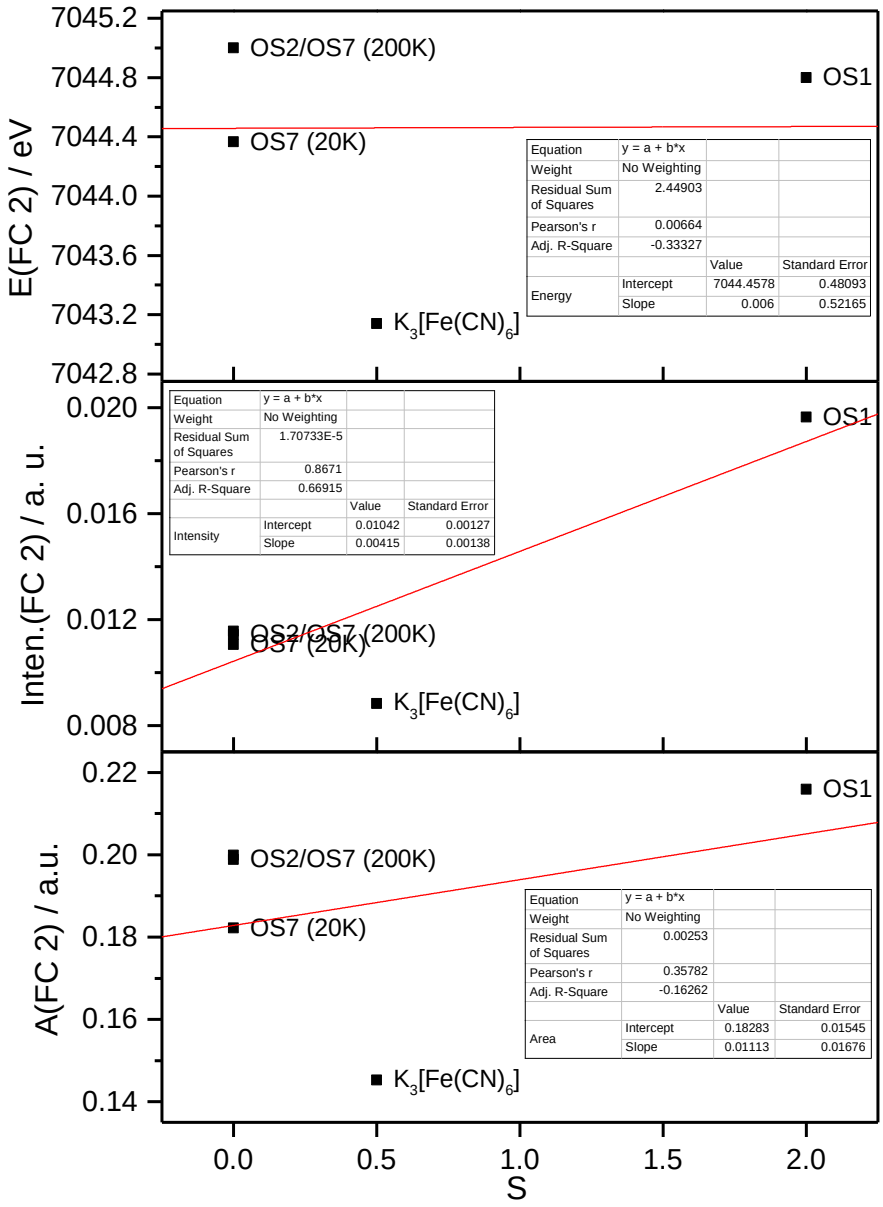

Figure 4.7: Calibration curves based on energetic position (top) , intensity (middle) and area (bottom) of fit curve 2.

The calibration curves obtained by linear fitting of the parameters of fit curve 3 are shown in Figure 4.8. Since the HS reference **OS1** was deconvolved with only two signals, there are no parameters for a HS system available for the construction of the calibration curves. Therefore, these three calibration curves are of minor use for the determination of the spin state. The fits result in equations (31) to (33).

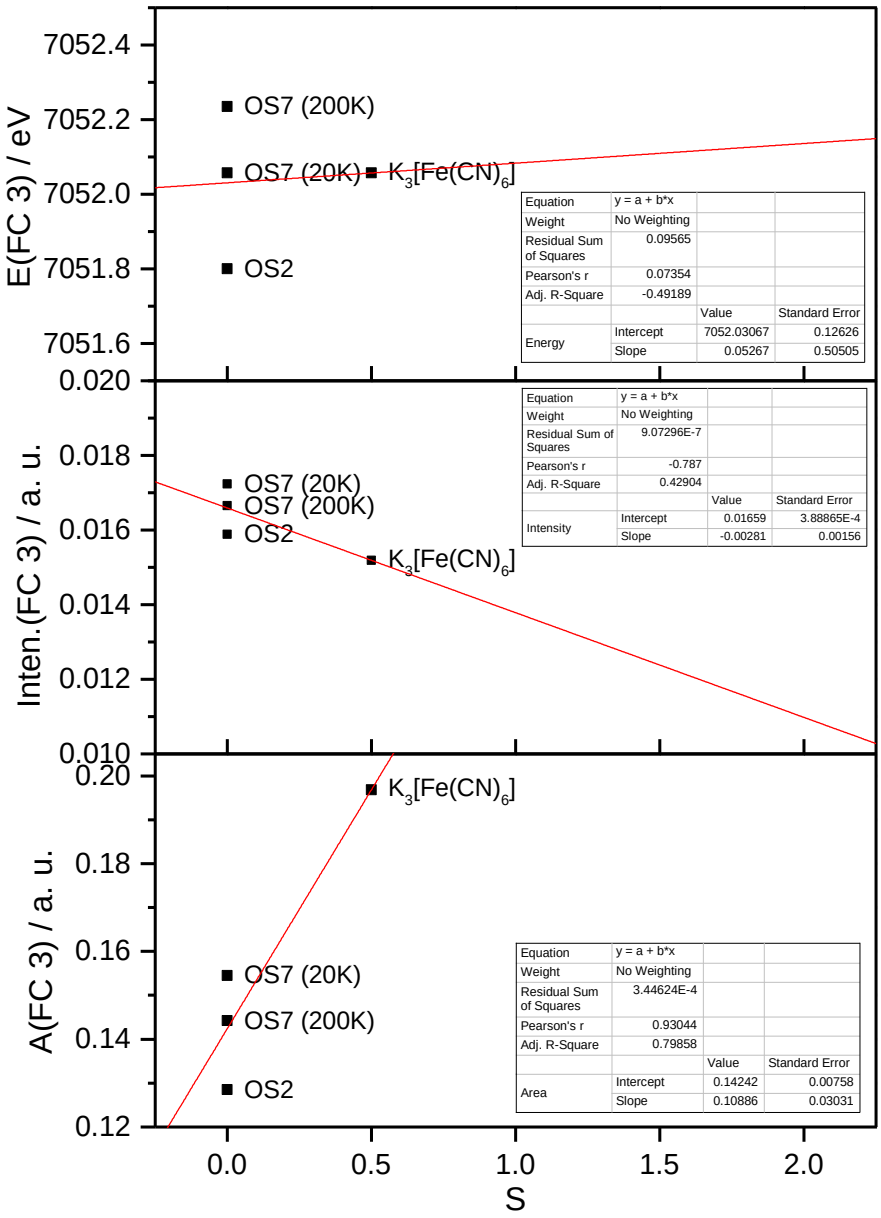

Figure 4.8: Calibration curves based on energetic position (top) , intensity (middle) and area (bottom) of fit curve 3.

$$S = \frac{E(FC3) - 7052.03067}{0.05267} \tag{31}$$

$$S = -\frac{Inten.(FC3) - 0.01659}{0.00281} \tag{32}$$

$$S = \frac{A(FC3) - 0.14242}{0.10886} \tag{33}$$

4.2.2.2 Deconvolution of temperature-dependent CtC Spectra of $[Fe(L\text{-}N_4Bn_2)(NCS)_2]$

The deconvolution of the area-normalized CtC emission spectra of all temperatures was performed with two symmetric and one asymmetric Pseudo-Voigt functions. During the fit procedure the two symmetric functions were fixed at emission energies of 7045.18 eV and 7052.50 eV, so only the function that reproduces the Kβ main line was iterated freely in energy. Intensity and full width at half maximum (FWHM) were iterated freely for all

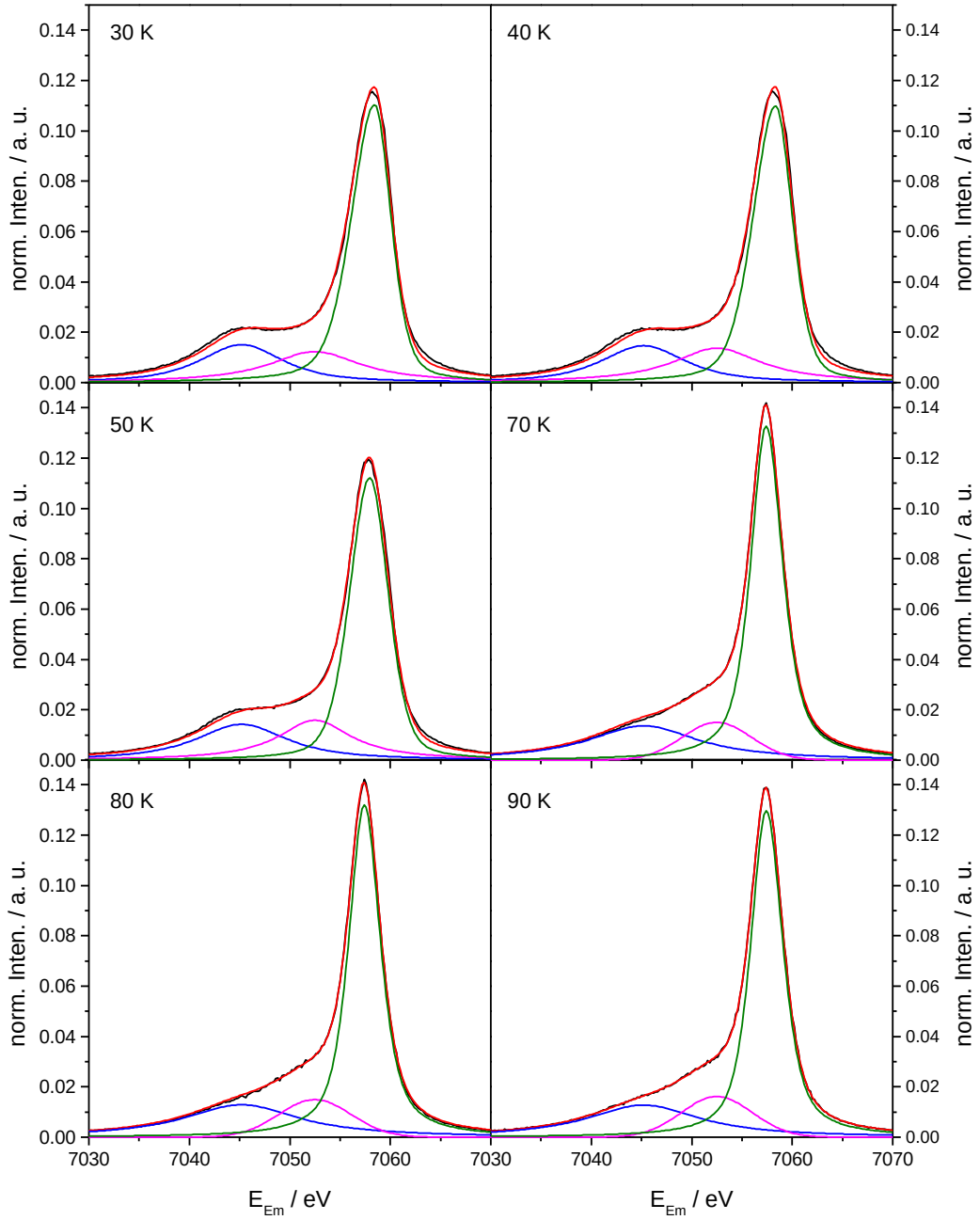

Figure 4.9: CtC emission spectra with resulting fit functions, temperature range from 30 to 90 K.

three functions. The emission spectra of all temperatures with the resulting fit functions are shown in Figure 4.9 to Figure 4.12.

It is observable, that the spectra at 30, 40 and 50 K show a distinct Kβ'signal, which disappears again at 70 K. This indicates that the complex is transformed from the LS state to a metastable HS state through irradiation with hard X-rays at low temperatures. This

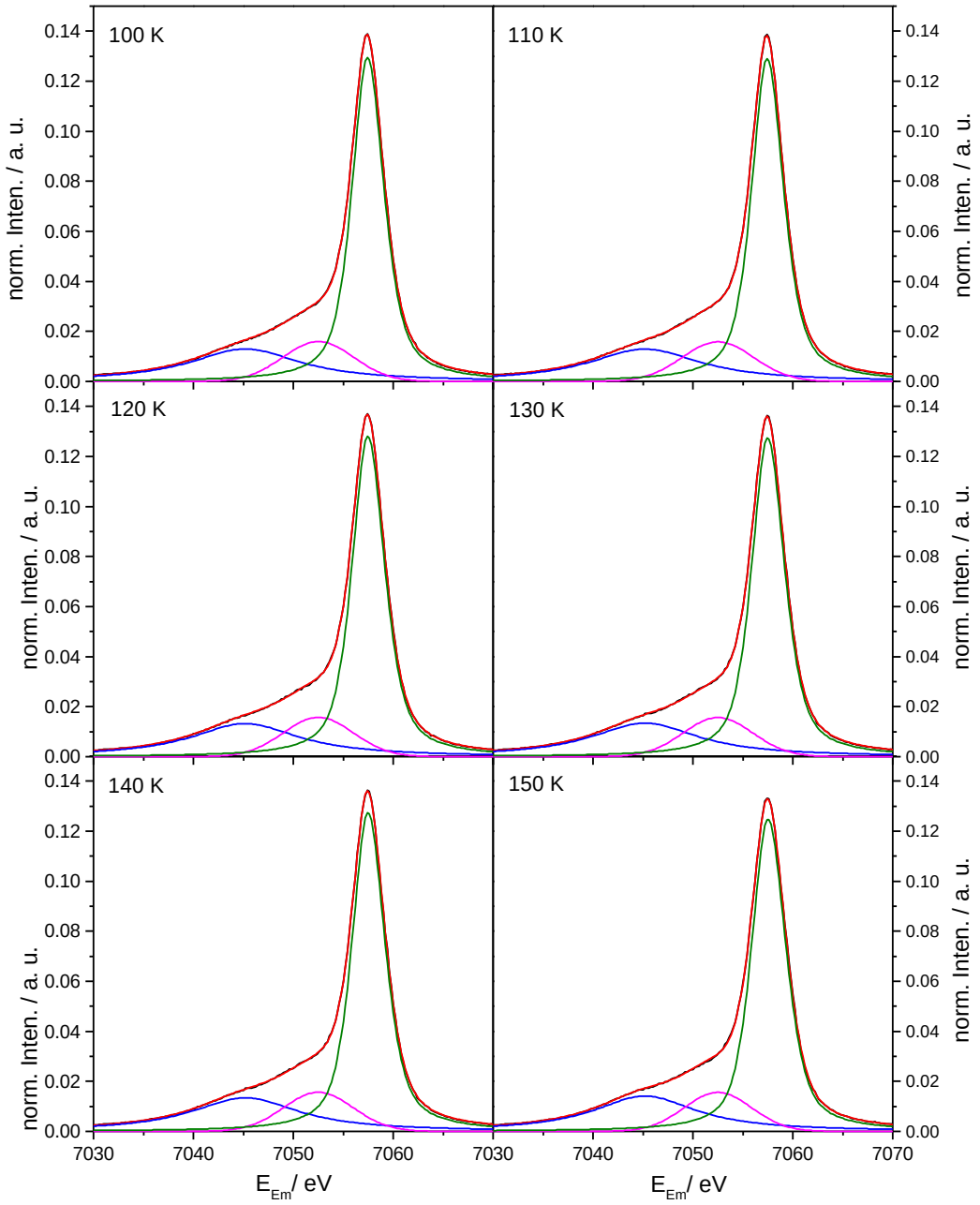

Figure 4.10: CtC emission spectra with resulting fit functions, temperature range from 100 to 150 K.

effect is again the so-called HAXIESST effect.[50] From 70 K up to around 150 K no Kβ' signal is observable. Starting from 160 K the signal emerges and steadily increases in intensity with rising temperature.

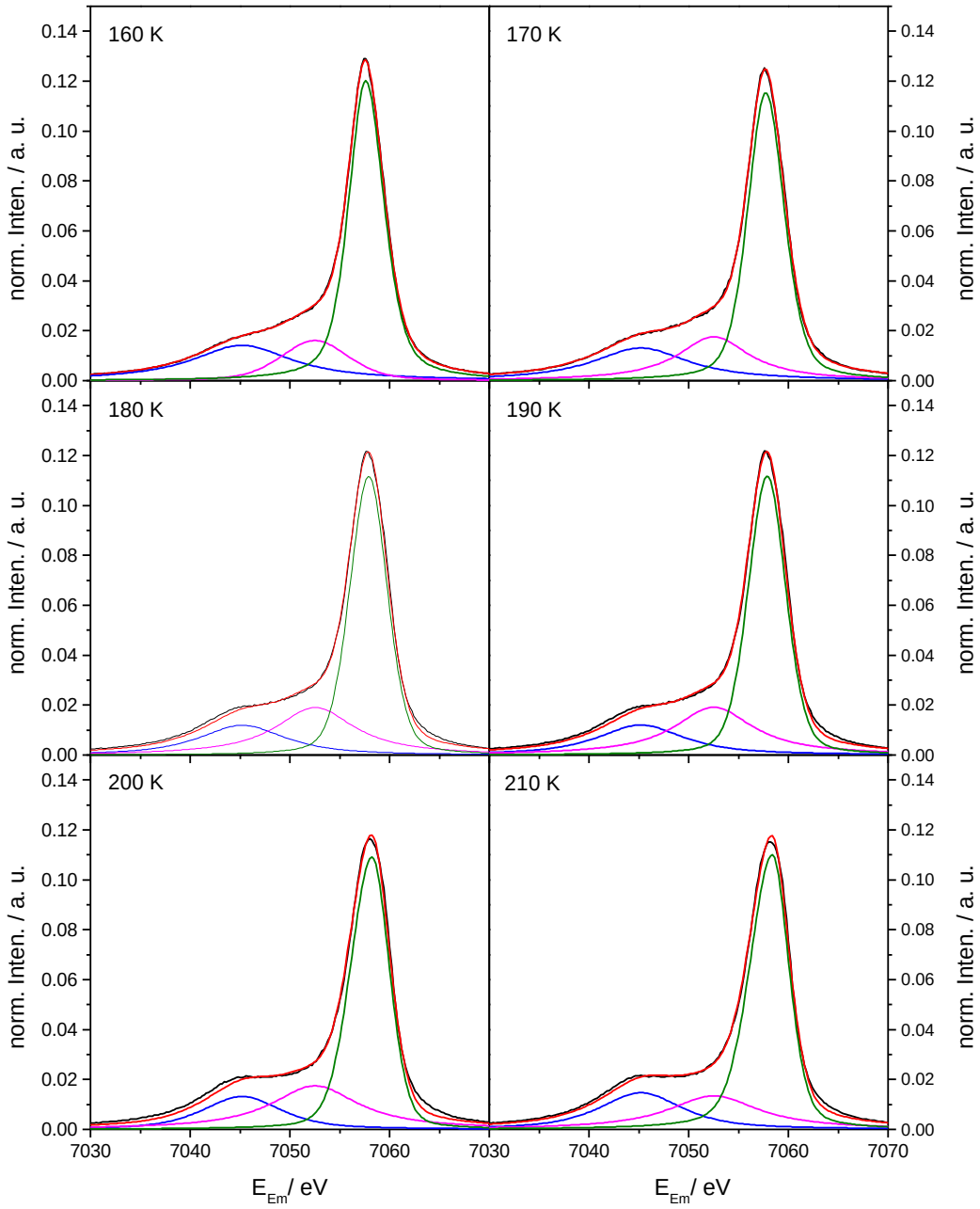

Figure 4.11: CtC emission spectra with resulting fit functions, temperature range from 160 to 210 K.

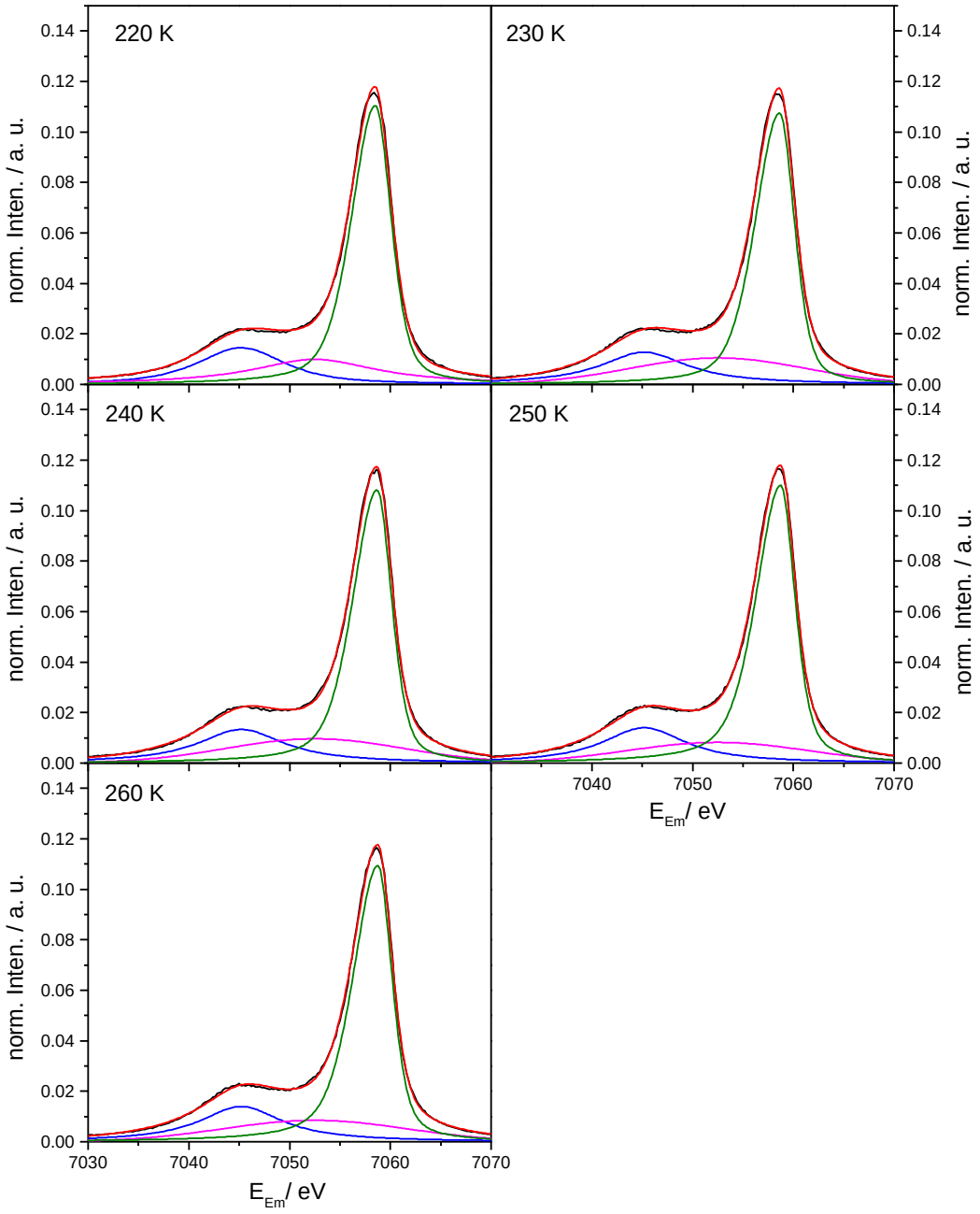

Figure 4.12: CtC emission spectra with resulting fit functions, temperature range from 220 to 260 K.

4.2.2.3 Determination of the Spin State with Use of Experimental Parameters

The first two methods for determination of the spin state of the SCO system are carried out with use of experimental parameters. The energy of the Kβ main line and the intensity of the Kβ' signal were read out at each temperature point and then the spin was calculated with use of the respective calibration curve constructed in chapter 4.2.2.1.

Spin Determination with Emission Energy of Kβ Main Line

For determination of the spin state of the complex at each temperature, the energy of the emission maximum of the Kβ main line was determined and the spin *S* was calculated with use of equation (23) (cf. Table 18). Additionally, the corresponding product of the molar magnetic susceptibility with temperature obtained by SQUID magnetometry is displayed for each temperature point.

Table 18: Determination of the spin state with use of emission maximum of Kβ main line.

T / K	$E_{Em}(K\beta_{1,3})$ / eV	S / a. u.	$\chi_M T$ / cm^3Kmol^{-1}
30	7058.2	1.05	0.07
40	7058.0	0.80	0.071
50	7057.8	0.55	0.074
70	7057.4	0.05	0.079
80	7057.4	0.05	0.082
90	7057.4	0.05	0.085
100	7057.4	0.05	0.089
110	7057.4	0.05	0.096
120	7057.4	0.05	0.105
130	7057.4	0.05	0.122
140	7057.4	0.05	0.154
150	7057.4	0.05	0.216
160	7057.4	0.05	0.335
170	7057.6	0.30	0.575
180	7057.6	0.30	1.05
190	7058.0	0.80	1.797
200	7058.0	0.80	2.467
210	7058.2	1.05	2.88
220	7058.4	1.30	3.122
230	7058.4	1.30	3.274
240	7058.6	1.55	3.374
250	7058.6	1.55	3.444
260	7058.6	1.55	3.495

To visualize the correlation of the maximum of the Kβ main line $E_{Em}(K\beta_{1,3})$ with temperature T and with the product of the molar magnetic susceptibility with temperature $\chi_M T$ the plots of these parameters are shown in Figure 4.13. In both graphs, the green marked data points depict the emission maximum of the spectra at very low temperatures, where the HAXIESST effect is observable. The energy of the emission maximum indicates that the complex shows a certain HS fraction at these temperatures because the maximum is shifted to higher energies compared to the other spectra in the temperature range from 70 to 160 K, where the complex should exist in the LS state. As an overall trend, the emission maximum of the Kβ main line shifts to higher energies with rising temperatures (exception 30, 40 and 50 K). The maximum stays constant at 7057.4 eV in the temperature range from 70 to 160 K and at 170 K the maximum starts to shift until it reaches 7058.6 eV at 260 K (Figure 4.13 left).

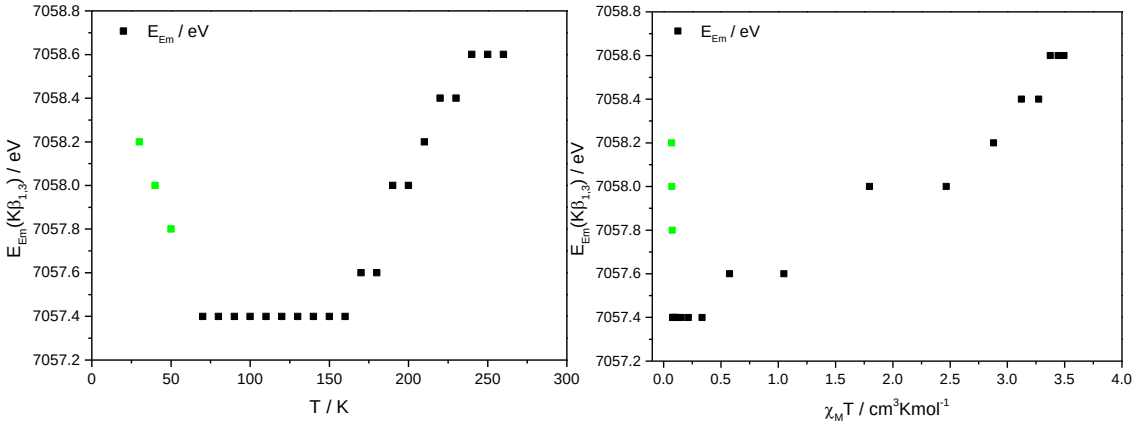

Figure 4.13: left: Plot of emission maximum $E_{Em}(K\beta_{1,3})$ vs. temperature T, right: Plot of emission maximum $E_{Em}(K\beta_{1,3})$ vs. product of molar magnetic susceptibility with temperature $\chi_M T$.

The plot of the energy of the Kβ main line versus the product of the molar magnetic susceptibility with temperature shows a similar behaviour (Figure 4.13 right). Small values of $\chi_M T$ are correlated with lower energies of the Kβ main line, whereas increasing $\chi_M T$ leads to a shift of the maximum to higher energies.

Since these three parameters depend on each other, a three dimensional plot is displayed, too (Figure 4.14). Therein, the 2D projections of the data are indicated in light blue, green and red. The X-Y-projection (red) corresponds to the magnetization curve (cf. Figure 1.25), while the X-Z-projection (green) and the Y-Z-projection (light blue) correspond to the two plots in Figure 4.13. It is remarkable that in the Y-Z-projection several data points appear at an emission energy of 7057.4 eV with only slightly changing values of $\chi_M T$. These data points correspond to the low temperatures where the system stays in the LS state.

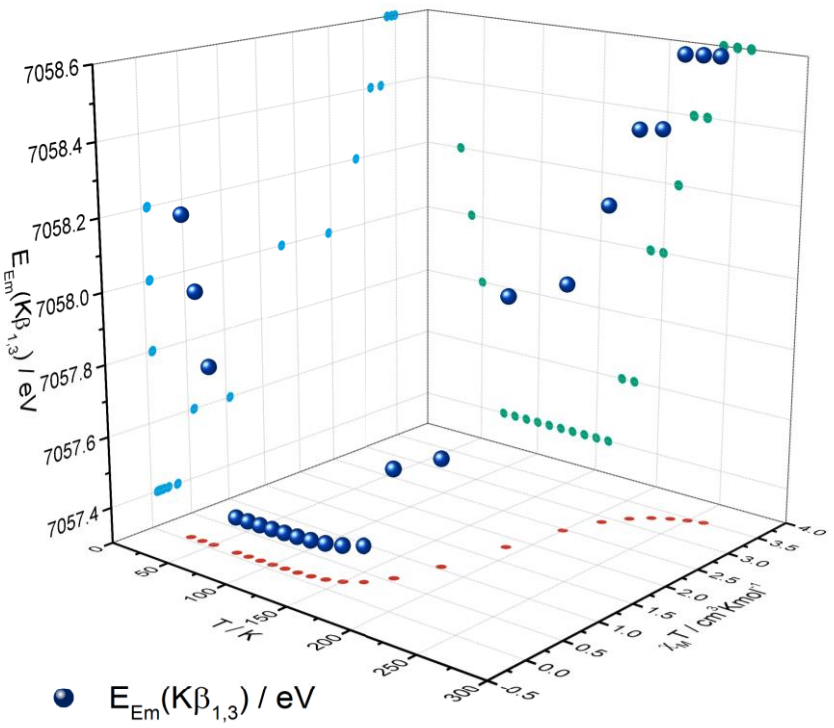

Figure 4.14: 3D-plot of emission maximum $E_{Em}(K\beta_{1,3})$ vs. temperature T vs. product of molar magnetic susceptibility with temperature $\chi_M T$.

The spin state is the most interesting information, which can be obtained by this analysis, therefore, the temperature dependence of the calculated spin values (shown in column 3 of Table 18) is shown in Figure 4.15 in comparison with the HS fraction obtained by SQUID magnetometry. The sigmoidal Boltzmann fit with the resulting fit parameters is shown in the appendix (cf. Appendix, Figure A.13). Because the spin state is directly correlated with the emission energy, the behaviour of the spin state is exactly the same as the behaviour of the emission energy. At 30 K, a spin of approximately one is obtained, therefore the system exhibits either an intermediate spin state or only half of the molecules is converted to the metastable HS state, while the other half remains in the LS state. Increase of temperature to 50 K leads to a continuous reduction of the spin to $S = 0.55$ and so to a lower HS fraction. In the temperature region from 70 K to 160 K the spin is nearly zero. As expected, the system exists almost completely in the LS state. With further rising temperature, the spin is increasing until it reaches a value of $S = 1.55$ at 260 K. According to the magnetization curve, at this temperature the system is not fully converted to the HS state, which corresponds to a value of $S = 2$. But the HS fraction obtained with use of the emission energy $\gamma_{HS}(E_{Em}(K\beta_{1,3}) = 0.78$ is significantly lower than the one obtained by SQUID measurements $\gamma_{HS}(\text{SQUID}) = 0.95$. Furthermore, the spin transition temperature $T_{1/2}$ =198.1 ± 2.3 K is shifted by around 6 K to higher temperatures compared to the

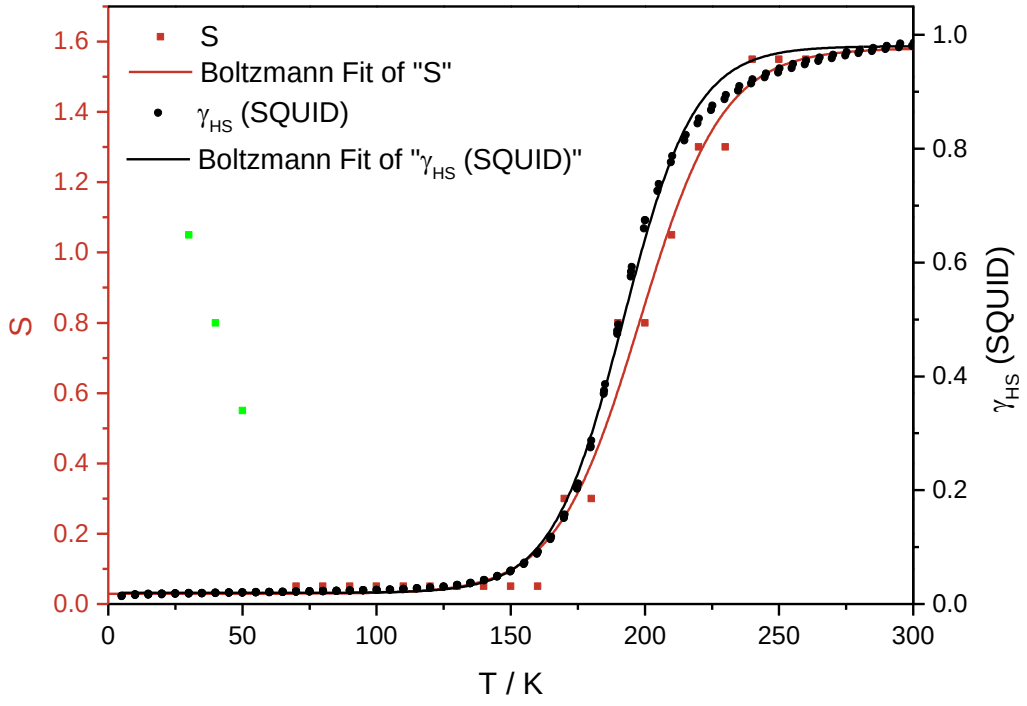

Figure 4.15: Comparison of HS fraction obtained by SQUID measurements and fit of the spin state S calculated with use of $E_{Em}(K\beta_{1,3})$ vs. temperature T.

SQUID data, whereas the curve shape is in rather good agreement with the magnetization curve. So altogether, this method seems to show certain deficiencies concerning the prediction of SCO behaviour and the determination of the spin state. Probably, the reference compounds used to create the calibration curve are not well suited due to their different structure motifs and thus, the resulting calibration curve is also not appropriate for the determination of the spin state of the investigated SCO complex. This could explain the problem that the calculated spin in case of the HS state differs so strongly from the expected value of $S = 2$.

Spin Determination with Intensity of Kβ' Signal

The second applied method takes the change in intensity of the Kβ' signal into account. In Table 19 the intensity of the Kβ satellite *Inten.(Kβ')*, the calculated spin *S* and the corresponding product of the molar magnetic susceptibility with temperature $\chi_M T$ are displayed for each temperature point. The spin was calculated with use of equation (24).

Table 19: Determination of the spin state with use of intensity of Kβ satellite.

T / K	Inten.(Kβ') / a. u.	S / a. u.	$\chi_M T$ / $cm^3 K mol^{-1}$
30	0.02149	1.29	0.07
40	0.02158	1.31	0.071
50	0.02022	1.02	0.074
70	0.01591	0.10	0.079
80	0.01586	0.09	0.082
90	0.01673	0.28	0.085
100	0.01627	0.18	0.089
110	0.01603	0.13	0.096
120	0.01634	0.20	0.105
130	0.01638	0.20	0.122
140	0.01705	0.35	0.154
150	0.01667	0.27	0.216
160	0.01769	0.48	0.335
170	0.01892	0.74	0.575
180	0.01923	0.81	1.05
190	0.02027	1.03	1.797
200	0.02078	1.14	2.467
210	0.02146	1.29	2.88
220	0.02185	1.37	3.122
230	0.02219	1.44	3.274
240	0.02204	1.41	3.374
250	0.02203	1.41	3.444
260	0.0231	1.63	3.495

As in the approach before, the correlations of the experimentally determined satellite intensity *Inten.(Kβ')* with temperature *T* and with the product of the molar magnetic susceptibility with temperature $\chi_M T$ are plotted and displayed in Figure 4.16. Again the three green marked data points indicate the satellite intensity caused by the HAXIESST effect at low temperatures. In this temperature region (30 – 50 K), the satellite intensity shows values of around 0.020. In the LS region from 70 K to around 150 K the intensity of the satellite emission is significantly lower and stays almost constant (0.016 – 0.017). With rising temperature *Inten.(Kβ')* increases in a sigmoidal manner, until it reaches a value of 0.0231 at 260 K (Figure 4.16 left).

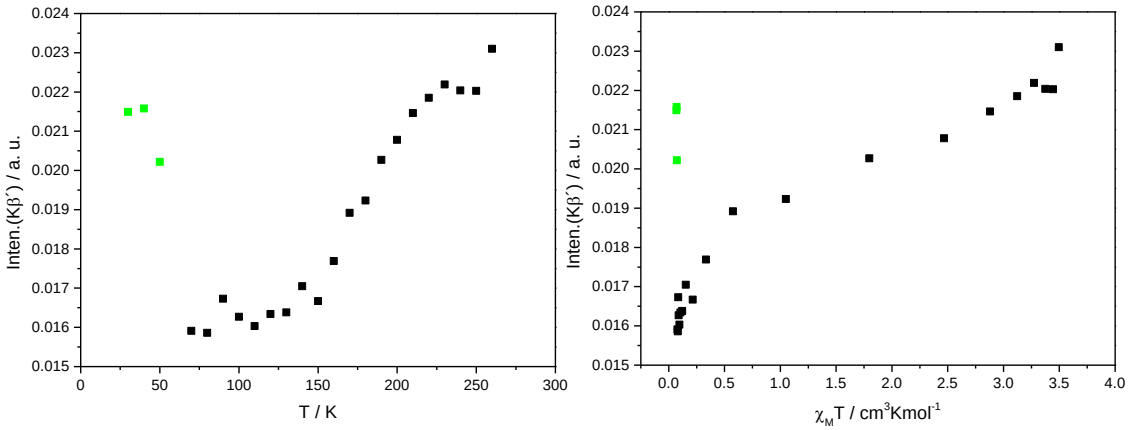

Figure 4.16: left: Plot of satellite intensity *Inten.(Kβ')* vs. temperature *T*; right: Plot of satellite intensity *Inten.(Kβ')* vs. product of molar magnetic susceptibility with temperature $\chi_M T$.

The plot of the satellite intensity versus $\chi_M T$ (Figure 4.16 right) does not show this clear sigmoidal shape since there are many data points at around 0 – 0.5 cm^3Kmol^{-1}, which correspond to similar intensities and the following increase of the intensity shows another behaviour. As an overall trend it can be observed that small values of $\chi_M T$ are correlated with low satellite intensities (except of the three data points in the HAXIESST region) and increasing $\chi_M T$ leads to an increase of the Kβ' intensity.

Since the three parameters depend on each other, a three dimensional plot is created, too (Figure 4.17). In this graph, the 2D projections are displayed in light blue, green and red. While the X-Y-projection (red) is equivalent to the magnetization curve (Figure 1.25), the X-Z-projection (green) and the Y-Z-projection (light blue) correspond to the plots in Figure 4.16. The 3D plot provides a better view especially on the plot of the satellite intensity versus $\chi_M T$ (Y-Z-projection, light blue). So the explanation for the number of data points in the region from 0 – 0.5 cm^3Kmol^{-1} can be found in the fact that the satellite intensity at low temperatures (LS region) is very similar.

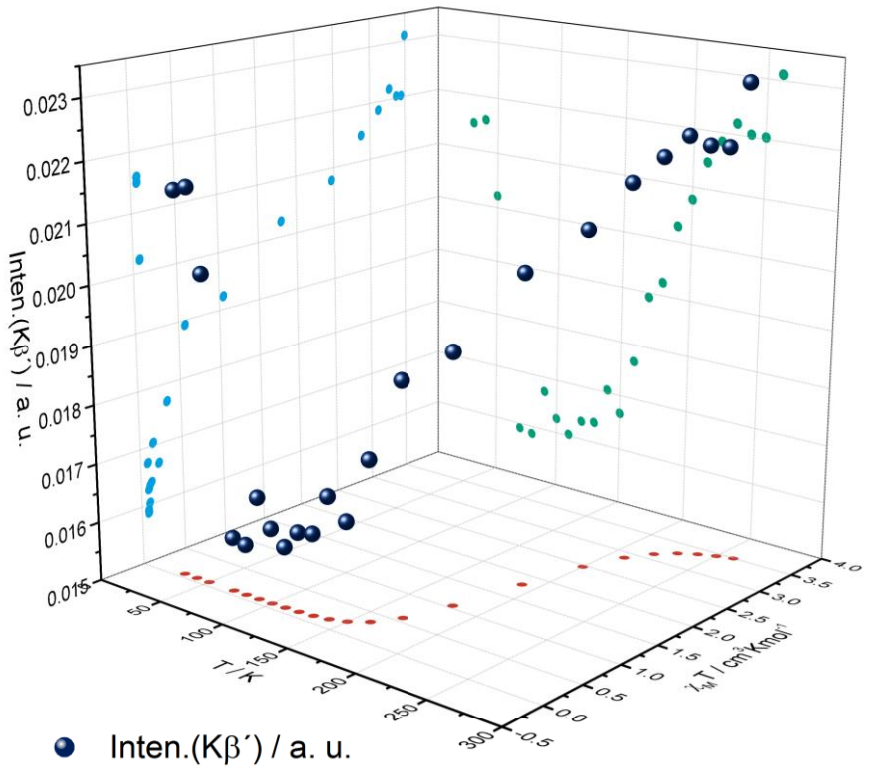

Figure 4.17: 3D-plot of satellite intensity *Inten.(Kβ')* vs. temperature *T* vs. product of molar magnetic susceptibility with temperature $\chi_M T$.

The spin, calculated using equation (24), is plotted versus temperature and compared to the magnetization curve obtained by SQUID magnetometry, as shown in Figure 4.18. The plot with the Boltzmann function and the resulting parameters are shown in the appendix (cf. Appendix, Figure A.14). The three green marked data points in the HAXIESST region were excluded from the fit. The spin-temperature correlation shows the same behaviour like the plot of the Kβ' intensity versus temperature since the spin *S* is directly depending on the satellite intensity, because the satellite intensity is the only variable in the calibration curve.

In the HAXIESST region the spin varies between around 1.3 (30 K, 40 K) and 1.0 (50 K). Compared to the spins obtained by the previous method, the spin values are 0.3 higher at 30 K and 40 K and almost twice as high at 50 K with the actual method. Thus the HS fraction is higher, too. In the temperature range from 70 to 150 K, the calculated spin varies between 0.09 and 0.34, what is also higher than in the previous method. In this range, the HS fraction is under 20 % and therefore the system exists in the LS state mainly. With rising temperature, the spin increases until it reaches its maximum of around 1.6 at 260 K and not as expected a value of approximately 2. The maximum spin state corresponds to a HS fraction of 80 %, so the system is not fully converted to the HS state at this temperature. As in the model described before, the obtained HS fraction is significantly lower than the one obtained by the SQUID data ($\gamma_{HS}(Inten.(K\beta')$ = 0.82 ↔

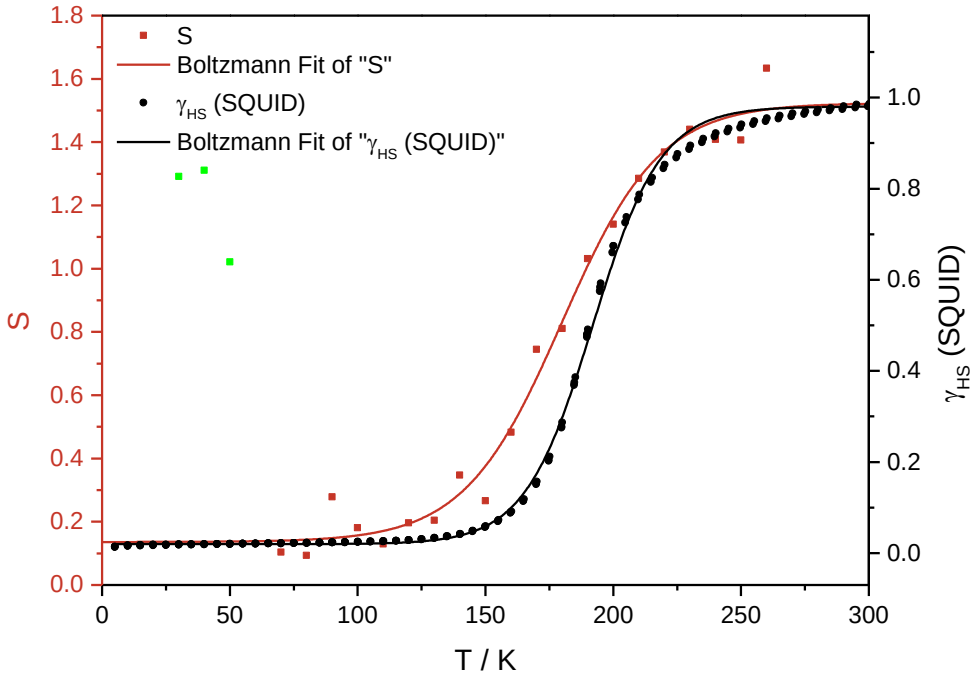

Figure 4.18: Comparison of HS fraction obtained by SQUID measurements and fit of the spin state S calculated with use of *Inten.(Kβ')* vs. temperature *T*.

γ_{HS}(SQUID) = 0.95). The received spin transition curve shows rather large deviations from the magnetization curve, since the spin state starts to increase at distinct lower temperature than the magnetization and the curve shows a more gradual behaviour. Additionally, the spin transition temperature $T_{1/2}$ = 179.9 ± 2.7 K is shifted to lower temperatures by around 12 K compared to the magnetization curve.
Both methods using experimental parameters for the extraction of the spin state of the SCO system suffer from certain disadvantages. It seems that the calibration curves used to calculate the spin states are not really suitable for the investigated complex. Maybe the structural differences between the reference compounds and [Fe(L-N_4Bn_2)(NCS_2) are still too large. Therefore, the determined spin states of both methods do not reach the expected value of S = 2 in case of the HS state, instead the maximum value reaches only a value of around 1.6.
Since it is not known if it is generally possible to reach a HS state with S = 2 with these two methods, it would be necessary to create other calibration curves with different references to investigate the effects on the calculated spin state. Despite this, the obtained transition curves show deviations from the magnetization curve in both methods. In case of the energy of the $K\beta_{1,3}$ emission maximum, the curve shape shows a similar gradual behaviour, but the transition temperature is shifted to higher temperatures compared to the SQUID data. A reverse behaviour was observed for the transition curve received from the intensity of the Kβ' satellite. Here, the transition temperature is shifted to lower temperatures significantly and a more gradual behaviour is obtained.

4.2.2.4 Determination of the Spin State with Use of the Fit Parameters

As a further approach, the spin state was extracted from fit parameters obtained from the deconvolved temperature-dependent spectra shown in chapter 4.2.2.2. The used parameters are the energetic position of the peaks, the intensity and the area. Several parameters were held fix during the deconvolution process (energetic position of fit curve 2 and 3), therefore not all parameters could be used for spin determination. Since the previous two approaches revealed, that the correlation of the different parameters with the product of the molar magnetic susceptibility with temperature gives only little information concerning the spin transition, only the correlation with temperature is shown for the fit parameters.

Spin Determination with Parameters of Fit Curve 1 (approx. 7058 eV)

The first fit parameter, which is used to determine the spin state of the SCO system is the energetic position of fit curve 1 that corresponds to the Kβ main line. The spin state is calculated with use of equation (25) and all obtained values are displayed in Table 20.

Table 20: Determination of the spin state with use of energetic position of fit curve 1.

T / K	E(FC1) / eV	S / a. u.
30	7058.4	1.16
40	7058.4	1.16
50	7058.0	0.72
70	7057.4	0.05
80	7057.4	0.05
90	7057.4	0.05
100	7057.4	0.05
110	7057.4	0.05
120	7057.4	0.05
130	7057.4	0.05
140	7057.4	0.05
150	7057.6	0.27
160	7057.6	0.27
170	7057.8	0.49
180	7057.8	0.49
190	7058.0	0.72
200	7058.2	0.94
210	7058.4	1.16
220	7058.4	1.16
230	7058.6	1.38
240	7058.6	1.38
250	7058.8	1.61
260	7058.8	1.61

The energetic position of fit curve 1 is plotted versus temperature to check if there is a correlation with temperature observable, displayed in the upper part of Figure 4.19. As can be seen, the three data points at very low temperatures (30 K to 50 K) deviate from the other low temperatures due to the HAXIESST effect. In the temperature range from 70 K to 140 K the energetic position stays constant at 7057.4 eV and with increasing temperature it is shifted stepwise to higher energies. At 250 K, it reaches the maximum value of 7058.8 eV. The lower part of Figure 4.19 shows the plot of the calculated spin values in correlation with temperature in comparison with the magnetization obtained by SQUID magnetometry. Due to the direct dependence, the course of the data points is the same as for the energetic position. At very low temperatures (30 K, 40 K), a spin of $S = 1.16$ is obtained, which decreases to $S = 0.05$ in the temperature range from 70 K to 140 K. Further rise of the temperature leads to an increase of the spin state, until it reaches a value of around $S = 1.6$ at 250 K. So similar to the previous fit models, it is not possible to reach a spin of $S = 2$ for the HS state. The Boltzmann fit of the calculated spin state shows large deviations from the magnetization curve, since the transition curve is much more gradual. Therefore, the spin starts to increase at much lower temperature than the magnetization and reaches its maximum at higher temperatures. Compared to the transition temperature determined by SQUID magnetometry, $T_{1/2}$(SQUID) = 192.0 K ± 0.2 K, the resulting temperature, $T_{1/2}(E(\mathrm{FC1}))$ = 196.9 K ± 2.9 K, is shifted by around 5 K to higher temperatures.

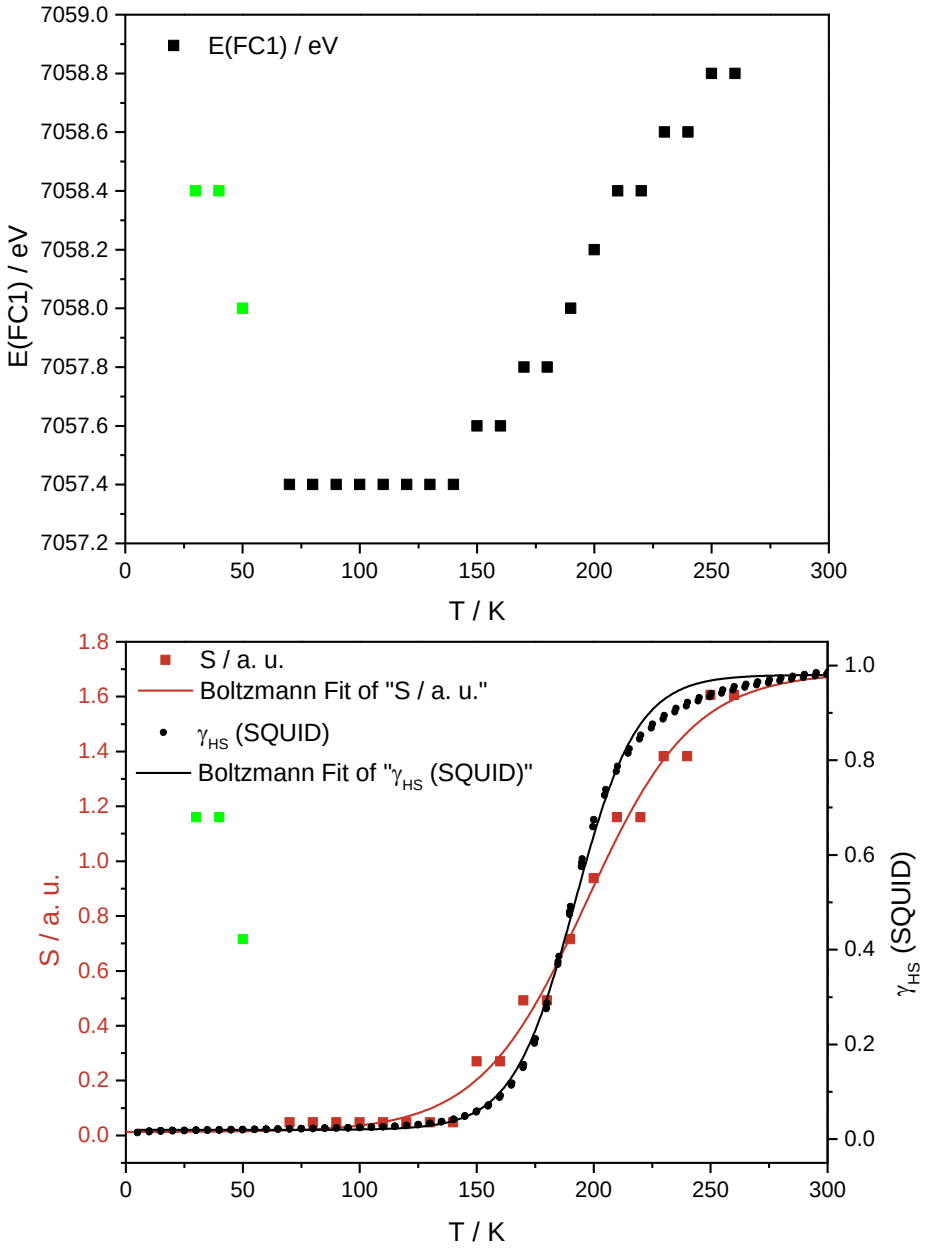

Figure 4.19: top: Plot of energetic position of fit curve 1 *E*(FC1) vs. temperature *T*; bottom: Comparison of HS fraction obtained by SQUID measurements and fit of the spin state S calculated with use of *E*(FC1) vs. temperature *T*.

The intensity of fit curve 1 is the next parameter, which will be evaluated for its temperature and therefore spin dependence. The obtained values for all temperatures, as well as the thereof calculated spin values are shown in Table 21. The spin was calculated with use of equation (26).

Table 21: Determination of the spin state with use of intensity of fit curve 1.

T / K	Inten.(FC1) / a. u.	S / a. u.
30	0.11038	3.70
40	0.10986	3.79
50	0.11209	3.41
70	0.13273	-0.03
80	0.13210	0.08
90	0.12977	0.47
100	0.12950	0.51
110	0.12909	0.58
120	0.12800	0.76
130	0.12728	0.88
140	0.12542	1.19
150	0.12464	1.32
160	0.12014	2.07
170	0.11525	2.89
180	0.11166	3.48
190	0.11099	3.60
200	0.10904	3.92
210	0.10999	3.76
220	0.11040	3.70
230	0.10749	4.18
240	0.10815	4.07
250	0.10998	3.76
260	0.10940	3.86

The intensity, as well as the calculated spin are plotted versus temperature. Figure 4.20 shows the temperature dependence of the intensity in the upper part and that of the spin in the lower part. Obviously, the intensity shows an inverse trend compared to the energetic position of fit curve 1. At temperatures with a dominating HS fraction (30 – 50 K and 170 – 260 K) the intensity is reduced in contrast to the temperatures with predominating LS fraction. Altogether, the intensity shows a sigmoidal decrease with increasing temperature. The plot of the calculated spin values also shows a sigmoidal curve shape,

which is fitted with a Boltzmann function to determine the transition temperature. As can be seen, the resulting spin values are much too high, since there are values up to $S = 4$, although only a maximum of $S = 2$ could be reached in the HS state. Additionally, the determined transition temperature $T_{1/2}$(*Inten.*(FC1)) = 158.8 ± 2.2 K is shifted by around 35 K to lower temperatures compared to the transition temperature obtained by SQUID magnetometry.

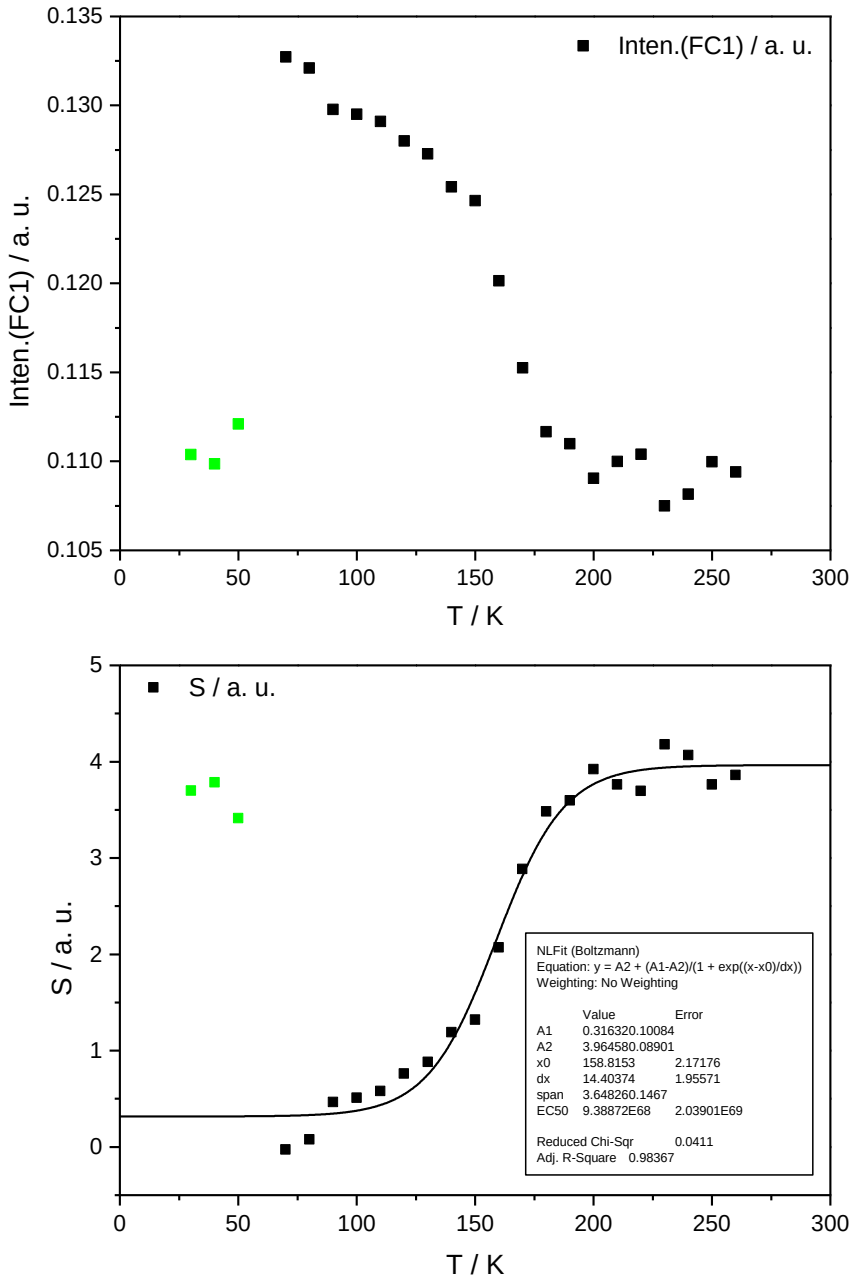

Figure 4.20: top: Plot of intensity of fit curve 1 *Inten.*(FC1) vs. temperature *T*; bottom: Plot of spin state *S* calculated with use of *Inten.*(FC1) vs. temperature *T*.

The last parameter of fit curve 1, which is used for the evaluation of the temperature dependence and for calculation of the spin state, is the area. The area of fit curve 1 is shown in Table 22 for all temperature points. The spin, which was calculated with use of equation (27) is displayed as well.

Table 22: Determination of the spin state with use area of fit curve 1.

T / K	A(FC1) / a. u.	S / a. u.
30	0.62108	-0.60
40	0.60707	-0.84
50	0.60065	-0.95
70	0.66571	0.16
80	0.66104	0.08
90	0.64716	-0.16
100	0.64776	-0.15
110	0.64709	-0.16
120	0.64911	-0.13
130	0.64819	-0.14
140	0.64764	-0.15
150	0.64757	-0.15
160	0.63101	-0.43
170	0.60060	-0.95
180	0.57473	-1.39
190	0.58839	-1.16
200	0.57307	-1.42
210	0.60759	-0.83
220	0.63570	-0.35
230	0.60354	-0.90
240	0.61223	-0.75
250	0.64022	-0.28
260	0.63130	-0.43

The area and the calculated spin were plotted versus temperature, shown in Figure 4.21. At very low temperatures, the three green marked data points indicate the HAXIESST effect. Compared to the LS region from around 70 K to 150 K, the trapping in the metastable HS state leads to a reduction of the area from approximately 0.65 a. u. to 0.61 a. u.. In the SCO region, the intensity also decreases but with further increasing temperature and therefore HS fraction, the data points show a wide distribution, so that no obvious

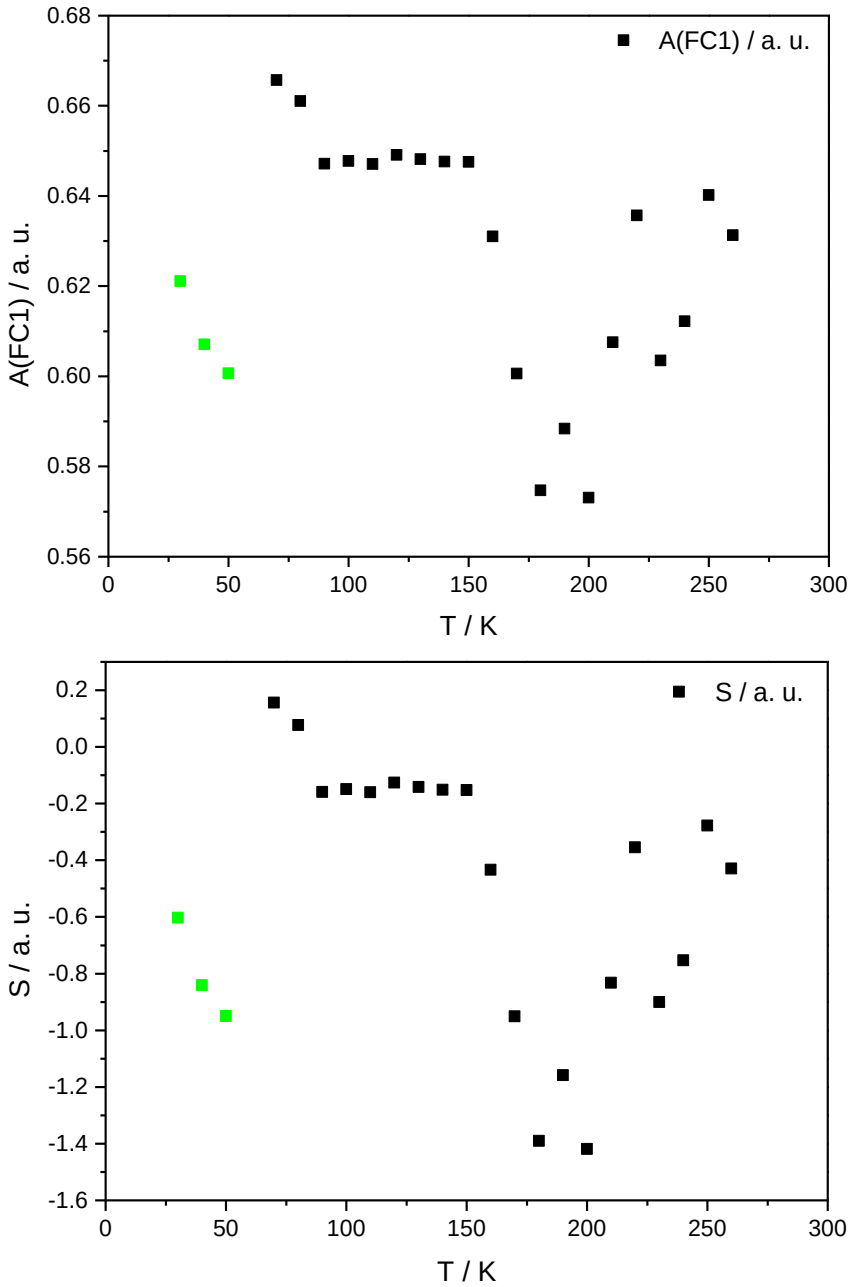

Figure 4.21: top: Plot of area of fit curve 1 *A*(FC1) vs. temperature *T*; bottom: Plot of spin state *S* calculated with use of *A*(FC1) vs. temperature *T*.

trend is observable. The calculated spin values show the same behaviour; thus no fit could be applied to determine the transition temperature. Furthermore, the obtained spin shows physically unreasonable values, ranging from around -1.4 – 0.2 a. u.

Summarising the results obtained from the parameters of fit curve 1, it can be said that obviously only the energetic position of the fit curve corresponding to the Kβ main line, can be used to determine the spin state and the transition temperature of the system reasonably. The plots of the parameters versus temperature result in a sigmoidal increase for the energetic position and the intensity, but not for the area of fit curve 1. Therefore, only for the first two parameters the transition curves and temperatures could be determined. For the energetic position, the transition temperature shows a shift of around 5 K to higher temperatures and the curve shape a more gradual behaviour compared to the SQUID data, while the transition temperature determined by the intensity is shifted by 35 K to lower temperatures and thus is far of the SQUID value. Additionally, the calculation of the spin only gives reasonable values in case of the energetic position (S = 0 – 1.6 a. u.), while the values obtained with use of intensity and area give physically unrealistic results.

Spin Determination with Parameters of Fit Curve 2 (approx. 7045 eV)

Since the energetic position of fit curve 2, which corresponds to the Kβ' signal, was held fix for the deconvolution of the spectra, this parameter cannot be used to determine the spin state. Thus, the first considered parameter is the intensity of fit curve 2, which is shown in Table 23 for all temperatures together with the spin values that were calculated with use of equation (29).

Table 23: Determination of the spin state with use of intensity of fit curve 2.

T / K	Inten.(FC2) / a. u.	S / a. u.
30	0.01505	1.12
40	0.01466	1.02
50	0.01426	0.93
70	0.01367	0.78
80	0.01289	0.59
90	0.01275	0.56
100	0.01298	0.62
110	0.01290	0.60
120	0.01323	0.68
130	0.01343	0.73
140	0.01389	0.84
150	0.01414	0.90
160	0.01418	0.91
170	0.01306	0.64
180	0.01204	0.39
190	0.01341	0.72
200	0.01316	0.66
210	0.01470	1.03
220	0.01451	0.99
230	0.01275	0.56
240	0.01331	0.70
250	0.01401	0.87
260	0.01396	0.85

In accordance to the evaluation of the experimental parameters in chapter 4.2.2.3, the intensity of fit curve 2 should probably be a good tool to measure the changes of the spin state. Therefore, the intensity is plotted versus temperature to obtain the correlation between these two parameters, shown in the upper part of Figure 4.22. In the HAXIESST region at very low temperatures, the intensity shows the highest values (*Inten.*(FC2) =0.0143 – 0.0151 a. u) , which decrease with rising temperature to around 0.013 a. u. at 100 K. A further increase of temperature leads to a wide spreading of the

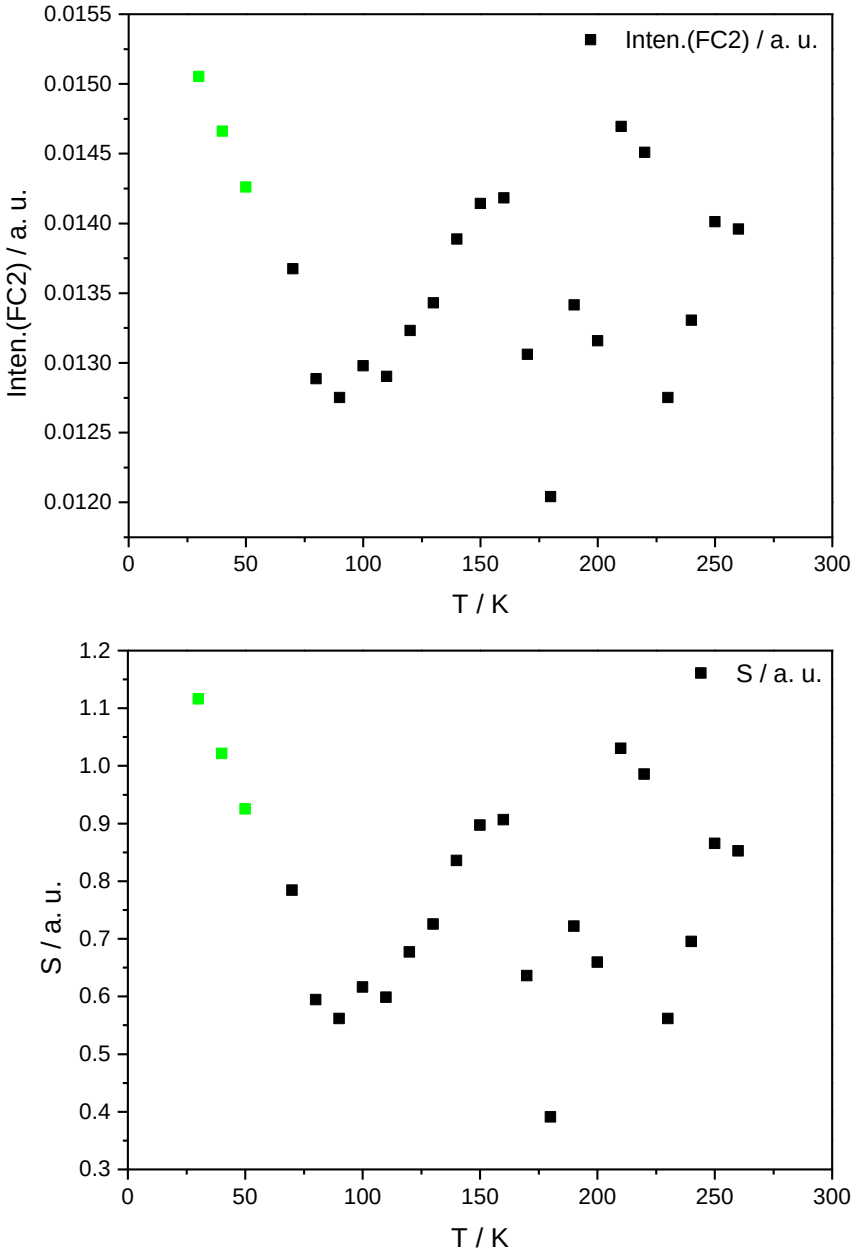

Figure 4.22: top: Plot of intensity of fit curve 2 *Inten.*(FC2) vs. temperature *T*; bottom: Plot of spin state *S* calculated with use of *Inten.*(FC2) vs. temperature *T*.

data points, so no clear trend can be observed. The lower part depicts the plot of the calculated spin values versus temperature, which shows the same distribution of the data points like the intensity, due to the direct correlation of the two parameters. The spin values vary in a range from S = 0.39 – 1.12 a. u., what is at least in a physically reasonable range, but still these values are not realistic. Since no clear trend is observable, no sigmoidal fit could be applied to determine the spin transition curve and the transition temperature.

Besides the intensity of fit curve 2, the area was analysed for its temperature dependence. The received area and the calculated spin values are shown in Table 24 for all temperature points. The spin was calculated with use of equation (30).

Table 24: Determination of the spin state with use of area of fit curve 2.

T / K	A(FC2) / a. u.	S / a. u.
30	0.18294	0.00988
40	0.18156	-0.11411
50	0.19392	0.99641
70	0.22179	3.50003
80	0.21729	3.09572
90	0.21038	2.47562
100	0.21410	2.80972
110	0.21362	2.76644
120	0.21506	2.89559
130	0.21741	3.10736
140	0.21953	3.29759
150	0.22149	3.47336
160	0.21642	3.01784
170	0.19218	0.84025
180	0.15660	-2.35706
190	0.17298	-0.88532
200	0.14978	-2.96919
210	0.18051	-0.20846
220	0.18341	0.05215
230	0.17342	-0.84515
240	0.17971	-0.27993
250	0.18257	-0.02379
260	0.18200	-0.07484

To check if the changes of the area and therefore the spin state can be correlated with temperature, both parameters are plotted versus temperature. The upper part of Figure 4.23 shows the plot of the area versus temperature and the lower part the plot of the spin. Looking at the whole covered temperature range, the area varies between 0.14978 a. u. at 200 K and 0.22179 a. u. at 70 K. In the region assigned to the HAXIESST effect, the area shows values in the middle of these. In the LS region from 70 to 160K, the area stays

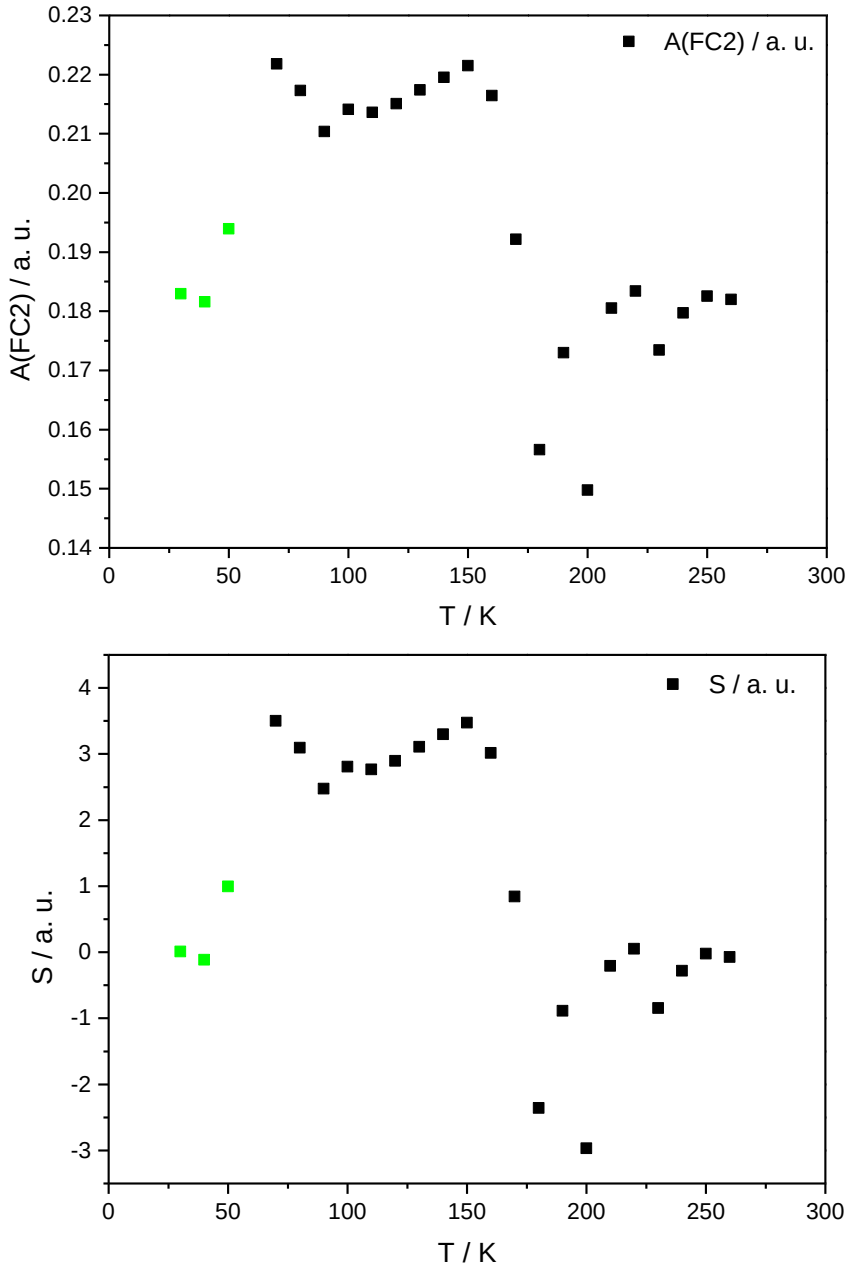

Figure 4.23: top: Plot of area of fit curve 2 *A*(FC2) vs. temperature *T*; bottom: Plot of spin state *S* calculated with use of *A*(FC2) vs. temperature *T*.

more or less constant at 0.21 a. u.. A further increase of the temperature leads to a reduction of the area, but the values do not show a constant behaviour in the HS region. In fact, there is a variation between around 0.15 and 0.19 a. u. observable. Since the calculated spin shows the same behaviour with increasing temperature and no sigmoidal course of the data is present, it is not possible to apply a reasonable fit function for determination of the transition temperature. In addition, the obtained spin values do not make sense physically, since they are spread from around -3 to 4, instead from 0 to 2, what would be realistic.
Altogether, both evaluated parameters of fit curve 2 cannot provide useful information concerning the SCO behaviour. The calculation of the spin states, with use of either the intensity or area of fit curve 2, results in physically unreasonable values for both cases. Apart from this, both parameters do not show a clear trend with increasing temperature, which can be correlated with the changes of the spin state during the SCO process.

Spin Determination with Parameters of Fit Curve 3 (approx. 7052eV)
As already mentioned in chapter 4.2.2.1, the HS reference compound **OS1** was deconvolved with only two signals. As a consequence, the creation of the calibration curves corresponding to the parameters of fit curve 3 cannot give reasonable results, since the used references cover only a very small range of spin values. An evaluation of the parameters of fit curve 3 is therefore omitted.

4.2.3 Spin Determination with the ΔE_{CP} Method

Another approach to relate the Kβ spectra to the spin state of the system is the so-called ΔE_{CP} method.[88] In this method the energy splitting between the centre of mass (COM) of the spectrum and the Kβ main peak is used to obtain a correlation with the spin state. In the first version of this method a calibration curve with the different reference compounds from chapter 4.2.1 was constructed. The spectra of the references were normalized to the maximum of the Kβ main line and integrated. Additionally, the COM and the energetic position of the Kβ maximum were read out. The difference of these two values was then plotted versus the known spin state and fitted linearly (Figure 4.24). Table 25 displays the obtained ΔE_{CP} values and the parameters used for the calculation of these.

Table 25: Necessary parameters for determination of ΔE_{CP} values.

Reference	$E_{Em}(K\beta_{1,3})$ / eV	COM / eV	ΔE_{CP} / eV	S / a. u.
OS1	7059.0	7054.29023	4.70977	2
OS2	7057.4	7054.23769	3.16231	0
OS7 (20 K)	7057.4	7054.20904	3.19096	0
OS7 (200 K)	7057.4	7054.21030	3.18970	0
$K_3[Fe(CN)_6]$	7057.6	7054.10897	3.49103	0.5

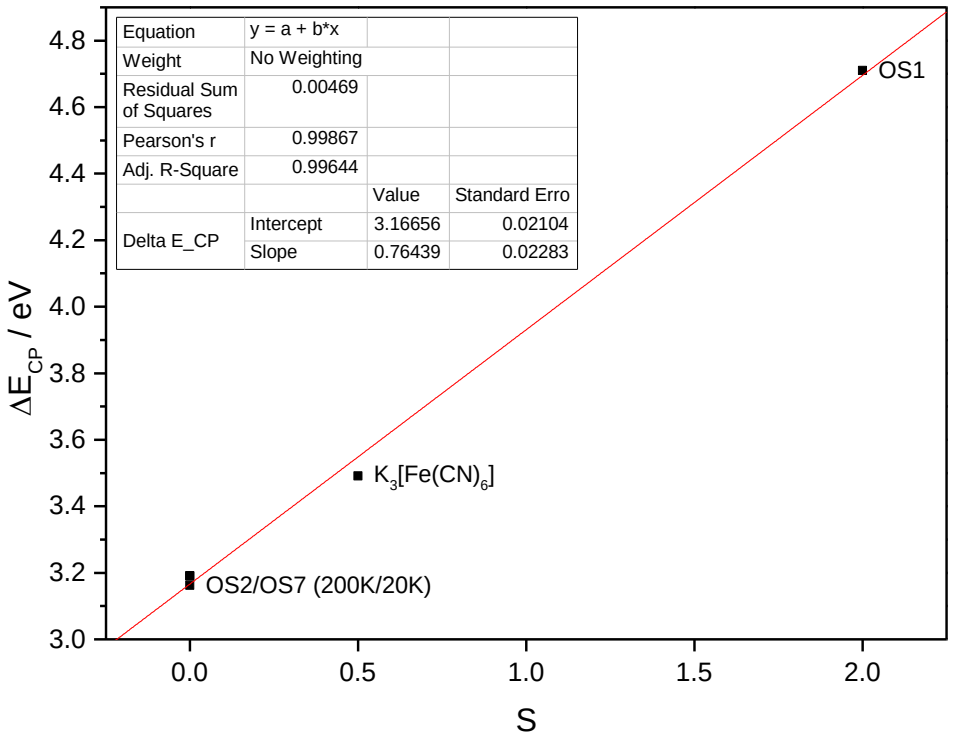

Figure 4.24: Calibration curve obtained by the ΔE_{CP} method.

With use of the ΔE_{CP} values the above calibration curve was constructed (Figure 4.24), which leads to equation (34):

$$S = \frac{\Delta E_{CP} - 3.16656}{0.76439} \tag{34}$$

The temperature-dependent spectra of [Fe(L-N_4Bn_2)$(NCS)_2$] were treated in the same way as the reference spectra and the respective spin values were calculated using equation (34). The obtained parameters are shown in Table 26.

Table 26: Necessary parameters for determination of ΔE_{CP} values of [Fe(L-N_4Bn_2)$(NCS)_2$] and calculated spin values.

T / K	$E_{Em}(K\beta_{1,3})$ / eV	COM / eV	ΔE_{CP} / eV	S / a. u.
30	7058.2	7054.2106	3.9894	1.08
40	7058.0	7054.19758	3.80242	0.83
50	7057.8	7054.20499	3.59501	0.56
70	7057.4	7054.28183	3.11817	-0.06
80	7057.4	7054.26792	3.13208	-0.05
90	7057.4	7054.25926	3.14074	-0.03
100	7057.4	7054.24933	3.15067	-0.02
110	7057.4	7054.2427	3.1573	-0.01
120	7057.4	7054.27039	3.12961	-0.05
130	7057.4	7054.26242	3.13758	-0.04
140	7057.4	7054.27059	3.12941	-0.05
150	7057.4	7054.28027	3.11973	-0.06
160	7057.4	7054.2549	3.1451	-0.03
170	7057.6	7054.23931	3.36069	0.25
180	7057.6	7054.26435	3.33565	0.22
190	7058.0	7054.26603	3.73397	0.74
200	7058.0	7054.21565	3.78435	0.81
210	7058.2	7054.20403	3.99597	1.096
220	7058.4	7054.22173	4.17827	1.32
230	7058.4	7054.21544	4.18456	1.33
240	7058.6	7054.21493	4.38507	1.59
250	7058.6	7054.2454	4.3546	1.55
260	7058.6	7054.22353	4.37647	1.58

To show the correlation of the ΔE_{CP} values with temperature T and with the product of the molar magnetic susceptibility with temperature $\chi_M T$ (cf. Table 18, column 4), Figure 4.25 shows the respective 2D plots of ΔE_{CP} versus both parameters. And since there is a direct correlation between all three mentioned parameters, also the corresponding 3D plot is shown in Figure 4.26. The three green marked data points depict again the values in case of the HAXIESST effect.

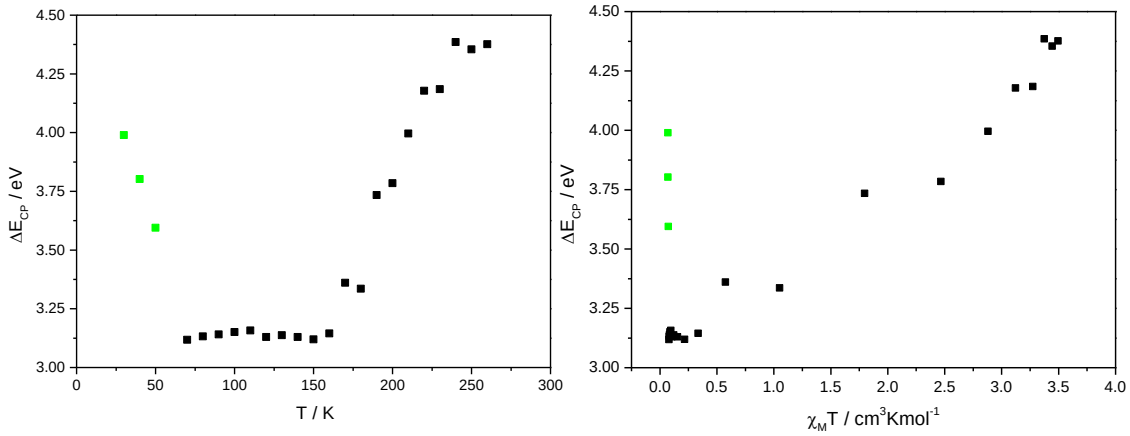

Figure 4.25: left: Plot of ΔE_{CP} vs. temperature T, right: Plot of ΔE_{CP} vs. product of molar magnetic susceptibility with temperature $\chi_M T$.

The 2D projections of the 3D-plot are shown in light blue, green and red. The X-Y-projection (red) corresponds to the magnetization curve (cf. Figure 1.25), while the X-Z-projection (green) and the Y-Z-projection (light blue) correspond to the two plots in Figure 4.25. The difference between the COM of the spectra and the Kβ main peak is nearly constant in the temperature region from 70 to 160 K. With increasing temperature, the main peak is shifted to higher energies, while the COM stays almost constant in the whole temperature range, therefore the ΔE_{CP} values increase with higher temperatures (light blue). In the Y-Z-projection several data points appear at a ΔE_{CP} value of around 3.1 eV while $\chi_M T$ is only slightly changing. These data points correspond to the low temperatures where the system stays in the LS state.

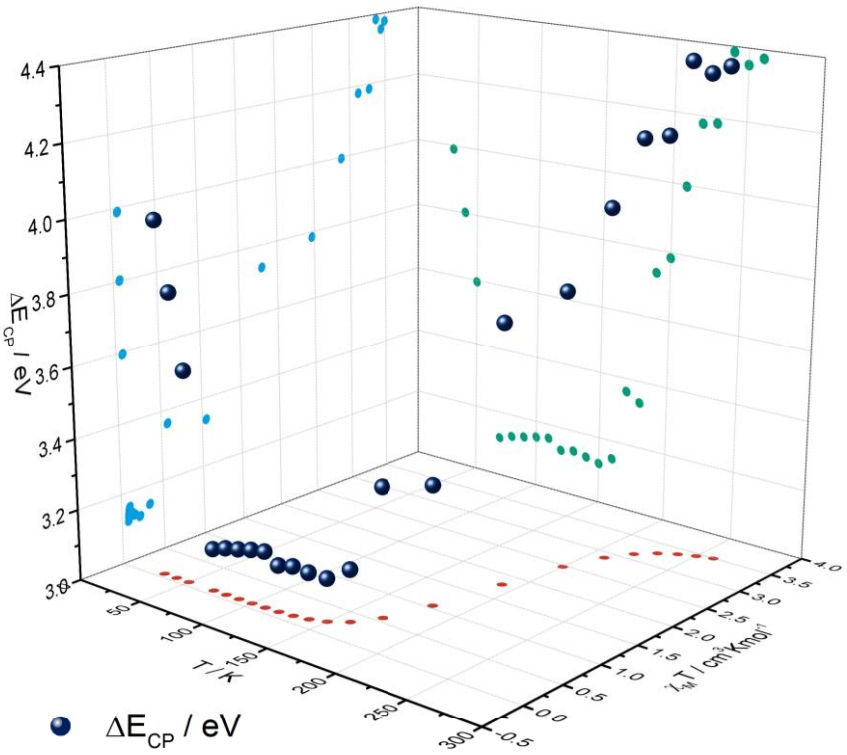

Figure 4.26: 3D-plot of ΔE_{CP} vs. temperature T vs. product of molar magnetic susceptibility with temperature $\chi_M T$.

Finally the spin state was calculated with use of equation (34), as already mentioned before. The resulting spin values are listed in Table 26 and to obtain a spin-temperature correlation, the spin was plotted versus temperature and fitted with a sigmoidal Boltzmann function, as shown in Figure 4.27. At this point the problems of this approach are revealed. The calculated spin values are negative in the temperature range from 70 to 160 K. In this region the system should be in the LS state and therefore the spin should be zero or slightly positive in the event of small HS fractions. The negative spin values are physically not plausible. Additionally, like in the methods described before, no spectrum of a pure HS state is available and therefore the sigmoidal fit curve does not give a reliable value for the spin transition temperature, since the fit would probably change with further temperature points.

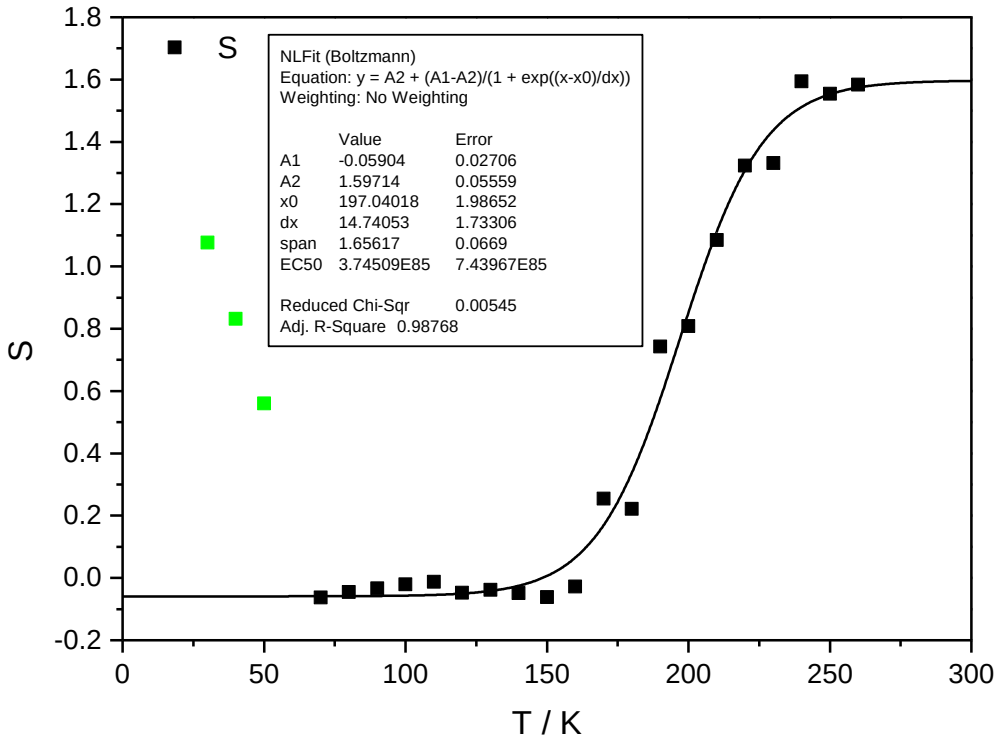

Figure 4.27: Plot of spin state *S* calculated with use of ΔE_{CP} vs. temperature *T*.

4.2.3.1 Modified ΔE_{CP} Method

Maybe the structural differences between the LS reference compounds and the SCO complex are too large, so that these complexes are not the optimal references for this purpose. Therefore, a new calibration curve was created to improve the results of the ΔE_{CP} method. The difference compared to the former one is, that the LS reference points were replaced by the ΔE_{CP} value of the investigated SCO complex [Fe(L-N_4Bn_2)$(NCS)_2$] at 70 K, where the complex should be present in the LS state according to the SQUID measurements. The energy of the emission maximum $E_{Em}(K\beta_{1,3})$, the centre of mass COM, the resulting ΔE_{CP} values and the corresponding spin states are displayed in Table 27.

Table 27: Necessary parameters for determination of ΔE_{CP} values used for the modified ΔE_{CP} method.

Reference	$E_{Em}(K\beta_{1,3})$ / eV	COM / eV	ΔE_{CP} / eV	S
OS1	7059.0	7054.29023	4.70977	2
[Fe(L-N_4Bn_2)$(NCS)_2$] 70 K	7057.4	7054.28183	3.11817	0
K_3[Fe$(CN)_6$]	7057.6	7054.10897	3.49103	0.5

The ΔE_{CP} values were plotted versus the spin state and fitted linearly to obtain the new calibration curve (see Figure 4.28).

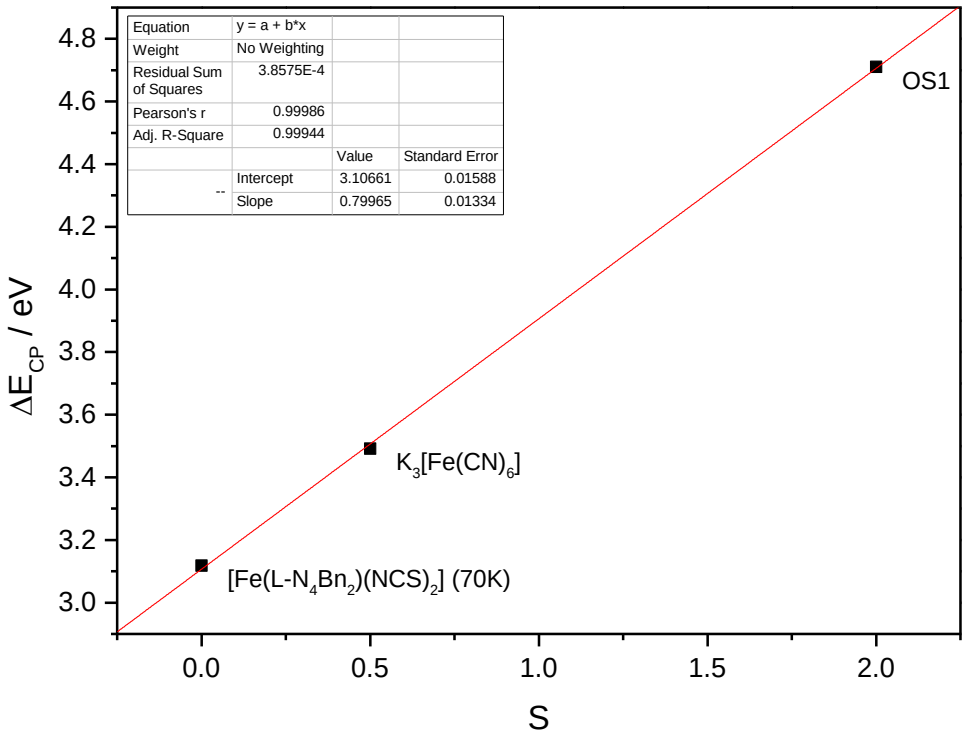

Figure 4.28: Calibration curve obtained by the modified ΔE_{CP} method with use of [Fe(L-N_4Bn_2)$(NCS)_2$] as LS reference.

The fit resulted in equation (35), which was then used to calculate the spin states of the SCO complex [Fe(L-N_4Bn_2)$(NCS)_2$] at the different temperature points, listed in Table 28. For the calculation of the spin states, the ΔE_{CP} values from Table 26, column 4 were used, like in the model before.

$$S = \frac{\Delta E_{CP} - 3.10661}{0.79965} \tag{35}$$

Table 28: Determination of the spin states of [Fe(L-N_4Bn_2)$(NCS)_2$] with use of the modified ΔE_{CP} method.

T / K	S / a. u.	T / K	S / a. u.
30	1.11	**160**	0.06
40	0.88	**170**	0.33
50	0.62	**180**	0.29
70	0.02	**190**	0.79
80	0.04	**200**	0.85
90	0.05	**210**	1.12
100	0.06	**220**	1.35
110	0.07	**230**	1.36
120	0.04	**240**	1.61
130	0.05	**250**	1.57
140	0.04	**260**	1.60
150	0.02	--	--

In contrast to the previous method, which leads to negative spin values in the temperature range from 70 to 160 K, the modified method does not give negative spin values anymore. Instead the spin values are positive and nearly zero in the LS range as expected. Below 70 K the spin varies between 1.1 (30 K) and 0.6 (50 K) in course of the HAXIESST effect. Above 160 K the spin increases with rising temperature until it reaches a value of around 1.6 at 260 K. Similar to the methods described in chapter 4.2.2, the spin only reaches a value of around 1.6 in the high temperature range, even though a spin of approximately $S = 2$ should be reached in the HS case.

To obtain the spin-temperature-correlation, the calculated spin S was plotted versus temperature T and a sigmoidal Boltzmann fit was applied, which is shown in the appendix with the resulting fit parameters (cf. Appendix, Figure A.16). Although the modified ΔE_{CP} method eliminates the negative spin values in the LS region, the second problem remains. Without a suitable HS spectrum, the Boltzmann fit of the spin cannot yield a reliable spin transition temperature, since the fit will presumably change with further temperature points. Even though, a direct comparison with the SQUID data is critical as long as no pure HS spectrum is available, the comparison of the adjusted curves is shown in Figure 4.29. Since it is not known if the pure HS state would show a spin of $S = 2$ or rather below in the range of 1.6 or 1.7, the resulting spin values were compared as they are to the SQUID data. Despite the described difficulties of this method, the obtained transition temperature $T_{1/2}(\Delta E_{CP}) = 197.0 \pm 2.0$ K is shifted by only 5 K to higher temperatures compared to the SQUID data and the overall curve shape shows still a quite good accordance with the magnetization curve.

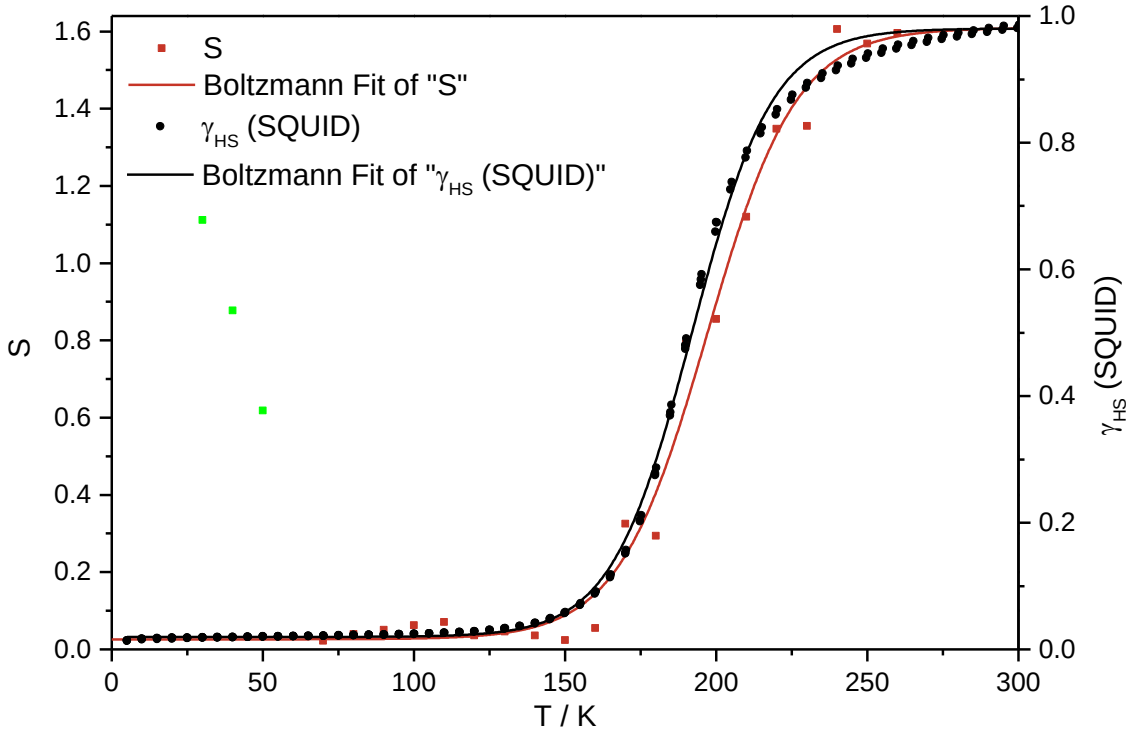

Figure 4.29: Comparison of spin state *S* calculated with use of modified ΔE_{CP} method (red) and HS fraction obtained by SQUID (black).

So altogether, the determination of the spin state of a system with the ΔE_{CP} method contains several difficulties. First, the success of this method strongly depends on a suitable choice of reference compounds for the construction of the calibration curve. The reference compounds should show a very similar molecular structure compared to the complex to investigate, meaning the atomic arrangement and the bond situation need to be comparable with the sample complex. Additionally, it is important that spectra of the pure LS and HS state (extreme spectra) of the system are available to adjust the spin values obtained by the data analysis to the expected values.

The two different approaches described above show that the construction of the calibration curve is the most crucial point of the evaluation. Only small variations in the calibration curve can lead to unreasonable results (e.g. negative spin values).

4.2.4 Spin Determination with the IAD Method

Since the methods to determine the spin state applied so far did not gave fully satisfactory results compared to the magnetization measurements, another promising approach was tested. With the so-called IAD method, which will be explained in detail subsequently, the variation of the spin state is monitored through the integrals of the absolute values of the area of the difference spectra between the complex to investigate and a suitable reference compound (IAD). [88,89,161]

The IAD method is based on the fact that the spectral shape of the Kβ emission spectra shows distinct changes during the SCO process from LS to HS. The largest variations are observable for the intensity of the Kβ main line and the Kβ' satellite, as well as for the energetic position of the Kβ main line. Figure 4.30 shows the temperature-dependent emission spectra which are normalized to unit area. The Kβ main line is shifted from 7054.4 eV at low temperatures (except of 30, 40 and 50 K → HAXIESST effect) to 7058.6 eV at high temperatures and the Kβ' satellite appears at 7045.0 eV at high temperatures and is diminished to a shoulder of the low energy side of the Kβ main line.

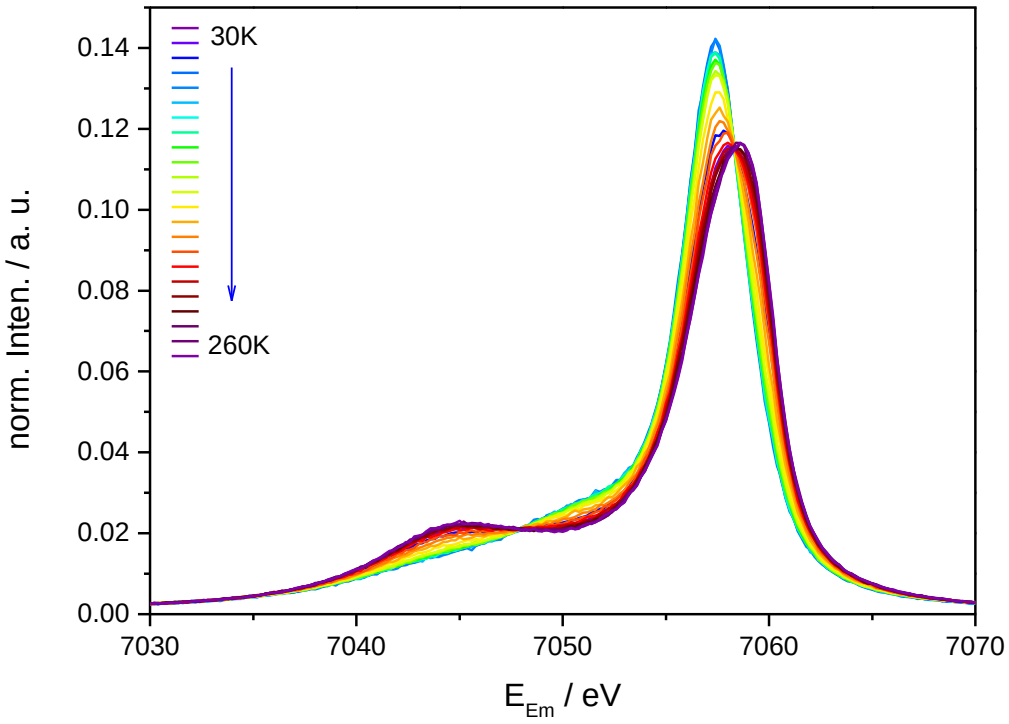

Figure 4.30: Normalized CtC spectra of [Fe(L-N_4Bn_2)$(NCS)_2$] in the temperature range from 30 to 260 K.

For the correlation of these spectral changes with the spin state of the system, the difference spectrum of each temperature point with a reference is built and integrated. The resulting integrals of the absolute values of the difference spectra (IAD) are then proportional to the HS fraction γ_{HS} (cf. equation (39)). The considerations explained subsequently were applied to extract the spin state from the spectra.
The so-called IAD value for the complete transition from HS to LS can be given as:

$$\mathrm{IAD_{HL}} = \int |h(E) - l(E)|\,\mathrm{d}E. \tag{36}$$

Where *h(E)* and *l(E)* stand for the spectral functions of the HS and LS state, which are normalized to unit area. A spectrum in between these two states can be described as a superposition (*s*) of HS and LS:

$$s = \gamma_{HS} h + (1 - \gamma_{HS}) l. \tag{37}$$

For the IAD analysis the difference spectrum of the spectrum of the respective temperature *s* with the LS reference spectrum *l* is:

$$s - l = \gamma_{HS}(h - l). \tag{38}$$

To obtain the requested IAD values, the integrals of the absolute values of the difference spectra are built:

$$\mathrm{IAD}(s) = \int |(s(E) - l(E))|\mathrm{d}E = \gamma_{HS}(\mathrm{IAD_{HL}}). \tag{39}$$

Based on these considerations the temperature-dependent emission spectra were analysed. To improve the accordance with the magnetization data, several variations concerning the data preparation were tested in the following paragraphs.

4.2.4.1 Spin Determination with the IAD Method, no Alignment of the Spectra

For the first described variation of the IAD method the emission spectra were used with their initial energetic position, no alignment of the spectra to a certain energy value was performed. Data preparation started with normalization of the spectra to unit area. With these normalized spectra the difference spectra with the LS reference were calculated. In this case an intrinsic LS reference was used with the spectrum of $[Fe(L\text{-}N_4Bn_2)(NCS)_2]$ at 70 K, where the complex exists in a pure LS state according to SQUID magnetometry. The advantage of this procedure is, that there are no structural differences between the complex to investigate and the reference compound and all the spectra were obtained under the same conditions. The difference spectra with the LS reference are displayed in Figure 4.31 for the temperature range from 80 to 260 K. The difference spectra at 30, 40 and 50 K are not shown in this figure, since they do not line up with the other temperatures because of the HAXIESST effect. The blue spectrum depicts the spin transition temperature (190 K), the LS spectra are shown below and the HS spectra above the blue one.

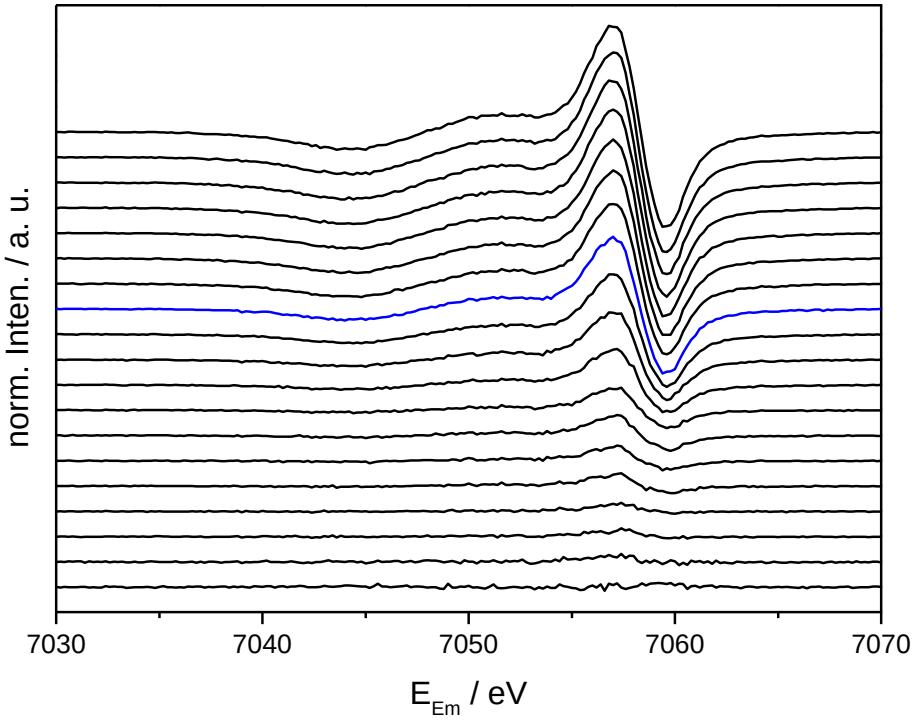

Figure 4.31: Difference spectra of $[Fe(L\text{-}N_4Bn_2)(NCS)_2]$ in the temperature range from 80 to 260 K with $[Fe(L\text{-}N_4Bn_2)(NCS)_2]$ 70 K as LS reference, blue spectrum indicates spin transition temperature (190 K).

As expected, the changes of the spectra in relation to the LS reference increase with rising temperature and are extended over the whole energy range nearly. For quantification of the differences, the spectra were integrated in the range from 7030 to 7070 eV to yield the absolute values of the area. Figure 4.32 shows the difference spectrum between 70 K and 260 K exemplarily.

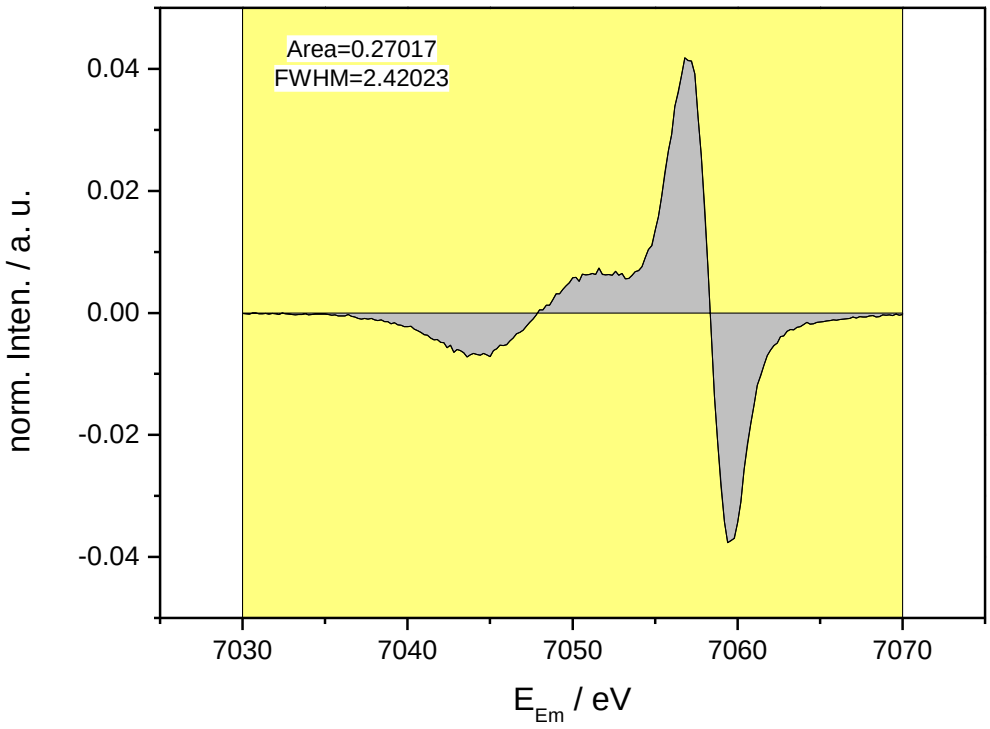

Figure 4.32: Integration of the difference spectrum between 70 and 260 K.

The resulting IAD values are displayed in Table 29 in column two and Figure 4.33 shows the plot of the IAD values versus temperature with the corresponding sigmoidal Boltzmann fit function. The fit leads to a spin transition temperature of $T_{1/2}$(IAD) = 178.6 ± 0.8 K, what is significantly lower than the value obtained by the SQUID measurements ($\Delta T_{1/2}$ = 13.4 K).

Table 29: IAD values determined with the IAD method without alignment of the spectra.

T / K	IAD / a. u.	γ_{HS} (IAD)	$\gamma_{HS, corr}$ (IAD)
30	0.22884	0.84534	0.83042
40	0.21750	0.80343	0.78852
50	0.16484	0.60891	0.59400
80	0.01183	0.04371	0.02880
90	0.01498	0.05535	0.04044
100	0.01428	0.05274	0.03783
110	0.01507	0.05567	0.04076
120	0.02519	0.09307	0.07815
130	0.03033	0.11205	0.09714
140	0.04447	0.16429	0.14938
150	0.05110	0.18878	0.17387
160	0.08394	0.31007	0.29516
170	0.11586	0.42799	0.41307
180	0.14749	0.54481	0.52990
190	0.18022	0.66572	0.65080
200	0.20285	0.74932	0.73441
210	0.22181	0.81935	0.80444
220	0.23500	0.86807	0.85316
230	0.24961	0.92207	0.90716
240	0.25930	0.95785	0.94294
250	0.26701	0.98634	0.97142
260	0.27017	0.99801	0.98309

For a direct comparison of the behaviour of the spin transition curve with the magnetization measurements, the IAD values have to be converted to HS fraction values. Since no $K\beta_{1,3}$ emission spectrum of a clear HS state exists, it is not possible to calculate the HS fraction γ_{HS} with the experimental data solely, because the required IAD_{HL} value (equation (39)) is not available. Therefore, the calculation of the HS fraction was performed with use of the HS IAD value at 300 K (IAD = 0.27071) that was obtained from the applied

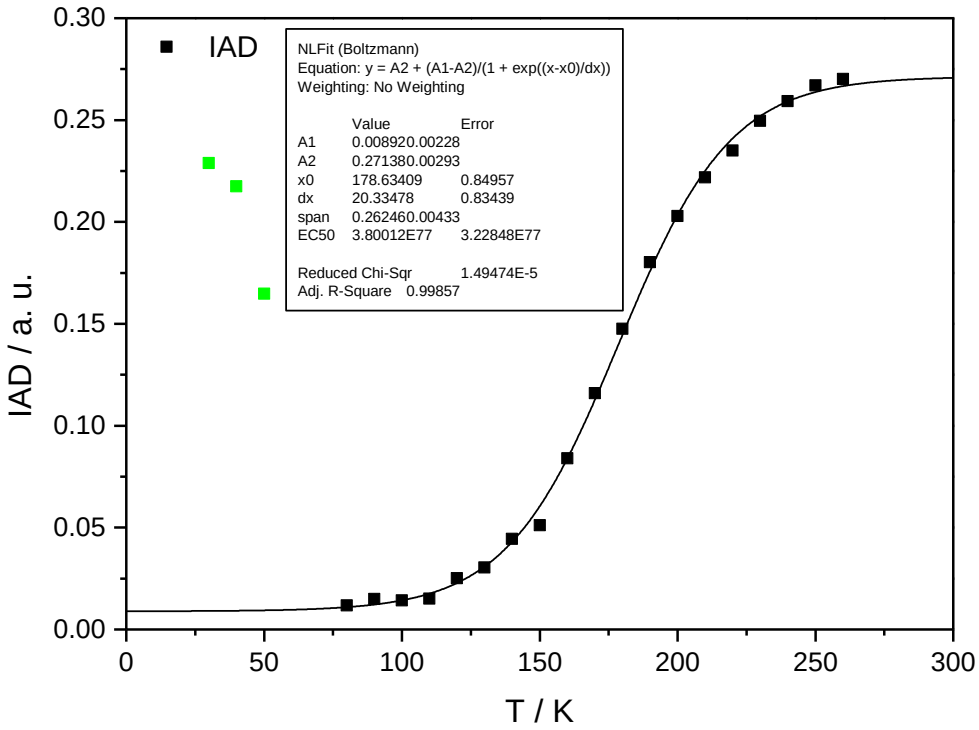

Figure 4.33: Plot of the IAD values with the corresponding Boltzmann fit function; IAD method without alignment of the spectra.

Boltzmann fit function. The resulting HS fractions γ_{HS} are shown in column three of Table 28. In Figure 4.34 the HS fractions obtained by the IAD method and by the SQUID measurements are compared to each other. It is observable that the values received by the IAD method show a little offset compared to the SQUID γ_{HS} values. Thus, the IAD HS fraction values were corrected by an offset of 0.01492 to ensure a better comparability. The corrected values ($\gamma_{HS,\,corr}$(IAD)) are shown in column four of Table 29 and the plot versus temperature is shown in Figure 4.35. After the offset correction, the two fit curves show the same HS fraction values up to around 80 K. It is to mention that the high experimental values for 30, 40 and 50 K (marked green in Figures 4.33 to 4.35) result from the fact that the system is trapped in the metastable HS state at low temperatures due to the HAXIESST effect. Therefore, these three values are not considered for the fit of the data. The two fit curves show significant differences concerning the curve shape in the temperature range from 90 to around 260 K. The HS fraction obtained by the IAD method starts to increase at lower temperatures and the transition from LS to HS is of a more gradual type than the transition obtained by SQUID magnetometry.

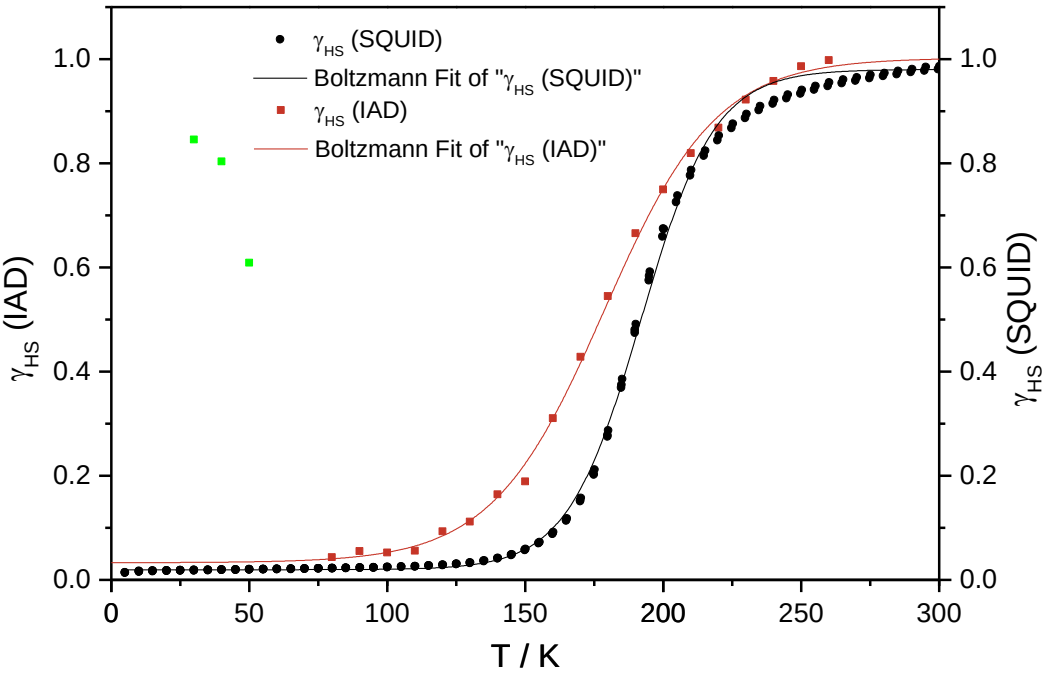

Figure 4.34: Comparison of HS fractions obtained by IAD method without alignment of the spectra (red) and by SQUID (black).

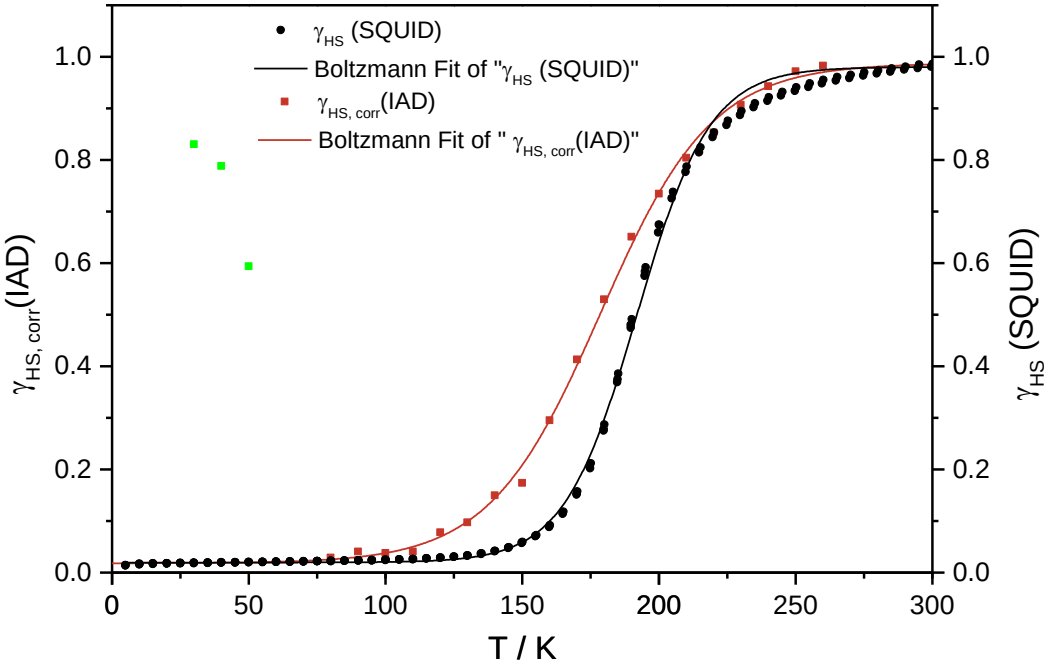

Figure 4.35: Comparision of offset corrected HS fractions by IAD method without alignment of the spectra (red) and by SQUID (black).

4.2.4.2 Spin Determination with the IAD Method, Alignment to Centre of Mass

The second variation of the IAD method is based on a different data preparation. In contrast to the approach described in chapter 4.2.4.1, where no alignment of the spectra was performed, in this case the spectra were aligned to the COM of the LS reference spectrum of [Fe(L-N_4Bn_2)$(NCS)_2$] at 70 K.
For this, the spectra of all temperatures were integrated first and the COM of each spectrum was determined. Then the spectra were normalized to unit area. The energetic differences between the centres of mass were calculated and then the spectra were shifted by these values to the COM of the reference at 70 K, resulting in the spectra displayed in Figure 4.36. With these normalized and aligned spectra the difference spectra with the LS reference were calculated. Since the spectra were aligned to the COM of the reference spectrum, they exhibited different start and end points, what means that the energy values are shifted compared to the reference spectrum, so a simple subtraction of the spectra was not possible. Instead the spectra were subtracted by performing an interpolation between the energy values of the reference and the spectrum of the respective temperature using the implemented “difference spectra” function in the ATHENA software.[177,183]

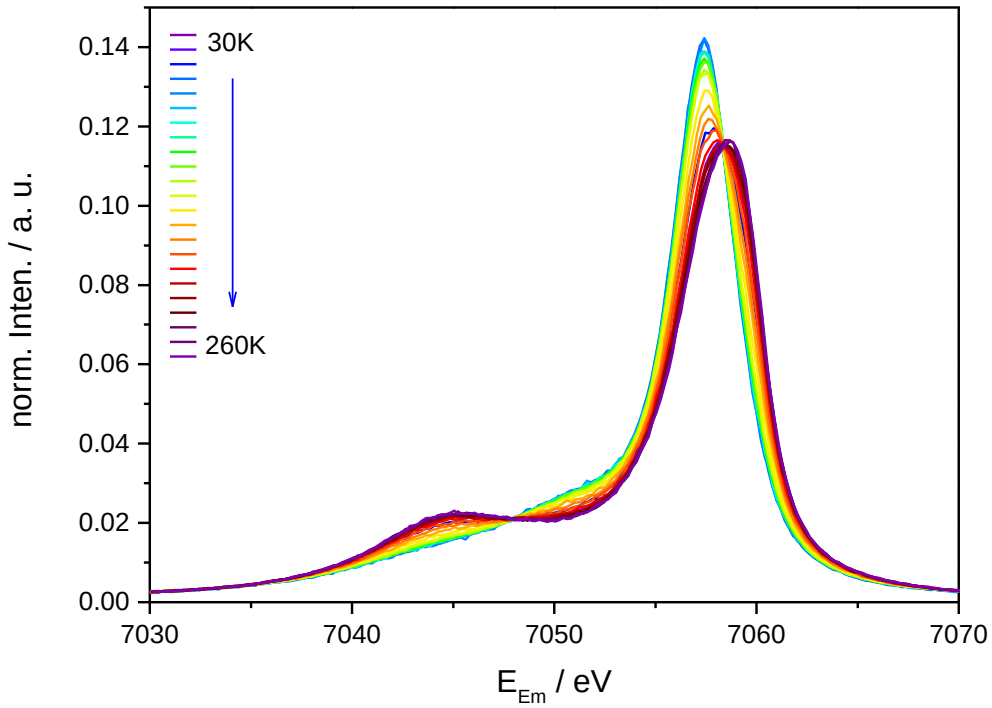

Figure 4.36: Normalized CtC spectra of [Fe(L-N_4Bn_2)$(NCS)_2$] in the temperature range from 30 to 260 K, aligned to the COM of spectrum of 70 K.

The difference spectra of all temperatures (except of 30, 40 and 50 K → HAXIESST effect) are shown in Figure 4.37, again the blue spectrum depicts the SCO temperature (190 K). The spectra above the blue one are assigned to increasing HS fraction and the ones below to decreasing HS fraction. The variation between the LS reference at 70 K and the respective temperature increases with rising temperature and therefore with higher HS amount.

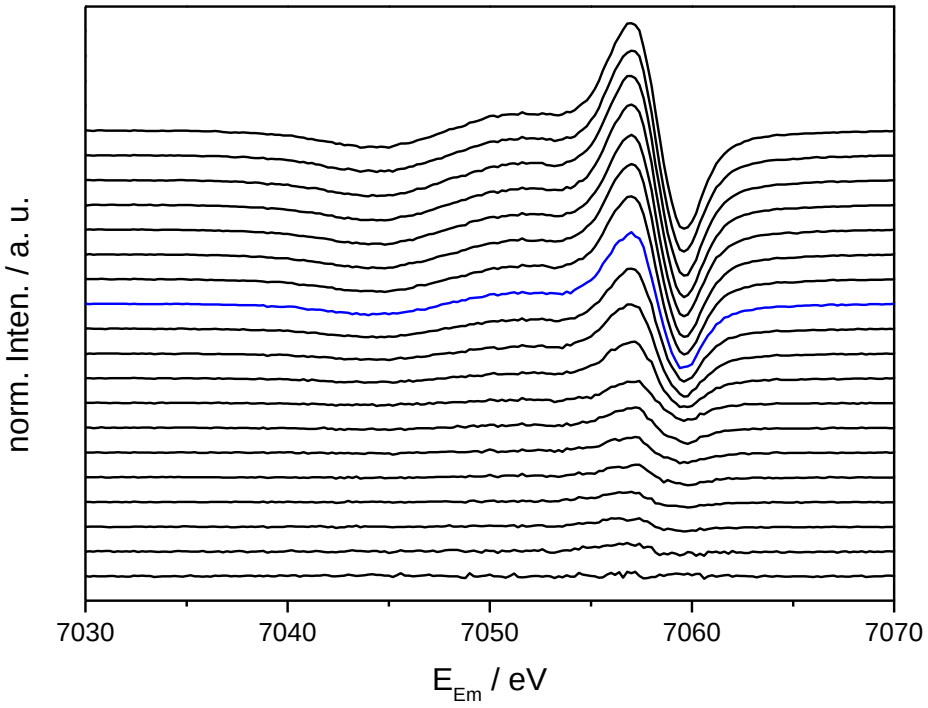

Figure 4.37: Difference spectra of [Fe(L-N_4Bn_2)$(NCS)_2$] in the temperature range from 80 to 260 K with [Fe(L-N_4Bn_2)$(NCS)_2$] 70 K as LS reference, blue spectrum indicates spin transition temperature (190 K), IAD method with alignment to COM

To quantify the variations with temperature, the absolute area of the difference spectra was determined by integration in the energy range from 7030 to 7070 eV. The integrated difference spectrum between 70 and 260 K is shown in Figure 4.38 as an example.

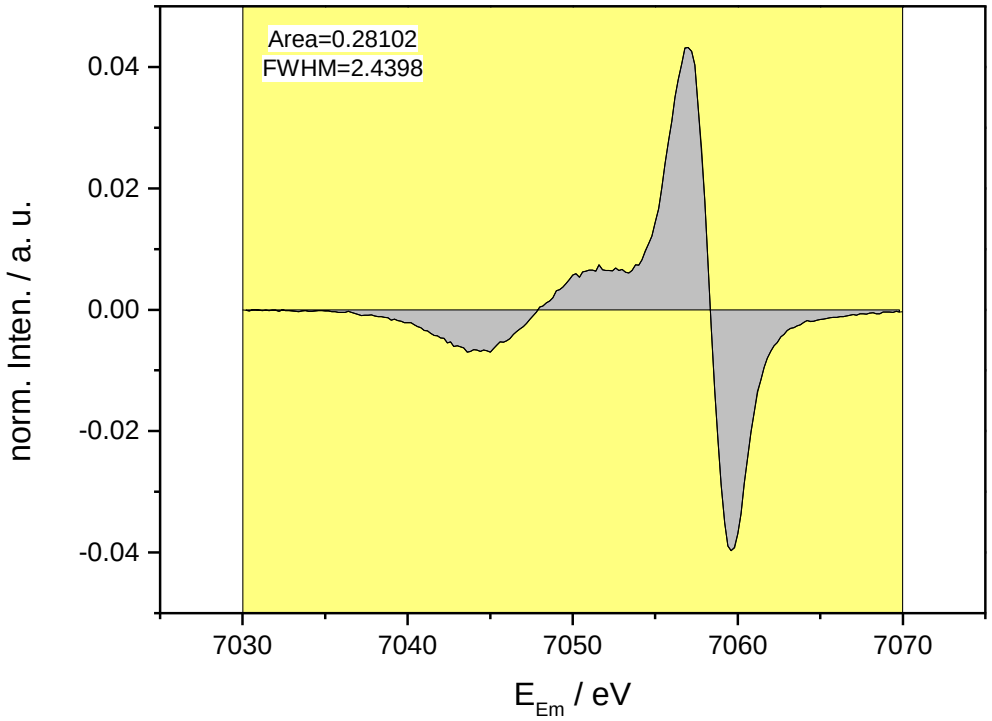

Figure 4.38: Integration of the difference spectrum between 70 and 260 K, alignment to COM.

The IAD values of all temperatures obtained by integration are shown in column 2 of Table 30. The high IAD values at 30, 40 and 50 K show that the system is partially transformed to the metastable HS state by the high energetic X-rays (HAXIESST effect). Therefore, these three data points (marked green in Figures 4.39 to 4.41) are excluded from the Boltzmann fit shown in Figure 4.39. The fit of the IAD values obtained by the IAD method with alignment to the COM results in a spin transition temperature of $T_{1/2}(\mathrm{IAD_{COM}}) = 178.9 \pm 0.9$ K. Compared to the IAD analysis without alignment of the spectra, the transition temperature is slightly shifted to higher temperatures ($\Delta T = 0.3$ K), but compared to the transition temperature obtained by SQUID magnetometry the difference is still 13.1 K.

Table 30: IAD values determined with the IAD method with alignment of the spectra to COM.

T / K	IAD / a. u.	γ_{HS} (IAD)	$\gamma_{HS, corr}$ (IAD)
30	0.24235	0.86215	0.83388
40	0.23341	0.83034	0.80206
50	0.17960	0.63892	0.61065
80	0.01066	0.03794	0.00966
90	0.01881	0.06691	0.03863
100	0.01976	0.07029	0.04202
110	0.02195	0.07810	0.04983
120	0.02745	0.09767	0.06939
130	0.03432	0.12210	0.09382
140	0.04668	0.16606	0.13778
150	0.05140	0.18285	0.15458
160	0.08915	0.31714	0.28887
170	0.12409	0.44144	0.41316
180	0.15084	0.53659	0.50832
190	0.18333	0.65217	0.62390
200	0.21533	0.76604	0.73776
210	0.23643	0.84110	0.81283
220	0.24632	0.87628	0.84800
230	0.26215	0.93258	0.90431
240	0.27189	0.96724	0.93896
250	0.27384	0.97416	0.94589
260	0.28102	0.99973	0.97145

For the comparison of the IAD values with the magnetization measurement the values were treated in the same way as described in the previous chapter. First the IAD values were converted into γ_{HS} values according to equation (39). Since no experimental HS IAD value (IAD_{HL}) was available, the calculation of the HS fraction was performed with the IAD value at 300 K (IAD_{300K} = 0.2811), that was obtained by the Boltzmann fit. The resulting γ_{HS} values are shown in column three of Table 30. As the Boltzmann fit of the γ_{HS} values shows an offset compared to the data obtained by SQUID (cf. Figure 4.40), the γ_{HS} values were corrected by an offset of 0.02828. The corrected values are listed in column four of Table 30 and the plot versus temperature is displayed in Figure 4.41 in comparison with the HS fractions obtained by the magnetization measurements.

As can be seen, the two fit curves show significant differences in the whole transition region. The IAD fit curve starts to increase at around 90 K, whereas the SQUID fit curve first starts to increase at around 130 K. Additionally, the slopes of the two fit curves differ distinctly. The fit curve of the IAD values shows a smaller slope than the curve resulting from the SQUID data. Therefore, the spin change appears more gradual in the IAD case than in the SQUID case.

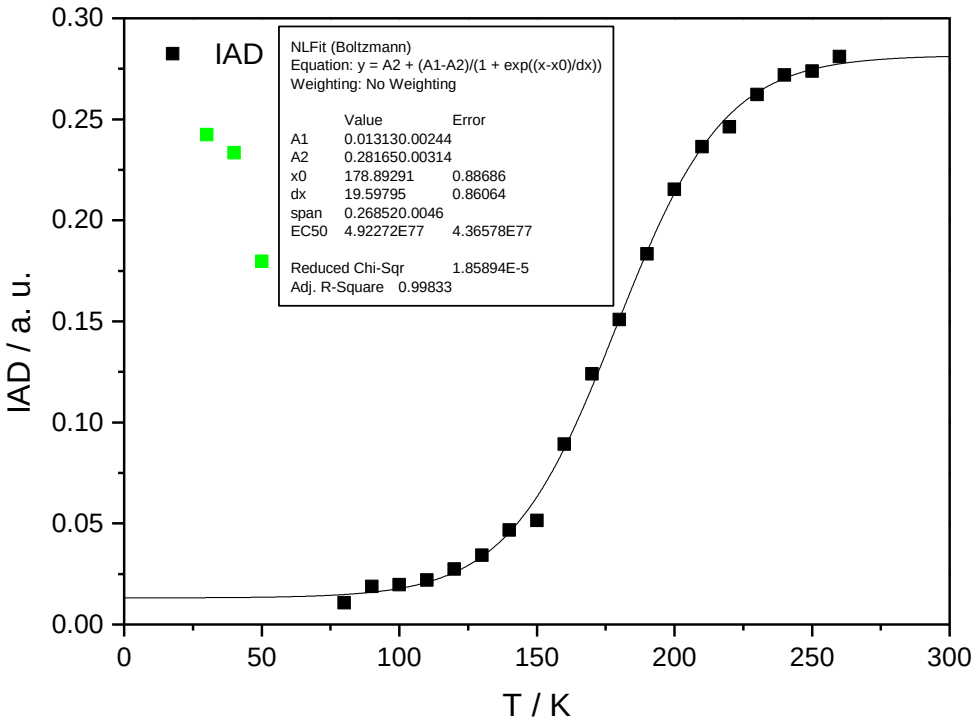

Figure 4.39: Plot of the IAD values with the corresponding Boltzmann fit function; IAD method with alignment to COM.

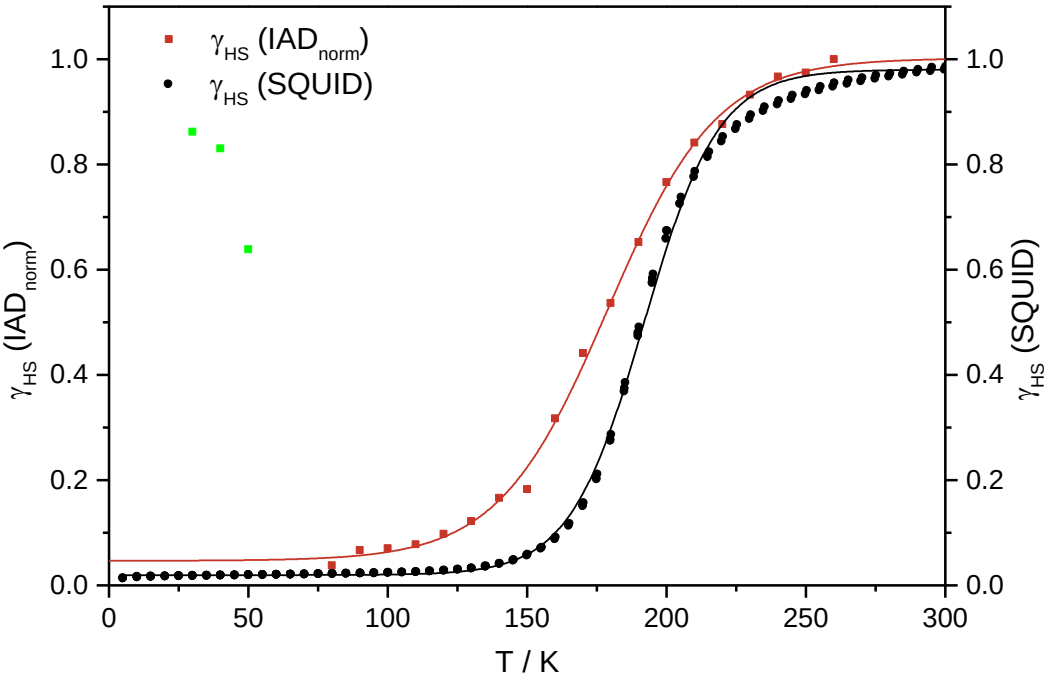

Figure 4.40: Comparison of HS fractions obtained by IAD method with alignment of the spectra to COM (red) and by SQUID (black).

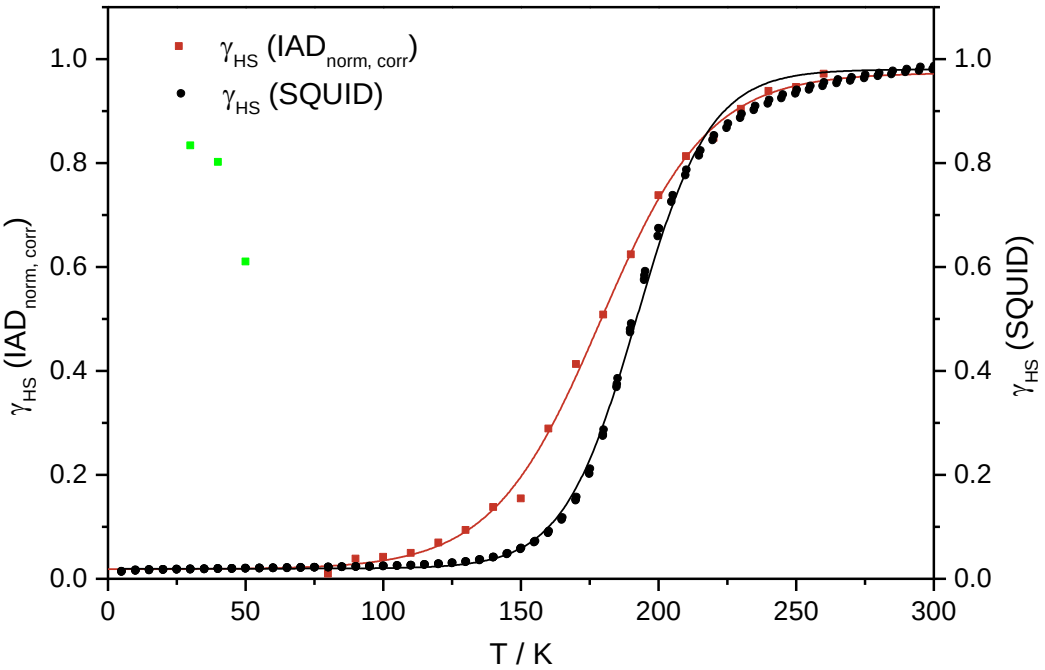

Figure 4.41: Comparision of offset corrected HS fractions by IAD method with alignment of the spectra to COM (red) and by SQUID (black).

4.3 Summary

This chapter was focused on the analysis of the temperature-dependent CtC emission spectra. For the analysis, a number of different methods was applied and if necessary modified to improve the results. Since some of the methods require a calibration curve for determination of the spin state, reference compounds with known spin states (S = 0, 0.5, 2) were measured, too. The first described method used the experimentally determined energetic position of the Kβ main line and the intensity of the Kβ' signal for correlation with temperature and for calculation of the spin state. Both parameters showed a sigmoidal increase with rising temperature and in both cases reasonable spin values could be obtained, even though only a spin of S = 1.6 was reached in case of the HS state, instead of the expected value of S = 2. This deviation might be explained by the choice of reference compounds used for the creation of the calibration curves, since the structural differences between the SCO complex and the references are perhaps too large. The determined transition temperature in case of the emission energy of the Kβ main line is in quite good accordance with the SQUID data ($\Delta T_{1/2} \approx 6$ K), as well as the curve shape, which shows a slightly more gradual behaviour than the magnetization curve. In case of the intensity of the Kβ' signal, the transition temperature is shifted by around 12 K to lower temperatures and the accordance with the SQUID data is worse, since the spin change shows a much more gradual behaviour.
The next described method did not use the experimentally determined parameters, instead fit parameters were used. The spectra of all compounds (references and SCO complex) and all temperature points were deconvolved with either two or three signals. Afterwards, the energetic position, the intensity and the area of these signals were plotted versus temperature and used to calculate the spin states. Summarising the results of these approaches, it can be said that only the energetic position of fit curve 1, which is assigned to the Kβ main line, gave reasonable results. The resulting transition temperature and the spin values are nearly identical to the values determined in case of the experimental position of the Kβ main line. Evaluation of the other fit parameters gave unsatisfactory results in each case. For most parameters no sigmoidal trend could be observed and the calculated spin values showed physically unrealistic values (e.g. negative or too high).
As a further method the so-called ΔE_{CP} method was applied. In this method, the energy splitting between the COM and the Kβ main peak was correlated with the spin state. It could be shown that the success of this method strongly depends on a suitable choice of reference compounds. The calibration curve, which was constructed with the reference compounds **OS1**, **OS2**, **OS7** and **K_3[Fe(CN)$_6$]** lead to negative spin values in the LS region. Therefore, the calibration curve was modified using the spectrum of [Fe(L-N_4Bn_2)$(NCS)_2$] at 70 K as LS reference. This modification lead to positive spin values in the whole examined temperature range and the fit of the sigmoidal curve shape resulted

in a transition temperature $T_{1/2}(\Delta E_{CP}) = 197.0 \pm 2.0$ K that is again very similar to the methods using the energy of the Kβ main line. Additionally, the overall curve shape is in good accordance with the SQUID data.

The last applied method was the so-called IAD method, where the integrals of the absolute values of the area of the difference spectra between the SCO complex and a LS reference spectrum were used to calculate the HS fractions. Two different approaches were tested, one without alignment of the data and one with alignment to the COM of the LS reference spectrum. In general, both methods yielded more or less the same results concerning spin transition temperature and curve shape. Therefore, the method without alignment of the data seems to be more appropriate, since a number of data treatment steps can be avoided. Compared to the SQUID data, the results of this method show relatively large deviations, since the transition temperature is shifted by around 13 K to lower temperatures and the curve shape differs significantly.

Altogether it can be said, that all applied methods using different parameters of the CtC emission spectra for the correlation with the spin state showed certain deficiencies. Some of the methods lead to comparable results, for example the IAD method and the correlation of the intensity of the Kβ' signal showed almost the same transition temperature and curve shape. Moreover, the correlation of the experimentally determined energetic position of the Kβ main line and the energetic position of fit curve 1 with the spin state showed nearly the same results as the modified ΔE_{CP} method. So it seems, that the more elaborate methods cannot provide much better results and a rough estimate of the transition temperature and the SCO behaviour can also be obtained by simply reading out the energetic position of the $K\beta_{1,3}$ feature.

5 Valence-to-Core Emission Spectroscopy

The last chapter is focused on the analysis of the temperature-dependent VtC emission experiments. As already described in chapter 1.3.4.3, the VtC spectra show only small variations with changes of the spin state. In the HS state, the VtC spectrum shows almost no Kβ'' signal and the intensity of the $K\beta_{2,5}$ feature is diminished compared to the LS state. Additionally, the HS spectrum shows a broadening of the $K\beta_{2,5}$ signal in relation to the LS spectrum. With evaluation of the mentioned spectral changes, it will be checked if it is possible to correlate these changes with temperature and therefore with the spin state. For the analysis of the data, a method for background correction is established first, which is suitable for all temperature points. Afterwards, different approaches based on changes of the FWHM or the intensity are described, which are supported by DFT calculations of the LS and HS state.

5.1 Experimental Section

VtC emission experiments were performed at beamline ID26 at the ESRF (Grenoble, France). The ring current varied between 180 and 200 mA and the electron energy was 6.0 GeV. A cryogenically cooled Si(111) double-crystal monochromator was used for the measurements at the iron K-edge (7.112 keV). Energy calibration was performed using an iron foil. On the sample position the incident X-ray beam had a flux of approximately 2×10^{13} photons/s. The emission spectra were measured at a scattering angle of 90°with a 1 m diameter Rowland-circle spectrometer arranged in horizontal plane with spherically bent Ge(620) analyser crystals. The sample was diluted in boron nitride and pressed to a pellet to avoid self-absorption effects. Measurements were carried out using a closed cycle helium cryostat in a temperature range of 50 to 260 K. To avoid radiation damages several quick HERFD scans just above the edge were performed at one sample spot to calculate the time in which the sample was stable. The measurement time was then adjusted to this time span and additionally each spectrum was measured at a new sample spot. Several spectra were averaged to improve the signal-to-noise ratio.

5.2 Data Analysis and Results

For analysis of the VtC emission spectra, the data were prepared according to the procedure described in the following section. First, all raw data of one temperature were normalized to the maximum and then merged to one spectrum. Then the background resulting from the high energetic side of the $K\beta_{1,3}$ emission had to be removed. For this, the VtC signal was masked in the energy range from 7090 to 7115 eV and the spectrum was fitted with an exponential decay according to equation (40)

$$y = y_0 + A_1 e^{-x/t_1} + A_2 e^{-x/t_2} \tag{40}$$

with y_0 = offset
A_1, A_2 = amplitudes
t_1, t_2 = decay constants.

Figure 5.1 exemplarily shows the experimental VtC spectrum at 120 K with the masked data range in red and additionally the resulting background fit in blue.

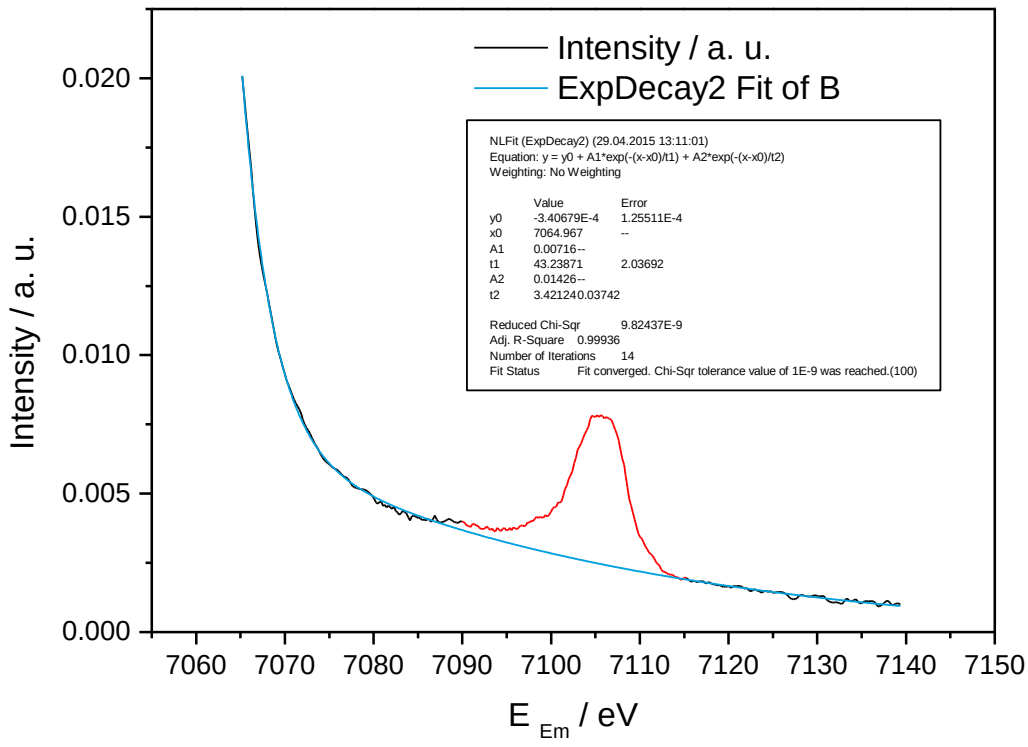

Figure 5.1: Background fit (blue) of the experimental VtC emission spectrum at 120 K (red: masked data range).

The obtained background fit function was then subtracted from the VtC spectrum and the uncorrected and the background corrected spectrum are shown in Figure 5.2. The background correction reveals one signal at around 7105.5 eV with a slightly asymmetric peak structure, due to a weak shoulder on the low energetic side. Additionally, a very weak feature at around 7090 eV is observable.

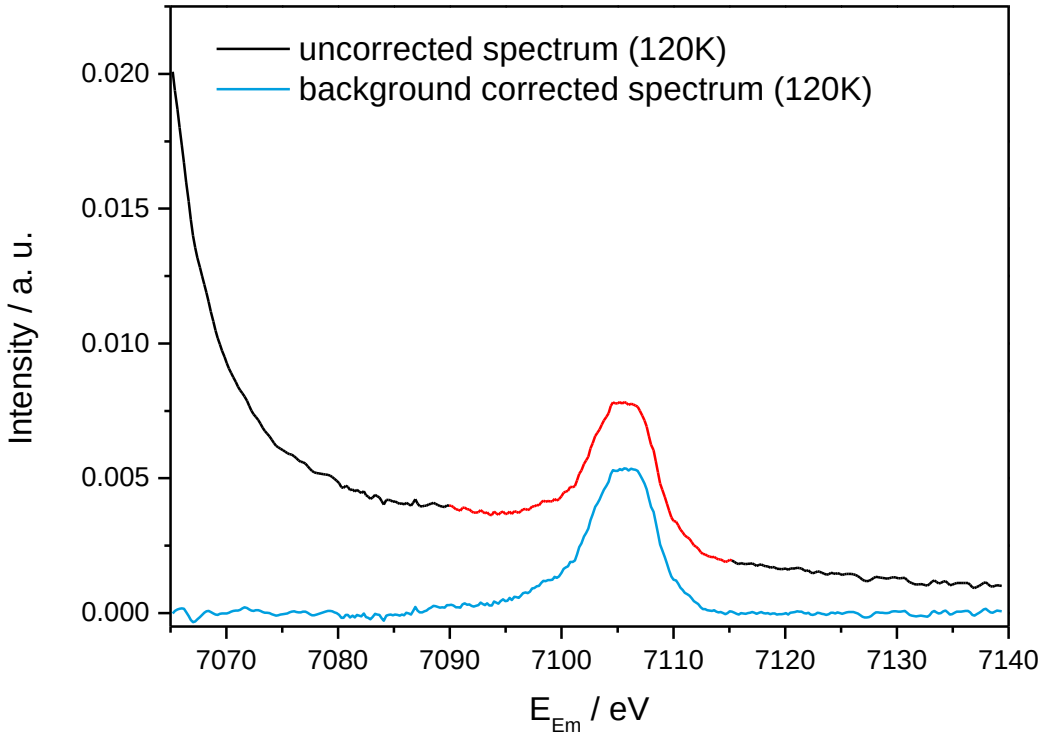

Figure 5.2: Uncorrected and background corrected VtC emission spectrum (120 K).

This procedure for background correction was applied to the spectra of all temperature points (50 to 293 K) and the resulting spectra were normalized to unit area afterwards. The background corrected and normalized spectra are shown in Figure 5.3. The VtC emission spectra show only small variations with increasing temperature. The peak at 7105 eV loses intensity with rising temperature and thus increasing HS fraction and elongated Fe-N bond lengths. With a calculated series of hypothetical spectra with increasing Fe-ligand distance, Lee *et al*. showed that the intensity of the corresponding signal decreases with longer distances.[165] The origin of this effect seems to be the reduced ligand/Fe-np overlap and therefore the weaker orbital interactions. Furthermore, the signal with very low intensity at around 7090 eV decreases, too. At the high energetic side of the $K\beta_{2,5}$ signal, the intensity is increased in the range from 7110 eV to 7115 eV. Additionally, the signal becomes broader with rising temperature.

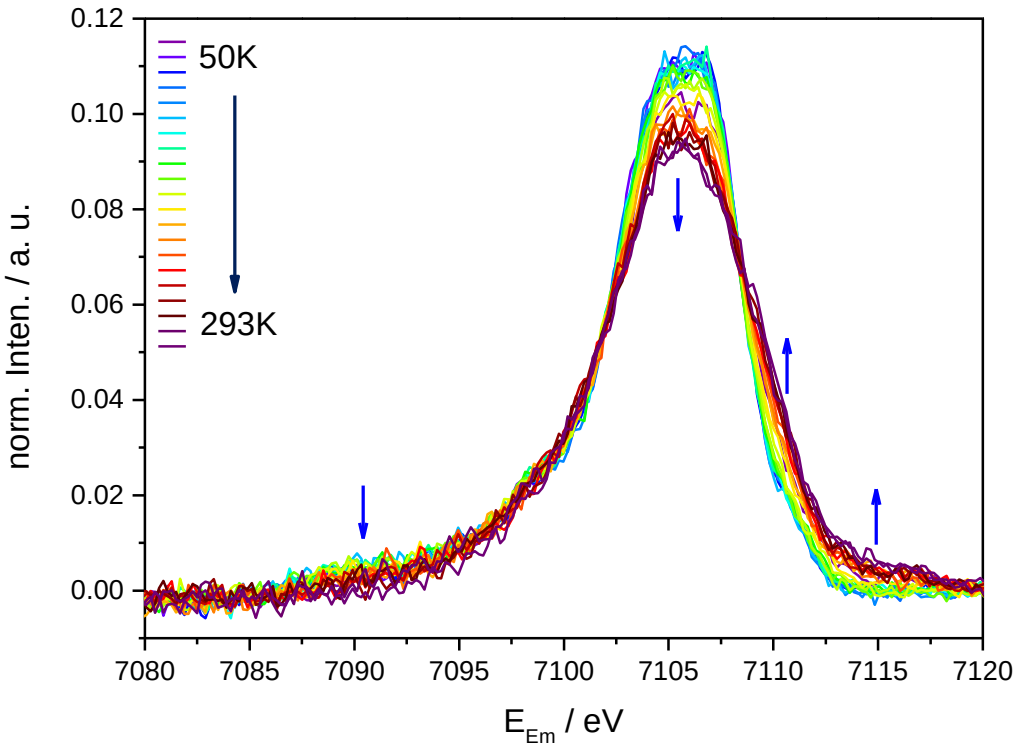

Figure 5.3: Background corrected and normalized VtC emission spectra in the temperature range from 50 to 293 K.

The experimentally obtained values for the full width at half maximum (FWHM) are shown in Table 31 and the plot versus temperature is shown in Figure 5.4 in comparison with the magnetization data. The plot reveals that the increasing FWHM values arise not only from higher temperatures but are also due to an increasing HS fraction, since the FWHM does not increase in a linear shape as one would expect, instead it increases in a

sigmoidal shape. The applied Boltzmann fit results in a spin transition temperature of $T_{1/2}$ = 202.9 ± 3.2 K, which is around 10 K higher than the one obtained by SQUID magnetometry. In addition, the fit of the FWHM shows a much more gradual behaviour than the SQUID data Thus the determination of the FWHM values seems to be no appropriate method for the correlation of the spectral information with the spin state of the system, since it overestimates the transition temperature.

Table 31: Determined FWHM values for all temperatures.

T / K	FWHM / eV	T / K	FWHM / eV
50	7.35760	**170**	7.15243
70	6.77034	**180**	7.29582
80	6.74917	**190**	7.44233
90	6.70012	**200**	7.66366
100	6.73590	**210**	7.60009
110	6.73174	**220**	8.03520
120	6.88181	**230**	8.15557
130	6.79855	**240**	8.15952
140	6.82805	**250**	8.31422
150	6.81779	**260**	8.52795
160	6.99911	**293**	8.49684

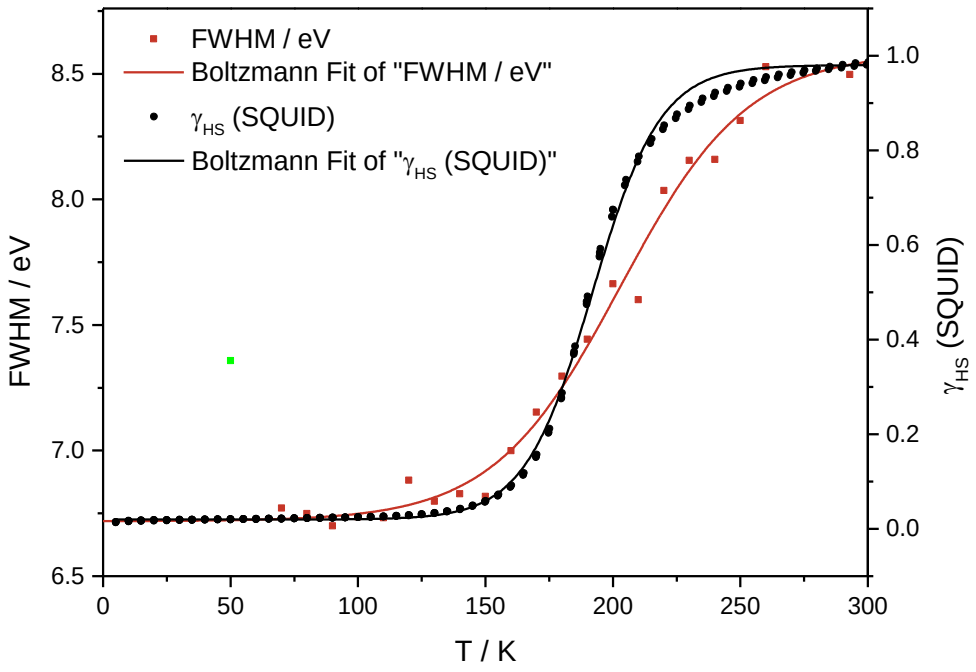

Figure 5.4: Comparison of HS fraction obtained by SQUID magnetometry and plot of FWHM versus temperature *T* with resulting sigmoidal Boltzmann fit function.

Additionally, to the loss of intensity and the broadening of the intense signal at 7105 eV the small signal at around 7090 eV decreases with rising temperature, too. Due to the high noise level of the spectra the effect is only difficult to quantify and therefore no further evaluation is performed on this signal.

For a better understanding of the spectral changes occurring during the SCO process from LS to HS, the spectra of both extreme cases (LS and HS) were calculated using a density functional theory (DFT) approach, which will be described subsequently.

The calculations of the VtC emission spectra were performed with the XES approach implemented in the quantum chemistry program ORCA (version 3.03).[184] The experimental X-ray structures were used as structural input. The non-hybrid GGA functional BP86[185,186] was used with the CP(PPP) basis set [187] for Fe (with a special integration accuracy of 7) and the scalar-relativistically recontracted def2-TZVP(-f) basis set [188] for all other atoms. This combination of functional and basis set was chosen because it has been successfully applied in previous studies dealing with the simulation of XAS and XES spectra. [165,189–192]

The obtained calculated VtC emission spectra were broadened according to the experimentally determined FWHM. Therefore, a broadening of 6.7 eV was applied to the LS spectrum at 110 K and a broadening of 8.5eV to the HS spectrum at 293 K. Since the calculated absolute transition energies are generally underestimated, the calculated spectra were shifted in energy to adjust to the experimental spectra. For determination of the energy shift, the COM of the experimental and the calculated spectra was determined. The calculated spectra were then shifted to the COM of the experimental spectra, resulting in an energy shift of 181.82 eV in the LS case and of 181.46 eV in the HS case. Figure 5.5 shows the experimental spectra at 110 K (bottom) and 293 K (top), each normalized to an area of one. Additionally, the energy corrected transitions and the broadened spectra are shown, normalized to unit area, too.

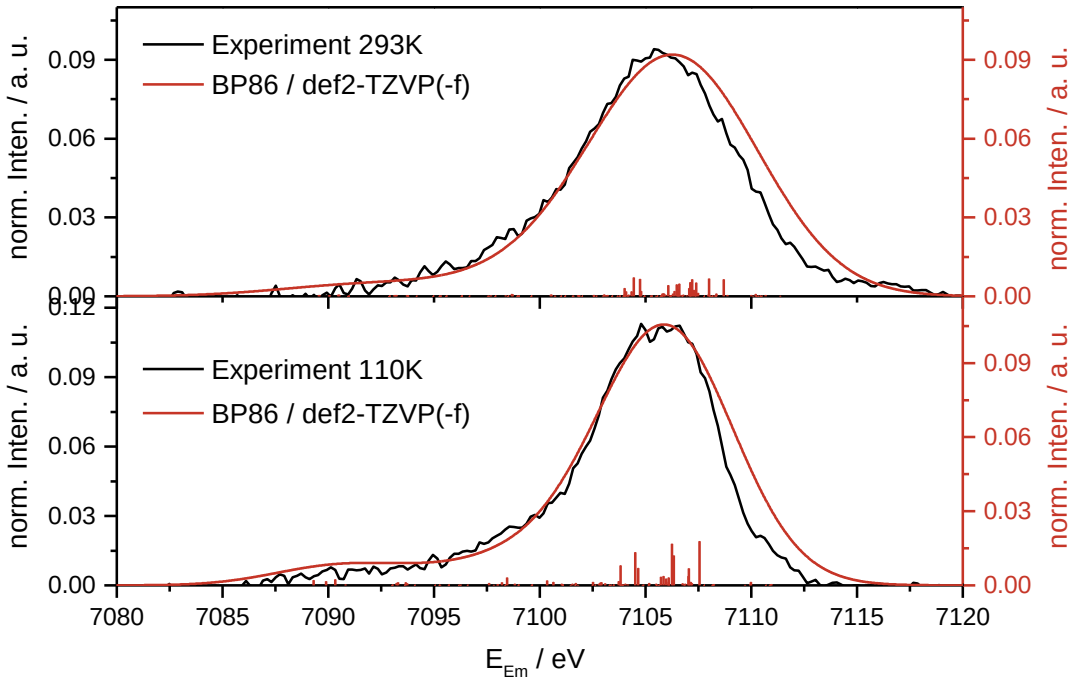

Figure 5.5: Experimental and corresponding calculated VtC emission spectra of [Fe(L-N_4Bn_2)$(NCS)_2$]. Top: HS at 293 K, a broadening of 8.5 eV and a shift of 181.46 eV has been applied to the calculated spectrum; Bottom: LS at 110 K, a 6.7 eV broadening and a shift of 181.82 eV has been applied to the calculated spectrum.

The agreement between the experimental and the calculated spectra is quite good, only the intensity at the high energetic side of the experimental spectra is overestimated in the calculated spectra. This effect is observable for both temperatures and it is not possible to adjust the calculated spectra to the experimental ones by using a smaller broadening, because then the agreement at the low energetic side becomes worse.

A hint for the explanation of the changes occurring with increasing temperature is provided by the calculated transition energies and intensities. Figure 5.6 shows the energy corrected and normalized transitions for the HS (blue) and LS state (red). The calculated transitions reveal that the LS state shows some more intense transitions in the low energy range (e. g. at around 7090 eV and 7098 eV) than the HS state. This observation could explain the higher intensity of the experimental LS spectrum in this energy region compared to the HS spectrum. Additionally, it is observable that the LS transitions in the energy range from around 7103.7 – 7107.5 eV exhibit a higher intensity than the respective HS transitions, resulting in the higher intensity of the $K\beta_{2,5}$ peak in the LS case. On the other hand, the HS state shows two intense transitions at 7108.0 eV and 7108.6 eV, whereas the LS spectrum shows only very weak transitions in this energy region. This results in the broadened $K\beta_{2,5}$ peak in the HS spectrum compared to the LS spectrum.

According to literature, the transitions in the highest energy range (7109 eV to 7112 eV) should be mainly attributed to Fe d based MOs.[191] In case of [Fe(L-N_4Bn_2)$(NCS)_2$],

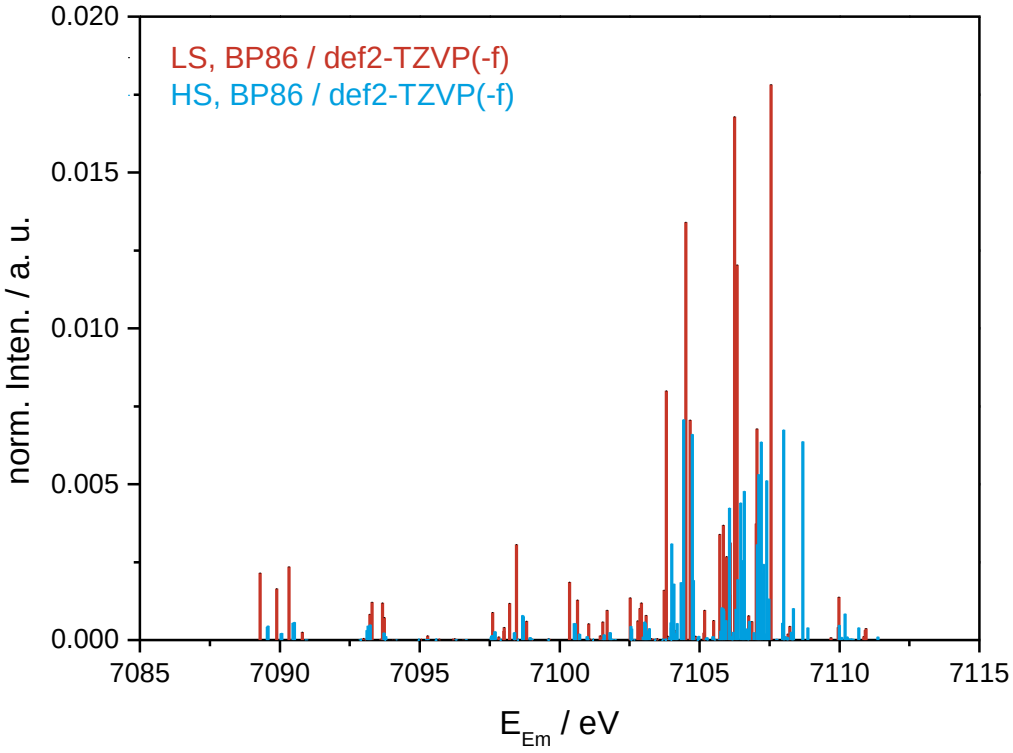

Figure 5.6: Calculated normalized transition energies, red: LS at 110 K, shifted by 181.82 eV; blue: HS at 293 K, shifted by 181.46 eV.

Loewdin population analysis revealed a strong mixing of Fe d and S p orbitals for most transitions in this region, especiallly in case of the LS state, as shown in Table A2 in the appendix. Therefore, a clear assignment to particular t_{2g} or e_g orbitals of the iron centre is not possible. Nevertheless, the transitions in this energy region show certain differences between LS and HS, as can be seen in Figure 5.7, that shows the enlarged energy region from 7109.5 to 7112.0 eV together with the molecular donor orbitals of the most intense transitions. In the LS case, a rather strong transition is located at 7110.0 eV and some weaker transition at around 7110.9 eV. The corresponding donor orbitals depict the before mentioned strong mixing of Fe d and S p orbitals. In contrast to this, the HS state shows a number of weaker transitions in the range from 7110.2 eV to 7110.7 eV and an additional transition at 7111.4 eV. The most intense transition at 7110.204 eV shows almost no Fe d contribution, whereas the other three show significant contributions of around 50 % Fe d. Furthermore, the donor orbitals of the transitions at 7109.996 and 7110.685 eV exhibit a significant N p population, in case of the transition at 7110.685 eV only the equatorial nitrogen atoms are involved, whereas axial and equatorial nitrogen atoms contribute to the lower lying transition.

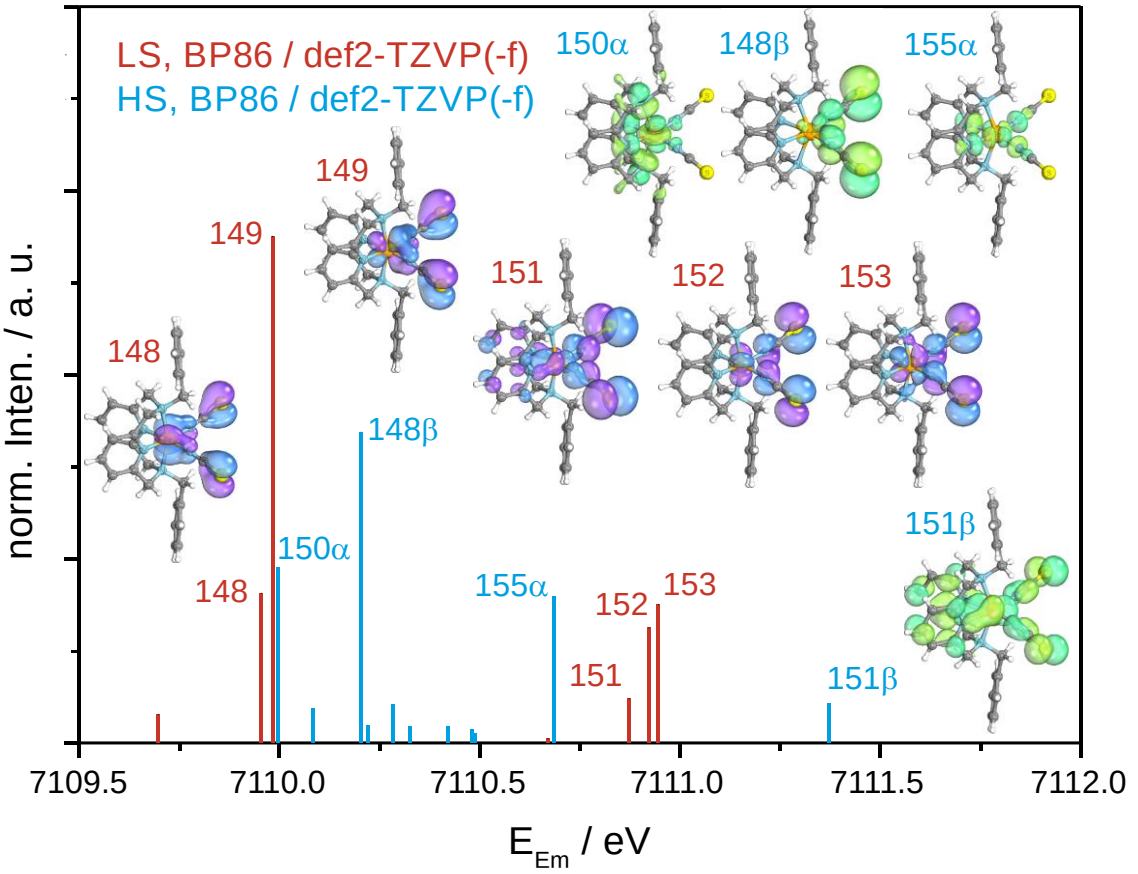

Figure 5.7: Calculated normalized transition energies in the energy range from 7109.5 to 7112 eV together with the donor orbitals of the most intense transitions, red: LS at 110 K, shifted by 181.82 eV; blue: HS at 293 K, shifted by 181.46 eV.

Since the differences between HS and LS state are more pronounced in case of the transitions in the range from 7109 eV to 7112 eV compared to the differences in the lower energy region, the changing intensity could be a possible measure for the changes occurring during the spin transition process. Looking at the experimental spectra again (Figure 5.8), the most intense changes are observed at the peak maximum at around 7105.5 eV. Since the noise level of the spectra is very high, it is not possible to read out the intensity of this point in a reliable way. Therefore, the intensity changes were read out at an energy value of 7110.627 eV, because this point shows the largest variation in this energy region. According to the calculated spectra, the changes at this energy should be distinct, since only the HS state shows a transition there, which is moreover strongly Fe d based and thus could maybe be used for a correlation with the changes of the spin state.

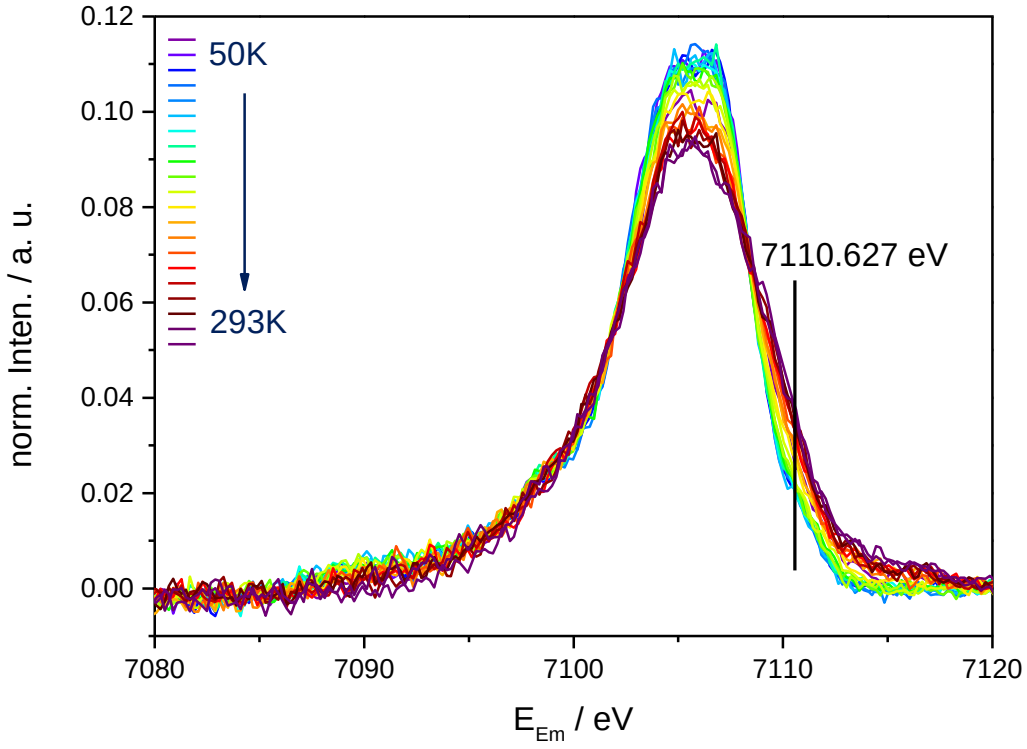

Figure 5.8: Background corrected and normalized VtC emission spectra in the temperature range from 50 to 293 K, black line indicates the energy where the changes of intensity were read out.

The obtained intensities are displayed in Table 32 and a plot versus temperature with the resulting Boltzmann fit function is shown in Figure 5.9.

Table 32: Normalized intensity at 7110.627 eV, obtained from $K\beta_{2,5}$ emission spectra.

T / K	norm. Inten. / a. u.	T / K	norm. Inten. / a. u.
50	0.02515±0.00181	**170**	0.02168±0.00181
70	0.02016±0.00181	**180**	0.02682±0.00181
80	0.02115±0.00181	**190**	0.02822±0.00181
90	0.02164±0.00181	**200**	0.02969±0.00181
100	0.01996±0.00181	**210**	0.03294±0.00181
110	0.02055±0.00181	**220**	0.03168±0.00181
120	0.01928±0.00181	**230**	0.03213±0.00181
130	0.02098±0.00181	**240**	0.03217±0.00181
140	0.02114±0.00181	**250**	0.03399±0.00181
150	0.02183±0.00181	**260**	0.03561±0.00181
160	0.02046±0.00181	**293**	0.03751±0.00181

Due to the high noise level of the experimental spectra the read out intensities show a rather large variation. Nevertheless, the plot of the intensities versus temperature still shows a clear sigmoidal curve shape, except for the green marked data point, which indicates again the HAXIESST effect at low temperatures. The fit results in a transition curve that follows the magnetization almost exactly within the error bars and the transition temperature was determined as $T_{1/2}$(VtC) = 191.3 ± 4.8 K, which is in good accordance with the transition temperature obtained by SQUID magnetometry ($T_{1/2}$(SQUID) = 192.0 ± 0.2 K). But due to the high noise level, the error of the determined temperature is much higher than in the SQUID case and therefore the variation of $T_{1/2}$ is much larger, too.

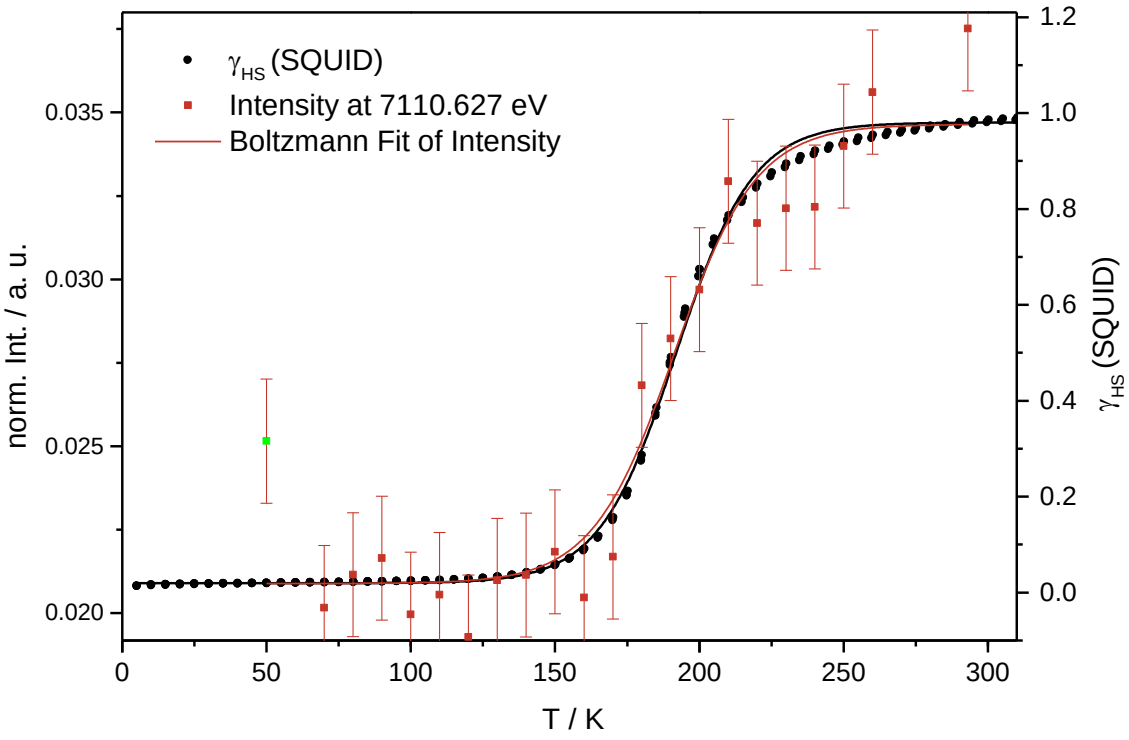

Figure 5.9: Comparison of normalized intensity at 7110.627eV (red) and HS fraction obtained by SQUID (black).

5.3 Summary

This chapter was focused on the analysis of the temperature-dependent VtC emission spectra. As a first step, a procedure for background correction of the experimental spectra was developed, which is applicable at all temperature points. To subtract the background arising from the $K\beta_{1,3}$ emission line, an exponential decay function turned out to be best suited. The resulting background corrected and normalized VtC emission spectra showed only rather small changes with increasing temperature. In general, one intense signal corresponding to the $K\beta_{2,5}$ signal and some weaker features were observable. The intensity of the $K\beta_{2,5}$ signal decreases with rising temperature and additionally, the signal is broadened. Therefore, as a first approach, the FWHM was determined and its temperature dependence was evaluated. Even though a sigmoidal increase of the FWHM could be observed, the determined transition temperature shows a shift of around 10 K to higher temperatures compared to the SQUID data.

For a better understanding of the spectral shape and the occurring temperature-dependent changes, DFT calculations of the LS and HS state were performed, which were in very nice accordance with the experimental spectra. The intensity changes of the respective signals, as well as the observed broadening could be reproduced by the calculated transitions quite well.

The second approach, which was tested for correlation of the spectral changes with temperature, was based on the changes of intensity. Since the signal-to-noise ratio of the spectra is rather bad, it was not possible to read out the intensity of the $K\beta_{2,5}$ signal, which shows the largest variation. Instead, the intensity was read out at an energy value of 7110.627 eV, since the high energy region (7109 – 7112 eV) showed the most relevant differences between the HS and LS state concerning the energetic distribution of the transitions as revealed by the DFT calculations. Furthermore, the calculations showed a strongly iron based transition in case of the HS state at this energy, while the LS state exhibits no transition there.

The plot of intensity versus temperature resulted in a sigmoidal curve shape that is almost exactly following the magnetization curve obtained by SQUID. Additionally, the determined transition temperature is in very nice accordance with the SQUID data.

Summarising the results of this chapter, it can be said that it is obviously possible to follow the changes of the spin state by careful evaluation of spectral changes in the VtC emission spectra. In doing so, the FWHM turned out to be less suitable compared to the changes of intensity. This can be explained by the fact that the nature of the transition, which was underlain the evaluation of the intensity changes is strongly iron based and thus probes the changes of the occupation of the 3d orbitals directly, whereas the changes of the FWHM might be influenced by other effects, too. Furthermore, the investigated transition shows significant contributions of the equatorial nitrogen atoms, what also seems to be responsible for the good agreement with the magnetization data, since the

previous chapters, especially the EXAFS analysis lead to the suggestion that the magnetic changes are strongly correlated with the changes of the equatorial Fe-N bond lengths.

6 Final Conclusion and Outlook

The aim of this work was the in-depth analysis of existing methods and their improvement by development of new approaches for the analysis of temperature-dependent SCO processes with hard X-ray absorption and emission spectroscopic techniques. As a model compound, the quasi-octahedral Fe(II) SCO complex $[Fe(L\text{-}N_4Bn_2)(NCS)_2]$, which exhibits a gradual SCO behaviour with a transition temperature of $T_{1/2}$(SQUID) =192.0 ± 0.2 K, was investigated. A number of different techniques, namely EXAFS, HERFD-XANES, RIXS and CtC-XES as well as VtC emission spectroscopy were applied in a temperature range from 10 K to 293 K, to obtain a detailed overview of the possibilities of these methods for the investigation of SCO processes. In general, all applied techniques showed an interesting behaviour at the different temperature points that could be used to follow the spin transition process. Using EXAFS spectroscopy (chapter 2), the structural changes caused by an elongation of the Fe-N bond lengths, during the transition from the LS to HS state were analysed. Different approaches to fit the experimental data with theoretical models were tested, based on either one nitrogen shell with six backscattering atoms or with two nitrogen shells with four equatorial and two axial N atoms. Additionally, either unfiltered or Fourier filtered data were used. Basically, all fit models revealed a clear sigmoidal increase of the bond lengths with rising temperature. The determined HS fractions were in good agreement with the magnetization data obtained by SQUID magnetometry. In case of the fit models with one nitrogen shell, the transition curves followed the magnetization nearly exactly, while in case of the models with two N shells differences between the axial and equatorial Fe-N distances were observable. Even though both resulting fit curves followed the magnetization within the error bars, in almost all models the axial distances tended to start the elongation at lower temperatures than the equatorial ones. This obviously does not seem to affect the magnetization, since the magnetic changes rather follow the changes of the equatorial bonds. The Debye-Waller-like factors, as well as the afac, showed a temperature-dependent behaviour in some cases, too. The resulting maxima respective minima could be used to roughly determine the spin transition region, but not for a precise determination of the transition temperature.

In contrast to EXAFS spectroscopy, the (HERFD-)XANES technique (chapter 3) provides structural and electronic information of the investigated systems. The prepeak region, which is caused by transitions from 1s into the 3d or 3d/4p hybridized orbitals, provides useful information about the distribution of the d electrons and therefore of the spin state of the system. Prior to the evaluation of the temperature-dependent changes, a

method for background correction was established, which allowed the extraction of the prepeak features at all temperature points. The extracted prepeak exhibited two distinct features, whereof the signal at lower energies could be correlated with the HS fraction. Two different approaches were described, which used either the area or the intensity of signals obtained by a performed deconvolution of the experimental spectra. While the area and intensity of the higher energetic signal stayed more or less constant, the changing intensity and area of the lower lying signal were used to quantify the HS fraction. Both approaches resulted in a sigmoidal increase with rising temperature, but only in case of the intensity changes, the transition curve followed the magnetization almost exactly. Additionally, the obtained transition temperature showed a very good agreement with the one determined by SQUID magnetometry. This good agreement can be ascribed to the nature of the probed transitions. In case of the HS state, the LUMO and LUMO+1 orbitals, which can be assigned to the lowest lying transitions in the prepeak region and so to the examined HS signal, showed a very dominant Fe d character. Therefore, the changes of the intensity can be directly correlated to the changes of the distribution of the 3d electrons and thus to changes of the magnetization. In contrast to this, the method based on the changes of the area resulted in a lower transition temperature and a more gradual transition curve. The deviations from the magnetization curve might probably be explained by the simplified model with two signals used for the deconvolution of the spectra, since the recorded RIXS planes revealed at least three signals in case of the HS state.

Of all spectroscopic techniques, which were applied in this work, CtC emission spectroscopy maybe the one that shows the most prominent changes in case of the LS $\rightarrow$ HS transition. As already described in chapter 1.3.4.3, the Kβ emission spectrum shows two prominent features depending on the spin state of the probed metal ion: The intense $K\beta_{1,3}$ line at higher energies and at lower fluorescence energies the Kβ' signal. Since the CtC emission spectrum is strongly influenced by the number and distribution of 3d electrons, it is supposed to be a promising tool for the investigation of SCO processes. Therefore, a large number of different methods for the analysis of the CtC XES spectra was tested in this thesis.

One approach was based on experimentally determined values, namely the intensity of the Kβ' peak and the energetic position of the $K\beta_{1,3}$ line. For another approach, a deconvolution of the spectra was performed and the resulting energetic position, intensity and area of the fit curves were used to calculate the spin states. Additionally, the so-called ΔE_{CP} method (energy splitting between the $K\beta_{1,3}$ line and the COM) and the IAD method (integrals of absolute area of difference spectra) were tested and the results were improved by minor modifications of these methods.

Altogether it can be said, that all applied methods using different parameters of the CtC XES spectra for the correlation with the spin state showed certain deficiencies. Some of the methods lead to comparable results, for example the IAD method and the correlation

of the intensity of the Kβ' signal showed almost the same transition temperature and curve shape. Moreover, the correlation of the experimentally determined energetic position of the Kβ main line and the energetic position of fit curve corresponding to the $K\beta_{1,3}$ line with the spin state showed nearly the same results as the modified ΔE_{CP} method. So it seems, that the more elaborate methods cannot provide much better results and a rough estimate of the transition temperature and the SCO behaviour can also be obtained by simply reading out the energetic position of the $K\beta_{1,3}$ feature.

VtC XES probes transitions from the HOMOs into the metal 1s orbital. Since the HOMOs are influenced by the ligand environment and the spin state at the metal centre, there is a direct correlation with the spectral shape of the VtC spectra. Prior to the evaluation of the temperature-dependent measurements, a method for background correction was developed and the spectra were normalized to unit area. The processed data revealed only one intense signal ($K\beta_{2,5}$) and some very weak features, which exhibited rather small changes with increasing temperature. With change from LS to HS, the $K\beta_{2,5}$ signal showed a broadening and the intensity decreased. Correlation of the FWHM of this signal with the spin state revealed a sigmoidal shape, but the determined transition temperature differed significantly from the SQUID value. Since the signal-to-noise ratio of the spectra was rather bad, it was not possible to quantify the changes of intensity at the $K\beta_{2,5}$ maximum in a reasonable way. Performed DFT calculations at the LS and HS state revealed further distinct changes of the distribution of the transitions in the high energetic range. The HS state showed a transition at an energy where the LS state showed none. The donor orbital of this transition is strongly iron d based with a significant contribution of the equatorial N atoms. and thus this transition was used for the correlation with the spin state. Therefore, the intensity changes at the energy of this transition at the high energetic side of the $K\beta_{2,5}$ signal were used for the correlation with the spin state. The determined transition temperature, as well as the spin transition curve were in nice accordance with the SQUID data. Similar to the EXAFS results, it seems that the changes of the equatorial Fe-N distances, are directly correlated with the changes of the magnetization. This suggestion is strengthened by the composition of the donor orbital of the examined transition, which shows strong contributions of the Fe d as well as of the equatorial N p orbitals.

So, taking all applied techniques together, X-ray absorption and emission spectroscopy turned out to be well suited for the investigation of solid SCO compounds. All techniques showed distinct spectral changes, which could be used to follow the transition from LS to HS and to determine the transition temperature. The Debye-Waller-like factor and the amplitude reducing factor, obtained by analysis of the EXAFS data, turned out to be useful parameters for the rough determination of the transition temperature as well as the SCO region. In contrast to this, the changes of the Fe-N bonds, especially of the equatorial distances, can be used to follow the SCO process and to determine the transition temperature quite precisely. The same applies for the HERFD-XANES prepeak features, as well as the VtC-XES spectra: In combination with DFT calculations both methods can be used

to follow the spin transition and to determine the transition temperature. Interestingly the analysis of the CtC emission spectra revealed that this method seems to show certain difficulties concerning the determination of the course of the spin transition as well as the transition temperature. Even though a rough determination of both is possible, the obtainable results are worse compared to the other described techniques. But since the acquisition time of CtC spectra is rather short and the spectral changes between HS and LS are very conspicuous, this technique can certainly be used for a quick determination of the present spin state.

Following the results of this work, an application of the developed and modified evaluation methods to other SCO complexes has to be carried out to prove their applicability for other systems. In a first step, further temperature-dependent experiments on mononuclear SCO complexes should be performed. These complexes could be selected either in terms of a different SCO behaviour (e.g. abrupt or with hysteresis) or in terms of a variation of the central metal ion and its oxidation state (e.g. Fe(III) or Co(II)). A further step would be the examination of binuclear complexes to investigate the effects of the second metal ion to the spectral features. Additionally, it would be interesting to examine the SCO behaviour in (frozen) solution. Since the mentioned X-ray techniques are generally not limited to a specific aggregation state, such experiments could be performed with a suitable liquid cell in the He cryostat.

7 References

[1] A. Bousseksou, G. Molnár, G. Matouzenko, *Eur. J. Inorg. Chem.* **2004**, *2004*, 4353.

[2] P. Gütlich, Y. Garcia, T. Woike, *Coord. Chem. Rev.* **2001**, *219-221*, 839.

[3] A. Bousseksou, G. Molnar, L. Salmon, W. Nicolazzi, *Chem. Soc. Rev.* **2011**, *40*, 3313.

[4] O. Kahn, C. J. Martinez, *Science* **1998**, *279*, 44.

[5] O. Kahn, J. Kröber, C. Jay, *Adv. Mater.* **1992**, *4*, 718.

[6] J.-F. Létard, P. Guionneau, L. Goux-Capes in *Topics in Current Chemistry, Vol. 235* (Eds.: P. Gütlich, H. A. Goodwin), Springer, Berlin/Heidelberg, **2004**, pp. 221–249.

[7] C. Jay, F. Groliere, O. Kahn, J. Kröber, *Mol. Cryst. Liq. Cryst. Sci. Technol., Sect. A* **1993**, *234*, 255.

[8] P. Gütlich, H. A. Goodwin in *Topics in Current Chemistry, Vol. 233* (Eds.: P. Gütlich, H. A. Goodwin), Springer, Berlin/Heidelberg, **2004**, pp. 1–47.

[9] L. Cambi, L. Szegö, *Ber. dtsch. Chem. Ges. A/B* **1931**, *64*, 2591.

[10] M. A. Halcrow (Ed.) *Spin-Crossover Materials. Properties and Applications*, Wiley, Chichester, **2013**.

[11] P. Gütlich, A. B. Gaspar, Y. Garcia, *Beilstein J. Org. Chem.* **2013**, *9*, 342.

[12] P. Gütlich, H. A. Goodwin (Eds.) *Topics in Current Chemistry, Vol. 233*, Springer, Berlin/Heidelberg, **2004**.

[13] P. Gütlich, H. A. Goodwin (Eds.) *Topics in Current Chemistry, Vol. 235*, Springer, Berlin/Heidelberg, **2004**.

[14] P. Gütlich, H. A. Goodwin (Eds.) *Topics in Current Chemistry, Vol. 234*, Springer, Berlin/Heidelberg, **2004**.

[15] Y. Garcia, P. Gütlich in *Topics in Current Chemistry, Vol. 234* (Eds.: P. Gütlich, H. A. Goodwin), Springer, Berlin/Heidelberg, **2004**, pp. 49–62.

[16] O. Kahn, *Molecular magnetism*, VCH, New York, NY, **1993**.

[17] V. Ksenofontov, A. B. Gaspar, P. Gütlich in *Topics in Current Chemistry, Vol. 235* (Eds.: P. Gütlich, H. A. Goodwin), Springer, Berlin/Heidelberg, **2004**, pp. 23–64.

[18] J.-F. Létard, P. Guionneau, L. Rabardel, Howard, Judith A. K., A. E. Goeta, D. Chasseau, O. Kahn, *Inorg. Chem.* **1998**, *37*, 4432.

[19] P. Gütlich, A. Hauser, *Coord. Chem. Rev.* **1990**, *97*, 1.

[20] P. Gütlich, A. Hauser, H. Spiering, *Angew. Chem. Int. Ed.* **1994**, *33*, 2024.

[21] P. Gütlich, V. Ksenofontov, A. B. Gaspar, *Coord. Chem. Rev.* **2005**, *249*, 1811.

[22] R. C. Stoufer, D. H. Busch, W. B. Hadley, *J. Am. Chem. Soc.* **1961**, *83*, 3732.

[23] M. A. Robinson, J. D. Curry, D. H. Busch, *Inorg. Chem.* **1963**, *2*, 1178.
[24] P. E. Figgins, D. H. Busch, *J. Am. Chem. Soc.* **1960**, *82*, 820.
[25] K. Madeja, E. König, *J. Inorg. Nucl. Chem.* **1963**, *25*, 377.
[26] E. König, K. Madeja, *Inorg. Chem.* **1967**, *6*, 48.
[27] E. König, K. Madeja, *Chem. Commun.* **1966**, 61.
[28] W. A. Baker, H. M. Bobonich, *Inorg. Chem.* **1964**, *3*, 1184.
[29] A. H. Ewald, R. L. Martin, I. G. Ross, A. H. White, *Proc. R. Soc. A* **1964**, *280*, 235.
[30] E. Frank, C. R. Abeledo, *Inorg. Chem.* **1966**, *5*, 1453.
[31] R. M. Golding, K. F. Mok, J. F. Duncan, *Inorg. Chem.* **1966**, *5*, 774.
[32] R. L. Mössbauer, *Z. Physik* **1958**, *151*, 124.
[33] E. König, *Coord. Chem. Rev.* **1968**, *3*, 471.
[34] H. A. Goodwin, *Coord. Chem. Rev.* **1976**, *18*, 293.
[35] P. Gütlich in *Structure and Bonding*, *Vol. 44* (Eds.: R. Bau, P. Gütlich, R. G. Teller), Springer, Berlin, Heidelberg, **1981**, pp. 83–195.
[36] P. Gütlich, Y. Garcia, H. A. Goodwin, *Chem. Soc. Rev.* **2000**, *29*, 419.
[37] M. A. Halcrow, *Chem. Soc. Rev.* **2011**, *40*, 4119.
[38] P. Gütlich, J. Jung, *J. Mol. Struct.* **1995**, *347*, 21.
[39] P. J. van Koningsbruggen, Y. Maeda, H. Oshio in *Topics in Current Chemistry*, *Vol. 233* (Eds.: P. Gütlich, H. A. Goodwin), Springer, Berlin/Heidelberg, **2004**, pp. 259–324.
[40] S. Hayami, Y. Komatsu, T. Shimizu, H. Kamihata, Y. H. Lee, *Coord. Chem. Rev.* **2011**, *255*, 1981.
[41] S. Hayami, M. R. Karim, Y. H. Lee, *Eur. J. Inorg. Chem.* **2013**, *2013*, 683.
[42] I. Krivokapic, M. Zerara, M. L. Daku, A. Vargas, C. Enachescu, C. Ambrus, P. Tregenna-Piggott, N. Amstutz, E. Krausz, A. Hauser, *Coord. Chem. Rev.* **2007**, *251*, 364.
[43] J. J. McGarvey, I. Lawthers, *J. Chem. Soc., Chem. Commun.* **1982**, 906.
[44] S. Decurtins, P. Gütlich, C. P. Köhler, H. Spiering, A. Hauser, *Chem. Phys. Lett.* **1984**, *105*, 1.
[45] S. Decurtins, P. Gütlich, K. M. Hasselbach, A. Hauser, H. Spiering, *Inorg. Chem.* **1985**, *24*, 2174.
[46] A. Hauser in *Topics in Current Chemistry*, *Vol. 234* (Eds.: P. Gütlich, H. A. Goodwin), Springer, Berlin/Heidelberg, **2004**, pp. 155–198.
[47] A. Hauser, *J. Chem. Phys.* **1991**, *94*, 2741.
[48] A. Hauser, *Chem. Phys. Lett.* **1986**, *124*, 543.
[49] D. Collison, C. D. Garner, C. M. McGrath, Mosselmans, J. Frederick W., M. D. Roper, J. M. W. Seddon, E. Sinn, N. A. Young, *J. Chem. Soc., Dalton Trans.* **1997**, 4371.

[50] G. Vankó, F. Renz, G. Molnár, T. Neisius, S. Kárpáti, *Angew. Chem. Int. Ed.* **2007**, *46*, 5306.

[51] P. Gütlich in *Topics in Current Chemistry, Vol. 234* (Eds.: P. Gütlich, H. A. Goodwin), Springer, Berlin/Heidelberg, **2004**, pp. 231–260.

[52] B. Weber, *Koordinationschemie. Grundlagen und aktuelle Trends*, Springer Spektrum, Berlin [u.a.], **2014**.

[53] H. Lueken, *Magnetochemie. Eine Einführung in Theorie und Anwendung*, Vieweg+Teubner Verlag, Wiesbaden, **1999**.

[54] D. F. Evans, *J. Chem. Soc.* **1959**, 2003.

[55] P. Gütlich, *Z. anorg. allg. Chem.* **2012**, *638*, 15.

[56] P. Gütlich, *Chemie in unserer Zeit* **1970**, 133.

[57] H. Paulsen, V. Schünemann, A. X. Trautwein, H. Winkler, *Coord. Chem. Rev.* **2005**, *249*, 255.

[58] A. Hauser, J. Adler, P. Gütlich, *Chem. Phys. Lett.* **1988**, *152*, 468.

[59] J. H. Takemoto, B. Hutchinson, *Inorg. Chem.* **1973**, *12*, 705.

[60] Y. Saito, J. Takemoto, B. Hutchinson, K. Nakamoto, *Inorg. Chem.* **1972**, *11*, 2003.

[61] J. H. Takemoto, B. Streusand, B. Hutchinson, *Spectrochim. Acta, Part A* **1974**, *30*, 827.

[62] D. C. Figg, R. H. Herber, *Inorg. Chem.* **1990**, *29*, 2170.

[63] R. H. Herber, *Inorg. Chem.* **1987**, *26*, 173.

[64] E. W. Müller, J. Ensling, H. Spiering, P. Gütlich, *Inorg. Chem.* **1983**, *22*, 2074.

[65] M. Sorai, S. Seki, *J. Phys. Chem. Solids* **1974**, *35*, 555.

[66] J.-P. Tuchagues, A. Bousseksou, G. Molnár, J. J. McGarvey, F. Varret in *Topics in Current Chemistry, Vol. 235* (Eds.: P. Gütlich, H. A. Goodwin), Springer, Berlin/Heidelberg, **2004**, pp. 84–103.

[67] M. Sorai in *Topics in Current Chemistry, Vol. 235* (Eds.: P. Gütlich, H. A. Goodwin), Springer, Berlin/Heidelberg, **2004**, pp. 153–170.

[68] E. König in *Structure and Bonding, Vol. 76* (Eds.: M. J. Clarke, J. B. Goodenough, J. A. Ibers, C. K. Jørgensen, D. M. P. Mingos, J. B. Neilands, G. A. Palmer, D. Reinen, P. J. Sadler, R. Weiss et al.), Springer, Berlin, Heidelberg, **1991**, pp. 51–152.

[69] E. M. Schubert, *J. Chem. Educ.* **1992**, *69*, 62.

[70] D. Ostfeld, I. A. Cohen, *J. Chem. Educ.* **1972**, *49*, 829.

[71] J. G. Schmidt, W. S. Brey, R. C. Stoufer, *Inorg. Chem.* **1967**, *6*, 268.

[72] J. Zarembowitch, O. Kahn, *Inorg. Chem.* **1984**, *23*, 589.

[73] M. D. Timken, S. R. Wilson, D. N. Hendrickson, *Inorg. Chem.* **1985**, *24*, 3450.

[74] B. J. Kennedy, K. S. Murray, P. R. Zwack, H. Homborg, W. Kalz, *Inorg. Chem.* **1986**, *25*, 2539.

[75] P. Guionneau, M. Marchivie, G. Bravic, J.-F. Létard, D. Chasseau in *Topics in Current Chemistry, Vol. 234* (Eds.: P. Gütlich, H. A. Goodwin), Springer, Berlin/Heidelberg, **2004**, pp. 97–128.

[76] P. C. Healy, A. H. White, *J. Chem. Soc. D* **1971**, *22*, 1446.

[77] H. Winkler, A. I. Chumakov, A. X. Trautwein in *Topics in Current Chemistry, Vol. 235* (Eds.: P. Gütlich, H. A. Goodwin), Springer, Berlin/Heidelberg, **2004**, pp. 137–152.

[78] J. A. Real, I. Castro, A. Bousseksou, M. Verdaguer, R. Burriel, M. Castro, J. Linares, F. Varret, *Inorg. Chem.* **1997**, *36*, 455.

[79] G. Sankar, J. M. Thomas, V. Varma, G. U. Kulkarni, C.N.R. Rao, *Chem. Phys. Lett.* **1996**, *251*, 79.

[80] S. Mebs, B. Braun, R. Kositzki, C. Limberg, M. Haumann, *Inorg. Chem.* **2015**, *54*, 11606.

[81] C. M. McGrath, C. J. O'Connor, C. Sangregorio, J. M.W. Seddon, E. Sinn, F. E. Sowrey, N. A. Young, *Inorg. Chem. Commun.* **1999**, *2*, 536.

[82] N. A. Young, *J. Chem. Soc., Dalton Trans.* **1996**, *38*, 1275.

[83] L. X. Chen, Z. Wang, J. K. Burdett, P. A. Montano, J. R. Norris, *J. Phys. Chem.* **1995**, *99*, 7958.

[84] R. Boča, M. Vrbová, R. Werner, W. Haase, *Chem. Phys. Lett.* **2000**, *328*, 188.

[85] S. B. Erenburg, N.V. Bausk, L.G. Lavrenova, L.N. Mazalov, *J. Magn. Magn. Mater.* **2001**, *226-230*, 1967.

[86] C. Hannay, M.-J. Hubin-Franskin, F. Grandjean, V. Briois, A. Polian, S. Trofimenko, G. J. Long, *Inorg. Chem.* **1997**, *36*, 5580.

[87] G. Vankó, A. Bordage, P. Glatzel, E. Gallo, M. Rovezzi, W. Gawelda, A. Galler, C. Bressler, G. Doumy, A. M. March et al., *J. Electron. Spectros. Relat. Phenom.* **2013**, *188*, 166.

[88] G. Vankó, T. Neisius, G. Molnar, F. Renz, S. Karpati, A. Shukla, F. M. F. de Groot, *J. Phys. Chem. B* **2006**, *110*, 11647.

[89] G. Vankó, J.-P. Rueff, A. Mattila, Z. Németh, A. Shukla, *Phys. Rev. B* **2006**, *73*.

[90] A. Bousseksou, J. J. McGarvey, F. Varret, J. A. Real, J.-P. Tuchagues, A. C. Dennis, M. L. Boillot, *Chem. Phys. Lett.* **2000**, *318*, 409.

[91] B. Gallois, J. A. Real, C. Hauw, J. Zarembowitch, *Inorg. Chem.* **1990**, *29*, 1152.

[92] J. A. Real, B. Gallois, T. Granier, F. Suez-Panama, J. Zarembowitch, *Inorg. Chem.* **1992**, *31*, 4972.

[93] E. J. MacLean, C. M. McGrath, C. J. O'Connor, C. Sangregorio, J. M. W. Seddon, E. Sinn, F. E. Sowrey, S. J. Teat, A. E. Terry, G. B. M. Vaughan et al., *Chem. Eur. J.* **2003**, *9*, 5314.

[94] D. C. Koningsberger, R. Prins, *X-ray absorption. Principles, applications, techniques of EXAFS, SEXAFS, and XANES*, Wiley, New York, **1988**.

[95] B. K. Teo, *EXAFS: Basic Principles and Data Analysis*, Springer Berlin Heidelberg, Berlin, Heidelberg, **1986**.

[96] G. Bunker, *Introduction to XAFS. A practical guide to X-ray absorption fine structure spectroscopy*, Cambridge University Press, Cambridge, New York, Melbourne, Madrid, Cape Town, Singapore, São Paulo, Delhi, Dubai, Tokyo, **2010**.

[97] J. C. Maxwell, *Philosophical Transactions of the Royal Society of London* **1865**, *155*, 459.

[98] H. Winick in *Proceedings of the 1997 Particle Accelerator Conference. Vancouver, B.C., Canada, 12 - 16 May 1997*, IEEE Operations Center, Piscataway, NJ, **1998**, pp. 37–41.

[99] A. Balerna, S. Mobilio in *Synchrotron Radiation. Basics, Methods and Applications* (Eds.: S. Mobilio, F. Boscherini, C. Meneghini), Springer, Heidelberg, **2015**, pp. 3–28.

[100] A. Sommerfeld, *Ann. Phys.* **1916**, *356*, 1.

[101] M. de Broglie, *Comptes Rendus* **1913**, *157*, 924.

[102] F. W. Lytle, *J. Synchrotron Rad.* **1999**, *6*, 123.

[103] H. Fricke, *Phys. Rev.* **1920**, *16*, 202.

[104] G. Hertz, *Z. Physik* **1920**, *3*, 19.

[105] A. E. Lindh, *Z. Physik* **1921**, *6*, 303.

[106] A. E. Lindh, *Z. Physik* **1925**, *31*, 210.

[107] A. E. Lindh, *Z. Physik* **1930**, *63*, 106.

[108] D. Coster, J. Veldkamp, *Z. Physik* **1931**, *70*, 306.

[109] D. Coster, J. Veldkamp, *Z. Physik* **1932**, *74*, 191.

[110] B. Kievit, G. A. Lindsay, *Phys. Rev.* **1930**, *36*, 648.

[111] G. A. Lindsay, *Z. Physik* **1931**, *71*, 735.

[112] W. Kossel, *Z. Physik* **1920**, *1*, 119.

[113] R. d. L. Kronig, *Z. Physik* **1931**, *70*, 317.

[114] R. d. L. Kronig, *Z. Physik* **1932**, *75*, 191.

[115] L. V. Azároff, *Rev. Mod. Phys.* **1963**, *35*, 1012.

[116] D. E. Sayers, E. A. Stern, F. W. Lytle, *Phys. Rev. Lett.* **1971**, *27*, 1204.

[117] E. A. Stern, *Phys. Rev. B* **1974**, *10*, 3027.

[118] F. W. Lytle, D. E. Sayers, E. B. Moore, *Appl. Phys. Lett.* **1974**, *24*, 45.

[119] E. A. Stern, D. E. Sayers, F. W. Lytle, *Phys. Rev. B* **1975**, *11*, 4836.

[120] F. W. Lytle, D. E. Sayers, E. A. Stern, *Phys. Rev. B* **1975**, *11*, 4825.

[121] D. C. Koningsberger, B. L. Mojet, G. E. van Dorssen, D. E. Ramaker, *Top. Catal.* **2000**, *10*, 143.

[122] M. Bauer, H. Bertagnolli, *Bunsen-Magazin* **2007**, *6*, 216.

[123] T. Yamamoto, *X-Ray Spectrom.* **2008**, *37*, 572.

[124] S. Nozawa, T. Sato, M. Chollet, K. Ichiyanagi, A. Tomita, H. Fujii, S.-i. Adachi, S.-y. Koshihara, *J. Am. Chem. Soc.* **2010**, *132*, 61.

[125] W. Gawelda, V.-T. Pham, M. Benfatto, Y. Zaushitsyn, M. Kaiser, D. Grolimund, S. L. Johnson, R. Abela, A. Hauser, C. Bressler et al., *Phys. Rev. Lett.* **2007**, *98*, 57401.

[126] S. J. Gurman, R. F. Pettifer, *Phil. Mag. B* **2006**, *40*, 345.

[127] P. A. Lee, J. B. Pendry, *Phys. Rev. B* **1975**, *11*, 2795.

[128] P. A. Lee, G. Beni, *Phys. Rev. B* **1977**, *15*, 2862.

[129] P. A. Lee, B.-K. Teo, A. L. Simons, *J. Am. Chem. Soc.* **1977**, *99*, 3856.

[130] C. A. Ashley, S. Doniach, *Phys. Rev. B* **1975**, *11*, 1279.

[131] W. H. Bragg, W. L. Bragg, *Proc. R. Soc. Lond. A* **1913**, *88*, 428.

[132] W. Friedrich, P. Knipping, M. Laue, *Ann. Phys.* **1913**, *346*, 971.

[133] W. H. Bragg, W. L. Bragg, *X rays and crystal structure*, G. Bell and Sons, Ltd., London, **1915**.

[134] P. Glatzel, R. Alonso-Mori, D. Sokaras in *X-ray absorption and X-ray emission spectroscopy. Theory and applications* (Eds.: J. A. van Bokhoven, C. Lamberti), John Wiley & Sons Inc, Chichester West Sussex, **2016**, pp. 125–149.

[135] A. H. Compton, *Phys. Rev.* **1923**, *21*, 409.

[136] A. H. Compton, *Phys. Rev.* **1923**, *21*, 483.

[137] H.G.J. Moseley, *Phil. Mag.* **1913**, *26*, 1024.

[138] H. H. Johann, *Z. Physik* **1931**, *69*, 185.

[139] T. Johansson, *Z. Physik* **1933**, *82*, 507.

[140] L. von Hámos, *Naturwissenschaften* **1932**, *20*, 705.

[141] B. B. Watson, *Rev. Sci. Instrum.* **1937**, *8*, 480.

[142] Y. Cauchois, *C. R. Acad. Sci.* **1932**, *194*, 362.

[143] Y. Cauchois, *J. Phys. Radium* **1932**, *3*, 320.

[144] J. W. M. DuMond, B. B. Watson, *Phys. Rev.* **1934**, *46*, 316.

[145] B. Beckhoff, B. Kanngießer, N. Langhoff, R. Wedell, H. Wolff, *Handbook of Practical X-Ray Fluorescence Analysis*, Springer Berlin Heidelberg, Berlin, Heidelberg, **2006**.

[146] J. A. van Bokhoven, C. Lamberti (Eds.) *X-ray absorption and X-ray emission spectroscopy. Theory and applications*, John Wiley & Sons Inc, Chichester West Sussex, **2016**.

[147] P. Glatzel, U. Bergmann, *Coord. Chem. Rev.* **2005**, *249*, 65.

[148] M. Rovezzi, P. Glatzel, *Semicond. Sci. Technol.* **2014**, *29*, 23002.

[149] L. J. P. Ament, M. van Veenendaal, T. P. Devereaux, J. P. Hill, J. van den Brink, *Rev. Mod. Phys.* **2011**, *83*, 705.

[150] J. J. Sakurai, *Advanced quantum mechanics*, Addison-Wesley, Reading, Mass., **1998**.

[151] H. A. Kramers, W. Heisenberg, *Z. Physik* **1925**, *31*, 681.

[152] R. Kurian, K. Kunnus, P. Wernet, S. M. Butorin, P. Glatzel, F. M. F. de Groot, *J. Phys.: Condens. Matter* **2012**, *24*, 452201.

[153] F. de Groot, A. Kotani, *Core level spectroscopy of solids*, CRC Press, Boca Raton, **2008**.

[154] R. D. Cowan, *The theory of atomic structure and spectra*, Univ. of California Press, Berkeley, Calif., **1981**.

[155] K. Tsutsumi, *J. Phys. Soc. Jpn.* **1959**, *14*, 1696.

[156] P. Glatzel, *Ph.D. Thesis*, Hamburg University, Hamburg, **2001**.

[157] J.-P. Rueff, C.-C. Kao, V. V. Struzhkin, J. Badro, J. Shu, R. J. Hemley, H. K. Mao, *Phys. Rev. Lett.* **1999**, *82*, 3284.

[158] H. Osawa, T. Iwazumi, H. Shoji, E. Hirai, T. Nakamura, Y. Ogawa, T. Ishikawa, S. Koshihara, Y. Isozumi, S. Nanao, *Phase Transitions* **2010**, *75*, 919.

[159] G. Peng, F. M. F. de Groot, K. Hämäläinen, J. A. Moore, X. Wang, M. M. Grush, J. B. Hastings, D. P. Siddons, W. H. Armstrong, *J. Am. Chem. Soc.* **1994**, *116*, 2914.

[160] S. D. Gamblin, D. S. Urch, *J. Electron. Spectros. Relat. Phenom.* **2001**, *113*, 179.

[161] J. P. Rueff, A. Shukla, A. Kaprolat, M. Krisch, M. Lorenzen, F. Sette, R. Verbeni, *Phys. Rev. B* **2001**, *63*.

[162] U. Bergmann, C. R. Horne, T. J. Collins, J. M. Workman, S. P. Cramer, *Chem. Phys. Lett.* **1999**, *302*, 119.

[163] U. Bergmann, P. Glatzel, *Photosynth. Res.* **2009**, *102*, 255.

[164] F. de Groot, *Chem. Rev.* **2001**, *101*, 1779.

[165] N. Lee, T. Petrenko, U. Bergmann, F. Neese, S. DeBeer, *J. Am. Chem. Soc.* **2010**, *132*, 9715.

[166] C. J. Pollock, S. DeBeer, *Acc. Chem. Res.* **2015**, *48*, 2967.

[167] F. M. F. de Groot, M. H. Krisch, J. Vogel, *Phys. Rev. B* **2002**, *66*, 621.

[168] K. Hämäläinen, D. P. Siddons, J. B. Hastings, L. E. Berman, *Phys. Rev. Lett.* **1991**, *67*, 2850.

[169] P. Glatzel, M. Sikora, G. Smolentsev, M. Fernández-García, *Catal. Today* **2009**, *145*, 294. Reproduced with permission from Catalysis Today, Elsevier. License ID 4352121064599.

[170] P. Glatzel, M. Sikora, G. Smolentsev, M. Fernández-García, *Catal. Today* **2009**, *145*, 294.

[171] E. Kleimenov, A. Bergamaschi, J. van Bokhoven, M. Janousch, B. Schmitt, M. Nachtegaal, *J. Phys.: Conf. Ser.* **2009**, *190*, 12035.

[172] M. Schmitz, *Dissertation*, Technische Universität, Kaiserslautern, **2016**.

[173] H.-J. Krüger, *Coord. Chem. Rev.* **2009**, *253*, 2450.

[174] M. Newville, *J. Synchrotron Rad.* **2001**, *8*, 322.

[175] M. Newville, P. Livins, Y. Yacoby, J. J. Rehr, E. A. Stern, *Phys. Rev. B* **1993**, *47*, 14126.

[176] T. S. Ertel, H. Bertagnolli, S. Hückmann, U. Kolb, D. Peter, *Appl. Spectrosc.* **1992**, *46*, 690.

[177] B. Ravel, M. Newville, *J. Synchrotron Rad.* **2005**, *12*, 537.

[178] N. Binsted, J. F. W. Mosselmans, *EXCURV98 Manual*, Daresbury, UK.
[179] N. Binsted, S. S. Hasnain, *J. Synchrotron Rad.* **1996**, *3*, 185.
[180] M. Bauer, H. Bertagnolli, *J. Phys. Chem. B* **2007**, *111*, 13756.
[181] N. Binsted, R. W. Strange, S. S. Hasnain, *Biochemistry* **1992**, *31*, 12117.
[182] R. W. Joyner, K. J. Martin, P. Meehan, *J. Phys. C: Solid State Phys.* **1987**, *20*, 4005.
[183] B. Ravel, M. Newville, *Phys. Scr.* **2005**, 1007.
[184] F. Neese, *WIREs Comput Mol Sci* **2012**, *2*, 73.
[185] J. P. Perdew, *Phys. Rev. B* **1986**, *33*, 8822.
[186] A. D. Becke, *Phys. Rev. A* **1988**, *38*, 3098.
[187] F. Neese, *Inorg. Chim. Acta* **2002**, *337*, 181.
[188] D. A. Pantazis, X.-Y. Chen, C. R. Landis, F. Neese, *J. Chem. Theory Comput.* **2008**, *4*, 908.
[189] S. DeBeer George, F. Neese, *Inorg. Chem.* **2010**, *49*, 1849.
[190] S. DeBeer George, T. Petrenko, F. Neese, *J. Phys. Chem. A* **2008**, *112*, 12936.
[191] M. U. Delgado-Jaime, S. DeBeer, M. Bauer, *Chem. Eur. J.* **2013**, *19*, 15888.
[192] S. DeBeer George, T. Petrenko, F. Neese, *Inorg. Chim. Acta* **2008**, *361*, 965.

8 List of Figures

9 List of Tables

Appendix

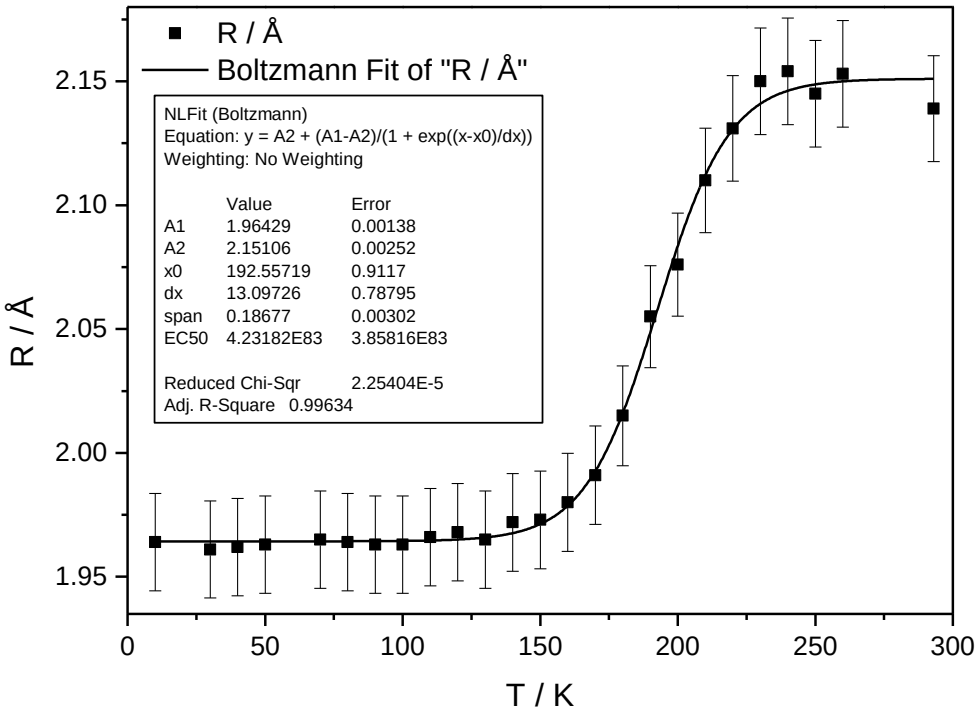

Figure A.1: EXAFS spectroscopy, Fit model 1A: Boltzmann fit of the Fe-N distances.

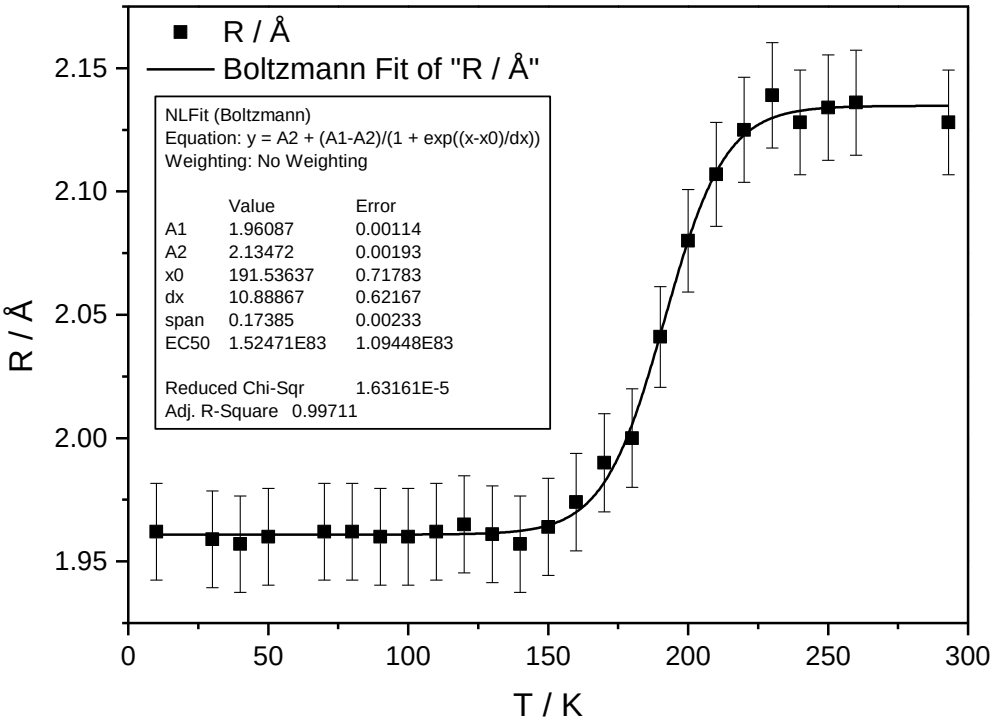

Figure A.2: EXAFS spectroscopy, Fit model 1B: Boltzmann fit of the Fe-N distances.

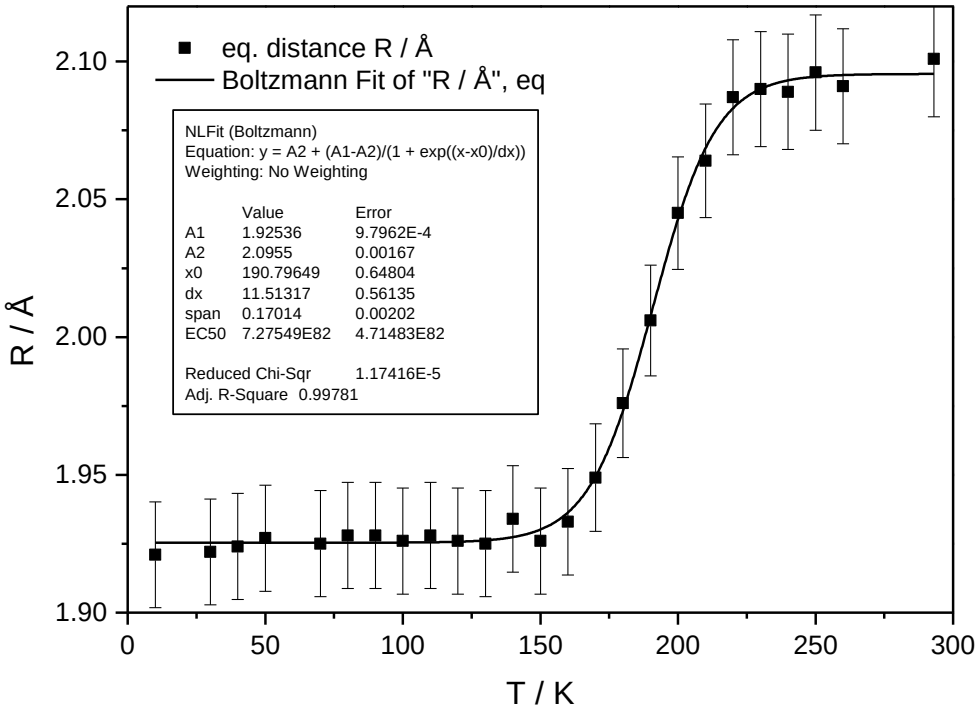

Figure A.3: EXAFS spectroscopy, Fit Model 2A: Boltzmann fit of the equatorial Fe-N bond lengths.

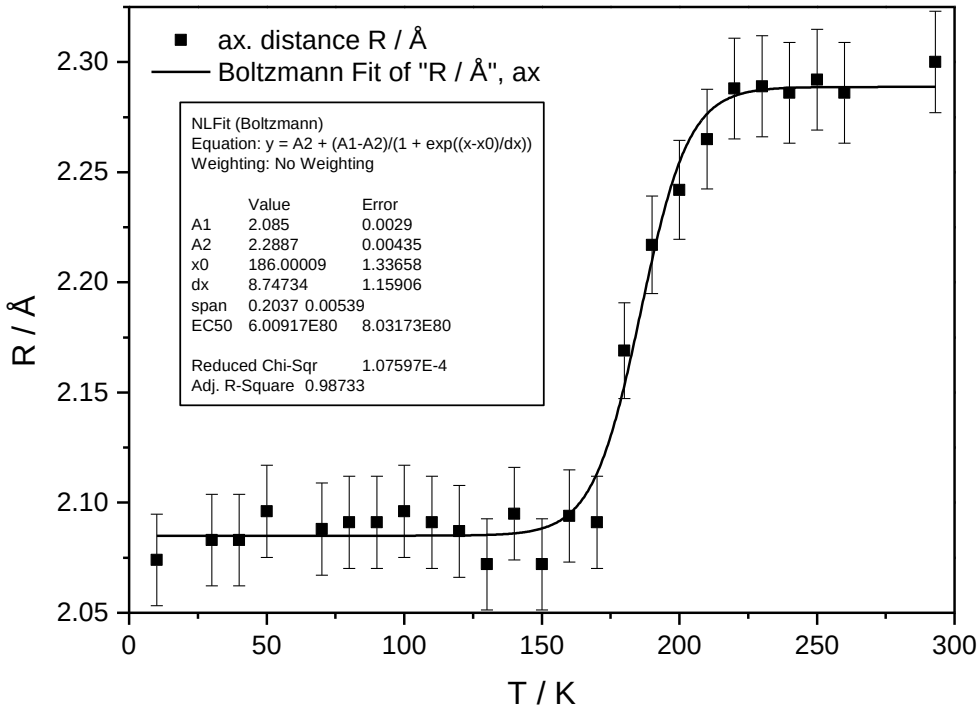

Figure A4: EXAFS spectroscopy, Fit Model 2A: Boltzmann fit of the axial Fe-N bond lengths.

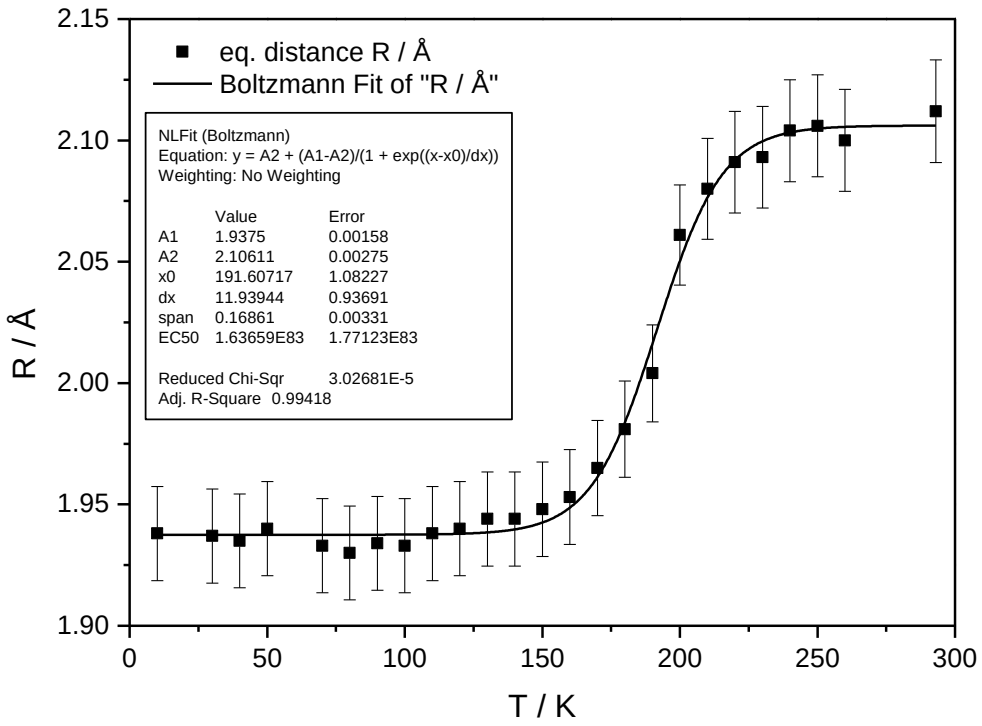

Figure A.5: EXAFS spectroscopy, Fit Model 2C: Boltzmann fit of the equatorial Fe-N bond lengths.

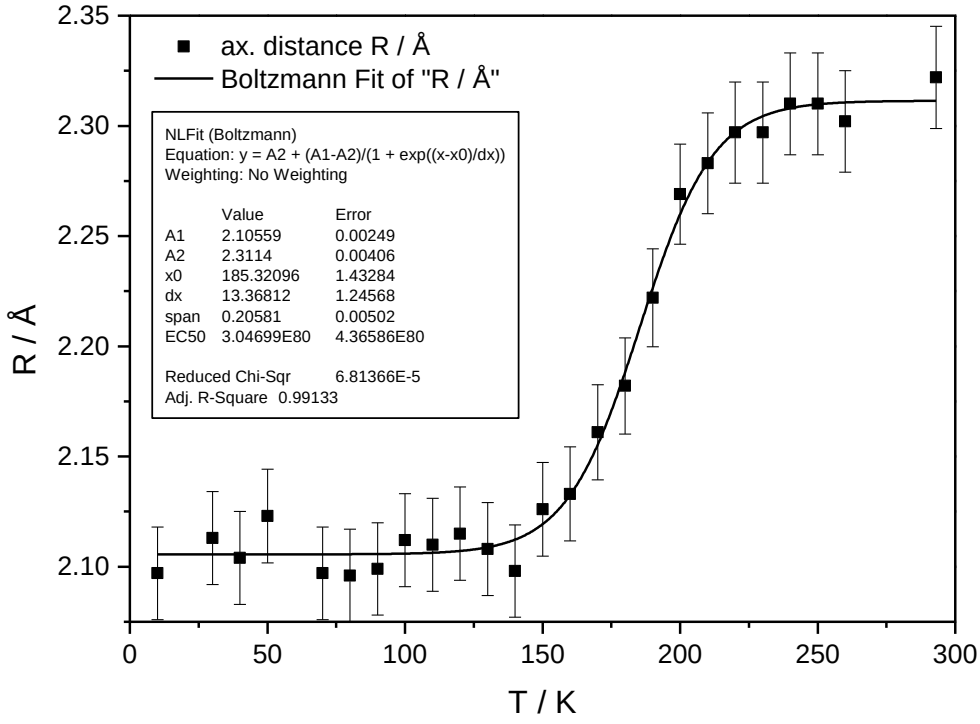

Figure A.6: EXAFS spectroscopy, Fit Model 2C: Boltzmann fit of the axial Fe-N bond lengths.

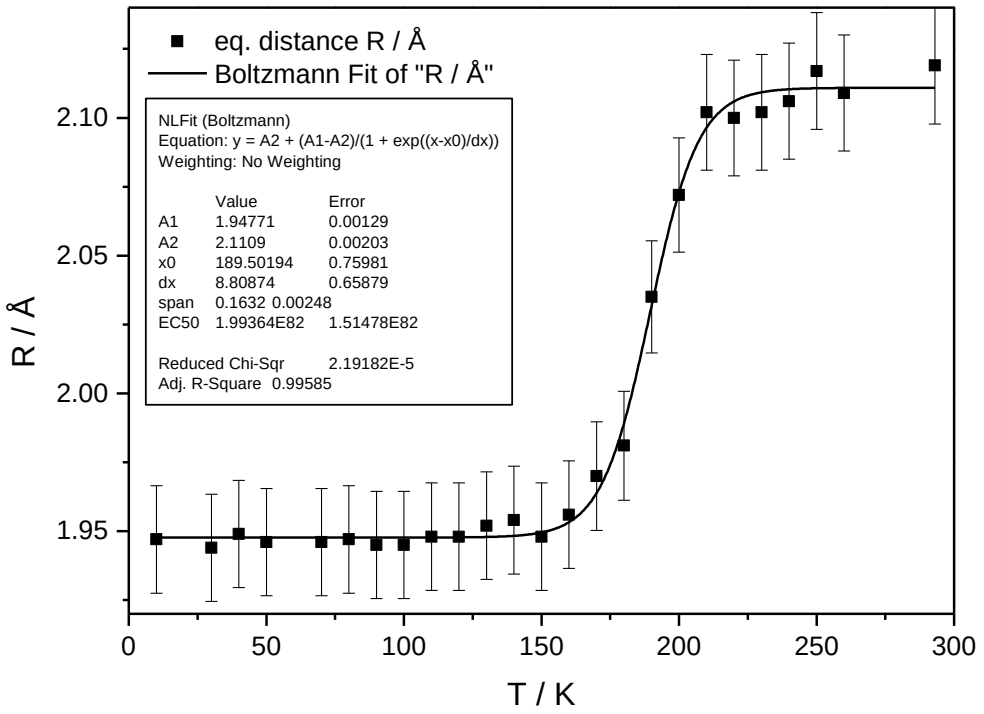

Figure A.7: EXAFS spectroscopy, Fit Model 2E: Boltzmann fit of the equatorial Fe-N bond lengths.

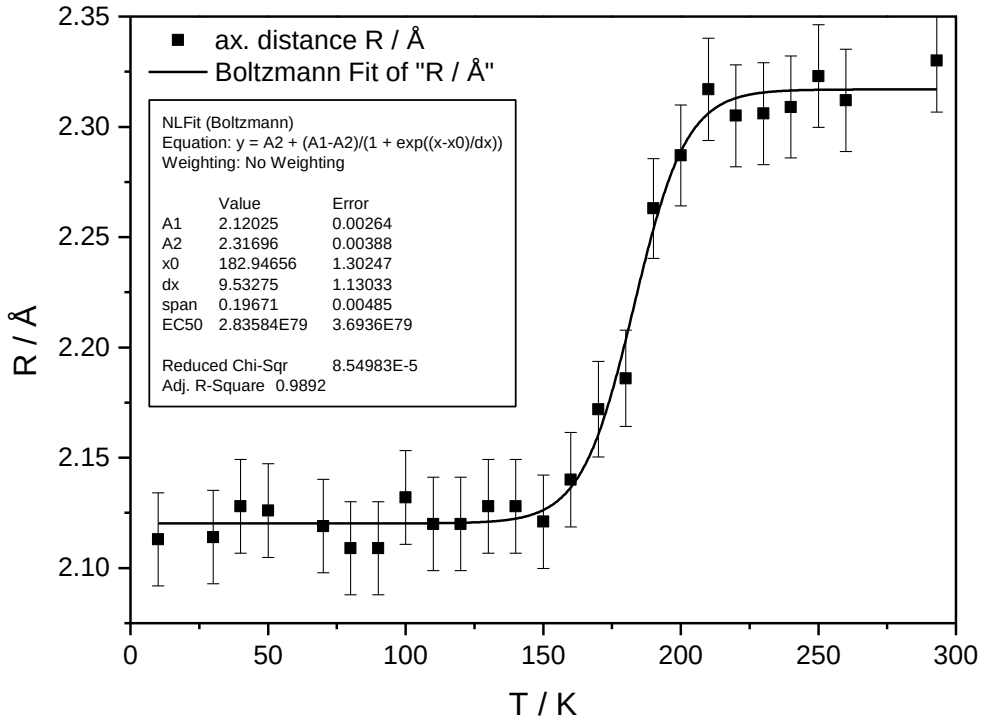

Figure A.8: EXAFS spectroscopy, Fit Model 2E: Boltzmann fit of the axial Fe-N bond lengths.

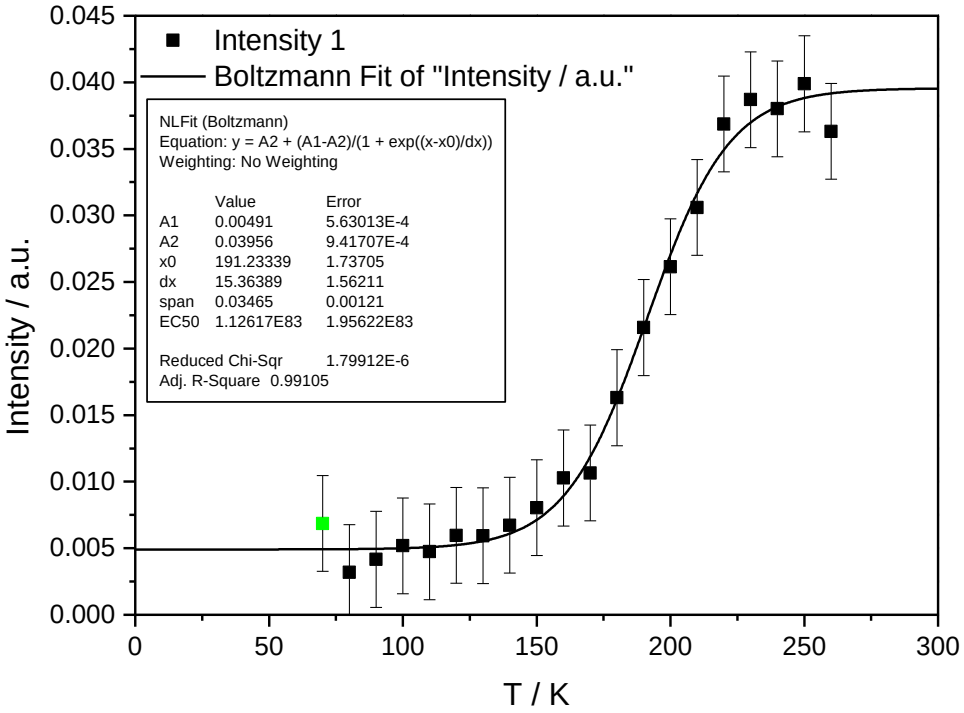

Figure A.9: HERFD-XANES spectroscopy: Plot of intensity 1 versus temperature with resulting sigmoidal Boltzmann fit function.

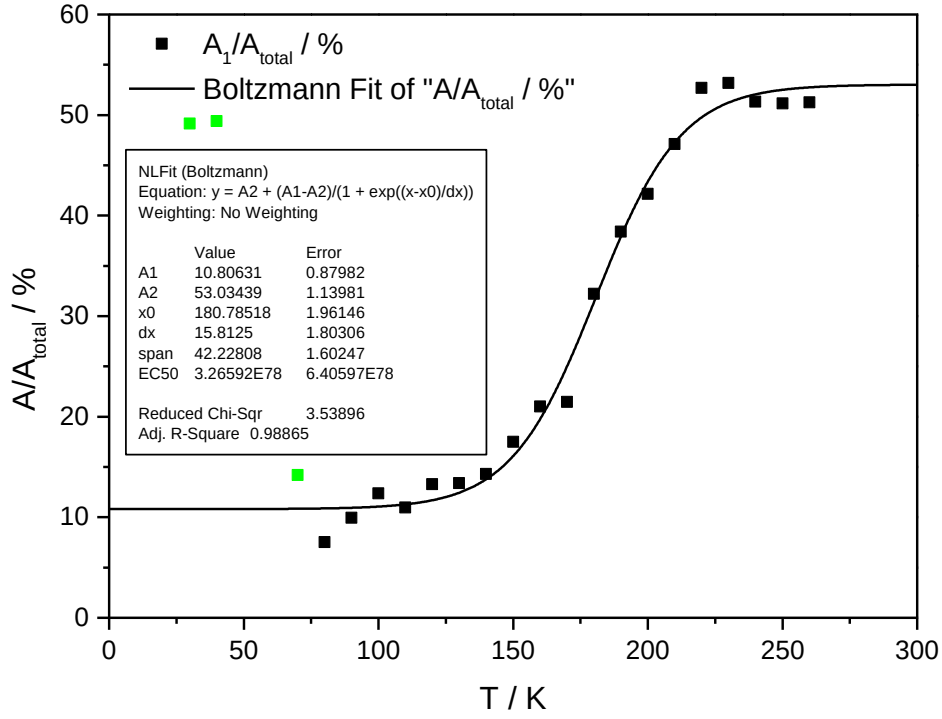

Figure A.10: HERFD-XANES spectroscopy: Plot of ratio between area of signal 1 and total area with the resulting sigmoidal Boltzmann fit function. Green marked data points were excluded from the fit.

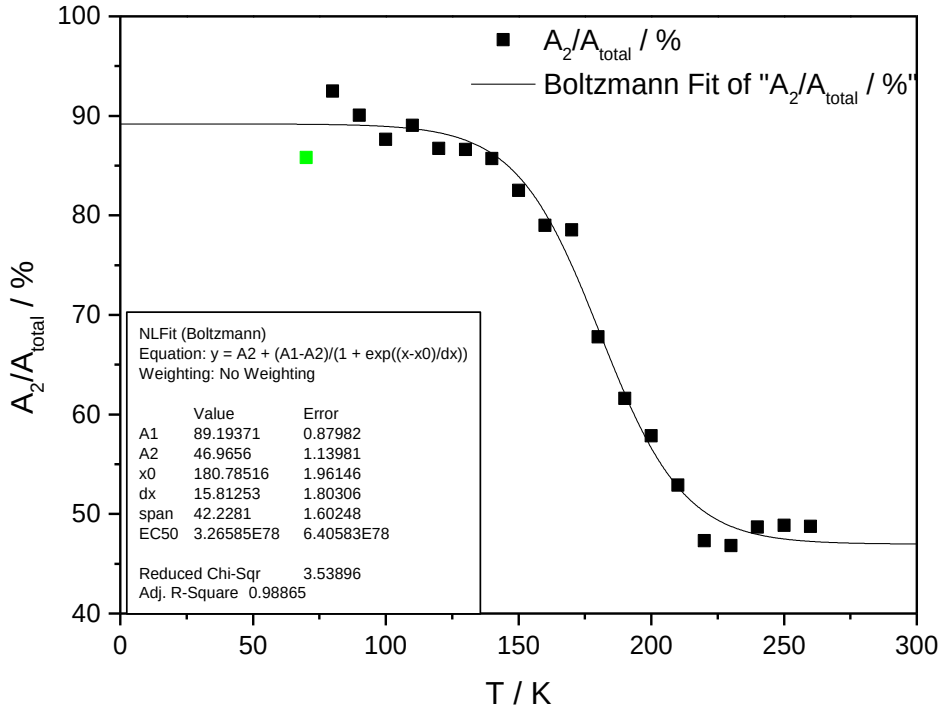

Figure A.11: HERFD-XANES spectroscopy: Plot of ratio between area of signal 2 and total area with the resulting sigmoidal Boltzmann fit function. Green marked data points were excluded from the fit.

Table A.1: HERFD-XANES spectroscopy: Orbital composition of relevant donor and acceptor orbitals of the HS state of [Fe(L-N_4Bn_2)$(NCS)_2$]. In the simplified ligand field picture, these orbitals can be assigned to the t_{2g} and e_g orbitals.

Element character [a)]	**HOMO 151β**	**LUMO 152β**	**LUMO+1 153β**	**LUMO+2 154β**	**LUMO+3 155β**
Fe (s, p, d)	50.2%	71.6%	79.1%	34.2%	1.8%
Fe (d)	50.1%	71.6%	78.3%	33.6%	1.8%
S (s, p, d)	14.0%	9.4%	6.6%	2.6%	--
N (s, p, d)	9.6%	5.6%	5.6%	15.0%	4.6%
C (s, p, d)	24.2%	11.0%	5.8%	44.6%	86.8%

a) The element character of the involved orbitals was determined via Loewdin population analysis. Details of the calculation can be found in chapter 5.2.

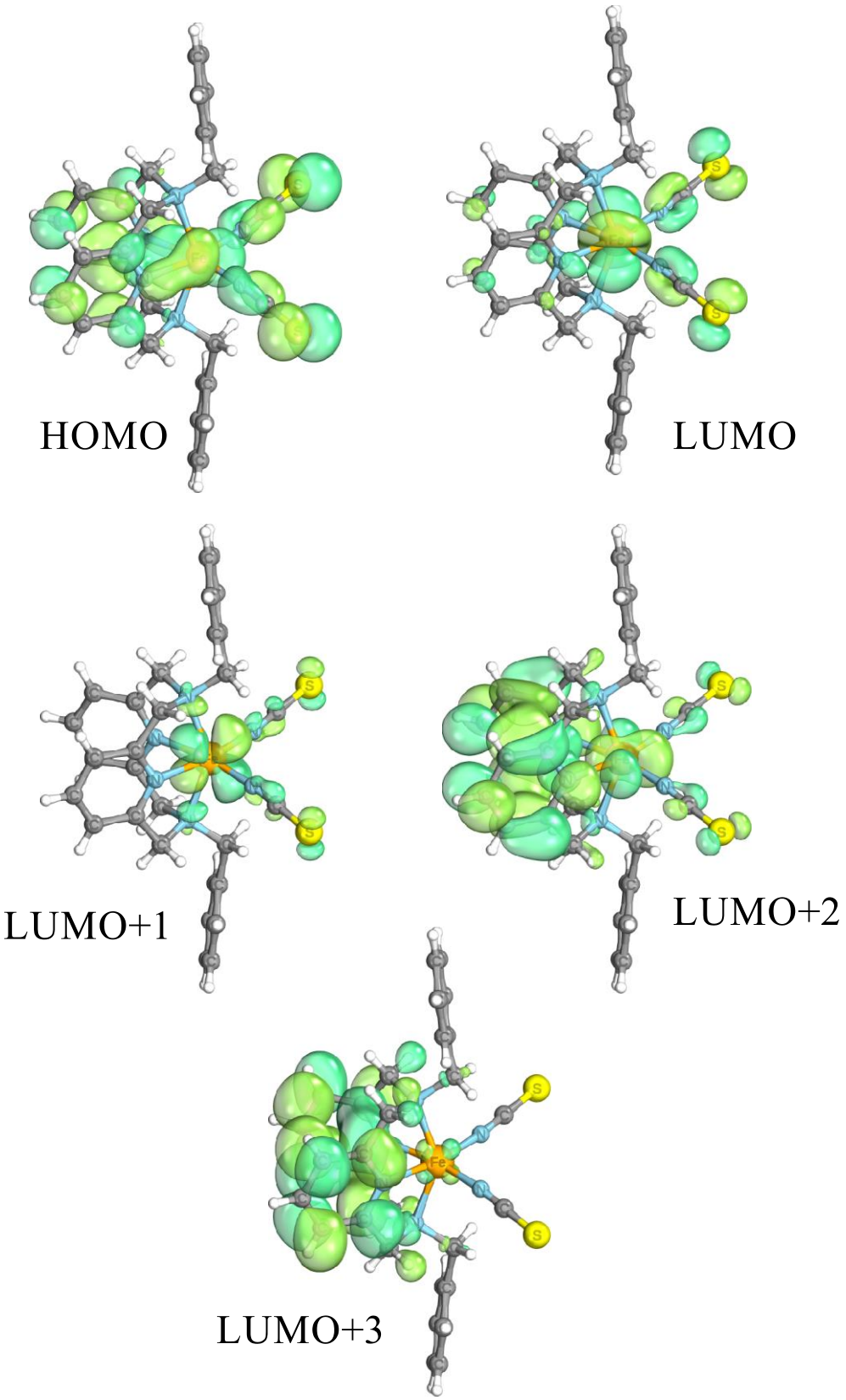

Figure A.12: HERFD-XANES spectroscopy: Selected molecular β-orbitals of relevant donor and acceptor states.

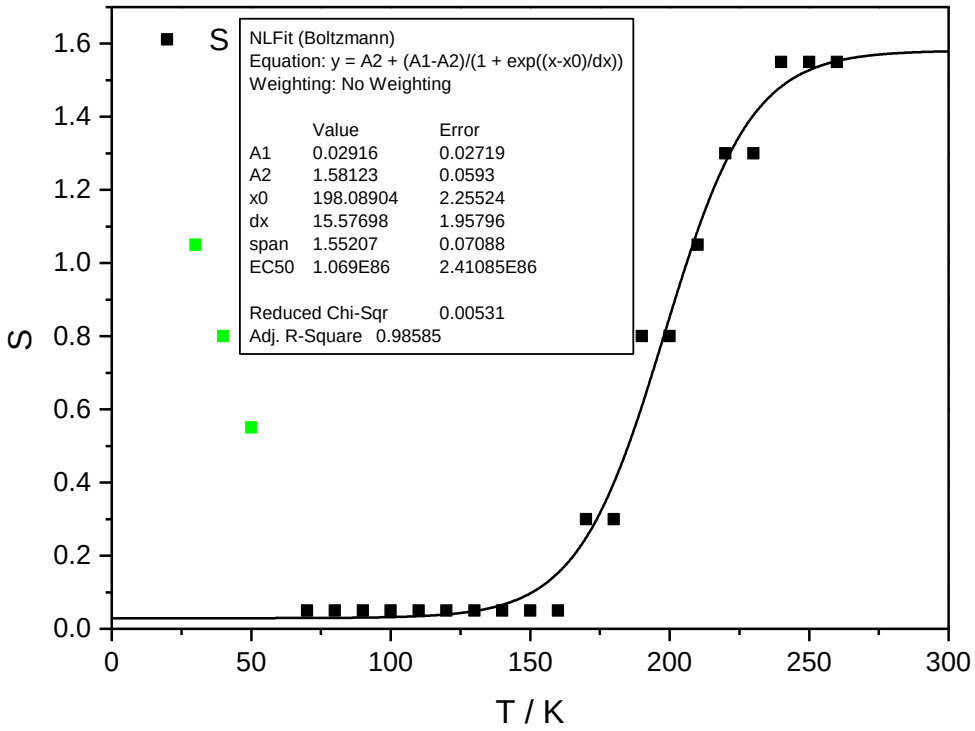

Figure A.13: CtC emission spectroscopy: Plot of spin state *S* calculated with use of $E_{Em}(K\beta_{1,3})$ vs. temperature *T*.

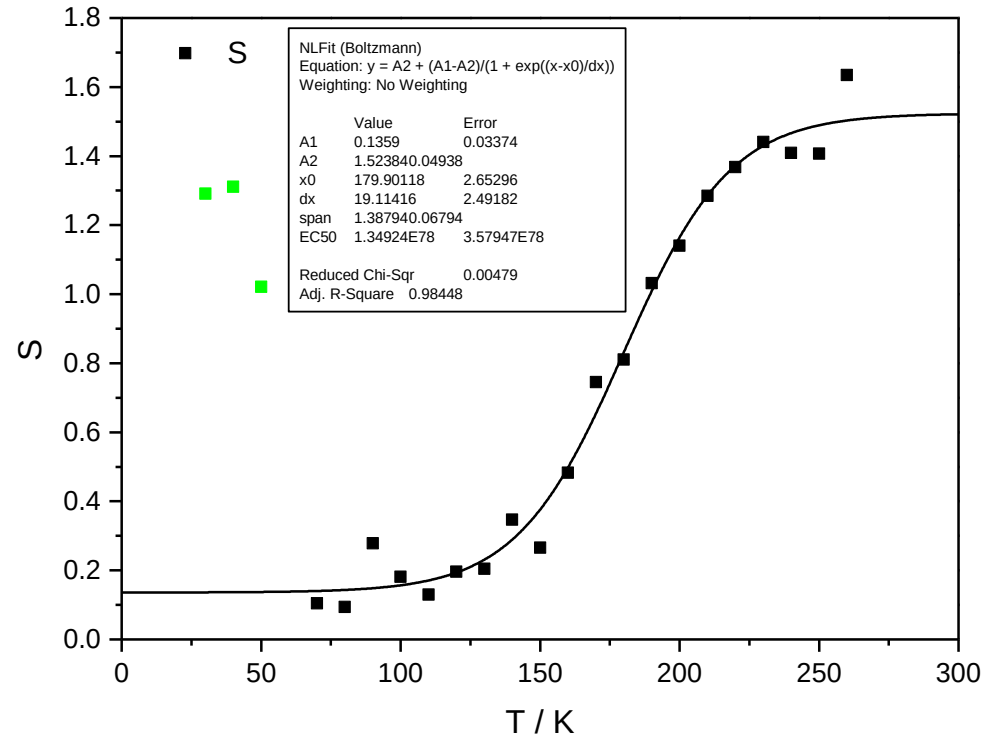

Figure A.14: CtC emission spectroscopy: Plot of spin state *S* calculated with use of *Inten.(Kβ′)* vs. temperature *T*.

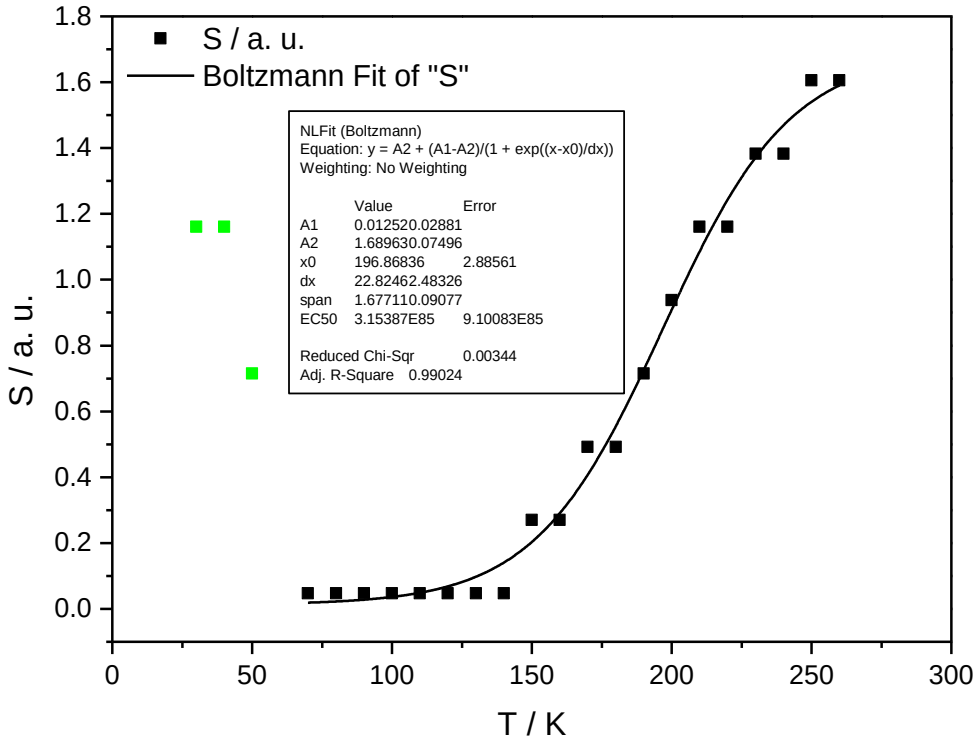

Figure A.15: CtC emission spectroscopy: Plot of spin state *S* calculated with use of *E*(FC1) vs. temperature *T*.

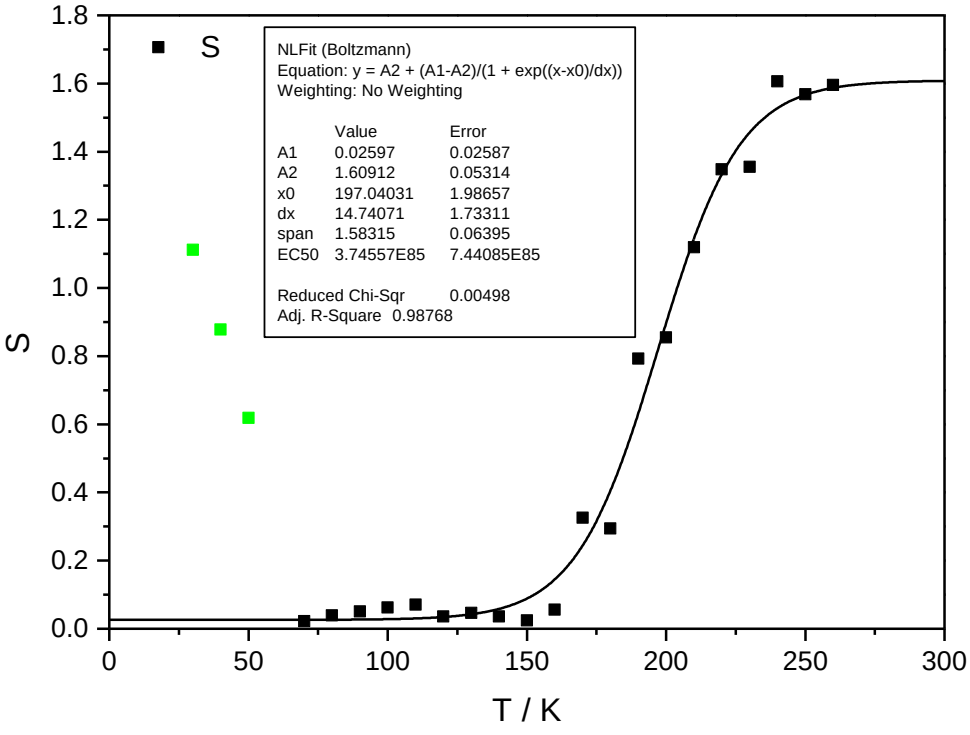

Figure A.16: CtC emission spectroscopy: Plot of spin state *S* calculated with use of ΔE_{CP} vs. temperature *T*; modified calibration curve.

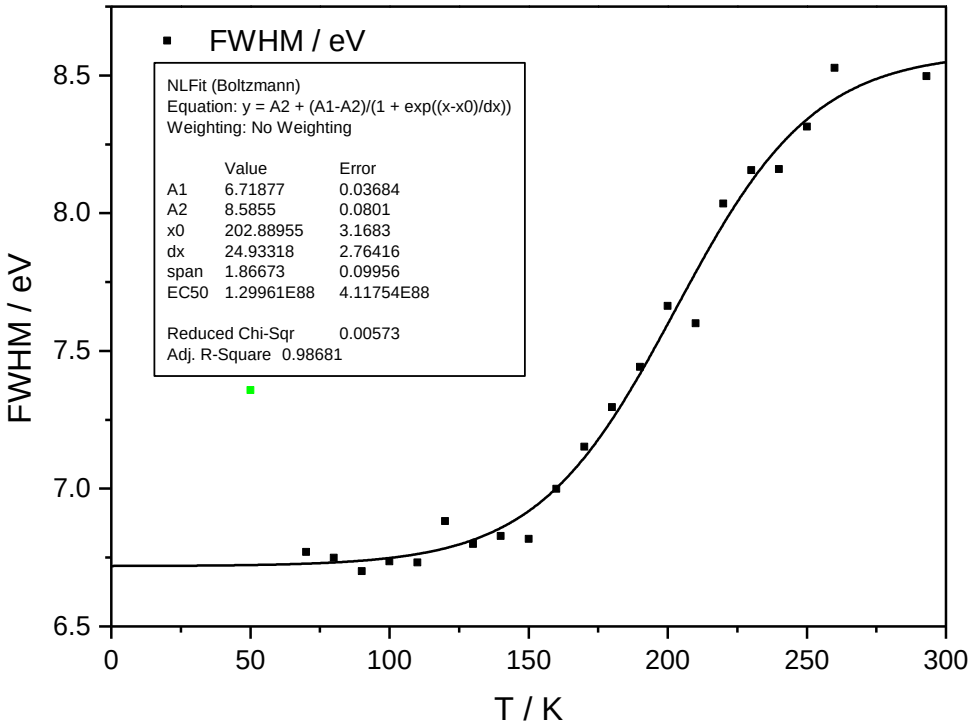

Figure A.17: VtC emission spectroscopy: Plot of FWHM versus temperature with resulting sigmoidal Boltzmann fit function.

Table A.2: VtC emission spectroscopy: Orbital composition of donor orbitals of most intense transitions in the energy range from 7109 to 7112 eV for LS and HS.

Transition	E / eV	Elemental character [a)]
LS 153 → Fe 1s	7110.947	40.5 % Fe d 12.2 % N 6.8 % C 37.6 % S
LS 152 → Fe 1s	7110.923	33.9 % Fe d 12.0 % N 7.4 % C 44.4% S
LS 151 → Fe 1s	7110.873	19.2 % Fe d 15.2 % N 16.6 % C 47.4 % S
LS 149 → Fe 1s	7109.983	44.9 % Fe d 8.8 % N 9.8 % C 33.6 % S
LS 148 → Fe 1s	7109.955	54.7 % Fe d 7.0 % N 7.6 % C 27.4 % S
HS 151β → Fe 1s	7111.371	50.1 % Fe d 9.6 % N 24.2 % C 13.8 % S
HS 148β → Fe 1s	7110.204	6.9 % Fe d 17.4 % N 11.6 % C 62.4 % S
HS 155α → Fe 1s	7110.685	58.4 % Fe d 28.8. % N 8.4 % C 1.4 % S
HS 150α → Fe 1s	7109.996	47.6 % Fe d 34.6 % N 12.2 % C 0.6 % S

a) The element character of the involved orbitals was determined via Loewdin population analysis. Details of the calculation can be found in chapter 5.2.